The Role of Pre-Implanted Helium and Carbon on Cavity Evolution in Ion-Irradiated T91

by

Anthony Manuel Monterrosa

A dissertation submitted in partial fulfillment
of the requirements for the degree of
Doctor of Philosophy
(Nuclear Engineering and Radiological Sciences)
in The University of Michigan
2018

Doctoral Committee:

Professor Gary S. Was, Chair
Professor Fei Gao
Professor Amit Misra
Adjunct Professor Roger Stoller

Anthony Manuel Monterrosa

amonterr@umich.edu

ORCID iD: 0000-0002-3915-706X

To my friends and family

ACKNOWLEDGEMENTS

I would like to thank my advisor, Gary Was, for providing the opportunity to pursue my passion for science at the next level and providing insight, advice, and guidance throughout my years as a Ph.D. student. I can most definitely say that I have become a better scientist as a result. I would also like to thank my committee members, Dr. Amit Misra, Dr. Fei Gao, and Dr. Roger Stoller for their input, which greatly improved the thesis.

I am very grateful to all members of the Was research group, Dr. Janelle Wharry, Dr. Anne Campbell, Dr. Cheng Xu, Dr. Mike McMurtrey, Dr. Tyler Moss, Dr. Gokce Gulsoy, Dr. Kale Stephenson, Dr. Stephen Raiman, Dr. Shyam Dwaraknath, Dr. George Jiao, Dr. Peng Wang, Dr. Miao Song, Dr. Mi Wang, Dr. Wenjun Kuang, Dr. Calvin Lear, Justin Hesterberg, Gerrit VanCoevering, Drew Johnson, Rigel Hanbury, Robert Wahlen, Samara Levine, Katey Thomas, Rajan Bhambroo, and Michael Higgins. I am especially grateful to the heavy ion irradiation crew, Dr. Elizabeth Getto, Stephen Taller, and David Woodley, for the scientific discussions, advice, and help watching irradiations.

Thank you to the MIBL Staff, Dr. Ovidiu Toader, Dr. Fabian Naab, Dr. Ethan Uberseder, Thomas Kubley and Dr. Prabir Roy, who were instrumental in performing the helium implantations and ion irradiations, and who were always willing to help, even in the wee hours of the night. I couldn't have done it without you.

I also want to thank the $(MC)^2$ staff for help with FIB liftouts and TEM, especially Dr. Kai Sun, who was always patient and willing to pass on his mastery of the microscopes.

Thank you to the NSF and NEUP, which funded my work throughout the Ph.D. This work would not have been possible without the support.

To my parents, Alex and Silvia Monterrosa, who formed the backbone of my support throughout the years. Thank you for always being there, listening, and for encouraging me, and

believing in me, even when I couldn’t make it home for the holidays. Your unconditional love has helped me make it this far. To Nicholas and Jonathan Monterrosa, for instilling my drive to always better myself. You served as my confidence and motivation to constantly keep improving and overcoming whatever challenge came my way.

Lastly, a special thanks to Taini Yang and Isaac. I knew that no matter what happened, I could always count on you to cheer me up and set my mind straight. Your support was invaluable in my success, and I absolutely could not have done it without you. Thank you for being an ear, a diversion, and always a smile.

TABLE OF CONTENTS

DEDICATION ii
ACKNOWLEDGEMENTS iii
LIST OF FIGURES viii
LIST OF TABLES xv
LIST OF APPENDICES xvi
ABSTRACT xvii
CHAPTER 1: INTRODUCTION 1
CHAPTER 2: BACKGROUND 4
2.1. Metallurgy and Microstructure of Ferritic-Martensitic Steel 5
2.1.1 Physical Metallurgy 5
2.1.2 Precipitates and Microstructure 10
2.2 Swelling in Ferritic-Martensitic Steels 14
2.3 Neutron Irradiation of Ferritic-Martensitic Steels 15
2.4 Heavy Ion Irradiation of Ferritic-Martensitic Steels 22
2.5 Factors Affecting Cavity Evolution 30
2.5.1 Temperature Effect on Cavity Evolution 30
2.5.2 Dislocation Microstructure Effect on Cavity Evolution 40
2.5.3 Gas Effect on Cavity Evolution 46
2.5.4 Effect of helium injection mode 47
2.5.5 Effect of helium at high damage 51
2.5.6 The Effect of Carbon on Cavity Evolution 57
CHAPTER 3: OBJECTIVE 64
CHAPTER 4: EXPERIMENTAL PROCEDURE 67
4.1 Alloy and Sample Preparation 67
4.2 Helium Pre-Implantation 75

4.3. Fe^{2+} Irradiations 81
4.3.1 Experiments and Characterization Performed 81
4.3.2 SRIM Damage Calculations 84
4.3.3 Beam Raster-Scanning 88
4.3.4 The Irradiation Stage 93
4.3.5 The Irradiation Beamline 97
4.3.6 Running the Irradiation 104
4.4 Post Irradiation Characterization Methods 105
4.4.1 TEM Specimen Preparation 105
4.4.2 Cavity Imaging 108
4.4.3 Cavity Characterization 110
4.4.4 Nominal Damage Level and Valid Depth of Analysis 113
4.4.5 Error Calculations 113
4.4.6 Dislocation Imaging and Characterization 117
4.4.7 Precipitate Imaging and Characterization 122
4.4.8 NRA Measurements 123
CHAPTER 5: EXPERIMENTAL RESULTS 126
5.1 Nominal Carbon Campaign Cavity Results 126
5.1.1 Low Damage, Low Helium Regime 133
5.1.2 High Damage, Low Helium Regime 133
5.1.3 High Helium Regime 136
5.3 Nominal Carbon Campaign Dislocations and Precipitates 139
5.4 Excess Carbon Campaign 146
5.5 Excess Carbon Campaign Cavity Results 146
5.6 Carbon Content of Samples in Excess Carbon Campaign 156
5.7 Excess Carbon Campaign Dislocations and Precipitates 165
CHAPTER 6: DISCUSSION 167
6.1 The Influence of Helium on Cavity Evolution 167
6.1.1 Sink strength-moderated cavity evolution 167
6.1.2 Formation of bimodal cavity distributions 170
6.1.3 Helium-suppressed cavity evolution 176
6.1.4 Influence of dislocations and precipitates on cavity evolution 178

6.2 The Influence of Carbon on Cavity Evolution 180
6.2.1 Carbon-induced suppression of cavity nucleation 180
6.2.2 Carbon-induced suppression of cavity growth 186
6.3 Interaction of Carbon and Helium 189
6.3.1 Carbon-induced helium bubble dissolution 191
6.5 Helium retention 193
6.6 Applications to reactor systems 195
CHAPTER 7: CONCLUSIONS 198
CHAPTER 8: FUTURE WORK 200
APPENDICES 202
REFERENCES 273

LIST OF FIGURES

Figure 2.1 The effect of increasing Cr concentration on the constitution of 0.1%C Fe alloys [13] 7
Figure 2.2 A schematic of typical tempered martensitic microstructure [14] 13
Figure 2.3 A compilation of swelling data available for a variety of heats and heat treatments of neutron irradiated HT9 and T91. 18
Figure 2.4 Swelling of ferritic-martensitic and austenitic alloys under a variety of irradiation spectra [25]. 20
Figure 2.5 Voids were observed in the 316 stainless steel at 10 dpa after irradiation with 4 MeV Fe ions at 525°C [28]. 23
Figure 2.6 Cavities were observed in HT9 at 150 dpa with C and Ni ions [30]. 26
Figure 2.7. Temperature dependence and dose dependence of swelling are shown for the alloys under C ion irradiation [30]. 27
Figure 2.8 Temperature dependence of swelling rate in EP-450 [33]. 32
Figure 2.9 Temperature dependence of swelling at 150 dpa for EM-12 and HT9 using 2.8 MeV Fe^{+} ions [35]. 34
Figure 2.10 Temperature dependence of swelling, diameter, and number density at 188 dpa for HT9 using 5 MeV Fe^{2+} ions [8]. 36
Figure 2.12 The swelling dependency for MA 957, HT9, and EP-450 are shown through ~600 dpa irradiated with 1.8 MeV Cr^{+} ions [37]. 39
Figure 2.13 Swelling Rate is plotted versus sink strength ratio Q for a collection of experiments in austenitic alloys and ferritic-martensitic alloys [38]. 42
Figure 2.14 The critical cavity radius is plotted as a function of dislocation density [40]. 44
Figure 2.15 Void microstructure produced at 70 dpa with (a) no helium (b) coinjection (c) pre-implantation at 627C and (d) pre-implantation at room temperature [50]. 50
Figure 2.16 Swelling dependence of HT9 for various helium levels at (a) 440°C and (b) 460°C [8]. 53
Figure 2.17 The dependence of swelling with damage for CNSI and CNSII for different helium levels at 460°C irradiated with 5 MeV Fe^{2+} ions [9]. 54
Figure 2.18 Normalized Cavity swelling vs. appm He/dpa taken from a variety of experiments for Cu and Cu-boron doped irradiation experiments [52–56]. 56
Figure 2.19 Swelling as a function of damage in 316 steel for various carbon levels [58]. 59

Figure 2.20 Profiles of carbon content as a function of sputtering time (related to depth) for a CO gas, normal vacuum, and unirradiated environment [4]. 61
Figure 2.21 SIMS profiles of carbon in HT9 with and without beam filtering [5]..... 62
Figure 3.1 A schematic showing the hypothesized swelling behavior as a function of pre-implanted helium with and without carbon uptake. 65
Figure 4.1 The unirradiated, as-received microstructure of T91, heat C2269 imaged under bright field scanning transmission electron microscopy. 69
Figure 4.2 A schematic of the electropolishing set-up. 73
Figure 4.3 The amount of material removed from the surface as a function of electropolishing time. 74
Figure 4.4 A diagram of the helium conditions implanted on each T91 sample. 76
Figure 4.5 The helium profile as a function of depth in T91 as estimated by SRIM calculation as a result of implantation at various energies. 78
Figure 4.6 Bright Field STEM cross-sectional image of T91 microstructure implanted with 1000 appm helium at room temperature. 80
Figure 4.7 The damage rate and implanted ion concentration as a function of depth for 5 MeV Fe^{2+} in alumina coated T91 as calculated by SRIM. 86
Figure 4.8 The path of the raster-scanned beam over the irradiated area and aperture. 89
Figure 4.9 A schematic of the raster-scanned area with overscanning the beam by a full beam width to fully irradiate a 5 x 6mm area. 91
Figure 4.10 The beam intensity profile in the x-direction due to overscanning a full beam width. 92
Figure 4.11 A side-view schematic of the Hastelloy X irradiation stage. 95
Figure 4.12 An image of a fully constructed irradiation stage. 96
Figure 4.13 A schematic of ion irradiation end-station detailing key components. 98
Figure 4.14 Samples aligned with the laser. 100
Figure 4.15 An image taken from the FLIR 2D imager of a heated irradiation stage with three square AOIs on each sample. 103
Figure 4.16 A schematic of the FIB process, showing a) platinum deposition on the surface, b) trenching around the platinum deposition, c) undercut of the sample at 52°, d) attaching of the Omniprobe to the sample, e) attaching of the sample to the copper grid and f) a thinned FIB specimen. 107
Figure 4.17 HAADF STEM (left) and BF STEM (right) micrographs of the same area on a T91 specimen irradiated to 150 dpa at 460°C using 4.4 MeV Fe^{2+} ions. 109
Figure 4.18 An example of profiling cavities through depth in 150 dpa T91 for A) number density B) average diameter and C) swelling. The resulting size distribution from the 500-700 nm region is shown in D). 112
Figure 4.19 The error in diameter, number density and swelling is plotted as a function of cavity diameter. 116
Figure 4.20 Schematic of what b<100> and ½ b<111> loops look like when imaged down the [100] axis. 118
Figure 4.21 BF STEM image taken down the [100] zone axis showing b<100> loops, ½ b<111> loops and dislocation lines in T91 irradiated to 150 dpa. 119

Figure 4.22 BF STEM image with a concentric circle grid used to count intersections with dislocation lines. 121
Figure 4.23 A typical NRA spectrum obtained from an unirradiated sample of T91 overlaid with the fit simulated with SimNRA. 125
Figure 5.1 HAADF STEM images of T91 irradiated to 300 dpa with pre-implanted helium levels of 0, 1, 10, 100, and 1000 appm. The damage (dashed) and helium (solid) profiles are overlaid on the 10 appm He image. 128
Figure 5.2 a) Average cavity diameter b) number density, c) swelling and d) cavity sink strength as a function of damage in T91 for pre-implanted He levels of 0, 1, 10, 100, and 1000 appm. 131
Figure 5.3 a) Average cavity diameter b) number density, c) swelling and d) sink strength as a function of helium concentration for 50, 150, and 300 dpa. 132
Figure 5.4 Cavity size distributions for the 0, 1, and 10 appm He conditions in T91 at 50, 150, and 300 dpa (500-700 nm depth). 134
Figure 5.5 HAADF STEM images showing the evolution of the T91 microstructure with damage for the 0, 1, and 10 appm He conditions at 460ºC. 135
Figure 5.6 High magnification (1Mx) HAADF STEM images of T91 irradiated to 150 dpa (500-700 nm depth) with pre-implanted helium levels of 0, 1, 10, 100, and 1000 appm. 137
Figure 5.7 Cavity size distributions for the 100 and 1000 appm He conditions at 50, 150, and 300 dpa (500-700 nm depth). 138
Figure 5.8 Dislocation loop densities and diameters for b<100> and ½ b<111> loops are plotted as a function of damage for the 10 appm He condition. Some loops are indicated in the images with white circles 140
Figure 5.9 Densities and diameters for b<100> dislocation loops are plotted as a function of helium content at 150 dpa. Some loops are indicated in the images with white circles..... 141
Figure 5.10 a) Network and <100> loop sink strength are plotted along with the total line length and b) ratio of total line length to cavity sink strength as a function of helium content at 150 dpa. 143
Figure 5.11 Number density, diameter, and volume fraction of G-phase plotted as a function of damage with 10 appm He pre-implanted in ion-irradiated T91. 144
Figure 5.12 a) Average cavity diameter b) number density, c) swelling and d) cavity sink strength as a function of damage in T91 for pre-implanted He levels of 0, 1, 10, 100, and 1000 appm irradiated with 5 MeV Fe2+ ions at 460°C. 149
Figure 5.14 HAADF STEM images showing the evolution of the T91 microstructure with damage for the 0, 1, 10, 100 and 1000 appm He conditions irradiated at 460°C with 5 MeV Fe^{2+} ions. 152
Figure 5.15 Cavity size distributions for the 0, 1, and 10 appm He conditions at 50, 150, and 300 dpa (500-700 nm depth). 153
Figure 5.16 Cavity size distributions for the 100 and 1000 appm He conditions at 50, 150, and 300 dpa (500-700 nm depth). 154
Figure 5.17 High magnification HAADF STEM images of T91 implanted with 1000 appm He at damage levels of 150, 300, and 450 dpa (500-700 nm depth) irradiated with 5.0 MeV Fe^{2+} at 460°C. 155

Figure 5.18 a) LAADF image, b) and a corresponding Cr XEDS along with c) HRTEM image of an M_2X carbide in T91 imaged along [001] with inlaid FFT taken from a sample irradiated to 450 dpa with 1 appm He. 157
Figure 5.19 LAADF (Low Angle Angular Dark Field) STEM images of carbides taken at 150, 300 and 450 dpa (500-700 nm depth) in T91 with 10 appm He implanted and irradiated with 5 MeV Fe^{2+} at 460°C. 158
Figure 5.20 The a) length, b) density, c) volume fraction, and d) sink strength evolution of carbides in T91 implanted with 10 appm He as a function of damage at 460°C. 159
Figure 5.21 BF STEM images showing the presence of a high density of carbides in T91 in all helium conditions at 450 dpa irradiated with 5.0 MeV Fe^{2+} at 460°C. 161
Figure 5.22 The a) length and density and b) volume fraction, and sink strength evolution of carbides in T91 at 300 and 450 dpa at 460°C as a function of He content. 163
Figure 5.23 The NRA carbon profiles through the depth in T91 in the 450 dpa (460°C) excess carbon condition and in the unirradiated condition. 164
Figure 6.1 Cavity sink strength is plotted as a function of helium content at damage levels of 50, 150, and 300 dpa in ion irradiated T91. 169
Figure 6.2 The critical cavity radius for a cavity plotted as a function of the number of helium atoms in the cavity for cavity sizes of 0.5, 1.0, 1.5, and 1.8 nm. 172
Figure 6.3 Cavity stability map for T91 showing dependence of the critical radius on the actual cavity radius for various numbers of contained gas atoms. The highlighted grey area shows the possible size range for the presence of stabilized bubbles. 173
Figure 6.4. Bright field STEM images of T91 irradiated to 300 dpa with nominal and excess carbon levels using 5.0 or 4.4 MeV Fe^{2+} ions at 460°C. 183
Figure 6.5 Swelling as a function of damage for nominal and excess carbon T91 with no helium implantation. 184
Figure 6.6 Cavity number density (red dashed) and cavity diameter (blue solid) as a function of damage for nominal and excess carbon samples of irradiated T91, implanted with no He. 185
Figure 6.7 The ratio of carbide sink strength to cavity sink strength for the excess carbon T91 samples at 300 and 450 dpa are plotted as a function of He content. 188
Figure 6.8 a) Cavity diameter, b) cavity number density, and c) swelling as a function of He content for the nominal and excess carbon conditions in T91 at 150 dpa. 190
Figure A1. Temperature histograms for the 50 dpa, 460°C irradiation of alumina-coated T91 C2269 with 4.4 MeV Fe^{2+} ions for implanted He levels of 0, 1, 10, 100, and 1000 appm. 203
Figure A2. Temperature histograms for the +100 dpa (150 dpa total), 460°C irradiation of alumina-coated T91 C2269 with 4.4 MeV Fe^{2+} ions for implanted He levels of 0, 1, 10, 100, and 1000 appm. 204
Figure A3. Temperature histograms for the 300 dpa, 460°C irradiation of alumina-coated T91 C2269 with 5.0 MeV Fe^{2+} ions for implanted He levels of 0, 1, 10, 100, and 1000 appm. 205
Figure A4. Temperature histograms for the 150 dpa, 460°C irradiation of uncoated T91 C2269 with 5.0 MeV Fe^{2+} ions for implanted He levels of 0, 1, 10, 100, and 1000 appm. 206
Figure A5. Temperature histograms for the +150 dpa (300 dpa total), 460°C irradiation of uncoated T91 C2269 with 5.0 MeV Fe^{2+} ions for implanted He levels of 0, 1, 10, 100, and 1000 appm. 207

Figure A6. Temperature histograms for the +150 dpa (450 dpa total), 460°C irradiation of uncoated T91 C2269 with 5.0 MeV Fe^{2+} ions for implanted He levels of 0, 1, 10, 100, and 1000 appm. 208
Figure B1. HAADF and corresponding BF STEM images for a liftout from the 50 dpa, 0 apppm He, nominal carbon condition. 210
Figure B2. HAADF and corresponding BF STEM images for a liftout from the 50 dpa, 1 apppm He, nominal carbon condition. 211
Figure B6. HAADF and corresponding BF STEM images for a liftout from the 150 dpa, 0 apppm He, nominal carbon condition. 215
Figure B10. HAADF and corresponding BF STEM images for a liftout from the 150 dpa, 1000 apppm He, nominal carbon condition..... 219
Figure B13. HAADF and corresponding BF STEM images for a liftout from the 300 dpa, 10 apppm He, nominal carbon condition..... 222
Figure B14. HAADF and corresponding BF STEM images for a liftout from the 300 dpa, 100 apppm He, nominal carbon condition..... 223
Figure B15. HAADF and corresponding BF STEM images for a liftout from the 300 dpa, 1000 apppm He, nominal carbon condition..... 224
Figure B16. HAADF and corresponding BF STEM images for a liftout from the 150 dpa, 0 apppm He, excess carbon condition. 225
Figure B17. HAADF and corresponding BF STEM images for a liftout from the 150 dpa, 1 apppm He, excess carbon condition. 226
Figure B18. HAADF and corresponding BF STEM images for a liftout from the 150 dpa, 10 apppm He, excess carbon condition. 227
Figure B19. HAADF and corresponding BF STEM images for a liftout from the 150 dpa, 100 apppm He, excess carbon condition. 228
Figure B21. HAADF and corresponding BF STEM images for a liftout from the 300 dpa, 0 apppm He, excess carbon condition. 230
Figure B22. HAADF and corresponding BF STEM images for a liftout from the 300 dpa, 1 apppm He, excess carbon condition. 231
Figure B23. HAADF and corresponding BF STEM images for a liftout from the 300 dpa, 10 apppm He, excess carbon condition. 232
Figure B30. HAADF and corresponding BF STEM images for a liftout from the 450 dpa, 1000 apppm He, excess carbon condition. 239
Figure C1. Cavity diameter, density and swelling are plotted as a function of depth for the 50 dpa, 0 appm He, nominal carbon condition. The cavity distribution at 500-700 nm is also shown..... 240
Figure C2. Cavity diameter, density and swelling are plotted as a function of depth for the 50 dpa, 1 appm He, nominal carbon condition. The cavity distribution at 500-700 nm is also shown..... 241
Figure C3. Cavity diameter, density and swelling are plotted as a function of depth for the 50 dpa, 10 appm He, nominal carbon condition. The cavity distribution at 500-700 nm is also shown..... 242

Figure C4. Cavity diameter, density and swelling are plotted as a function of depth for the 50 dpa, 100 appm He, nominal carbon condition. The cavity distribution at 500-700 nm is also shown. 243
Figure C5. Cavity diameter, density and swelling are plotted as a function of depth for the 50 dpa, 1000 appm He, nominal carbon condition. The cavity distribution at 500-700 nm is also shown. 244
Figure C6. Cavity diameter, density and swelling are plotted as a function of depth for the 150 dpa, 0 appm He, nominal carbon condition. The cavity distribution at 500-700 nm is also shown. 245
Figure C7. Cavity diameter, density and swelling are plotted as a function of depth for the 150 dpa, 1 appm He, nominal carbon condition. The cavity distribution at 500-700 nm is also shown. 246
Figure C8. Cavity diameter, density and swelling are plotted as a function of depth for the 150 dpa, 10 appm He, nominal carbon condition. The cavity distribution at 500-700 nm is also shown. 247
Figure C9. Cavity diameter, density and swelling are plotted as a function of depth for the 150 dpa, 100 appm He, nominal carbon condition. The cavity distribution at 500-700 nm is also shown. 248
Figure C10. Cavity diameter, density and swelling are plotted as a function of depth for the 150 dpa, 1000 appm He, nominal carbon condition. The cavity distribution at 500-700 nm is also shown. 249
Figure C11. Cavity diameter, density and swelling are plotted as a function of depth for the 300 dpa, 0 appm He, nominal carbon condition. The cavity distribution at 500-700 nm is also shown 250
Figure C12. Cavity diameter, density and swelling are plotted as a function of depth for the 300 dpa, 1 appm He, nominal carbon condition. The cavity distribution at 500-700 nm is also shown. 251
Figure C13. Cavity diameter, density and swelling are plotted as a function of depth for the 300 dpa, 10 appm He, nominal carbon condition. The cavity distribution at 500-700 nm is also shown. 252
Figure C14. Cavity diameter, density and swelling are plotted as a function of depth for the 300 dpa, 100 appm He, nominal carbon condition. The cavity distribution at 500-700 nm is also shown. 253
Figure C15. Cavity diameter, density and swelling are plotted as a function of depth for the 300 dpa, 1000 appm He, nominal carbon condition. The cavity distribution at 500-700 nm is also shown. 254
Figure C16. Cavity diameter, density and swelling are plotted as a function of depth for the 150 dpa, 0 appm He, excess carbon condition. The cavity distribution at 500-700 nm is also shown. 255
Figure C17. Cavity diameter, density and swelling are plotted as a function of depth for the 150 dpa, 1 appm He, excess carbon condition. The cavity distribution at 500-700 nm is also shown. 256

Figure C18. Cavity diameter, density and swelling are plotted as a function of depth for the 150 dpa, 10 appm He, excess carbon condition. The cavity distribution at 500-700 nm is also shown. 257
Figure C19. Cavity diameter, density and swelling are plotted as a function of depth for the 150 dpa, 100 appm He, excess carbon condition. The cavity distribution at 500-700 nm is also shown. 258
Figure C20. Cavity diameter, density and swelling are plotted as a function of depth for the 150 dpa, 1000 appm He, excess carbon condition. The cavity distribution at 500-700 nm is also shown. 259
Figure C21. Cavity diameter, density and swelling are plotted as a function of depth for the 300 dpa, 0 appm He, excess carbon condition. The cavity distribution at 500-700 nm is also shown. 260
Figure C22. Cavity diameter, density and swelling are plotted as a function of depth for the 300 dpa, 1 appm He, excess carbon condition. The cavity distribution at 500-700 nm is also shown. 261
Figure C23. Cavity diameter, density and swelling are plotted as a function of depth for the 300 dpa, 10 appm He, excess carbon condition. The cavity distribution at 500-700 nm is also shown. 262
Figure C24. Cavity diameter, density and swelling are plotted as a function of depth for the 300 dpa, 100 appm He, excess carbon condition. The cavity distribution at 500-700 nm is also shown. 263
Figure C25. Cavity diameter, density and swelling are plotted as a function of depth for the 300 dpa, 1000 appm He, excess carbon condition. The cavity distribution at 500-700 nm is also shown. 264
Figure C26. Cavity diameter, density and swelling are plotted as a function of depth for the 450 dpa, 0 appm He, excess carbon condition. The cavity distribution at 500-700 nm is also shown. 265
Figure C27. Cavity diameter, density and swelling are plotted as a function of depth for the 450 dpa, 1 appm He, excess carbon condition. The cavity distribution at 500-700 nm is also shown. 266
Figure C28. Cavity diameter, density and swelling are plotted as a function of depth for the 450 dpa, 10 appm He, excess carbon condition. The cavity distribution at 500-700 nm is also shown. 267
Figure C29. Cavity diameter, density and swelling are plotted as a function of depth for the 450 dpa, 100 appm He, excess carbon condition. The cavity distribution at 500-700 nm is also shown. 268
Figure C30. Cavity diameter, density and swelling are plotted as a function of depth for the 450 dpa, 1000 appm He, excess carbon condition. The cavity distribution at 500-700 nm is also shown. 269

LIST OF TABLES

Table 2.1. The change in δ-ferrite is shown for additions of particular alloying elements [13]..... 6
Table 2.2 The effect of alloying elements on austenization temperature (Ac1) [13] 9
Table 2.3 Microstructural developments in high chromium ferritic-martensitic steels during aging and creep straining at 600-650°C [13]..... 11
Table 2.4. A summary of the swelling observed in the materials studied by Gelles [19] is shown below. 16
Table 2.5. The swelling results of 21/4 Cr-1 Mo are summarized and divided into regions within the damage depth [32]. 29
Table 2.6 The swelling resulting from different methods of helium pre-implantation from [50]. 49
Table 4.1 The composition of T91 C2269 in wt%..... 70
Table 4.2. The experimental details and microstructural characterization for the first irradiation campaign with uncoated samples. 82
Table 4.3 The experimental details and microstructural characterization for the second irradiation campaign with coated samples. 83
Table 4.4 The calculated SRIM damage rates at a depth of 600 nm for relevant experimental conditions..... 87
Table 5.1 Summary of cavity results in T91 samples in the Nominal Carbon Campaign after ion irradiation for various combinations of damage and helium levels..... 129
Table 5.2 A summary of dislocation loops, dislocation network, and G-phase. 145
Table 5.3 Summary of cavity results in T91 in excess carbon samples after ion irradiation for all damage levels and helium levels. 147
Table 5.4 Summary of carbide length, density, volume fraction and sink strength in excess carbon T91 following irradiation with Fe^{2+} at 460°C..... 162
Table 5.5 Dislocation density, diameter and line length are shown for the conditions characterized in excess carbon T91. 166
Table 6.1 Key parameters for calculating the T91 cavity stability map. 174
Table D.1 Parameters used for calculation of vacancy super-saturation 272

LIST OF APPENDICES

APPENDIX A: TEMPERATURE HISTOGRAMS 202
APPENDIX B: LIFTOUT IMAGES 209
APPENDIX C: CAVITY DEPTH PROFILES AND DISTRIBUTIONS 240
APPENDIX D: CALCULATION OF VACANCY SUPERSATURATION FOR CRITICAL CAVITY RADIUS 270

ABSTRACT

The objective of this thesis is to understand the role of pre-implanted helium, with and without the presence of excess carbon, on the cavity evolution of ion-irradiated T91. Alloy T91, heat C2269, was pre-implanted at room temperature with helium concentrations varying over 4 orders of magnitude (0, 1, 10, 100, and 1000 appm). These samples were then irradiated with 5.0 or 4.4 MeV Fe^{2+} ions at 460°C up to damage levels of 450 dpa at the Michigan Ion Beam Laboratory. An alumina coating was utilized to prevent carbon contamination on some samples during irradiation. Samples without an alumina coating experienced carbon uptake during irradiation, providing for a study on the effect of excess carbon.

The swelling, precipitate, and dislocation evolution for the excess carbon and nominal carbon conditions for all helium concentrations was characterized. Scanning transmission electron microscopy (STEM) was used to characterize the microstructure of the irradiated specimens.

In the nominal carbon conditions, swelling decreased with increasing helium concentration. At low helium levels (0, 1, and 10 appm), the cavity evolution was determined by the cavity sink strengths. Differences in density were observed at 50 dpa, however the three low helium conditions achieved very similar cavity distributions by 300 dpa. At high helium levels (100 and 1000 appm), bimodal cavity distributions were observed at all damage levels. High helium levels served to stabilize a population of bubbles with sizes below the gas-free critical radius. A substantial cavity sink strength, helium trapping, and a cavity interstitial bias contributed to reduced growth of larger cavities.

In the excess carbon conditions, swelling was peaked at 10 appm He. The main role of carbon was to inhibit cavity nucleation, which reduced the cavity density at all damage and helium levels compared to the nominal carbon conditions. Additionally, excess carbon allowed for the formation of a very high density of M_2X carbides. These carbides were strongly associated with helium bubbles and provided an interface for any emitted helium atoms. A bubble population was

never observed in the 100 appm He condition, and bubbles in the 1000 appm He condition disappeared completely by 450 dpa.

This work provides substantial insight into the complex evolution of cavities at various helium and carbon levels.

CHAPTER 1: INTRODUCTION

Concerns about global climate change and a desire to shift from natural gas and coal-burning power plants to greener solutions for power generation have driven an interest in new nuclear power designs. These nuclear power plants, called Generation IV reactors, offer the advantages of increased safety, reduced radioactive waste, an extremely low carbon footprint, and efficient use of fuel via higher burnup. Driving reactors to higher burnups means that the structural materials of the reactors themselves will experience more extreme radiation and temperature conditions.

The high neutron fluxes in reactors cause atomic displacements in the crystal lattice of the structural materials. These displaced atoms result in the formation of radiation-induced defects in the form of interstitial atoms and vacancies. When enough of these defects are created, they become defect clusters and take on forms such as dislocation loops or cavities. Radiation damage can also cause chemical changes within the material, resulting in transmutation, radiation-induced or enhanced precipitation, and segregation of solutes to grain boundaries. These changes in the microstructure will have significant consequences on the mechanical properties and dimensional stability of materials—such as embrittlement, hardening, and swelling, which could eventually lead to material failure.

Historically, austenitic stainless steels have been used for structural materials in light-water reactors. However, it was discovered that their susceptibility to void swelling and creep made them unsuitable for high damage fast reactor applications. After showing promise in initial testing at the Fast Flux Test Facility (FFTF), ferritic-martensitic steels became the leading candidates for high temperature-high dpa applications. Ferritic-martensitic steels are body-centered cubic, iron-based alloys, with typically 7-15% chromium. Additions of minor solute elements such as Mo, Ni, Mn, Si, V, Cu, Ta, Ti and W are common. These solute elements serve to add strength, ductility, or

reduced activation to the alloys. In contrast to austenitic stainless steels, ferritic-martensitic steels have a very complex microstructure consisting of very small grains and subgrains, laths, precipitates, and a high dislocation density. It is this complex microstructure that contributes to the radiation tolerance of the material, as there are many sites for the point defects to annihilate.

The desire to test these radiation-tolerant materials to high damage levels has led to the use of accelerator-based methods of testing. Instead of waiting years equivalent to the lifetime of a reactor to determine if a material is viable for use, accelerated testing can provide answers in days or less. The use of ion beams to create displacement damage as a surrogate to neutron irradiation has risen as a method to induce high levels of radiation damage in a timely and cost-efficient manner. Whether the damage created by ion beams is directly applicable to neutron damage is still a matter of debate. However, ion beams have been used to a great degree of success in replicating similar radiation damage effects as neutrons [1][2][3].

While ion beams can achieve a very high damage rate, there are some important drawbacks that must be considered when using them. Ion irradiations suffer from a shallow penetration depth, varying damage rate with depth, lack of transmutation reactions, effects of injected interstitials, and most recently, carbon contamination [4,5]. Most of these limitations can be overcome with careful implementation of irradiation and characterization techniques.

Transmutation reactions, especially those leading to the production of noble gases such as (n,α) reactions, may have a dramatic effect on the microstructural stability of material in reactor. The lack of transmutation reactions in ion irradiation has been addressed by implanting transmutation gasses (such as helium) either prior to irradiation or simultaneously with irradiation in a dual-beam irradiation setup. The presence of helium in the microstructure can dramatically affect the radiation tolerance of the material. Helium is known to stabilize the formation of vacancy clusters, which evolve into cavities. At high damage levels these cavities contribute to significant swelling of the material. Many ion irradiation studies in the past have utilized pre-implanted helium to encourage cavity nucleation, but with little regard to the amount and its consequences. This is evident in the wide range of helium levels that have been explored—ranging from as little as 0 or 1 appm (atomic parts per million) to as much as 1800 appm. There is evidence that high levels of pre-implantation may actually serve to suppress swelling when compared to actual reactor conditions [6]. Additionally, there are conflicting reports of whether different helium levels may

affect the steady-state swelling rate [7][8][9]. A study that systematically explores a wide range of helium levels and captures the evolution of the cavity size distributions is necessary to understand the role of helium on cavity evolution.

Additionally, the issue of carbon contamination in ion irradiation has been plaguing ion beam community for years [4,10,11]. High amounts of carbon have been shown to suppress swelling and result in the formation of carbides. Its unintended uptake may compromise the integrity of any swelling measurements and of any meaningful comparison with neutron irradiation. The effect of carbon uptake on cavity evolution has yet to be quantified, and the implementation of a solution to the carbon problem was undiscovered until recently [12].

The objective of this thesis is to understand the role of pre-implanted helium and carbon on the cavity evolution of ion-irradiated T91. A combination of ion irradiation experiments, with careful post-irradiation characterization techniques coupled with a computational model were used to achieve this objective. Chapter 2 provides a background on the ferritic-martensitic steels and the effects of neutron and ion irradiation on their microstructure, with a special focus on helium and carbon effects. Chapter 3 summarizes the objective of the thesis and the approach taken to achieve the objective. Chapter 4 describes the experimental procedures and techniques used for the ion irradiation experiments and post-irradiation characterization. Chapter 5 summarizes the results gathered from the experiments. Chapter 6 offers an interpretation of the experimental results and addresses the objective. The conclusions and future work are provided in Chapters 7 and 8, respectively.

CHAPTER 2: BACKGROUND

With increasing demand for clean energy, Generation IV reactor designs have become a very attractive alternative to coal, natural gas, and fission power plants. These reactor designs boast higher energy yield, less waste, breakdown of existing radioactive waste, and improved safety. However, the harsh conditions of these reactors (both in temperature and radiation) require the use of highly resilient structural materials. The degradation of the structural materials is closely related to changes in their irradiated microstructure. Components in Generation IV fast reactors will experience damage levels in excess of 200 displacements per atom (dpa) and up to about 600 dpa. Understanding how this high damage affects the microstructure in reactor conditions is critical to determining the correct material for use.

Ferritic-martensitic steels have risen as a candidate for high damage applications. Their strength at elevated temperatures, swelling resistance, thermal stress resistance, and low activation makes them very desirable for high damage applications in reactor environments [13]. However, high damage neutron-irradiated samples are difficult to come by, as it takes a long time to irradiate samples. A typical damage rate for neutrons is on the order of 10^{-8} dpa/s. Therefore, both proton and heavy ion irradiations (10^{-6} and 10^{-3} dpa/s respectively) are being used to emulate neutron damage in a much faster and cost effective way. The major damage effects under irradiation include radiation-induced segregation, radiation-induced precipitation, dislocation evolution, and swelling.

This chapter will set the context for the work performed in this thesis by describing the microstructure of ferritic-martensitic steels and how it behaves under both neutron and ion irradiation. Existing experimental and theoretical work regarding swelling and other effects during

irradiation will be considered. Special attention will be given to swelling and the effect of helium and carbon on swelling, as these topics are the focus of the thesis.

2.1. Metallurgy and Microstructure of Ferritic-Martensitic Steel

2.1.1 Physical Metallurgy

Ferritic-martensitic (F-M) steels were originally developed from the combination of oxidation resistant high-Cr steels and high hardness martensitic steels. A typical F-M steel will contain from 9-12 wt% Cr with low additions of C, Mo,W, V, Nb, and N. To develop these F-M alloys, high chromium (9-12%) steel is austenitized at a temperature in the range of 850°C to 1200°C. These high chromium steels are either fully austenitic or duplex (austenite and δ-ferrite). After austenitizing, the steel is then rapidly quenched, which transforms the austenite to martensite. The martensite is subsequently tempered to improve ductility and toughness.

During austenitization, the δ-ferrite phase tends to inhibit austenite grain growth, which ultimately can reduce the strength and toughness of the final steel. Chromium is a ferrite promoting element, and will therefore increase the amount of δ-ferrite. As seen in **Table 2.1** [13], there is a 14% increase of δ-ferrite per %mass of Cr. The addition of austenite-forming elements can counteract this, and help achieve a purely austenitic steel.

Table 2.1. The change in δ-ferrite is shown for additions of particular alloying elements [13]

Element	Change in δ-ferrite Content, % per Mass % Alloy Addition
N	−220
C	−210
Ni	−20
Co	−7
Cu	−7
Mn	−6
W	+3
Mo	+5
Si	+6
Cr	+14
V	+18
Al	+54

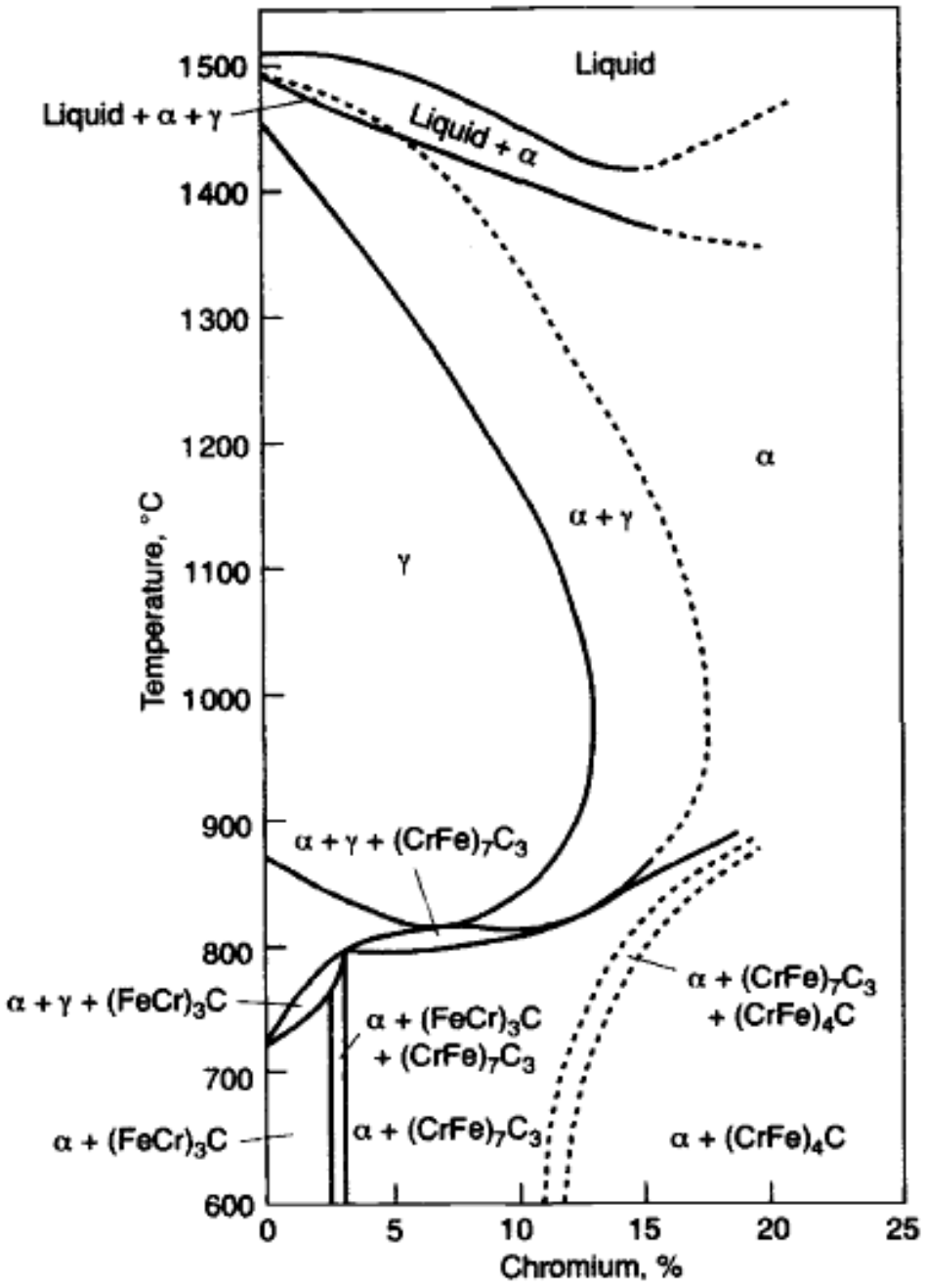

Figure 2.1 The effect of increasing Cr concentration on the constitution of 0.1%C Fe alloys [13]

The behavior of 0.1% C alloys with increasing amounts of Cr is shown in the **Figure 2.1** phase diagram [13]. Addition of austenite-promoting elements will tend to extend the γ phase region.

Upon rapid cooling, the austenite formed during the initial heating should fully form into martensite. The addition of austenite stabilizers, such as carbon, nitrogen, nickel, and manganese, can cause residual austenite to remain, which is undesirable as the strength of the alloy can be reduced.

Following the quenching step is a tempering step to increase the toughness of the steel. Care must be taken not to exceed the austenitizing temperature to avoid reaustenization of the sample. Additions of alloying elements can change austenization temperature. The effect of adding some common alloying elements on the austenization temperature are summarized in **Table 2.2** [13].

Table 2.2 The effect of alloying elements on austenization temperature (Ac1) [13]

Element	Change in Ac1 (°C) per Mass %
Ni	-30
Mn	-25
Co	-5
Si	+25
Mo	+25
Al	+30
V	+50

2.1.2 Precipitates and Microstructure

The development of precipitates and microstructure is highly dependent on the tempering temperature. As summarized by Klueh and Harries [13], the following are general properties of precipitates observed at different tempering temperatures:

- <350°C: A dispersion of Fe_3C precipitates changes morphology and increases in chromium content resulting in a slower growth rate. As a result, softening is retarded.
- 400-500°C: Needles of M_2X nucleate on dislocations and retard softening.
- 500-550°C: M_7C_3 and M_2X phases coarsen, increasing the softening.
- >550°C: Cr-rich $M_{23}C_6$ precipitates nucleate and replace M_7C_3 and M_2X at martensite laths and prior austenite grain boundaries resulting in a slowing of the softening. Dislocation density of the martensite decreases.
- >650°C: Continued growth of $M_{23}C_6$ and further reduction in dislocation density. Pronounced subgrain formation on the martensite laths
- >750°C: Subgrains grow into equiaxed grains, leaving little trace of original martensite lath. Growth of $M_{23}C_6$ continues, and almost all the carbon is precipitated as $M_{23}C_6$ for tempering >1 hour at 700 to 780°C.

Table 2.3 shows some detailed effects of aging and creep straining on high chromium ferritic- martensitic steels and how the distribution of precipitates changes.

Table 2.3 Microstructural developments in high chromium ferritic-martensitic steels during aging and creep straining at 600-650°C [13]

	Normalized and Tempered	**Aged, 10,000-30,000h**	**Strained, 10,000-30,000h**
Hardness	High	85% of N & T	70-80% of N &T
Phases	Tempered martensite; $M_{23}C_6$; δ-ferrite, depending on grade	Tempered martensite; $M_{23}C_6$; partly decomposed δ-ferrite	Tempered martensite; $M_{23}C_6$; partly decomposed δ-ferrite
Dislocation Density	High	Low	Very Low
Sub-grain/ martensite lath size	Small lath width	Martensite lath transformation to subgrains	Sub-grains fully recovered
$M_{23}C_6$	On lath boundaries, typically 50-150 nm	Partly coarsened on sub-grain boundaries	Partly coarsened on sub-grain boundaries
MX	Finely dispersed (20-50 nm)	Finely dispersed (20-50 nm)	Finely dispersed (20-50 nm)
Laves phase	None	Medium and large sized precipitates (200-500 nm)	Large sized precipitates (=500 nm)

The resulting microstructure after tempering can be very complex, consisting of martensite, austenite, and δ-ferrite phases. **Figure 2.2** shows a typical microstructure of a tempered martensitic steel [14]. The martensite is distinguished by the lath, string-like structure. These martensite areas contain high dislocation densities due to the quenching process. The prior-austenite grain boundaries (PAGBs) are also apparent. These sites often contain precipitates and other segregated particles. Each of these PAGs are divided into subgrains of aligned tempered martensite laths. The size of the grains, resulting precipitates at boundaries, and density of dislocations are all a function of the heat treatment and tempering.

The complexity of the microstructure developed in F-M steels is thought to be a critical feature in its radiation tolerance. The many interfaces between grain boundaries, subgrains, laths and precipitates, and the high density of dislocations all serve as sinks for vacancies and interstitials generated during irradiation.

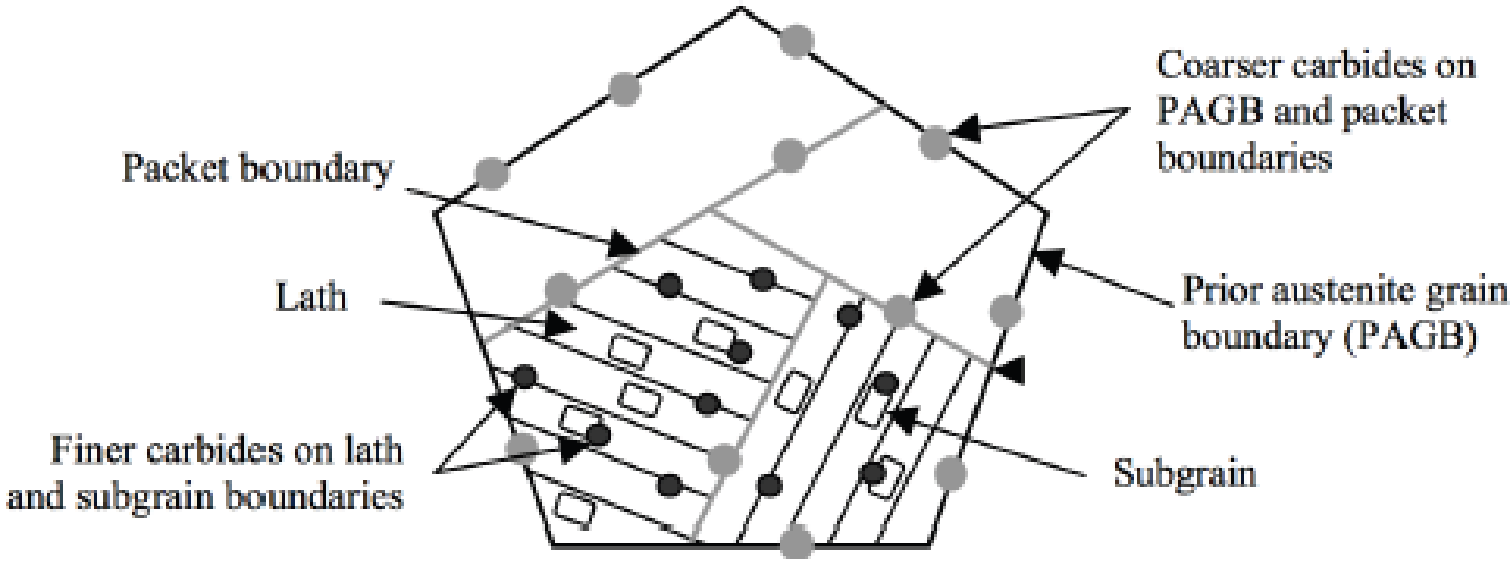

Figure 2.2 A schematic of typical tempered martensitic microstructure [14]

2.2 Swelling in Ferritic-Martensitic Steels

One of the greatest reasons ferritic-martensitic alloys are being pursued for high damage applications is their resistance to swelling. The complex microstructure of F-M steels provides strong sink strength for point defects generated during irradiation. If these point defects are annihilated at sinks rather than accumulate in the matrix, then it will become more difficult for voids to form. The driving force of void nucleation is the supersaturation of vacancies ($\frac{C_v}{C_v^0}$), where C_v is the concentration of vacancies in the matrix and C_v^0 is the thermal equilibrium concentration of vacancies [15]. The energetics lend themselves to a point where a critical void embryo size is required to nucleate a void. This occurs when the vacancy supersaturation overcomes the surface energy required to create the void, and can be represented by the following equation:

$$\Delta G = -nkT\ln\left(S_V\right) + (36\pi\Omega^2)^{1/3}\gamma n^{2/3} \quad \textbf{(2.1)}$$

Where ΔG is the free energy change, n is the number of vacancies, k is Boltzmann's constant, T is temperature, S_V is the vacancy supersaturation, Ω is the atomic volume, and is γ the surface energy. Void nucleation will be favored as long as ΔG is less than 0. In this equation, void nucleation can be seen as a competition between two forces: the extent of vacancy supersaturation (the first term) and the surface energy required to form a void (second term).

After a void has nucleated, its growth is determined by the flux of point defects to and away from it. A flux of vacancies into the void will grow it, while a flux of interstitials will cause it to shrink. The growth of a void (rate of change of volume) can be expressed by the net absorption rate multiplied by the defect volume:

$$\frac{dV}{dt} = 4\pi R\Omega\left[D_V\left(C_V - C_V^V\right) - D_i C_i\right] \quad \textbf{(2.2)}$$

Where D_V and D_i are the diffusion coefficients for vacancies and interstitials, respectively, C_V is the vacancy concentration in the solid, C_i is the interstitial concentration in the solid, R is the void radius, and C_V^V is the vacancy concentration at the void surface.

Under irradiation, both vacancies and interstitials are generated in equal numbers. This in and of itself will not allow for the growth of voids as there will be no net generation of vacancies and thus no supersaturation. Both the vacancies and interstitials will annihilate at sinks or recombine. However, in the presence of a sink that is biased for interstitials (such as dislocations), an excess of vacancies can accumulate in the matrix and lead to the creation of voids. Therefore, when examining the effects of irradiation on void swelling, it is important to also include an analysis of the other major sinks in the system, as they will heavily influence the swelling behavior.

2.3 Neutron Irradiation of Ferritic-Martensitic Steels

The high swelling resistance of ferritic-martensitic alloys has been the subject of many neutron irradiation experiments. Most of the studies were performed in fast reactors, so damage levels of 100 dpa or higher are very rare. Sencer *et. al.* [16] performed a study on ferritic-martensitic HT9 duct material irradiated to about 155 dpa over the course of 6 years. The HT9 was taken from a fuel duct in the Fast Flux Test Reactor Facility (FFTF). The average irradiation temperature was about 440°C. The irradiation resulted in the formation of dislocations, loops, precipitates, and voids. This study showed that HT9 retained a considerable resistance to swelling (0.3%) under reactor conditions which entailed a complex neutron flux and temperature history. However, because of the large distribution of void sizes, it was not apparent whether a steady state swelling rate was achieved or being approached.

In a separate study on the same HT9 duct material, Sencer et al. [17] irradiated specimens with up to 4 dpa at 505°C and 28 dpa, at 384°C. However, no significant swelling or void formation was observed.

Gelles [18] looked at HT9, T91 and ODS steel samples irradiated up to 200 dpa at a temperature of about 420°C in FFTF. This study constitutes one of the highest damage neutron irradiations performed on F-M steels, as the samples were irradiated in the reactor for its lifetime. Gelles performed microstructural analysis and density change measurements to determine swelling of the alloys. The results are summarized in **Table 2.4**.

Table 2.4. A summary of the swelling observed in the materials studied by Gelles [19] is shown below.

CODE	Alloy	Dose (dpa)	Swelling (density change) (%)	Highest Swelling (%)	Mean void size (nm)	Void density (#/cm^3)	Void shape	Dislocation Structure
PTFL	T91	203.2	1.76	5.0	21.4	4.8×10^{15}	Truncated between dodecahedra and cubes	a/2 <111> network and a<100> network
RFFL	HT-9	203.5	0.09	3.2	21.2	3.1×10^{15}	Truncated dodecahedra	a<100> loops and a/2 network
RHFL	HT-9	204.0	1.02	1.7	32.2	5.6×10^{14}	Truncated between dodecahedra and cubes	a<100> loops and a/2<111> network
RLH4	MA956	204.8	1.17	0.21	26.7	1.9×10^{14}	Truncated between dodecahedra and cubes	a<100> and a/2 <111> network
RMH4	MA957	205.7	1.75	3.73	6.1	9.2×10^{14}	Truncated between dodecahedra and cubes	a<100> and a/2 <111> loops and a/2 <111> network in recrystallized regions
RNH4	MA957	206.0	0.25	3.5	35.4	8.6×10^{14}	Truncated between dodecahedra and cubes	a<100> and a/2 <111> loops and a/2 <111> network in recrystallized regions

Based on **Table 2.4**, swelling in the steels ranged from 0.25% to 1.76%, showing excellent overall resistance to swelling across the board. The author noted that swelling varied between batches of the same steel and between different heats of the same steel by a difference of about 1% swelling. Voids were found in all of the specimens irradiated at these conditions.

A summary of neutron irradiations [16,17,19–24] conducted in FFTF is shown in **Figure 2.3**. This figure contains a compilation of results with a variety of heats of HT9 and T91. The general shape of the curve shows that a transition to growth-dominated behavior occurs for several of the cases by 200 dpa. Up to 200 dpa, these ferritic martensitic alloys show great swelling resistance, with an estimated swelling rate of ~0.01%/dpa or less. However, there is much variation between different heats and heat treatments of HT9 and T91. The work from Gelles [19] especially shows great variation in swelling behavior with heat treatment, which could vary between 0.09% and 1.02% for HT9. In fact, swelling differences between alloy (T91 and HT9) were just as comparable as swelling differences between the heats of HT9.

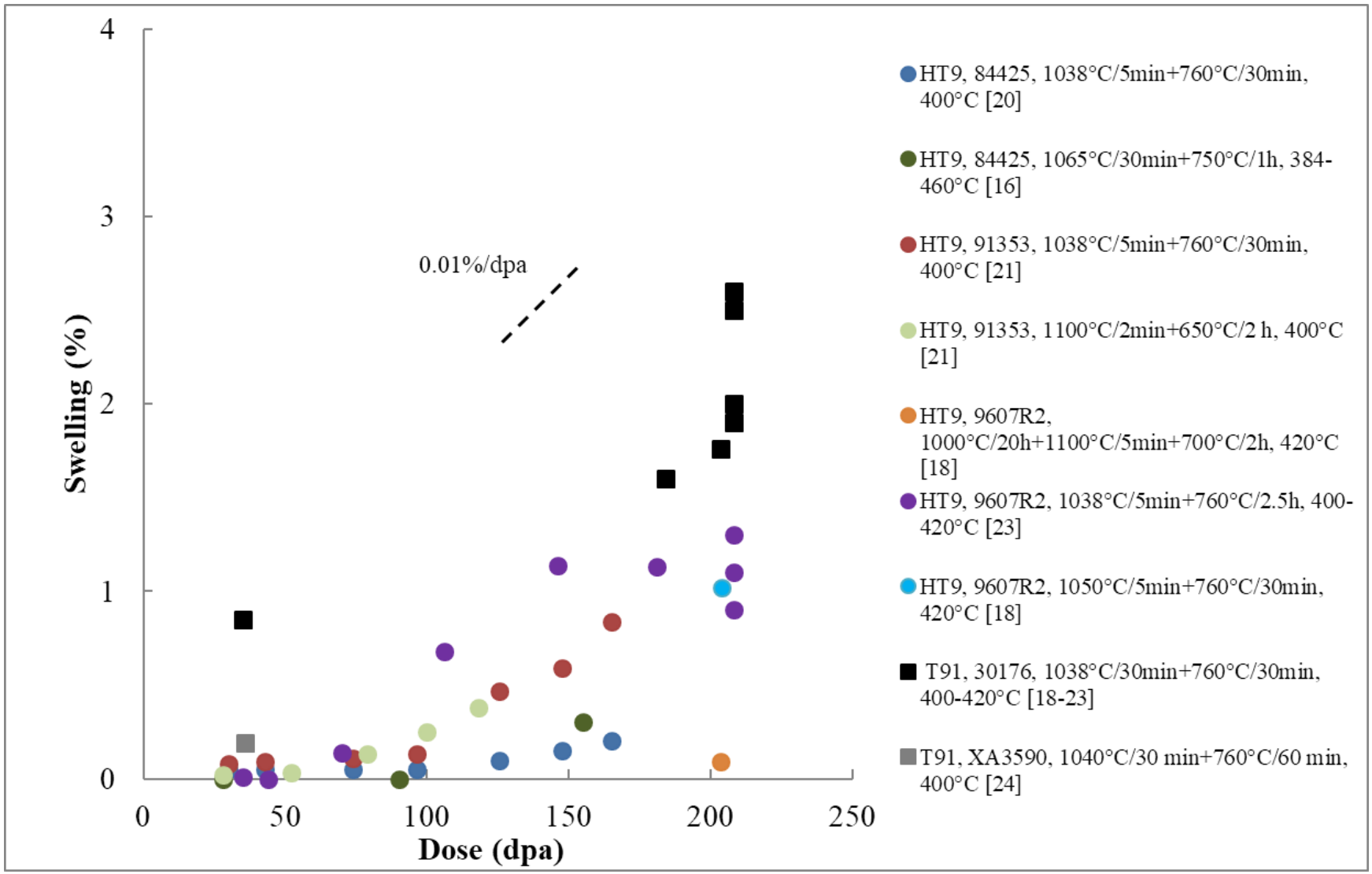

Figure 2.3 A compilation of swelling data available for a variety of heats and heat treatments of neutron irradiated HT9 and T91.

Little [25] presented an overview of the microstructural evolution of ferritic-martensitic steels under irradiation. In terms of void swelling, Little described the viability of using ferritic-martensitic steels for their superior swelling resistance as compared with austenitic steels. **Figure 2.4** shows how swelling in F-M steels is much lower compared to swelling in austenitic stainless steels for a given damage level under a variety of irradiation spectra.

In general, it is observed that increasing amounts of Cr from pure iron tend to increase the swelling resistance. Little proposed that F-M steels with 9-12% Cr exhibit the highest swelling resistance at dpa values >100. However lower levels of swelling (<0.5%) are also observed for higher Cr steels (14-22%). The resistance to swelling is also coupled with a large increase in the incubation period.

To account for the increased swelling resistance, Little proposed that a solute atom point defect trapping effect could be responsible. In this mechanism, vacancies bind to solute atoms such as carbon, nitrogen, or silicon, which can ultimately enhance recombination and prevent vacancy super-saturation. Additionally, the complex microstructure of F-M steels, consisting of many lath and grain boundaries can provide regions for strong point defect sinks to prevent super-saturation as well. At the onset of irradiation, α' precipitates could also serve as trapping sites and recombination centers. High concentrations of interstitial loops, dislocations, and even voids themselves serve to suppress swelling through serving as sinks for vacancies. Self-diffusion rates in ferritic alloys are higher than austenitic alloys, and this would lead to an increased incubation dose and lower helium production rates due to less nickel content also contribute.

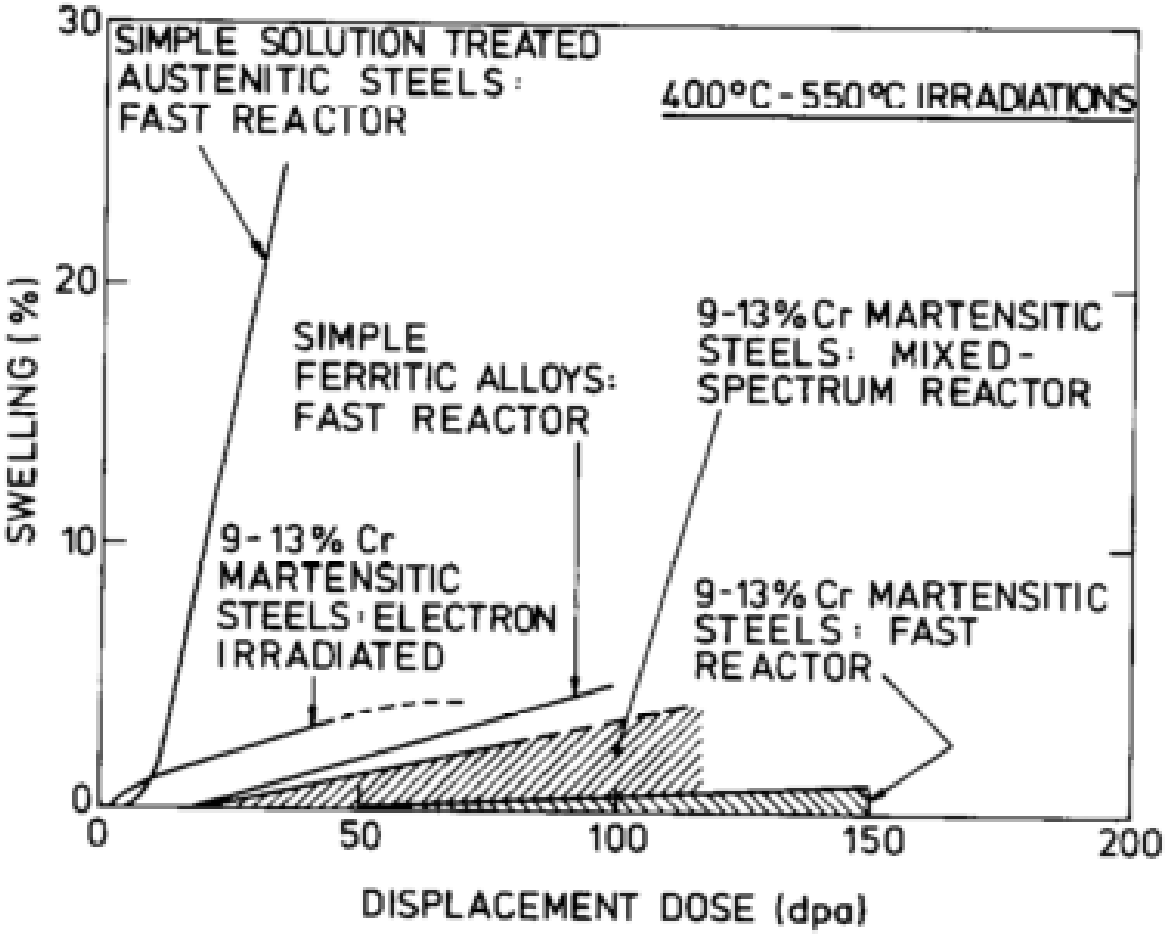

Figure 2.4 Swelling of ferritic-martensitic and austenitic alloys under a variety of irradiation spectra [25].

Odette [26] also reviewed the possible mechanisms for the lower observed swelling in F-M steels compared to austenitic steels. He also evaluated these factors using critical bubble-to-void and rate theory models. The following is a list of the possible mechanisms in Odette's references:

- A lower dislocation bias for interstitials in bcc compared to fcc. This is due to a smaller relaxation volume of point defects.
- The presence of a[100] loops. Interstitials would be partitioned to a[100] loops and vacancies to a/2[111] loops.
- Defect-solute trapping, which would promote recombination. However, at higher temperatures it is likely that this effect is small.
- Complex and fine-scale sub-grain structure. The high density of sinks would eliminate many point defects and also trap helium. However, sub-grain structures are not necessarily stable under irradiation and they would be qualitatively similar to cold-worked austenitics.
- The addition of solutes. Dislocation and void structures are affected. The addition of solutes could also affect surfaces energies and dislocation bias.
- Intrinsic self-diffusion rates are higher in F-M steels than in austenitics. This would expect to resist swelling especially at higher temperatures.
- There is a 3-4 times lower helium generation rate in F-M steels compared to austenitics. Helium serves to help nucleate voids so one would expect an increased incubation period required for F-M steels.

Using a critical bubble/rate theory, Odette attempted to further analyze some of the mechanisms. He concluded that low bias, high-self diffusion, low helium generation, and possibly high subgrain boundary sink strengths all contribute to observed swelling trends.

Dvoriashin et al. [27] analyzed the microstructure of EP-450 (an F-M alloy with compositions (0.1–0.15C, <0.8Mn, <0.5Si, 0.015S, <0.025P, 11.0–13.5Cr, 0.05– 0.30Ni, 1.2–1.8Mo, 0.1–0.3V, 0.3–0.6Nbwt%) irradiated in three Russian fast reactors. Hexagonal wrappers were taken from BN-350 and BN-600 and fuel pin claddings taken from BR-10 and BN-350. The authors prepared the samples using jet-thinning for TEM analysis. Voids were observed in the temperature range of 285-520ºC. A uniform void distribution was observed in the temperature

range of 285-460°C. At higher temperatures voids were not evenly distributed and were found along sub-grain boundaries and next to precipitates

2.4 Heavy Ion Irradiation of Ferritic-Martensitic Steels

In addition to neutron experiments, there have been several studies of heavy-ion irradiations performed on ferritic-martensitic steels to simulate the damage effects seen in reactor. Ward and Fisher [28] performed a heavy ion irradiation experiment with the goal of comparing swelling in ferritic steels and austenitic steels. They used 4 MeV iron ions to irradiate a Fe -10Cr ferritic steel (FV448) and a 316 stainless steel up to 10 dpa at temperatures between 510 and 540°C. Swelling was observed in the stainless steel, but not in the FV448. **Figure 2.5** shows voids observed in the stainless steel at 10 dpa.

The authors claim that the observed swelling resistance of FV448 is likely due to interstitial impurity concentrations. These experiments were performed at a rather low total damage level, and is therefore likely representative of difference in nucleation behavior between the alloys.

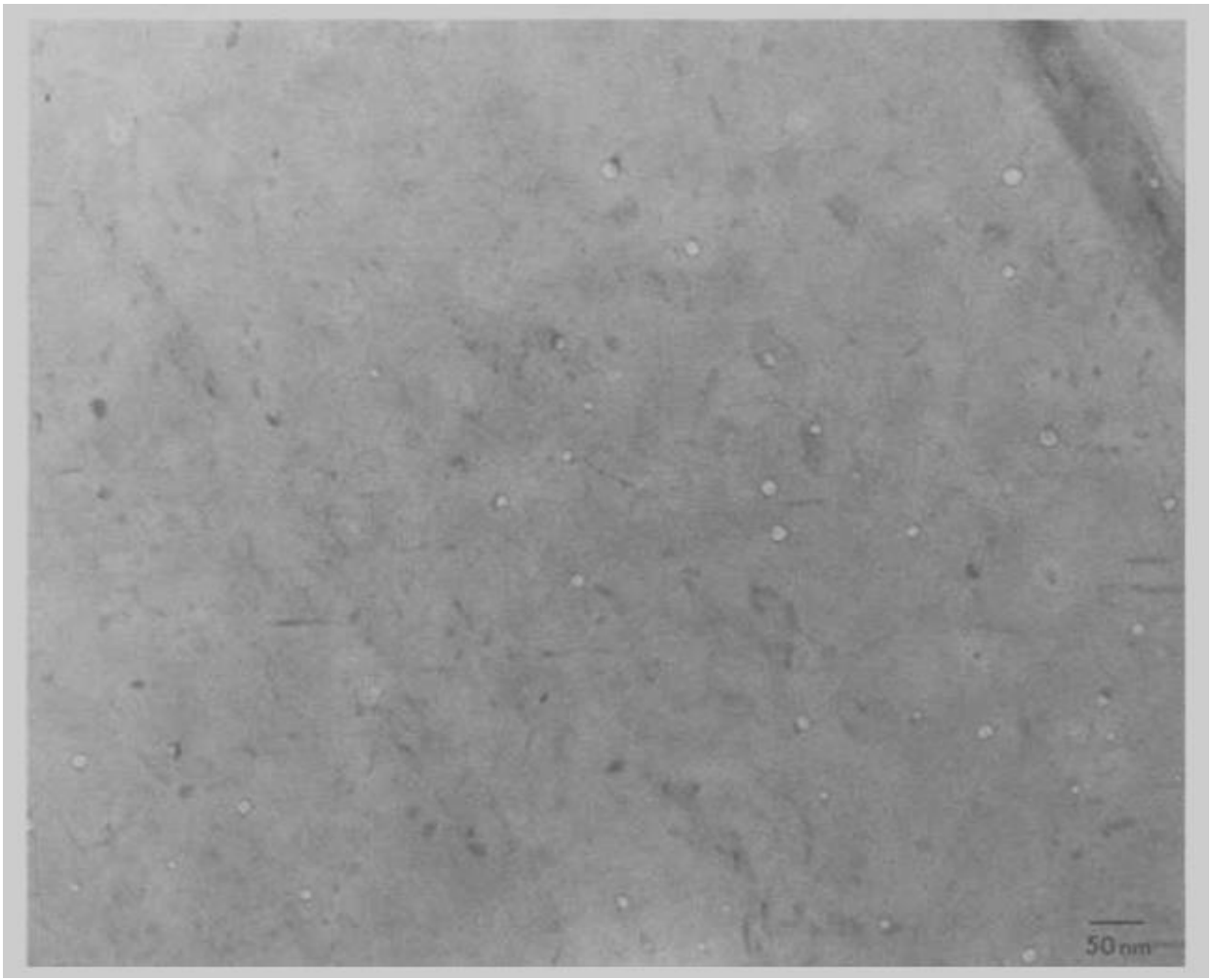

Figure 2.5 Voids were observed in the 316 stainless steel at 10 dpa after irradiation with 4 MeV Fe ions at 525°C [28].

Ayrault [29] performed an Ni^+ irradiation study on a 9Cr-1Mo ferritic steel. Ayrault sought to discern the temperature and damage dependence from single and dual beam heavy ion irradiations on the steel. The studies were performed at temperatures between 450-600°C and at damage levels of 5-25 dpa. The dual ion beam experiments used Ni^+ and He^+ ions and the single beam experiments utilized Ni^+ with preinjected He. For the dual beam experiments, cavity growth was observed with increasing dose (~ 3.5 nm at 5 dpa to ~ 9 nm at 25 dpa). The single beam experiments exhibited no cavity growth except at 450ºC. It was unexpected that swelling did not increase with increasing temperature, but that swelling was at a maximum at the lowest temperature studied. Overall, low swelling was observed (< 0.05%). Larger cavities seemed to form towards the centers of subgrains. The author suggests that the high swelling resistance is likely due to the high density of subgrain boundaries. While this study suggests high swelling resistance for the particular steel, it does not come to any conclusions about the peak swelling temperature. Additionally, the effects of helium pre-injection vs. simultaneous implantation are unclear because the amount of helium injected was different in both cases (the preinjected case had ~25 times less helium).

Hide et al. [30] studied the 200keV C^+ and 3 MeV Ni^+ irradiation of six different ferritic alloys: MA957 (a Fe-14Cr-1Ti alloy with 0.25% Y_2O_3 particles), HT9, Fe-12Cr, 12Cr-2Mo, 9Cr-8Mo-4Ni (solution anneal), 9Cr-8Mo-4Ni (aged). These metals were studied at damage levels from 50 – 200 dpa and temperatures from 425-625°C. All of the samples were pre-injected with helium to a fixed ratio of 0.1 appm/dpa.

The microstructure of MA957 is rather stable up through 150 dpa. A low density of cavities was observed under C^+ irradiation at 848K. These cavities still resulted in negligible swelling. Up to 0.3% swelling was observed in HT9 after irradiation. Cavities 3-5 nm in size were observed at temperatures greater than 798K, and they tended to increase in size with increasing damage and temperature. The cavity densities were calculated to be about 6×10^{22} /m^3. The irradiated microstructure of HT9 is shown in **Figure 2.6**. In the Fe-12Cr alloy larger cavities (~10.8 nm) were observed at a density of about 1×10^{22} /m^3 to a swelling value of about 0.28%. The 12Cr-2Mo alloy exhibited cavities from 4 – 10 nm in diameter and densities between 1- 3×10^{22}/m^3 up

to a swelling value of 0.42%. Large cavities (up to 280 nm) were observed in the austenite phase of the 9Cr-8Mo-4Ni alloy with densities around 3.4 x 10^{19} /m^3.

Overall, MA957 demonstrated the best swelling resistance, while HT9, 12Cr- 2Mo, and Fe-12Cr had similar cavity sizes and densities. The estimated swelling rate for the latter three steels is about 0.001% to 0.003%/dpa at the peak swelling temperatures. The temperature and damage dependence of swelling for all the alloys are shown in **Figure 2.7**.

While this study covered a large range of alloys and irradiation conditions, the authors did not address several important factors. They ignored the chemical effect of implanting C and Ni ions. The presence of additional due to both carbon uptake and irradiation with C ions would serve to suppress swelling and cavity formation. This excess carbon would promote the formation of carbides, which would serve as an additional sink for point defects. The authors did not address the presence of this carbides even though they are clearly present in **Figure 2.6**. This would potentially explain why minimal swelling was observed at temperatures between 400°C and 500°C, despite hundreds of dpa of damage. The low energy carbon ions (200 keV) required that the samples were back-thinned to be analyzed in the TEM, which means that the area of analysis was very close to the surface and susceptible to high amounts of additional carbon. Swelling observed at temperatures above 500°C were likely due to bubble agglomeration, as the high levels of implanted helium became more mobile. Furthermore, there was no discussion on whether steady state swelling had been achieved. The authors did note the marked difference between the voids in the austenitic phase versus the martensite/ferrite phase.

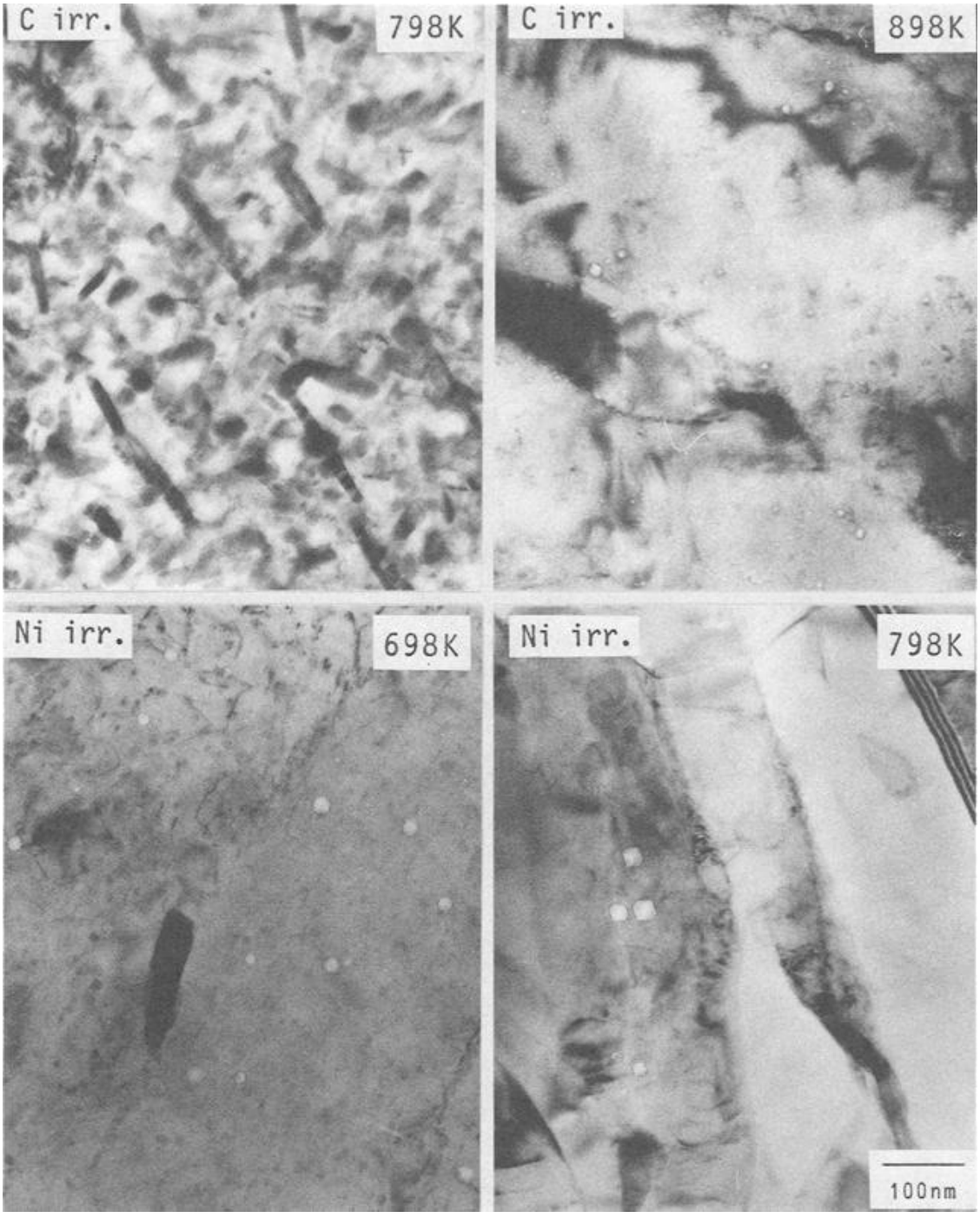

Figure 2.6 Cavities were observed in HT9 at 150 dpa with C and Ni ions [30].

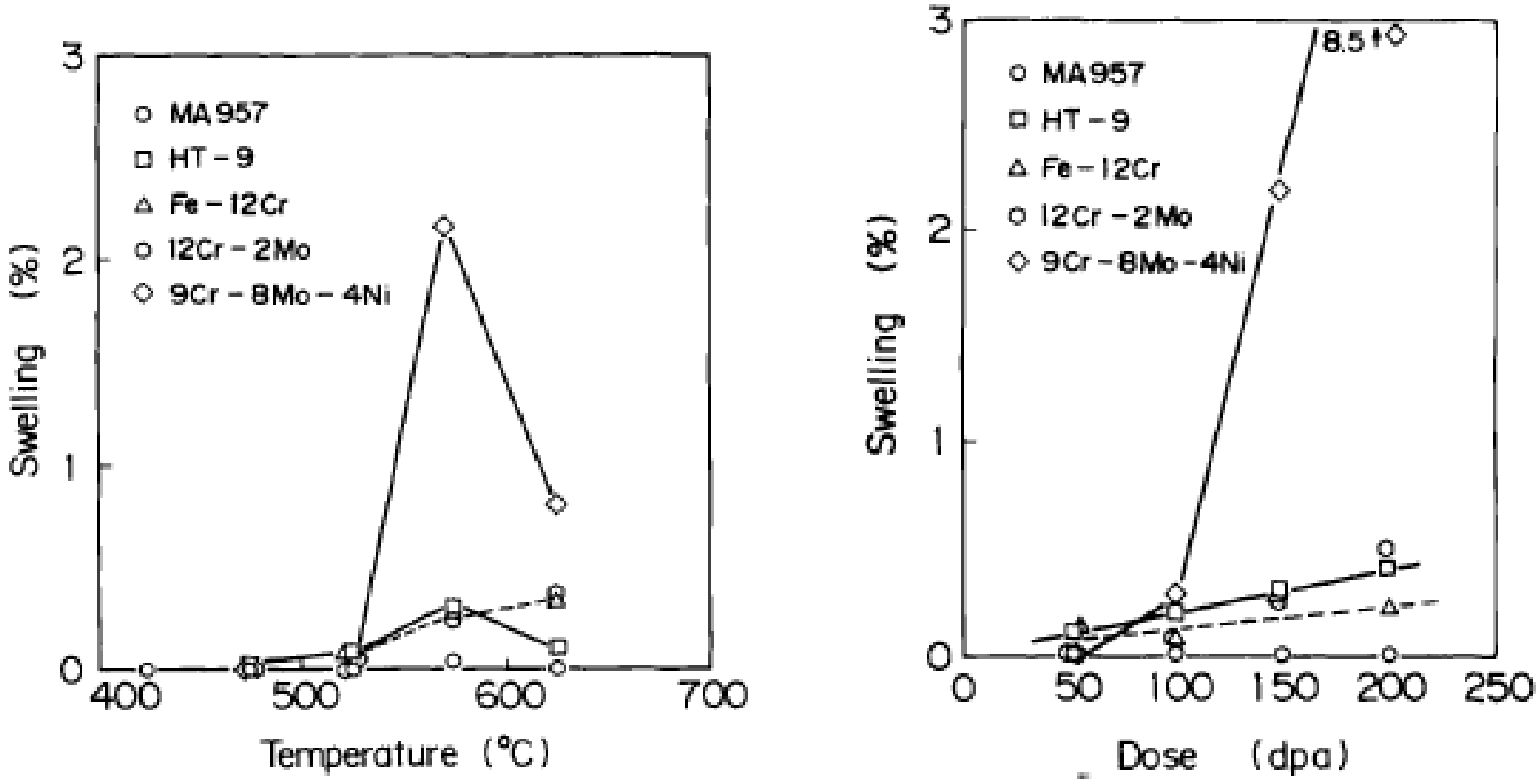

Figure 2.7. Temperature dependence and dose dependence of swelling are shown for the alloys under C ion irradiation [30].

Asano et al. [31] irradiated an ODS steel MA957 with single and dual beams up to 150 dpa at 723 and 923K. Ion irradiation was performed with 4 MeV nickel ions and 1 MeV helium ions. Large voids were only observed in the 15 appm He dual-irradiated case. Additionally, the voids were found to preferentially nucleate at sites thought to be Ti precipitates. High densities of smaller voids were observed in the other dual beam conditions, but no voids were observed in the single beam conditions. Swelling was calculated to be below 0.1% at 150 dpa.

Ferritic steel 21/4 Cr-1 Mo was studied by Sindelar *et al.* [32]. The focus of this studying was to determine the microstructural response to irradiation at various damage levels and in different phases of the material. Irradiation was performed up to 350 dpa at 500°C using 14 MeV nickel ions. No voids were present in any of the samples unless helium was pre-injected. Helium was pre-injected at 100 appm. The swelling results under this condition are summarized in **Table 2.5**.

The authors noted that the low swelling values were consistent with previous in-reactor irradiations of the same heat of material. Swelling values were determined both locally, and on a bulk basis. The authors also observed varying characteristics of the voids going further into the depth. Up to 0.7μm small cavities <10 nm in size were observed and were believed to be helium bubbles. Clusters of voids were observed from 0.7μm to 1.3μm, with no voids beyond 1.3μm. The authors seemed to be puzzled by the absence of voids near the damage peak. However, it is likely that they did not consider the effect of injected interstitials and their suppression of voids.

Table 2.5. The swelling results of 21/4 Cr-1 Mo are summarized and divided into regions within the damage depth [32].

Void density	
(0.3 μm, 50 dpa)	6×10^{14} cm^{-3}
(0.7 -1.3 μm, 100 dpa)	2×10^{14} (locally)
Average cavity diameter	
(0.3 μm, 50 dpa)	9 nm
(0.7 -1.3 μm, 100 dpa)	38 nm
Average swelling	
(0.3 μm, 50 dpa)	0.03%
(0.7 -1.3 μm, 100 dpa)	0.5% (locally)
(0.7 -1.3 μm, 100 dpa)	0.2% (homogenous)
Average bubble density	
(0.3 μm, 50 dpa)	8×10^{15} cm^{-3}
Average bubble diameter	
(0.3 μm, 50 dpa)	2 nm

These studies present a very clear picture, in both neutron and heavy ion irradiation experiments, that ferritic-martensitic steels exhibit very high swelling resistance. However, few of these studies systematically explored the void evolution at a variety of damage levels, temperatures, or materials. Ultimately this has resulted in a database of demonstrating the swelling resistance of ferritic-martensitic steels, but with little fundamental knowledge of why it is observed. Additionally, because of this high swelling resistance, studies have been unable to analyze the void swelling evolution in the growth regime. Therefore, the origins of the swelling resistance and the swelling behavior of these materials at high damage remain relatively unexplored. To attempt to understand the origin of this swelling resistance, it is important to determine factors which void swelling is very sensitive to, and to discuss their role in both nucleation and growth of voids.

2.5 Factors Affecting Cavity Evolution

In assessing the current state of knowledge of swelling in ferritic-martensitic steels, it is important to consider both the theoretical models and available body of experimental evidence. Swelling results from the formation of cavities, a term which is inclusive to both voids and bubbles. Voids are formed without the presence of a residual gas, and bubbles are defined as voids with gas pressure in mechanical equilibrium with the lattice. Cavity evolution is very sensitive to changes in temperature, dislocation microstructure, and gas content (usually in the form of helium). The expected changes in swelling behavior due to changes in these parameters can be assessed analytically. The experimental studies performed either refute or support these models to some extent. The following analyzes, in sequence, the effect of changes in temperature, dislocation microstructure, helium content, and carbon contamination on the cavity evolution of ferritic-martensitic steels. Each section first discusses the analytical models, and then proceeds to discuss the relevant body of experimental evidence. Conclusions on the state of knowledge of each effect are summarized at the end of each section.

2.5.1 Temperature Effect on Cavity Evolution

Cavity nucleation rate is strongly dependent on the vacancy super-saturation. Therefore, changes in temperature which affect the super-saturation of vacancies will affect the length of the nucleation region as well. Theory has shown that swelling follows a bell-curve temperature dependence [15]. Cavity formation and swelling tends to prevail at irradiation temperatures from about $0.2T_m$ to about $0.6T_m$. As temperature is increased, growth of cavities is enhanced due to

increased mobility of vacancies. As temperature increases further, nucleation and growth of cavities decreases with higher temperatures due to a higher emission of vacancies. At some optimal intermediate temperature, there is a maximum swelling where the inward vacancy flux is largest compared to the vacancy emission. At low temperatures, low point defect diffusivity restricts flow to the void nuclei. Vacancies have limited mobility at these temperatures and will also recombine with interstitials before clustering into voids. This behavior can be described by the number of vacancies required for a critically stable void to form:

$$n = \frac{36\pi\gamma^3\Omega^2}{3(kT)^3\left[\ln\left(\frac{B_v(n)-B_i(n+1)}{B_v^0(n)}\right)\right]^3} \quad \textbf{(2.3)}$$

Where γ is the surface energy, Ω is the atomic volume, k is Boltzmann's constant, T is temperature and $\frac{B_v(n)-B_i(n+1)}{B_v^0(n)}$ represents the vacancy super-saturation. Both temperature and vacancy super-saturation appear in the denominator, so at low temperatures and low vacancy super-saturations, the number of vacancies n becomes extremely large, and void nucleation is difficult. At high temperatures, the vacancy super-saturation is reduced due to increases in thermal vacancies and thermal of emission of vacancies to sinks and therefore n will also become extremely large.

Dvoriashin and colleagues [27] studied ferritic-martensitic steel EP-450 after irradiation in Russian fast reactors. Swelling was studied as a function of temperature in the range of 275ºC - 690ºC. **Figure 2.8** shows swelling rate as a function of temperature, demonstrating the characteristic bell-curve dependence. A peak is observed near 420ºC. Considering the low overall swelling observed, it is likely that these swelling rates are representative are more representative of a nucleation rate rather than a growth rate, and therefore demonstrating that nucleation follows a similar bell-curve.

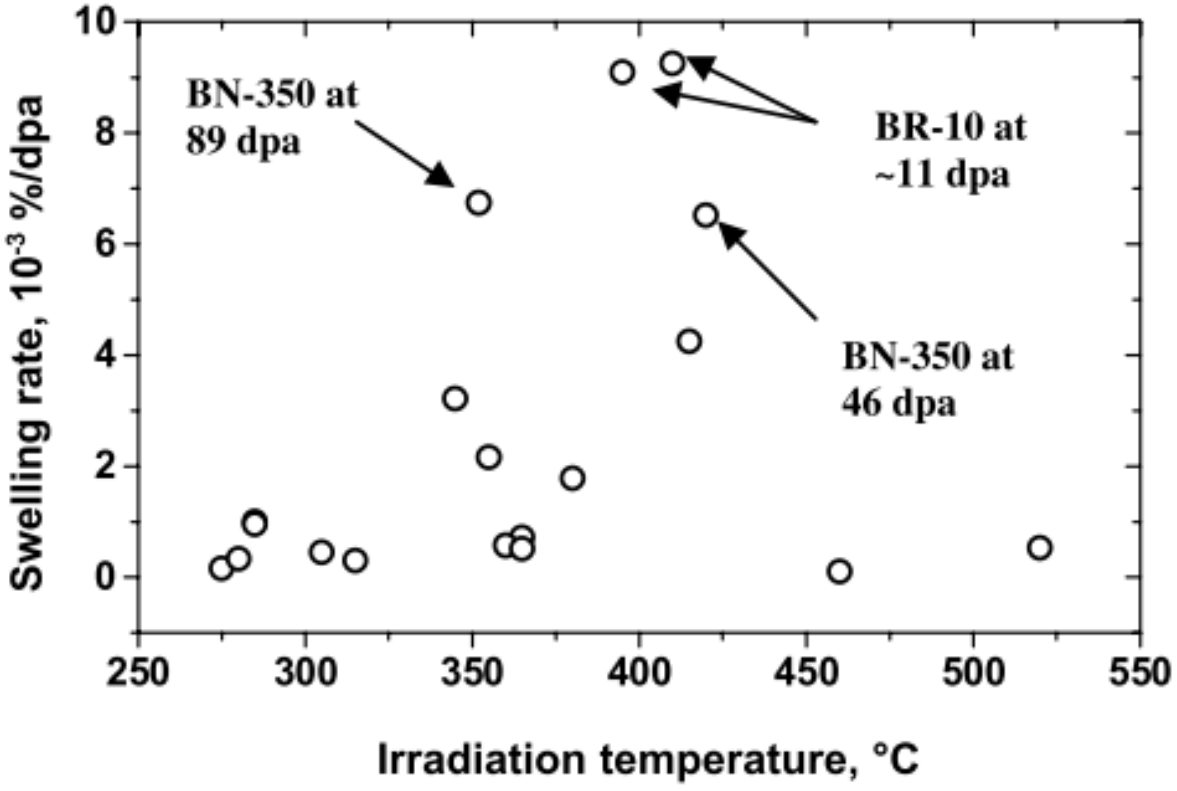

Figure 2.8 Temperature dependence of swelling rate in EP-450 [33].

Ayrault [29] studied the effect of irradiation temperatures above 450°C on a 9Cr-1Mo steel. No swelling peak was found, but the highest swelling occurred at 450ºC. This may suggest that the tail-end of a temperature peak was caught in this study and the peak would appear somewhere close to 450ºC.

Hide *et al.* [30] studied the 200keV C+ and 3 MeV Ni+ irradiation of six different ferritic alloys: MA957 (an ODS alloy), HT9, Fe-12Cr, 12Cr-2Mo, 9Cr-8Mo-4Ni (solution anneal), 9Cr-8Mo-4Ni (aged). These metals were studied at doses from 50 – 200 dpa and temperatures from 425-625°C. All of the samples were pre-injected with helium to a fixed ratio of 0.1 appm/dpa. The temperature and dose dependence of swelling was shown previously in **Figure 2.7.** Across the alloys, a common peak swelling temperature was observed at 575ºC. Based on the dose dependence, it is unclear whether steady-state swelling has been reached, especially considering the low overall values of swelling.

Kai and Kulcinski [34] studied HT9 irradiated with nickel ions at three different temperatures: 400ºC, 500ºC , and 600ºC. Voids were only observed at 500ºC. The intermediate temperature was the only temperature which exhibited void nucleation.

Schmidt *et al*. [35] observed a peak swelling temperature of 500ºC in HT9 and 550ºC in EM-12 after irradiation with 2.8 MeV Fe^{+} ions up to 250 dpa. The dependence of swelling as a function of temperature is shown in **Figure 2.9**.

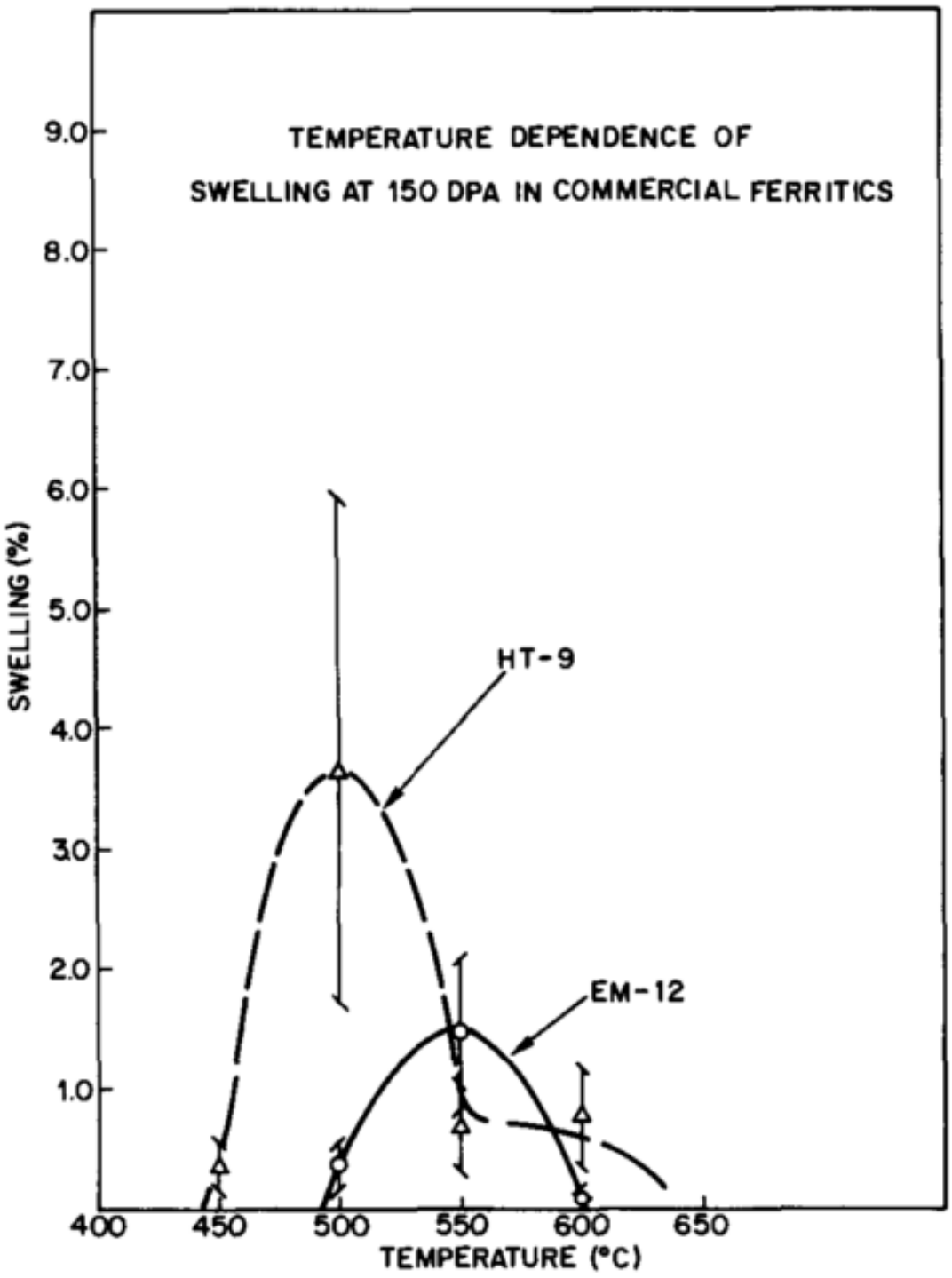

Figure 2.9 Temperature dependence of swelling at 150 dpa for EM-12 and HT9 using 2.8 MeV Fe^{+} ions [35].

Sencer *et al.* [17] irradiated HT9 in FFTF and found the highest swelling at a temperature of about 443ºC and a dose of 155 dpa. However, it must be noted that the damage level was also highest at this temperature (155 dpa at 443°C compared to 28 dpa at 384ºC), which may cloud the effect of temperature.

Wakai *et al*. [36] showed highest swelling at 470ºC, which then decreased with increasing temperature. Ferritic-martensitic steel F82H was irradiated with a triple beam system (Fe^+, He^+, and H^+) at temperatures from 470ºC to 600ºC. It is likely that a peak swelling temperature is present at a temperature lower than that studied.

Getto *et al.* [8] studied swelling in HT9 at temperatures ranging from 400°C to 480ºC after irradiation up to 375 dpa. The peak swelling temperature was determined to be near 460ºC. At lower and higher temperatures 480ºC and 440ºC, it was determined that the onset of swelling was delayed relative to experiments performed at 460ºC. The swelling behavior as a function of temperature at 188 dpa is shown in **Figure 2.10**. This set of experiments suggested that void nucleation was enhanced closer to the peak swelling temperature.

Toloczko *et al*. [37] performed a study on MA957 tube up to 500 dpa with no pre-injected helium at a variety of temperatures (400ºC, 420ºC, 450ºC, 500ºC). The peak swelling temperature was determined to be near 450ºC. The swelling results are shown in **Figure 2.11**. The study compared the swelling behavior at damage levels of 100 and 500 dpa. However, the coarseness of these damage levels does not allow us to determine whether steady-state swelling was achieved, or what the incubation period may have been. It does however, provide further evidence that nucleation was enhanced at damage levels closer to the peak temperature.

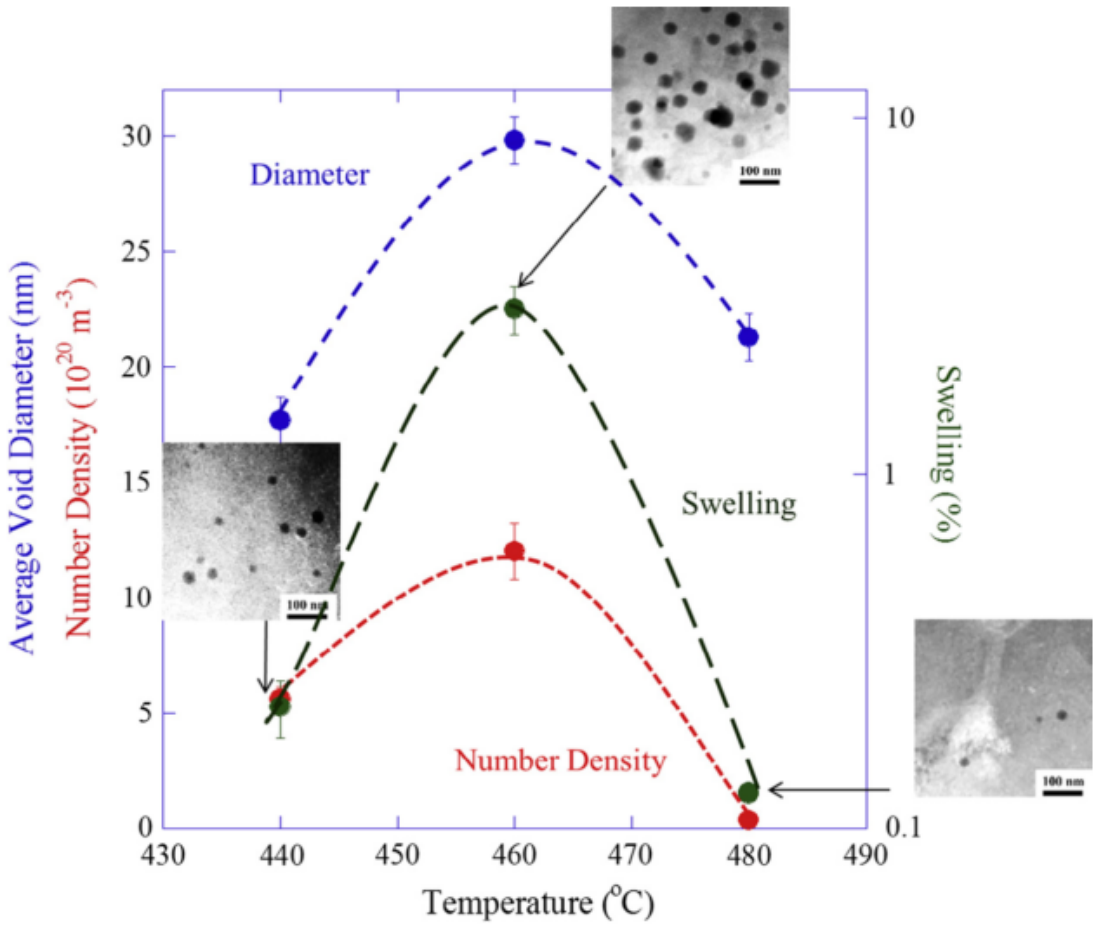

Figure 2.10 Temperature dependence of swelling, diameter, and number density at 188 dpa for HT9 using 5 MeV Fe^{2+} ions [8].

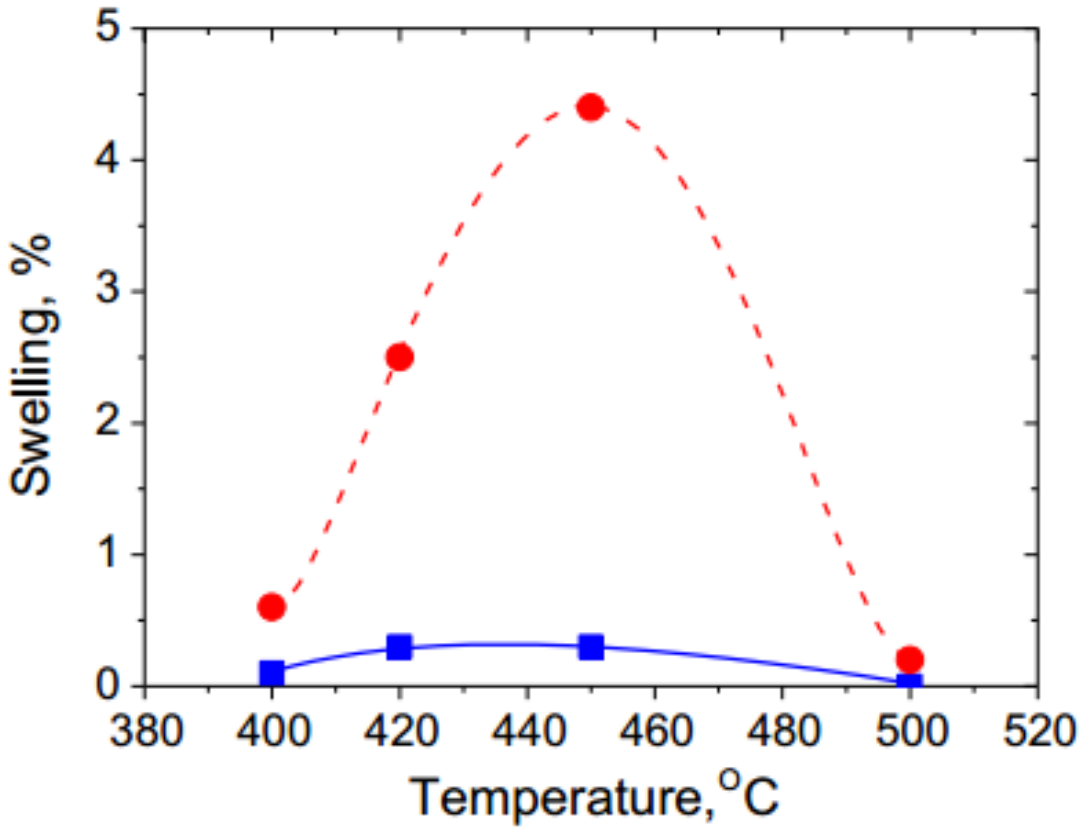

Figure 2.11. The temperature of dependence of swelling is shown for MA 957 at 500 dpa (red curve) and 100 dpa (blue curve) irradiated with 1.8 MeV Cr^{+} ions [37].

The authors compared the swelling behavior of MA-957 to that of HT9 and EP-450. The swelling as a function of dpa is shown up through about 500 dpa in **Figure 2.12**. A steady-state swelling value of 0.2%/dpa was determined for HT9 and EP-450. From this, a nucleation region of about 450 dpa for HT9 and ~150 dpa for EP-450 can be determined. However, it is important to note that EP-450 was irradiated at a different temperature (480°C) compared to MA-957 and HT9. MA-957 exhibited the lower swelling up to 500 dpa and the achievement of steady-state has not yet been confirmed. This is further supported by the void distributions in the paper, which are skewed to smaller sizes.

According to both theory and the studies described here, a swelling peak is expected at intermediate temperature. For neutron irradiations, this peak may be approximately centered at 440ºC. For ion irradiations, it may be higher from ~460ºC-500ºC. This swelling peak is usually referred to as occurring at steady-state, however since the processes affecting the growth of voids govern nucleation as well (i.e. super-saturation of vacancies), these concepts can also be extended to void nucleation. Therefore, we would expect the nucleation region to follow a similar trend, with the lowest incubation period seen at the peak swelling temperature.

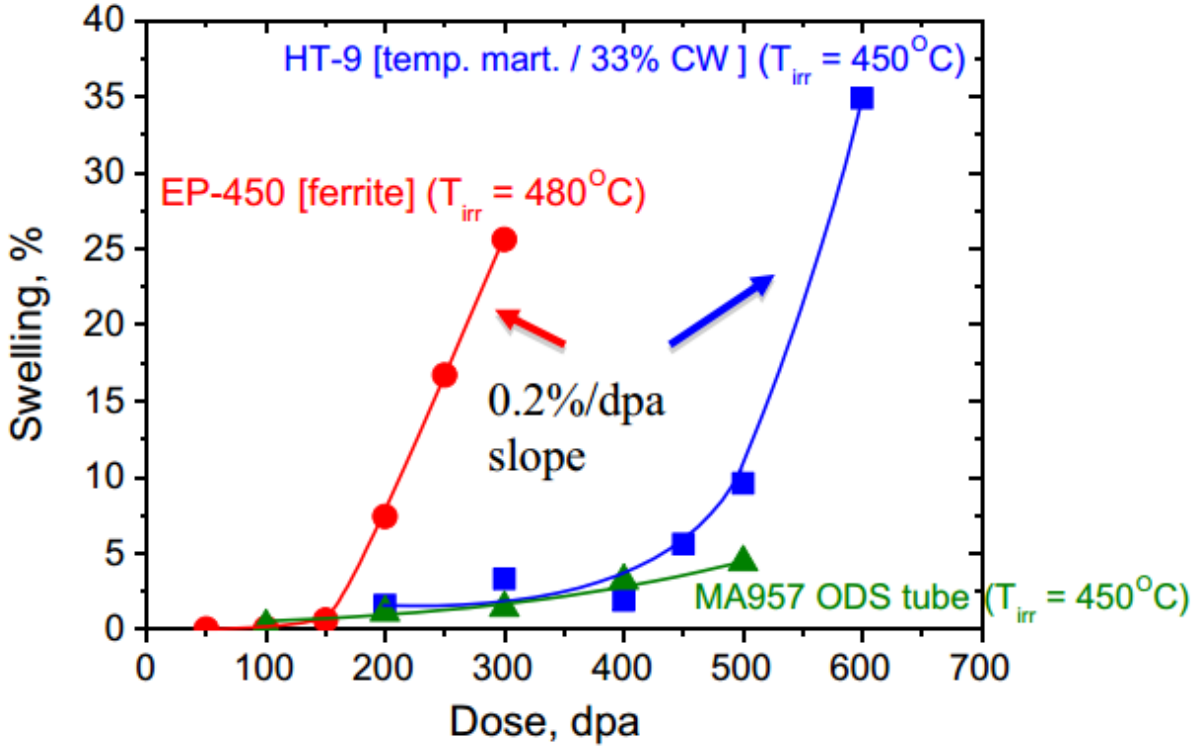

Figure 2.12 The swelling dependency for MA 957, HT9, and EP-450 are shown through ~600 dpa irradiated with 1.8 MeV Cr^{+} ions [37].

Qualitatively, there is evidence that swelling as a whole follows the expected bell-curve behavior, and so it is reasonable to assume that nucleation behavior will follow, due its large role in determining overall swelling behavior. Confirmation of the achievement of steady-state has not been achieved in many experiments, however the available body of literature all points to the same behavior of swelling with temperature. It is very likely that the steady-state growth rate will follow a similar bell-shaped curve. It has been postulated by Garner [7] that there exists a "universal steady-state swelling rate" which is independent of temperature, but this has not been experimentally confirmed. While a systematic set of experiments at incremental temperatures would be required to identify the location of the peak swelling temperature. Such a set of experiments will prove useful in determining the effect of varying the temperature from the peak on void nucleation and steady-state swelling rate, however there is little else to be explored in regard to the behavior of temperature with swelling.

2.5.2 Dislocation Microstructure Effect on Cavity Evolution

The dislocation microstructure of a material plays a critical role in the swelling behavior. In fact, the existence of the dislocation microstructure is what allows voids to exist. Since dislocations are sinks biased for interstitials, this results in a vacancy super-saturation, creating the possibility for vacancies to cluster and eventually become stable voids. However, as the dislocation strength of a material increases, the overall sink-strength may become too high to support a vacancy super-saturation, therefore a delicate balance between the sink strength of the dislocations and that of the voids is required to maintain a maximum swelling rate. The ratio between sink strength of dislocations to voids (Q) has been explored by Mansur [38]. It was determined that at a Q value of approximately 1, a maximum swelling rate is achieved.

Much work has been done on austenitic stainless steels to determine the effect of high dislocation densities on the microstructure. Studies have shown that increases in dislocation densities through cold working have resulted in higher swelling resistance for austenitic stainless steels [39]. However, ferritic-martensitic steels possess a much more complex dislocation microstructure, therefore changes in microstructure are much more difficult to achieve and to characterize. The origin of the swelling resistance of ferritic-martensitic steels is largely attributed to the high sink strength, of which the dislocation microstructure is a large contributor. Because of

high dislocation densities and the difficulty of characterization, few studies have explored the effects of dislocation densities on swelling in ferritic-martensitics, and even fewer have quantified the effects. **Figure 2.13** taken from Mansur's study [38] did show that swelling rate in F-M steels and austenitics follow the expected trend as a function of Q.

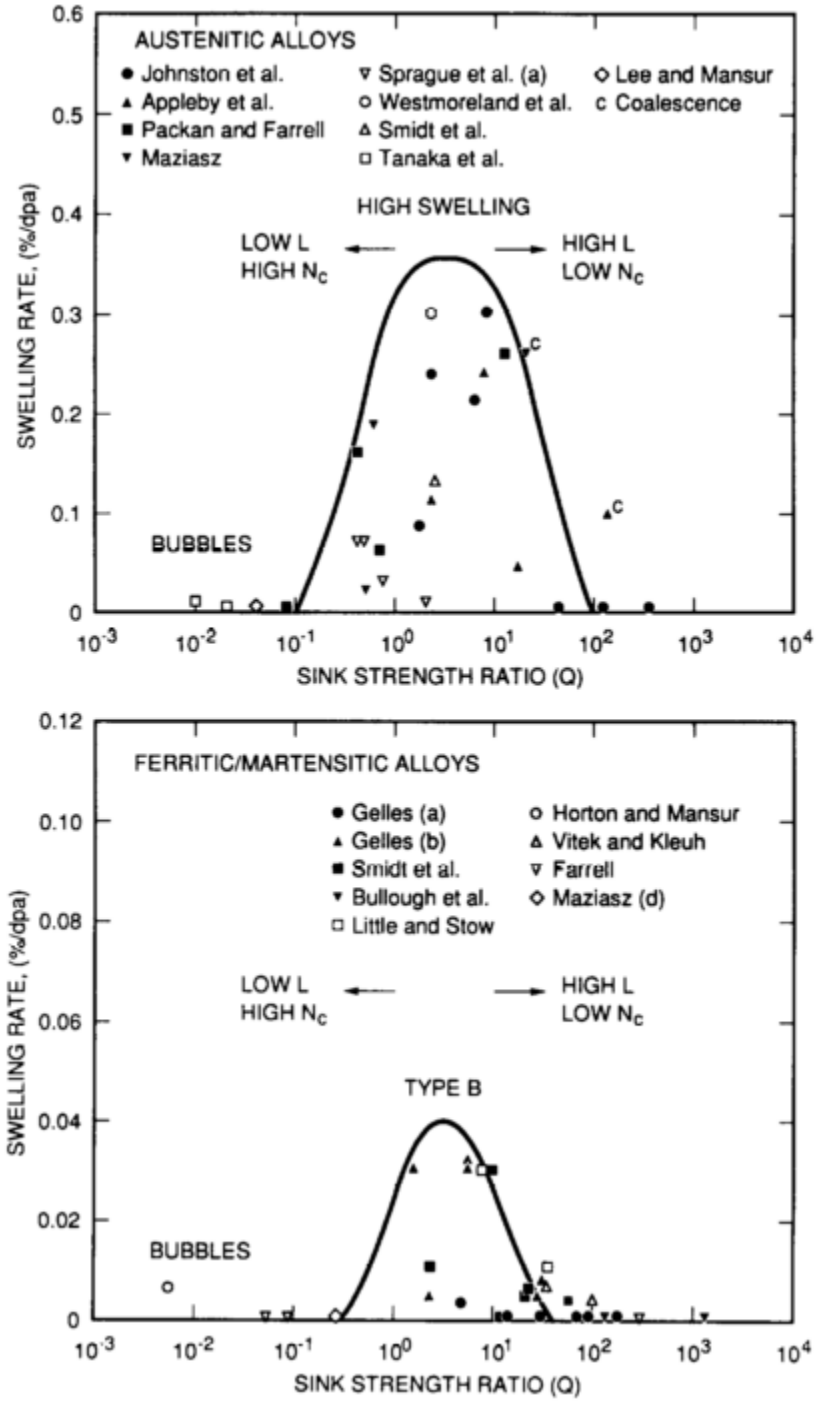

Figure 2.13 Swelling Rate is plotted versus sink strength ratio Q for a collection of experiments in austenitic alloys and ferritic-martensitic alloys [38].

Gelles [18] explored the swelling behavior of two different heats of the same alloy HT9 irradiated with neutrons up to 200 dpa. One heat was tempered at 700°C, and another heat was tempered at 760°C. The HT9 tempered at 700°C exhibited a higher density of dislocations compared to the 760°C temper. However, the dislocation microstructure was not quantified beyond reporting the existence of **a**/2<111> and **a**<100> loops. The heat with the higher reported dislocation density exhibited 0.09% swelling, while the more relaxed dislocation microstructure exhibited 1.7% swelling. While Gelles acknowledges that the precipitates between the two heats may be different, it is likely that the higher dislocation densities contribute more to the swelling resistance.

Kim *et al.* [40] studied the swelling resistance of a series of steels with increasing sink strengths (316 stainless, 9Cr ferritic-martensitic steel, and three ODS: 17Y3, 12Y1, and 12YWT). After irradiation using both 3.2 MeV Fe^{+} and 330keV He^{+} at 650°C, the authors observed smaller densities and sizes of voids in the materials with higher sink densities (both dislocation densities and ODS particles). However, a rigorous characterization of the swelling and dislocation densities is lacking. The authors suggest that the resistance to swelling is mainly due to the higher densities of dislocations. Additionally, calculations were made in an effort to show the effect of high dislocation densities on the critical cavity radius, as shown in **Figure 2.14**. The critical cavity radius as a function of dislocation density was calculated using the previously discussed rate theory formulation developed by Lee and Mansur [41], which took into account detailed material and irradiation parameters which are summarized in [40]. At some intermediate dislocation density, the critical cavity radius is the smallest. This suggests that not only swelling rate (growth) of cavities follows a Q-like relationship, but also nucleation as well.

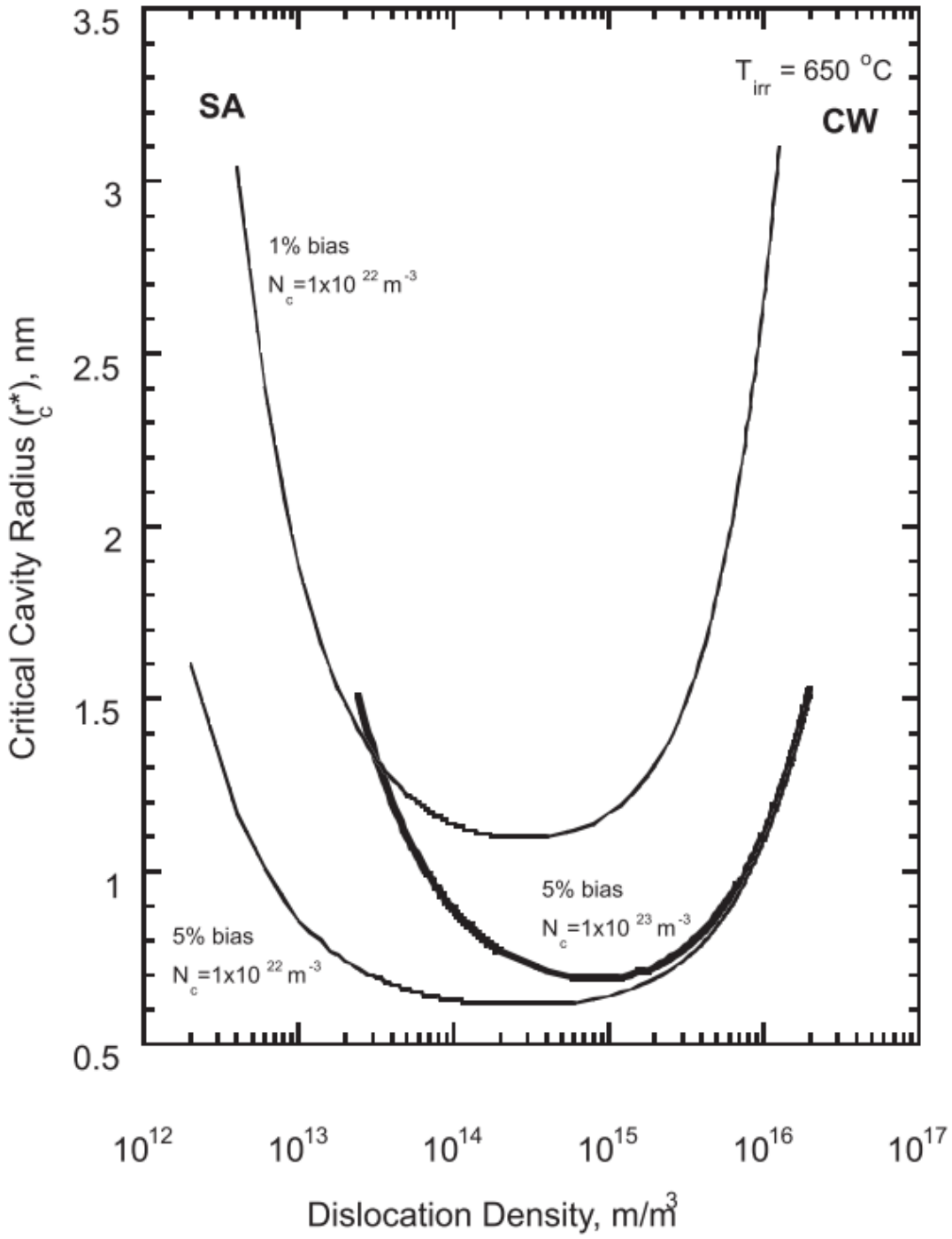

Figure 2.14 The critical cavity radius is plotted as a function of dislocation density [40].

Garner [7] showed that the swelling trends may be more complicated when it comes to dislocations. In materials where dislocations are not already heavily present but are resistant to swelling, cold-working may actually increase the swelling. The behavior of swelling with dislocation density also largely depends on the temperature of irradiation, with lower temperatures resulting in a larger transient regime, while higher temperatures resulting in a shorter one. However, most of this work was performed with austenitic stainless steels, where the effect of cold-working and dislocations is obvious.

Dubuisson [42] explored the irradiation effects on the microstructure of several steels: 17Cr ferritic, EM12, FV448, HT9, 1.4914, and 9-12Cr ferritic-martensitic steels. Of particular interest is the effect of irradiation on EM12, which is a duplex steel, contain grains of both ferrite and martensite. It is well established that martensite grains contain a higher dislocation density (~1 x $10^{15}m^{-2}$), compared to ferrite grains (~2 x $10^{14}m^{-2}$). Irradiation of this material allows for the determination of the effect of a higher dislocation density on swelling behavior. Additionally, the other materials covered in this study ranged from fully ferritic, to duplex, to fully martensitic. After irradiation at a variety of temperatures below 500°C, and doses up to ~116 dpa, voids were observed in all samples except the HT9. Only the fully ferritic steel and duplex steel exhibited a significant void density. The ferrite regions of EM12 and the ferritic steel F17 irradiated at 420°C, 75 dpa resulted in the same void microstructure with swelling values of 0.5%, while the martensitic regions of EM12 exhibited much lower amounts of swelling. The authors suggest that the origin of this swelling resistance is due largely to the greater amount of point defect sinks in the martensitic microstructure compared to the ferritic microstructure.

While it is clear that there is a stark difference between austenitic swelling resistance and ferritic swelling resistance, and a further difference between ferritics and martensitics, the role of dislocations on that swelling resistance is not entirely clear. The dislocation densities change by orders of magnitude when going from austenitics to martensitics, however little work has been done to quantify the effect—especially in martensitics. In austenitic steels it is relatively easy to observe changes in dislocation density in the material due to cold working or heat treatment. However, the martensitic microstructure is largely saturated with dislocations and quantifying the initial microstructure is challenging. Furthermore, the effects of cold working on ferritic-

martensitic alloys remain relatively unexplored—the increase in dislocation density or other microstructural changes are unknown. As mentioned above, studies have qualitatively seen changes in the dislocation microstructure and a resulting effect in the swelling resistance. Higher dislocation densities seem to delay the onset of swelling, likely due to contributions to a higher sink strength. This highlights the need for a rigorous quantitative study on the dislocation microstructure of ferritic-martensitic steels, perhaps with varied levels of cold-working is needed. However, the value of such a study is expected to be somewhat limited, as many experiments have shown to follow the expected behavior with sink strength balance. If that is the case, then such a study would be highly material specific, and not of much value to the scientific community.

2.5.3 Gas Effect on Cavity Evolution

The production of inert gas atoms in reactors may act to stabilize subcritical voids, and in the process, encourage nucleation of stable cavities. Helium is often the focus of inert gas studies as it is commonly produced in reactor materials, however other gasses, such as oxygen, have also been known to enhance cavity formation [43–45] . Helium is thought to enhance the nucleation of cavities by providing sites for vacancy clusters to form. This is achieved through lowering the free energy requirement to create a critical cavity embryo. In the presence of helium, **Equation 2.1** becomes:

$$\Delta G = -nkT\ln\left(S_V\right) + (36\pi\Omega^2)^{1/3}\gamma n^{2/3} - xkT\ln\left(\frac{MHn\Omega}{xkT}\right) \qquad (\mathbf{2.4})$$

Where x corresponds to the number of helium atoms in the cavity, M is the concentration of helium atoms in the solid (usually in atoms/cm^3 or equivalent), and H is the Henry's Law constant for the dissolution of helium in the metal. The entire third term in **Equation 2.4** represents the lowered free energy due to the work required to move the helium from the solid into the cavity. From comparing **Equations 2.1** and **2.4** it is clear that the presence of helium lowers the free energy required to form a stable void. This lower free energy results in a smaller critical void nucleus required for stable void formation, and thus enhances nucleation relative to a gas-free environment.

In attempting to answer the question of how important helium is to void nucleation, Stoller and Odette [46] studied the effect of the cluster composition (helium vs. vacancy) on the nucleation path of voids. Two paths limiting void formation: one limited to growth by helium accumulation

alone, the other limited by stochastic fluctuations in vacancy cluster population. Gas accumulation path seemed to be generally dominant. Specific cluster compositions and distributions are not analyzed, however. This work was done for austenitic stainless steels, and whether this is still relevant for ferritic-martensitic steels has yet to be established.

Stoller further suggests [47] that the relationship of helium with swelling is not monotonic, and depends on the sink structure which it forms. At low damage levels, the helium acts as vacancy traps which serve as nucleation sites for cavities. The resulting microstructure at higher damage levels would then be a function of the number of sites created. If helium is increased to the point where these sites become a major sink, the microstructure would then evolve along a different path—recombination rates at the cavities become high, and thus the vacancy supersaturation is decreased. Additionally, helium and vacancies must be distributed to a higher number of sites before growth can occur.

2.5.4 Effect of helium injection mode

In accelerator experiments, helium may be injected into the metallic lattice, rather than created through transmutation to simulate reactor environments. The implantation of helium is known to shorten the incubation period for cavity nucleation by stabilizing small clusters of vacancies and allowing them to more easily reach critical size. Farrell [48] [49] studied the effect extensively. The work is heavily theoretical, backed by some experiments, but explains in detail the role helium plays in cavity nucleation and growth, and effects on dislocations and precipitates. While the work is not specific to F-M steels, it still provides valuable insight into the formation and growth of cavities.

Gasses facilitate nucleation of cavities, especially non-reactive and insoluble gasses such as helium. Helium tends to reduce the incubation period required for the nucleation of voids, and tends to result in higher densities of smaller sized cavities. The implantation process also will affect the behavior of cavities. Pre-implanted helium at room temperature seems to be more effective at nucleating cavities than implanted helium during the irradiation or helium implanted at the irradiation temperature. High amounts of helium can actually depress growth and retard swelling. If cavities become the dominant sink, then they will tend to resist void growth.

Hot helium implantation tends to result in a larger cluster but smaller densities. The less mobile cold pre-implantation results in vacancies being trapped on a smaller scale and thus creates a high concentration of smaller cavities. Cold pre-implantation and co-implantation both tend to result in bimodal distribution of cavities with a large group smaller than the critical radius and a group that has stabilized beyond the critical radius.

Lastly, grain boundaries can serve as traps for helium, thus forming grain boundary bubbles. These bubbles are not bias driven, as the concentration of point defects near grain boundaries is usually very low so supersaturation of vacancies at these sites is very rare.

The most comprehensive work which explored the effects of the method of helium pre-implantation was performed by Packan and Farrell [50] on 316 stainless steel. Doses up to 70 dpa were explored with helium either simultaneously injected at 20 appm/dpa (to a total of 1400 appm), or pre-implanted at room temperature or 627°C at 1400 appm. The highest swelling was observed in the unimplanted material (18%), with simultaneous injection resulting in 11% and pre-implantation at 627°C resulting in 4% and only 1% at room temperature. These results are summarized in **Table 2.6** below.

From the images of the void microstructure (**Figure 2.15**) it is clear that the higher swelling in the unimplanted case is due to the fact that the voids were allowed to grow unimpeded. The addition of helium through any method resulted in lower swelling, likely due to the high void sink strength resulting from the very high density of nucleation.

Table 2.6 The swelling resulting from different methods of helium pre-implantation from [50]**.**

Implantation Condition	Swelling (%)
None	18
Co-Implantation (20 appm/dpa)	11
627°C Pre-implantation (1400 appm)	4
RT Pre-implantation (1400 appm)	1

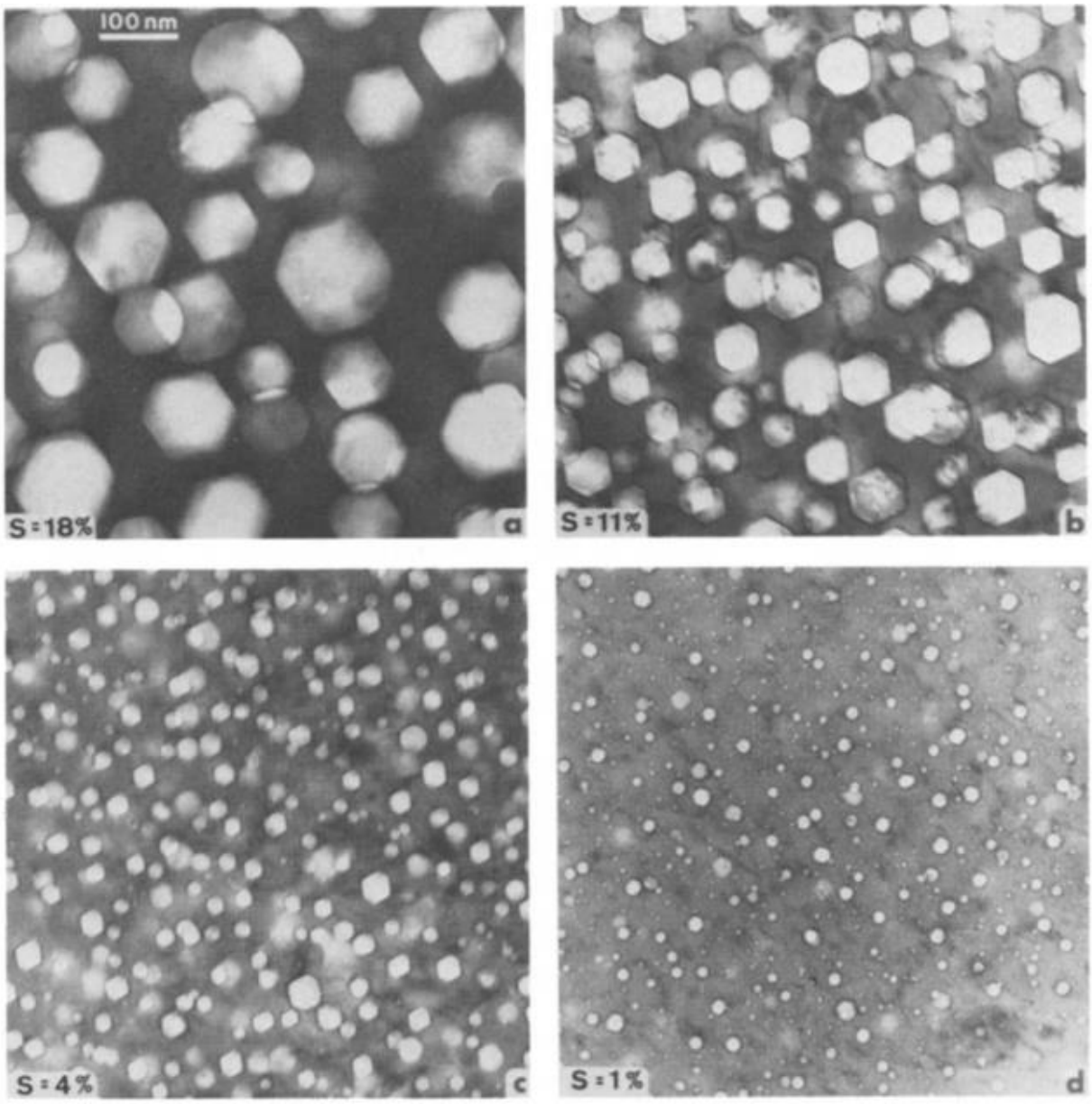

Figure 2.15 Void microstructure produced at 70 dpa with (a) no helium (b) coinjection (c) pre-implantation at 627C and (d) pre-implantation at room temperature [50]**.**

While the addition of helium causes a reduction in swelling in all cases, it should be noted that only relatively high amounts of helium were studied—likely resulting in excessive void nucleation which inhibited growth. It remains unclear whether the addition of a smaller amount of helium would enhance the swelling beyond that of the unimplanted condition. However, the difference in swelling behavior between the room temperature implantation and the 627°C implantation is likely due to a coarsening effect of the pre-implanted helium clusters. The higher temperature pre-implantation created fewer but larger void nuclei.

The authors suggest that for the room temperature pre-implantation the cavities were the overwhelming dominant sink and voids and dislocations were approximately equal in the co-injected and no helium cases. The defect partitioning ultimately determines whether the voids will grow unimpeded or not, but a thorough comparison of the Q ratios is not presented in the paper. Based on the results, it is likely that hot pre-implantation pushes the microstructure to a more dislocation-favored regime.

It is also postulated that the high levels of helium served to bind many vacancies, preventing them from clustering and promoting recombination. These helium-vacancy complexes served as non-biased sinks for point defects resulting in a decrease in the super-saturation and ultimately repressing the nucleation and growth of stable clusters. However, while this theory is postulated, there is no confirmation that this is the cause of repressed swelling. Furthermore, there is no comparison with other levels of pre-implanted helium, to be able to determine whether this is caused from pre-implantation, or just the high level of helium included.

2.5.5 Effect of helium at high damage

Some experimental studies have explored the effects of various helium levels on swelling. In a study mentioned previously, Kai and Kulsinki [34] irradiated sets of HT9 specimens up to 200 dpa. One set had no helium pre-implanted, while the second set had 100 appm He pre-implanted. Cavities were only observed in the 100 appm samples. While this study demonstrates that the presence of helium does indeed enhance nucleation, it does not discuss to what extent it may enhance it since only a single damage and helium level was considered. No evidence of steady-

state swelling is presented and thus, any information about the incubation period or the effect of helium on growth cannot be determined.

Jiao *et al*. [51] performed a series of proton irradiations on T91 implanted with various levels of helium. Experiments were performed at 450°C with implantation levels of 720 appm, 1260 appm, and 1800 appm helium. The irradiations were performed using 2 MeV protons to doses of 2.2 dpa, 7 dpa, and 9.2 dpa. At these high levels of helium, bubbles were observed in all pre-implanted cases and increased in diameter with increasing helium levels. Bubble sizes of 1.0nm, 1.2nm, and 1.4nm were found in the 720 appm, 1260 appm, and 1800 appm samples respectively, at a concentration of about $10^{23}m^{-3}$ were observed. After irradiation, the bubble sizes increased, and the swelling increased as well. However, since protons were used for irradiation high doses could not be achieved—and evaluations on the incubation period and steady-state swelling rates could not be determined. However, it is important to note that levels of helium pre-implantation of 720 appm and above caused the formation of visible bubbles prior to irradiation.

Getto *et al.*[8] performed a study at a variety of helium levels (0, 1, 10 and 100 appm). Overall, it was observed that increasing amounts of helium resulted in a decreasing damage level for cavities to appear. Steady-state swelling seemed to be achieved using 10 appm helium by 375 dpa, however steady-state swelling was not confirmed for any other helium level. It appeared that a helium level of 1 appm may have been approaching a lower steady-state swelling rate. These effects are shown in **Figure 2.16**. Helium levels of 100 appm seemed to suppress swelling in the transition regime, which may suggest a difference in the steady-state swelling behavior.

Wang *et al.*[9] studied RAFM steels similar to T91 and HT9 implanted with helium levels of 10 and 100 appm up to 188 dpa. Similar to Getto's experiments, higher helium levels decreased incubation period, however there was not an observed change in steady-state swelling rate. The effect of different helium levels is shown in **Figure 2.17**.

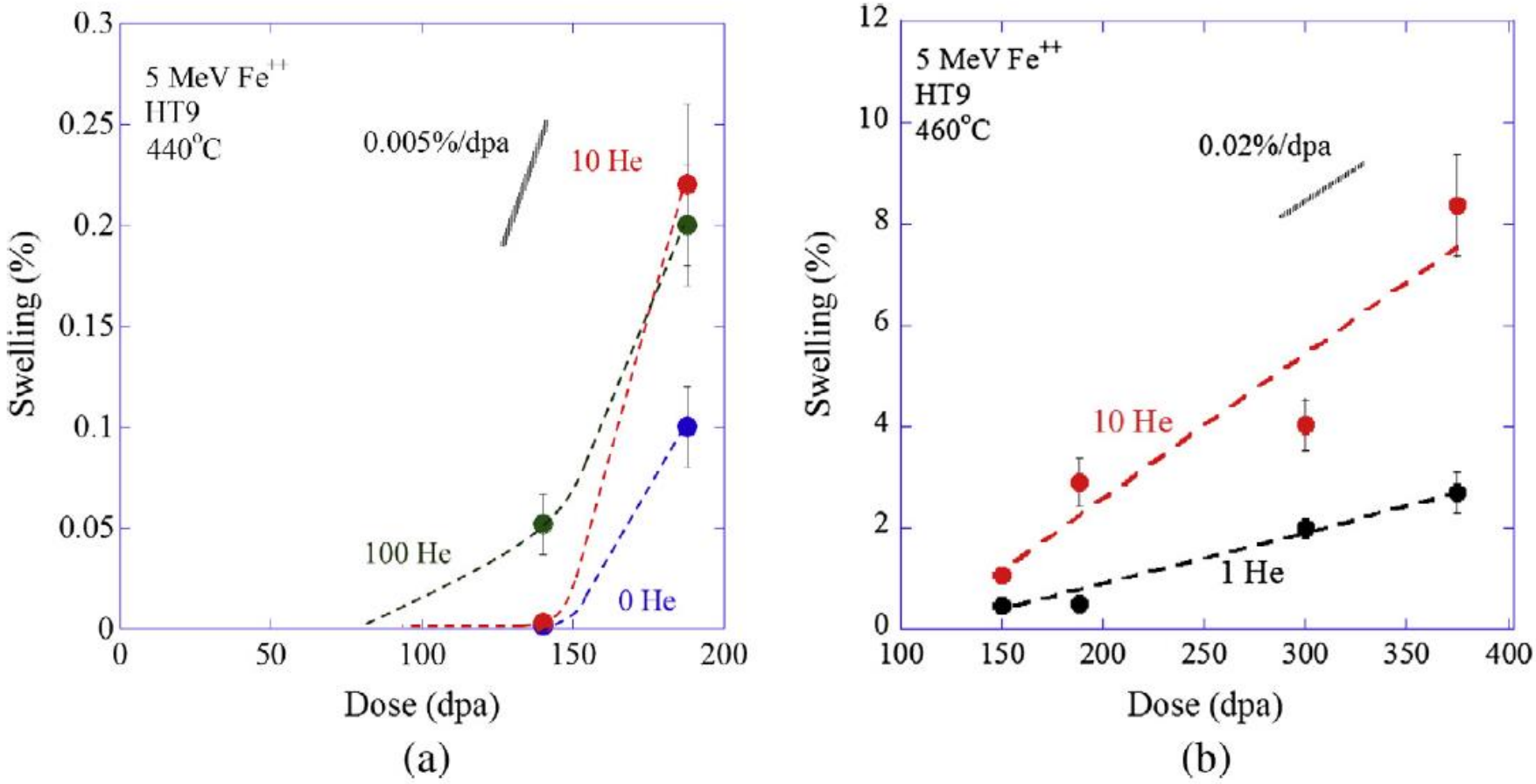

Figure 2.16 Swelling dependence of HT9 for various helium levels at (a) 440°C and (b) 460°C [8].

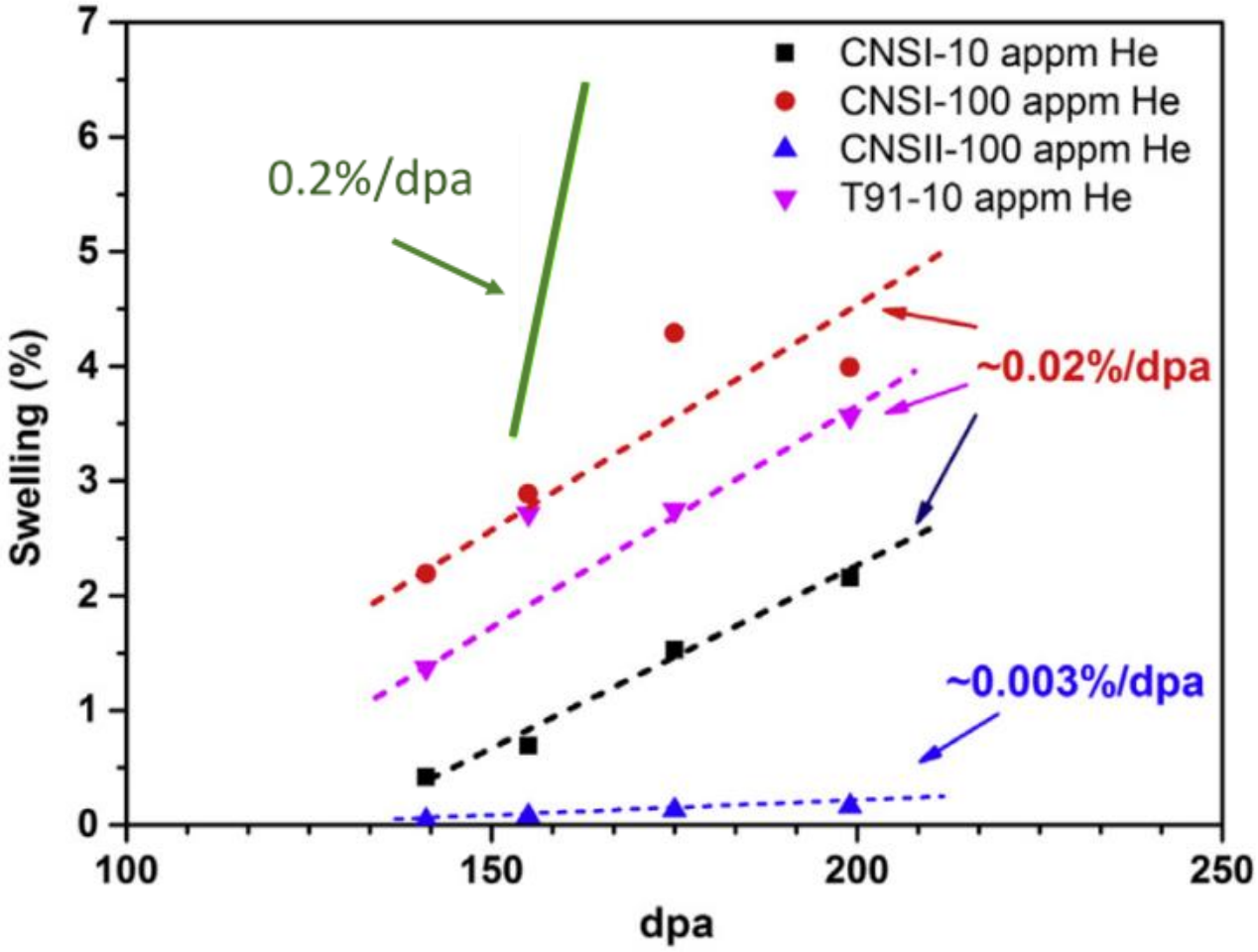

Figure 2.17 The dependence of swelling with damage for CNSI and CNSII for different helium levels at 460°C irradiated with 5 MeV Fe^{2+} ions [9].

A collection of experiments, utilizing both neutron and ions and spanning multiple He/dpa ratios has been performed on Cu and Cu-boron materials [52–56]. While the Cu system is face-centered-cubic, and the microstructure is fundamentally different than the ferritic-martensitic system, the effect of helium on cavity development is likely similar. **Figure 2.18** shows the normalized cavity swelling as a function of He/dpa ratio. The relationship is not monotonic, as a peak in swelling is observed at intermediate He/dpa ratios of about 5-10 appm. This peak occurs near the transition to a combination of both voids and bubbles is observed, before a high density of bubbles results in a reduction of swelling. Because of the variety in damage levels in the data, it is difficult to compare whether the normalized swelling is representative of cavity growth in all areas. It is unknown whether a maximum cavity density was achieved in the lower helium cases. However, combined with known results of helium with high levels in Fe-Cr systems, it is likely that this peak behavior with suppression at high helium and low nucleation at low helium levels causes this swelling behavior.

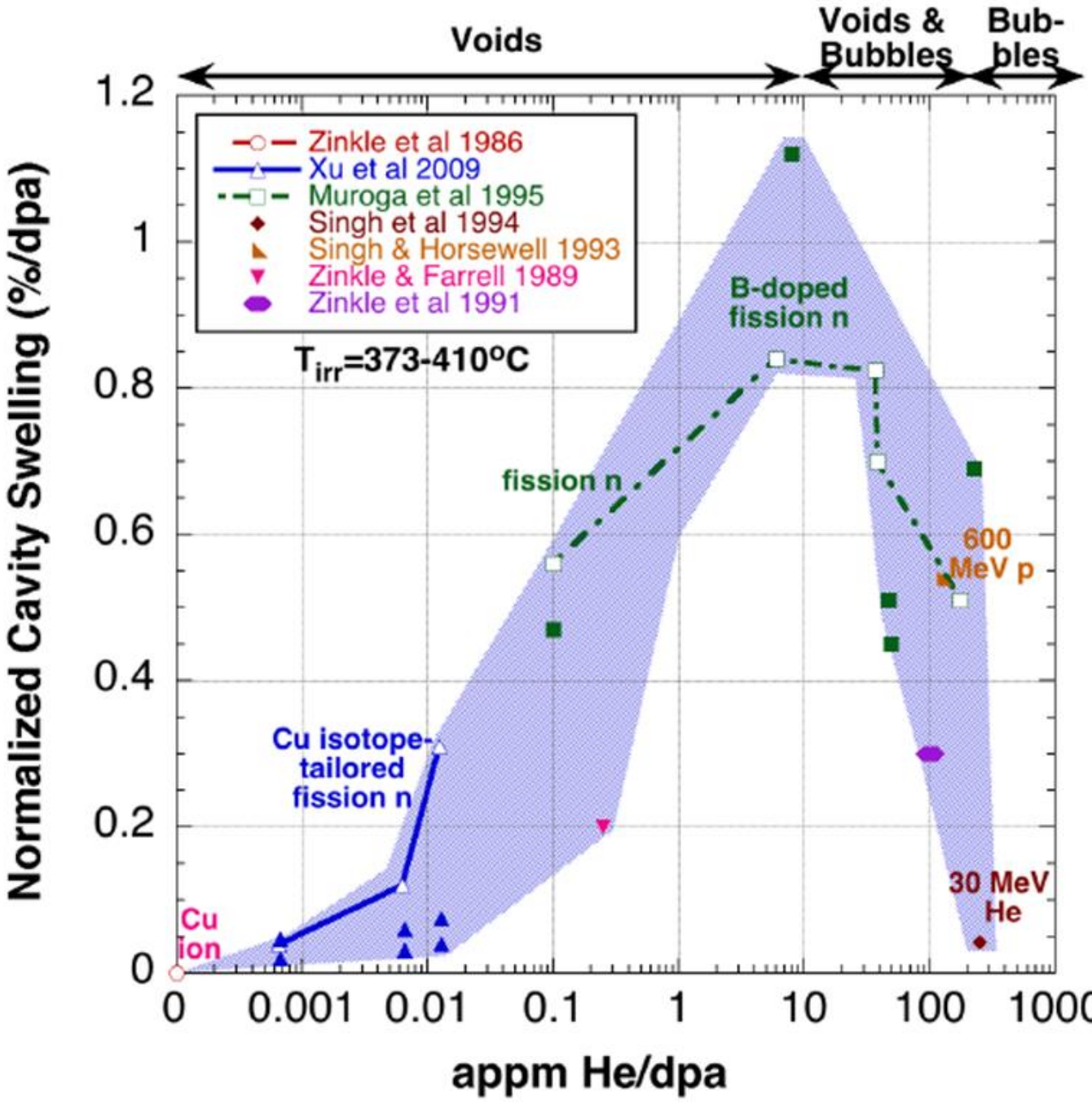

Figure 2.18 Normalized Cavity swelling vs. appm He/dpa taken from a variety of experiments for Cu and Cu-boron doped irradiation experiments [52–56]**.**

Qualitatively, the results from experiments along with theoretical predictions suggest that the pre-implantation of helium tends to encourage void nucleation, and thus shorten the incubation period. Experiments have been performed on ferritic-martensitic steels with pre-implantation levels from 0 appm all the way up to 1400 appm and beyond. Most studies only use helium to encourage void nucleation and provide little to no reason why a particular level is used. This is illustrated by the range of over three orders of magnitude that helium levels have been studied. Little care has been used to justify or explore the effects a particular helium level may have on void nucleation and steady-state growth. Stoller's [46] study in austenitic steels suggests that the helium-vacancy composition of a defect cluster may be critical to the formation and evolution of the void microstructure, however no experimental studies have been performed to explore this. Few studies have systematically explored the effect of increasing helium levels and the subsequent effect on the incubation dose and steady-state growth rate. Some studies [6][8][9][51] suggest that higher helium levels (100 appm and beyond) may actually suppress swelling; however, the point where and why this switch occurs is not well understood. Additionally, there is no consensus whether different helium levels affect the steady-state swelling regime. Some studies [9] [7] suggest that the steady-state swelling rate is unaffected by helium, while other studies [8] provide evidence that there may be a dramatic effect on the swelling rate.

It is likely that the cavity microstructure created during nucleation (as a result of a particular level of pre-implantation) will carry its effects into the growth regime. What these consequences are, at what helium levels they occur, and how they occur remain to be explored. There is a need for a systematic set of experiments at various helium levels in the same material which achieves steady-state swelling for each of the helium conditions. Such a set of experiments will provide invaluable information about the helium effect on cavity evolution in ferritic-martensitic steels—both about the incubation and steady-state region. This could serve as a guide for future experiments on which helium levels are relevant for use and the potential consequences of implanting too much or too little helium.

2.5.6 The Effect of Carbon on Cavity Evolution

The presence of carbon in ferritic-martensitic steel is unavoidable, as it is an essential component during the processing of the steel. Typically levels of 0.1 atom percent carbon or less

are present as interstitial impurities within the Fe-Cr matrix. During processing, most of the carbon precipitates as $M_{23}C_6$ carbides on the grain and lath boundaries. Section 2.1.2 details the typical precipitates formed as a result of various processing and heat treatment conditions.

Carbon, both in precipitates and as an interstitial impurity may have a dramatic influence on the development of cavities under irradiation. A number of studies on the irradiation of austenitic stainless steel have explored the effect of varying amounts of carbon on void swelling. Leitnaker [57] *et. al.* explored the effect of varying amounts of interstitial solutes (C, N, Si) on swelling. High purity steel (0.005% C, 0.0003% N, and 0.01% Si) was irradiated alongside Type 316 stainless steel (0.05% C, 0.05% N, and 0.75% Si). The samples were irradiated in EBR-II to fluences of ~10^{22} n/cm^2 and at temperatures between 450 and 600°C. Type 316 exhibited a much higher swelling resistance in all comparable cases: at 510°C, swelling was 0.05% in 316, while 11.8% in HPS at 500°C. At 580°C, 316 exhibited 0.21% swelling, while HPS suffered 5.03%. The authors attribute the higher swelling resistance in 316 to the higher concentration of interstitial impurities. Several mechanisms for the swelling resistance were proposed, such as the impurities creating a shell around void or dislocation sinks, preventing defects from being absorbed, and promoting recombination. They also suggest that the impurities may be acting as traps for point defects within the matrix and promoting recombination in that way as well.

A study by Makin *et al.* [58] explored the effect of increased carbon on 316 stainless steel. Samples were carburized to varying degrees, up to 1% wt. carbon. A high voltage electron microscope was used to induce the irradiation damage up to ~20 dpa. Since the solubility of carbon in the material was exceeded (~0.1% at 1050°C), the formation of $M_{23}C_6$ precipitates was observed on grain boundaries in the lower carbon samples and in the matrix for the higher carbon samples. **Figure 2.19** shows the estimated swelling rates for the 316 for various levels of carbon. As the carbon concentration is increased from 0.01% to 0.1% a dramatic decrease in the swelling rate is observed. The authors did not suggest any mechanisms for the reduction of swelling rate other than carbon trapping of vacancies. Void denuded zones around $M_{23}C_6$ precipitates were also observed.

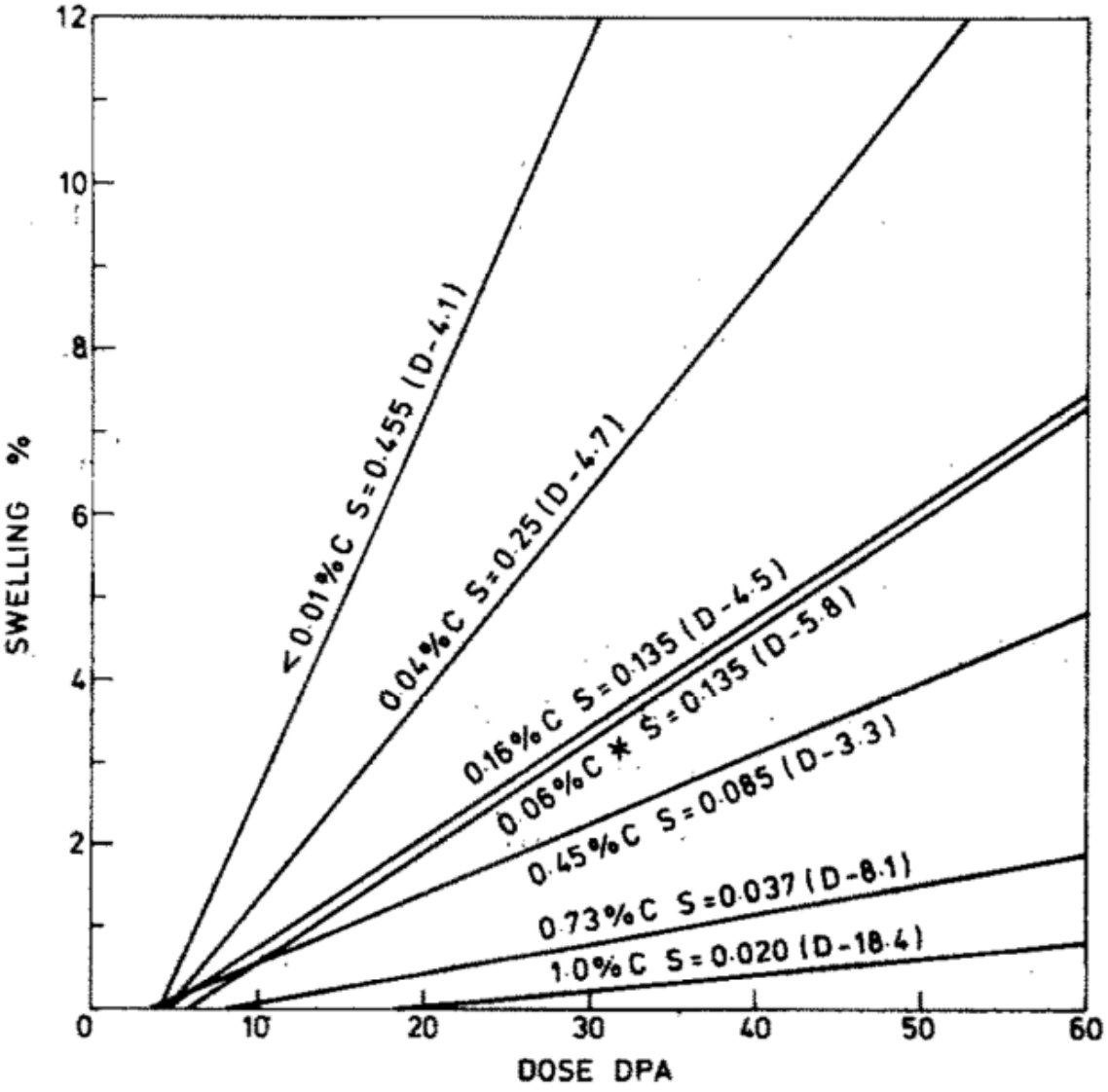

Figure 2.19 Swelling as a function of damage in 316 steel for various carbon levels [58]**.**

It is especially critical to understand the effect of carbon when considering experiments done with ion irradiation. The unintended beam-induced uptake of carbon has been observed in some ion irradiation experiments. Work done by Singer et al. [9,10] found that irradiation of steels with Ti, Cr, and Ta ions caused the uptake of carbon into the surface of the samples with a diffusion-like profile. **Figure 2.20** shows the carbon profiled through the surface of the sample after irradiation in normal vacuum conditions, and in the presence of additional CO. When compared with the normal vacuum profile, it is clear that significant carbon was taken up by the sample. The authors suggested that the uptake of carbon was due to vacuum carburization catalyzed by the ion beam. Residual CO and CO_2 molecules in the vacuum system, with the help of the ion beam, adsorbed onto the surface and then diffused inward. The appearance of an amorphous layer of C was observed in Ti-implanted Fe [59], which likely serves as the source for diffusion into the material, which is consequently enhanced by irradiation.

A proton irradiation study by Thomas and Bauer [60] observed carbide formation on Nb samples. The authors proposed that the most likely possibility for the cause of this was beam-enhanced or beam-induced adsorption and dissociation of residual vacuum components such as CO and CO_2.

This carbon contamination problem was also observed in an ion irradiation study on HT9 [5]. After irradiation up to 600 dpa (at the peak), excessive carbon uptake and precipitation was found. Up to 7% atomic carbon was observed using SIMS, and it was reduced to 2% atomic carbon after a "beam-filtering" technique was used. However, the 2% atomic carbon was still well above the solubility limit of carbon in HT9. **Figure 2.21** shows the SIMS carbon profiles, showing the enhanced carbon content in both the filtered and un-filtered beam conditions.

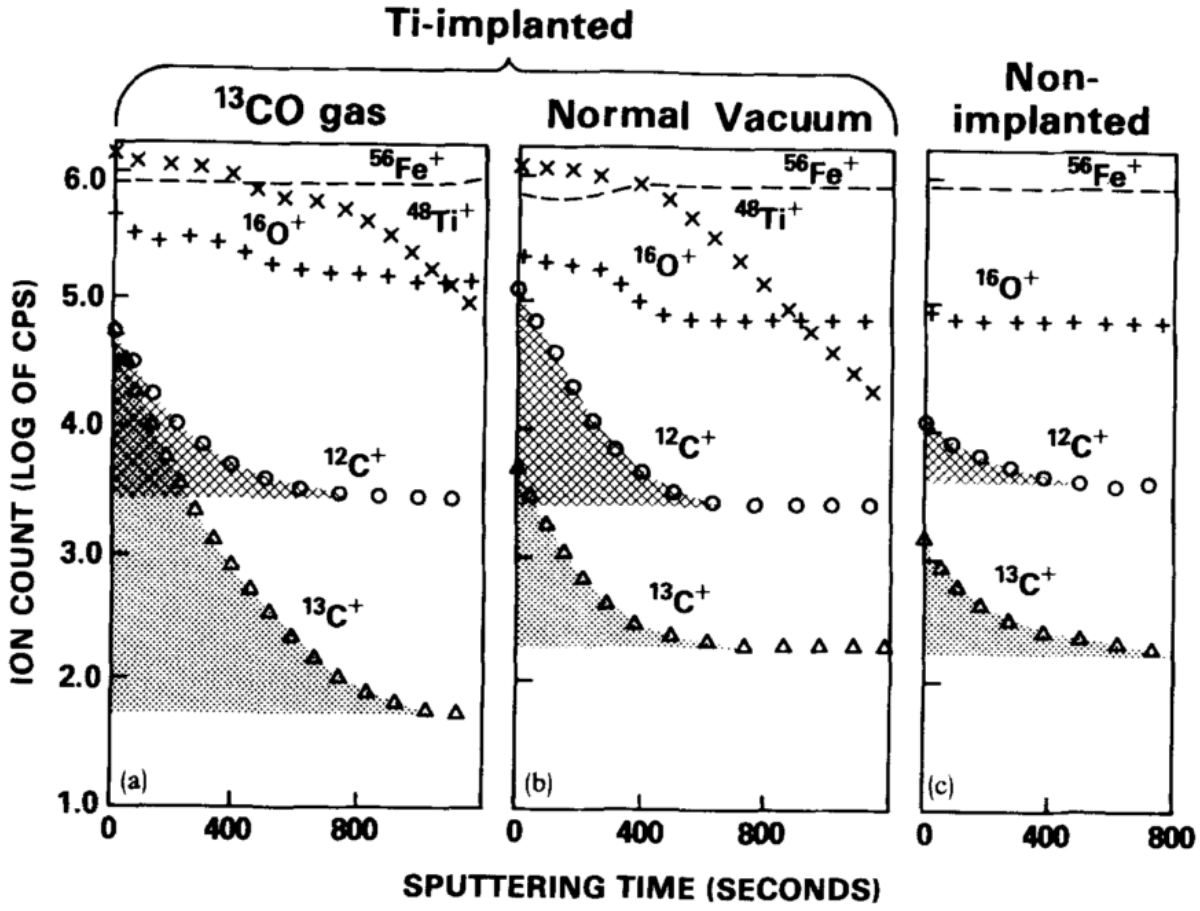

Figure 2.20 Profiles of carbon content as a function of sputtering time (related to depth) for a CO gas, normal vacuum, and unirradiated environment [4].

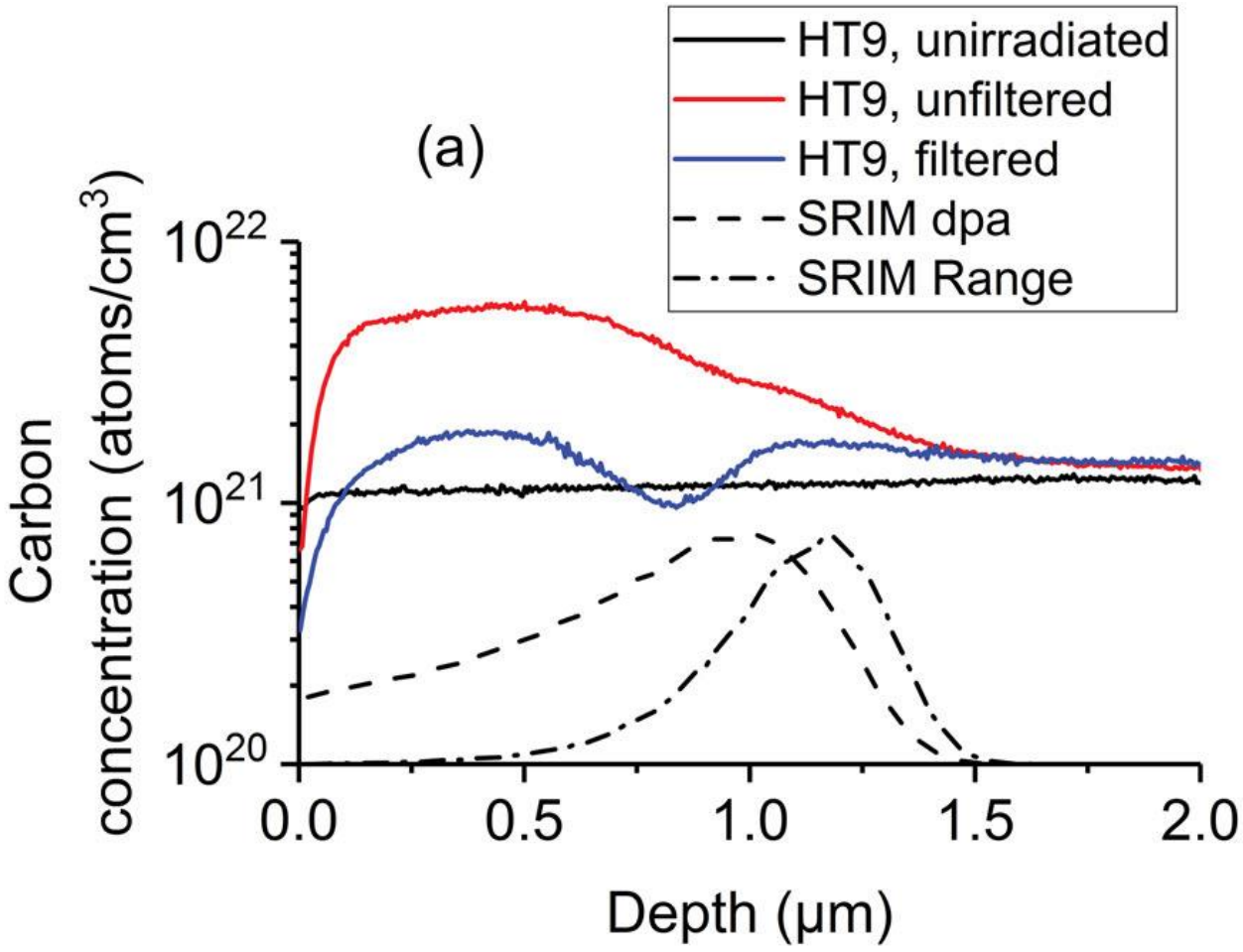

Figure 2.21 SIMS profiles of carbon in HT9 with and without beam filtering [5].

Additionally, the authors identified the formation of several carbides, including $M_{23}C_6$, M_7C_3, and M_3C. The authors concluded that the high sink strength of the carbides likely resulted in the suppression of swelling, when comparing the sample with 7% carbon to the sample with 2% carbon. An estimated for the swelling rates were made with ~0.001%/dpa for the 7% carbon sample and ~0.01%/dpa for the 2% carbon samples.

From these studies exploring the effect of carbon on swelling, it is apparent that carbon tends to suppress swelling behavior. Carbon interstitials in the matrix likely trap vacancies and promote recombination [57,58,61–63]. Additionally, carbon levels beyond the solubility limit result in precipitation of carbides. In addition to providing void-denuded zones at the boundaries, these carbides may serve as additional sinks for point defects, absorbing excess vacancies and reducing their super saturation. Since this carbon contamination has been shown to have a deleterious effect on swelling, its incorporation into the material must be taken into account when analyzing the microstructure of ion irradiations. When considering ion irradiation experiments it is essential to determine the effect of carbon on the microstructure and to assess whether the carbon contamination compromises the integrity of the experiments.

CHAPTER 3: OBJECTIVE

The objective of this thesis is to understand the role of pre-implanted helium, with and without the presence of excess carbon, on the cavity evolution of ion-irradiated T91. A hypothesis for the behavior of cavities both in the presence and absence of excess carbon uptake is presented as follows:

Ion-irradiated T91 will exhibit monotonically decreasing swelling as helium pre-implantation level is increased. This is due to a reduction of growth with higher pre-implantation levels because of a high sink strength of small cavities and helium traps which promote recombination.

In the presence of beam-induced carbon uptake, ion-irradiated T91 will exhibit peaked swelling behavior at an intermediate helium pre-implantation level. The suppression of nucleation by carbon and carbides will inhibit swelling at lower pre-implantation levels, while swelling at higher pre-implantation levels is suppressed by both carbon and a high cavity sink strength.

Figure 3.1 shows a schematic of the hypothesized behavior. The overall swelling in the presence of carbon is also expected to be lower due to an overall lower density and growth rate.

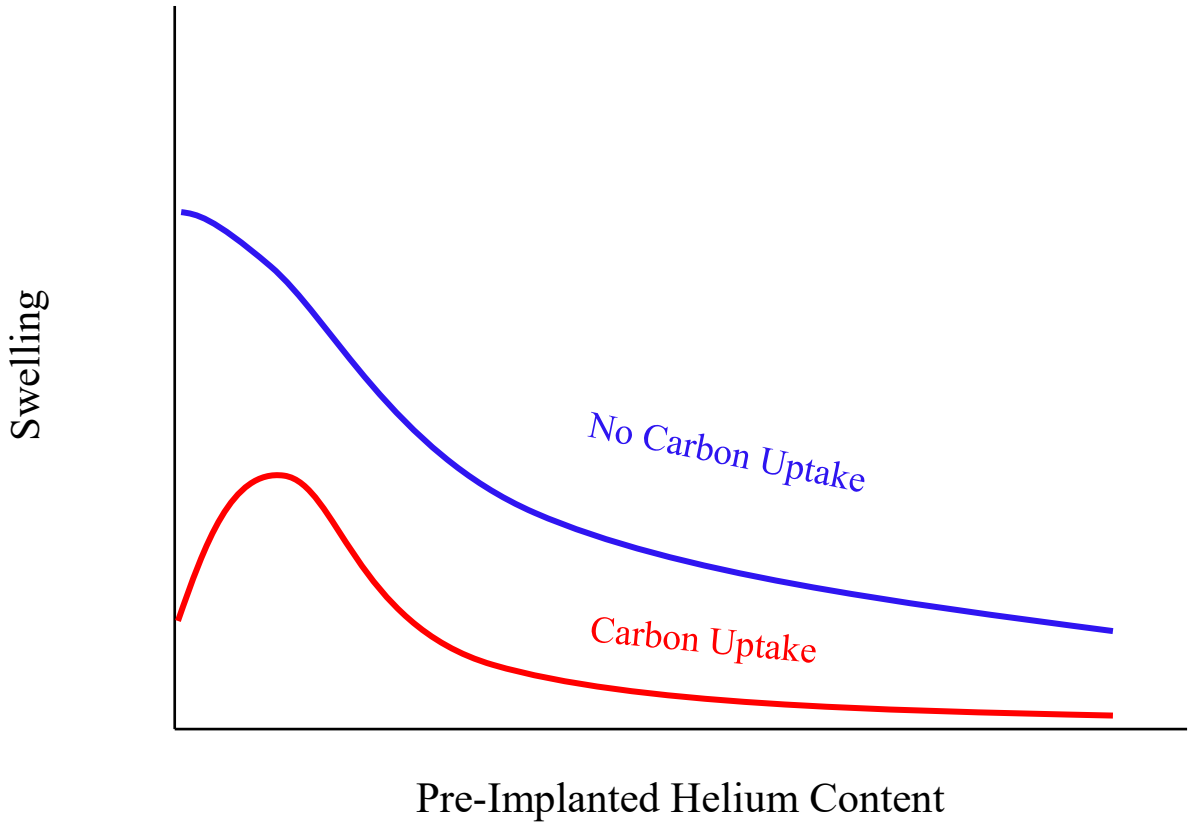

Figure 3.1 A schematic showing the hypothesized swelling behavior as a function of pre-implanted helium with and without carbon uptake.

To test this hypothesis a combination of ion-irradiation experiments with careful characterization of the microstructure was used.

To achieve the main objective, two sub-objectives were first completed. The first sub-objective required determining *what* happened to the swelling behavior as both helium and carbon uptake varied. To answer this, a series of experiments were performed in the laboratory with varying conditions. This required the establishment of a controlled and consistent process of performing the experiments and analyzing and processing the experimental data. The development of the following methods was essential in acquiring the relevant experimental data:

- A method for consistent and controlled helium implantation and ion irradiation
- A method for preventing the uptake of carbon during ion-irradiation
- A post-irradiation characterization technique utilizing STEM (scanning transmission electron microscopy) to image the microstructure
- A method for consistent quantification of the microstructure features (cavities, dislocations, precipitates, carbon)

By utilizing these methods, the magnitude and direction of changes in swelling with changes in helium pre-implantation and carbon uptake were determined. Swelling rates, cavity size distributions, and quantification of precipitates and dislocations all provided a comprehensive picture of the microstructure evolution with increased irradiation damage. As a whole, these results answered the question of *what* happened to the cavity behavior as a function of helium level, carbon uptake, and damage level.

The second sub-objective was to determine *why* a particular change in helium pre-implantation or carbon uptake resulted in the changes observed in cavity evolution. This was accomplished by a detailed analysis of the cavity size distributions, sink strengths, and other microstructural developments. The results gathered from this work were applied to existing cavity evolution theories and compared with the other available experimental results. This analysis ultimately provided insight into the causes of the changes in cavity evolution due to helium pre-implantation level and carbon uptake.

Completion of these two sub-objectives ultimately demonstrated the highly influential roles of pre-implanted helium and carbon uptake on the cavity evolution.

CHAPTER 4: EXPERIMENTAL PROCEDURE

This chapter presents the experimental procedures used to prepare, irradiate, and characterize the T91 samples explored in this thesis.

4.1 Alloy and Sample Preparation

The alloy used for the work in this thesis was T91, heat C2269. The composition in weight percent is shown in **Table 4.1**. The alloy was produced by American Alloy Steel Inc. in accordance with ASTM SA387. The composition was verified with combustion infrared detection and direct current plasma emission spectroscopy. As mentioned previously, T91 is a nominally 9-Cr ferritic-martensitic steel and is being considered as a candidate for fast reactor applications because of its high swelling resistance. This alloy was given a heat treatment consisting of a 46 min anneal at 1066°C, followed by an air cool which provided for the transition to reach a fully martensitic phase. This was followed by tempering at 790°C for 42 min, to allow for carbide growth and to recover some ductility, followed by a final air cool.

The resulting microstructure was a tempered, fully martensitic material. Metallography on the as-received T91 samples revealed a microstructure of prior austenite grain boundaries approximately 10 μm in size and martensite laths of about 0.5 μm in width and 5 μm in length [64]. **Figure 4.1** shows the microstructure of unirradiated, as-received T91 imaged using bright field scanning (BF-STEM) transmission electron microscopy. The presence of the martensite laths, carbides at grain boundaries, and a high dislocation density with the laths is very apparent. An initial dislocation density of 3.0×10^{14} m^{-2} was measured for the as-received condition.

Prior to irradiation, samples of T91 were cut in the form of 1.5 x 1.5 x 20mm bars using electrical discharge machining (EDM). EDM utilizes rapid current discharge through two

electrodes to break down material and effectively cut the metallic sample. The shape of the material can be programmed into the machine and can result in geometric precision of about 1µm.

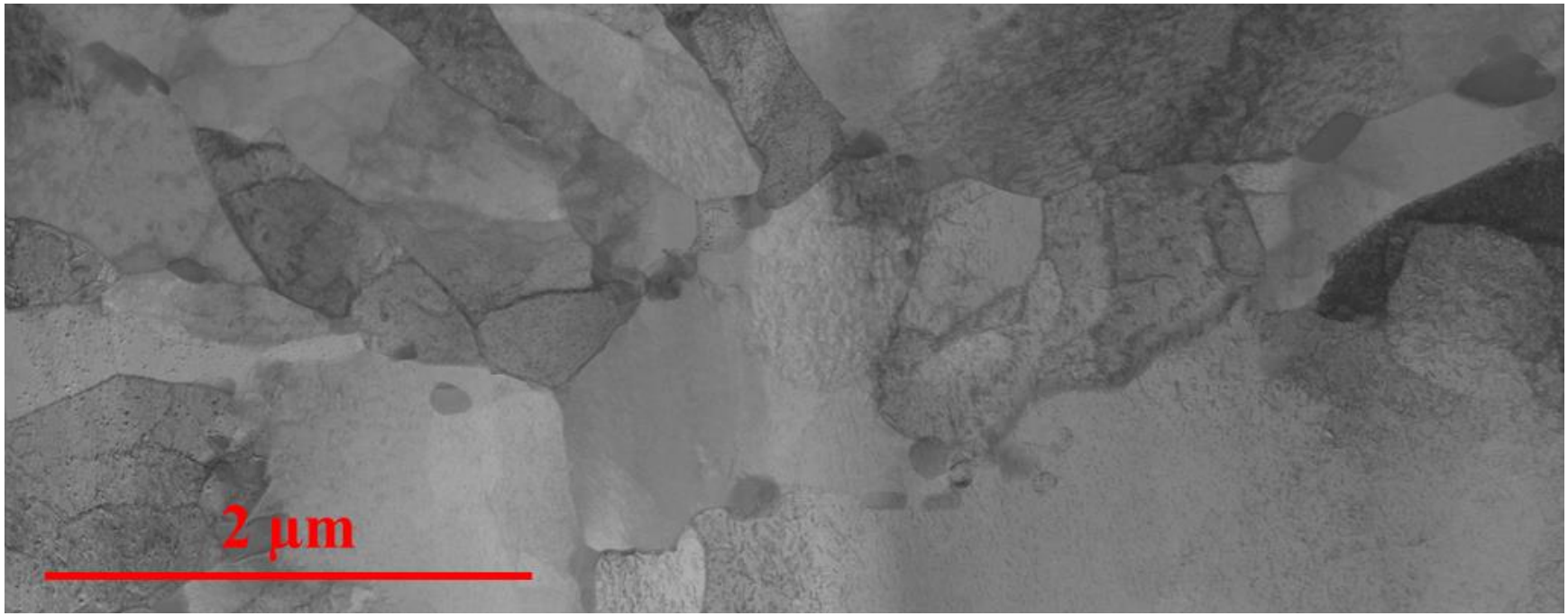

Figure 4.1 The unirradiated, as-received microstructure of T91, heat C2269 imaged under bright field scanning transmission electron microscopy.

Table 4.1 The composition of T91 C2269 in wt%.

Alloy Content (wt%)								
Cr	Mo	Ni	Mn	Si	V	C	Cu	Fe
8.37	0.9	0.21	0.45	0.28	0.22	0.1	0.17	Bal

The bar samples were then mechanically polished using successively lower grits of silicon carbide grinding paper. The samples were mounted on a metallic puck using Crystalbond™ adhesive glue. The metallic puck was heated on a hot plate such that a thin layer of adhesive melted. The T91 bar samples were then arranged on the adhesive in the center of the puck, side-by-side, as they would be on the irradiation stage. Extra "dummy" samples, called guide bars, were added bookend the irradiation samples. The guide bars allowed for more consistent polishing and for over-scanning during irradiation, and a welding point for thermocouples. It was necessary to ensure that the samples were adhered flat to the puck and at the same height. The puck was allowed to cool, usually with the help of deionized water so the adhesive would harden quickly. The samples were then hand-polished using a variable speed grinding wheel with silicon carbide grinding paper. Grits of 240, 320, 400, 600, 800 and 1200 were used to polish the sample. The polishing direction was rotated 90 degrees between each grit step so that it would be easy to identify when the previous damage had been removed. The samples were also rinsed with deionized water between grinding steps to remove rogue particles. After the 1200 grit grinding step, the puck was re-heated to melt the adhesive and the samples were flipped to the opposite side, while maintaining the same relative orientation. The grinding process was repeated for the opposite face. The to-be-irradiated surface was further polished with a cloth pad and diamond slurries of 1μm and 0.25μm to provide a mirror-like finish. The samples were then removed from the puck by heating once again. To remove any residual adhesive, the samples were allowed to rest in a beaker of acetone until the adhesive had completely dissolved. They were then successively cleaned with methanol and ethanol.

To remove any damage layer induced by mechanical polishing, the samples were then electropolished. The electropolishing solution consisted of a 10% perchloric acid, 90% methanol solution which was cooled to between -40 and -50°C using a methanol bath with dry ice or liquid nitrogen. The sample was completely submerged in a 1000 mL beaker containing approximately 500 mL of electropolishing solution. A magnetic stirrer rotating at ~250 rpm was used to create a vortex in the electropolishing solution which impacted the surface of the sample head on. The to-be-irradiated surface of the sample was oriented to face the cathode, a 25 x 25mm square platinum wire mesh, which was also submerged in the solution. The sample itself served as the anode. A

diagram of electropolishing set-up is shown in **Figure 4.2**. The samples were electropolished at an applied voltage of -40V for approximately 20 seconds. During the electropolishing, the sample was agitated within the vortex to refresh the flow of solution at the surface. This procedure was estimated to remove about 2μm of material. To determine the appropriate length of time to electropolishing, a polishing curve for T91, as shown in **Figure 4.3**, was obtained beforehand. Samples of T91 were half-coated with protective lacquer and electropolished at various times. A confocal microscope was used to verify the amount of material removed by comparing the heights of the electropolished surface and that of the protected surface. As the final mechanical polish utilized 0.25μm particles, removal of 2μm was deemed more than sufficient for removal of a remaining damage layer.

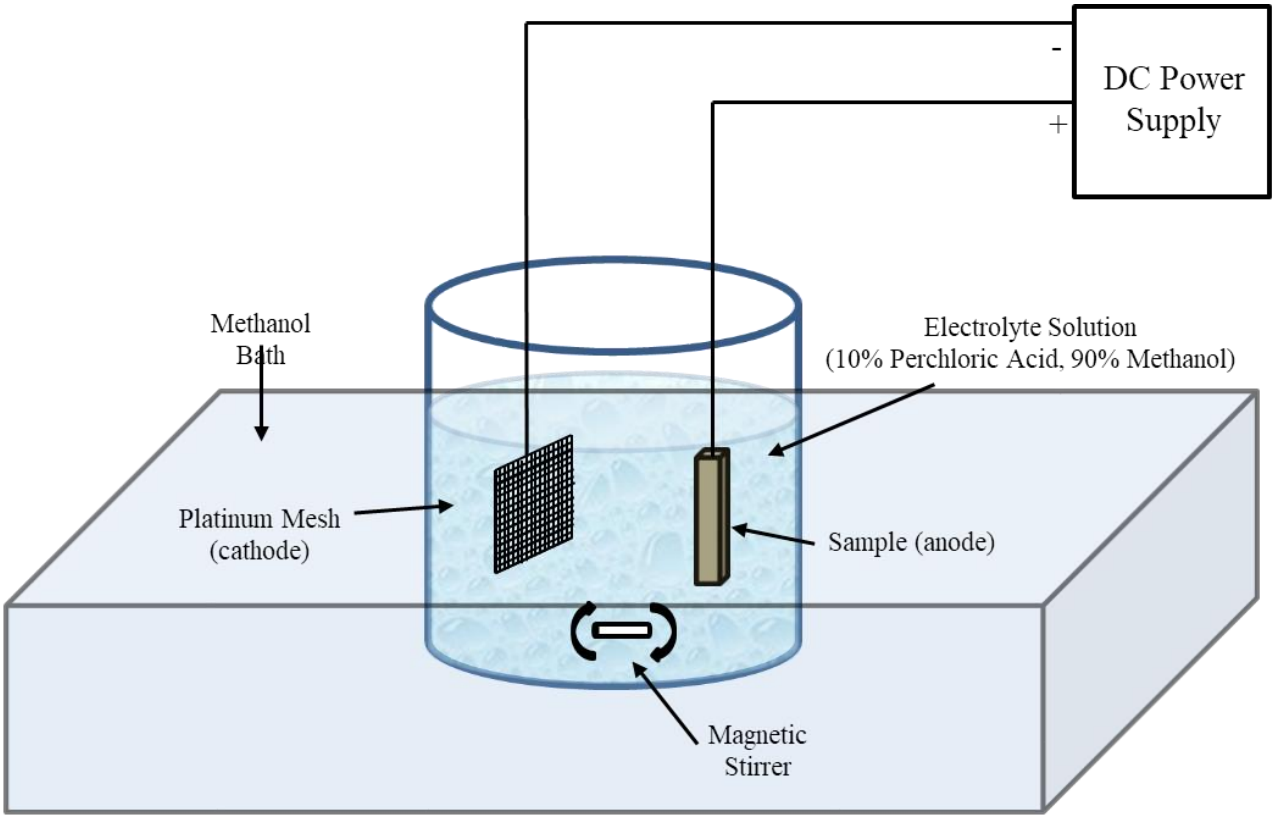

Figure 4.2 A schematic of the electropolishing set-up.

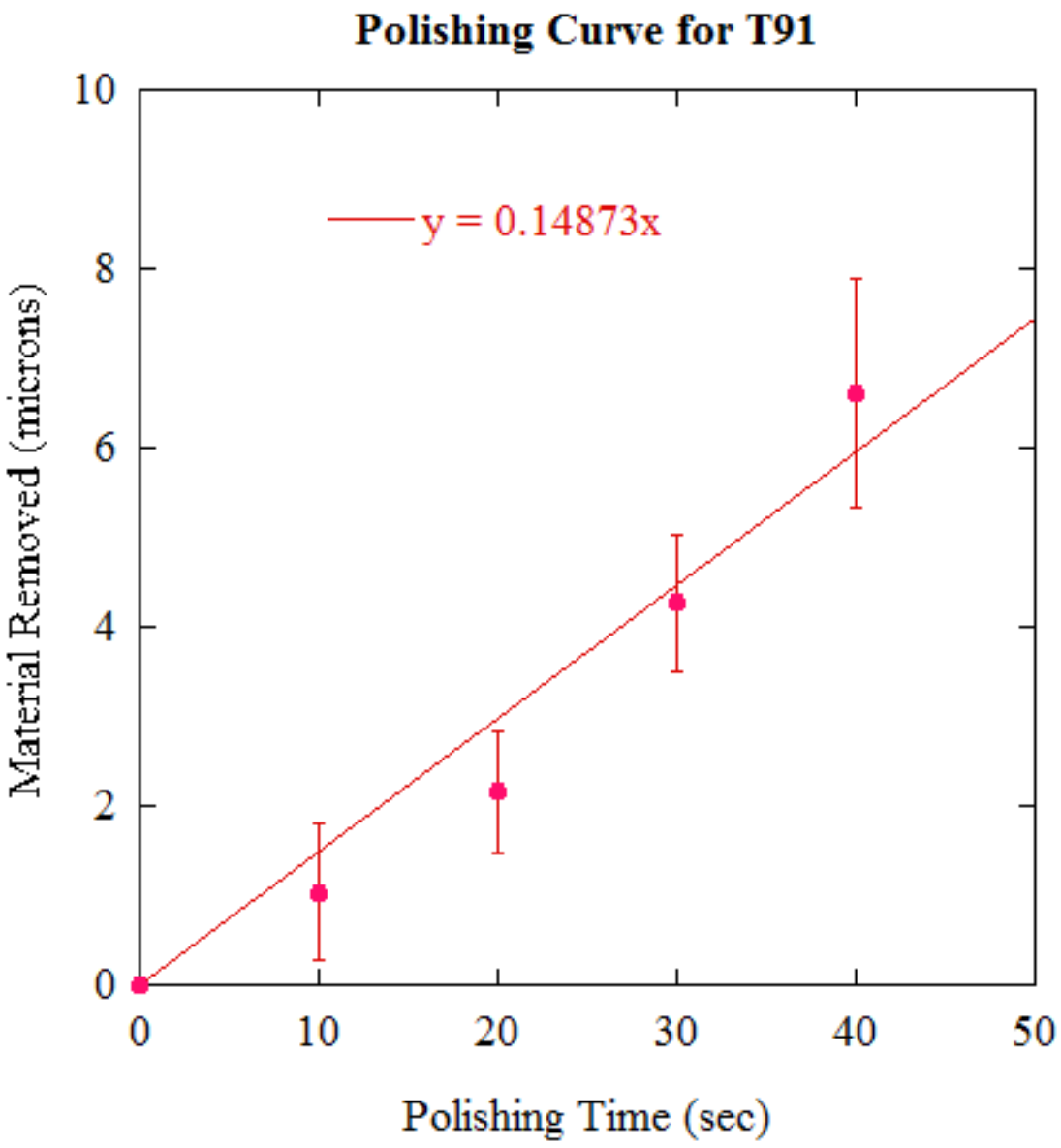

Figure 4.3 The amount of material removed from the surface as a function of electropolishing time.

For some samples, a coating of alumina was applied to the surface of the samples to prevent carbon uptake during ion irradiation. An ALD (atomic layer deposition) machine was used to apply the coating at a thickness of 100nm. ALD is a thin film deposition technique which utilizes gaseous precursors to deposit the film (in this case Al_2O_3). The specific details for the reaction are dependent on the particular ALD process (i.e. whether deposition of oxide, metal, nitrides, etc. is desired).

For the ALD of alumina, the substrates (T91 samples) were heated to 150°C in an inert argon environment. Trimethylaluminum (TMA, $Al(CH_3)_3$) was bubbled into the chamber and reacted with hydroxyl (OH) groups on the surface of the substrate. The TMA was then pumped out of the chamber and water was bubbled into the chamber to react with the methyl (CH_3) groups to produce alumina and methane. The reaction which took place was the following (molecules denoted with an asterisk are attached to the substrate surface):

$$2\ Al(CH_3)_3^* + 3\ H_2O \rightarrow Al_2O_3^* + 6\ CH_4$$

The water was then pumped out of the chamber. This process was repeated for a number of cycles (980-1000) to achieve a 100nm thick film. It was important that the TMA was completely pumped out before the water bubbled in, since TMA and water readily react and could result in poor alumina deposition.

4.2 Helium Pre-Implantation

Prior to irradiation with Fe^{2+} ions, some of the samples were implanted with helium at room temperature to concentrations of 0, 1, 10, 100, and 1000 appm. To reduce the irradiation area, one T91 bar sample was often used for two helium conditions. Half of the bar, lengthwise, was implanted with one helium level and the other half implanted with a second helium level. For example, one bar sample contained the 1 appm and 100 appm helium conditions, while a second bar sample contained the 10 appm and 1000 appm conditions (see **Figure 4.4**).

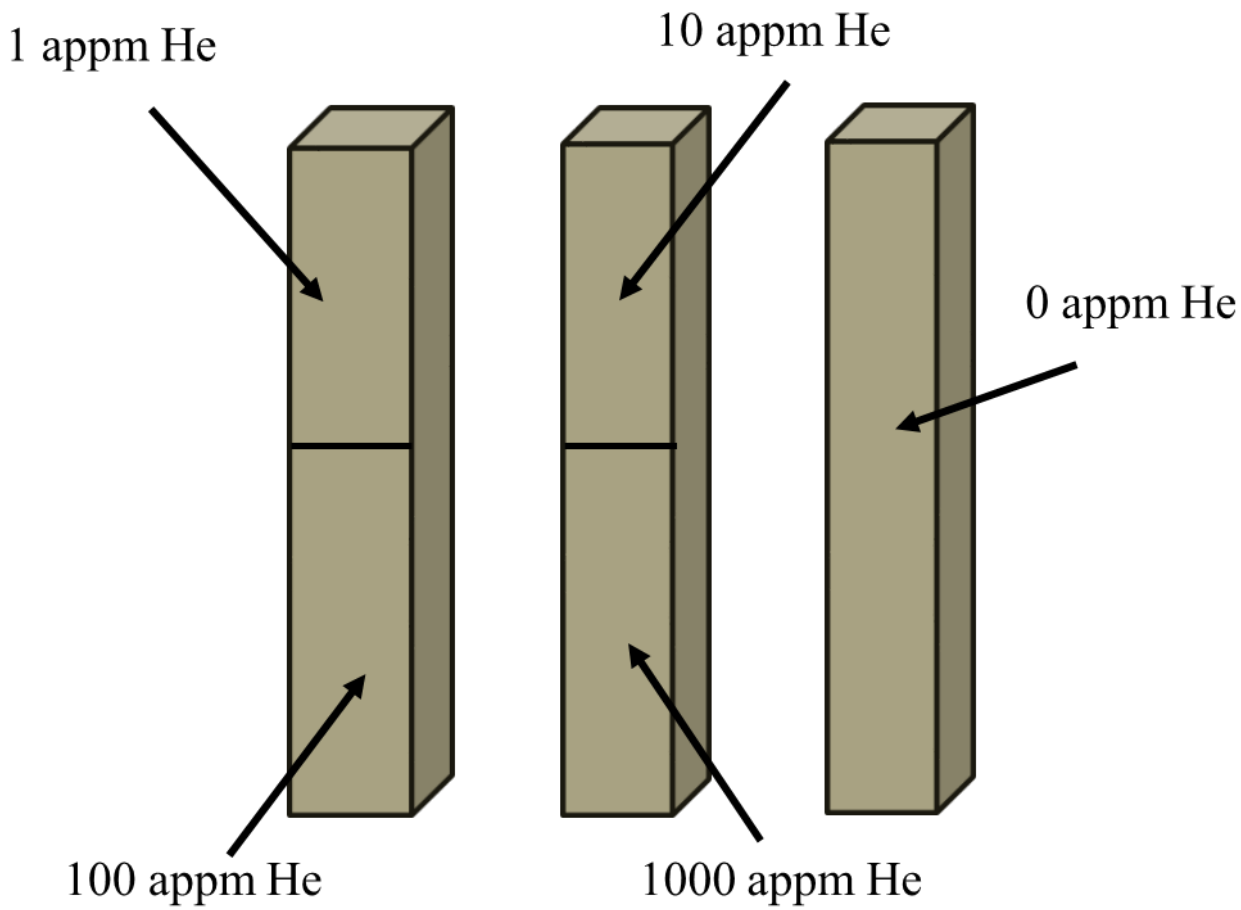

Figure 4.4 A diagram of the helium conditions implanted on each T91 sample.

A National Electrostatics Company (NEC) 400kV implanter was used to implant the helium. The samples were mounted on a rotatable wheel using copper tape. The tape was only used on the back end of the samples and cut such that it would not be irradiated or exposed to the beam. Care was taken to prevent any tape to contact the to-be-irradiated surface of the samples. A steel knife-edge was used to cover half of the sample so that each half could be implanted separately to the appropriate helium level. The rotatable wheel was placed in the implantation chamber, which allowed two helium conditions to be implanted without venting the chamber. The chamber was pumped down to a pressure of ~1 x 10^{-6} torr.

The helium implantations were performed with a rastered beam of He^{+}, with the samples at room temperature with no heating or cooling elements. Energies of 80, 140, 220, 310 and 420 kV were used to obtain an approximately flat damage profile (±10%) from the depth range of 300-1000nm from the samples surface. The presence of an alumina layer did not significantly alter this profile. The implantation profile was estimated using SRIM (Stopping Range of Ions in Matter). The resulting SRIM profile after He implantation at various energies is shown in **Figure 4.5**.

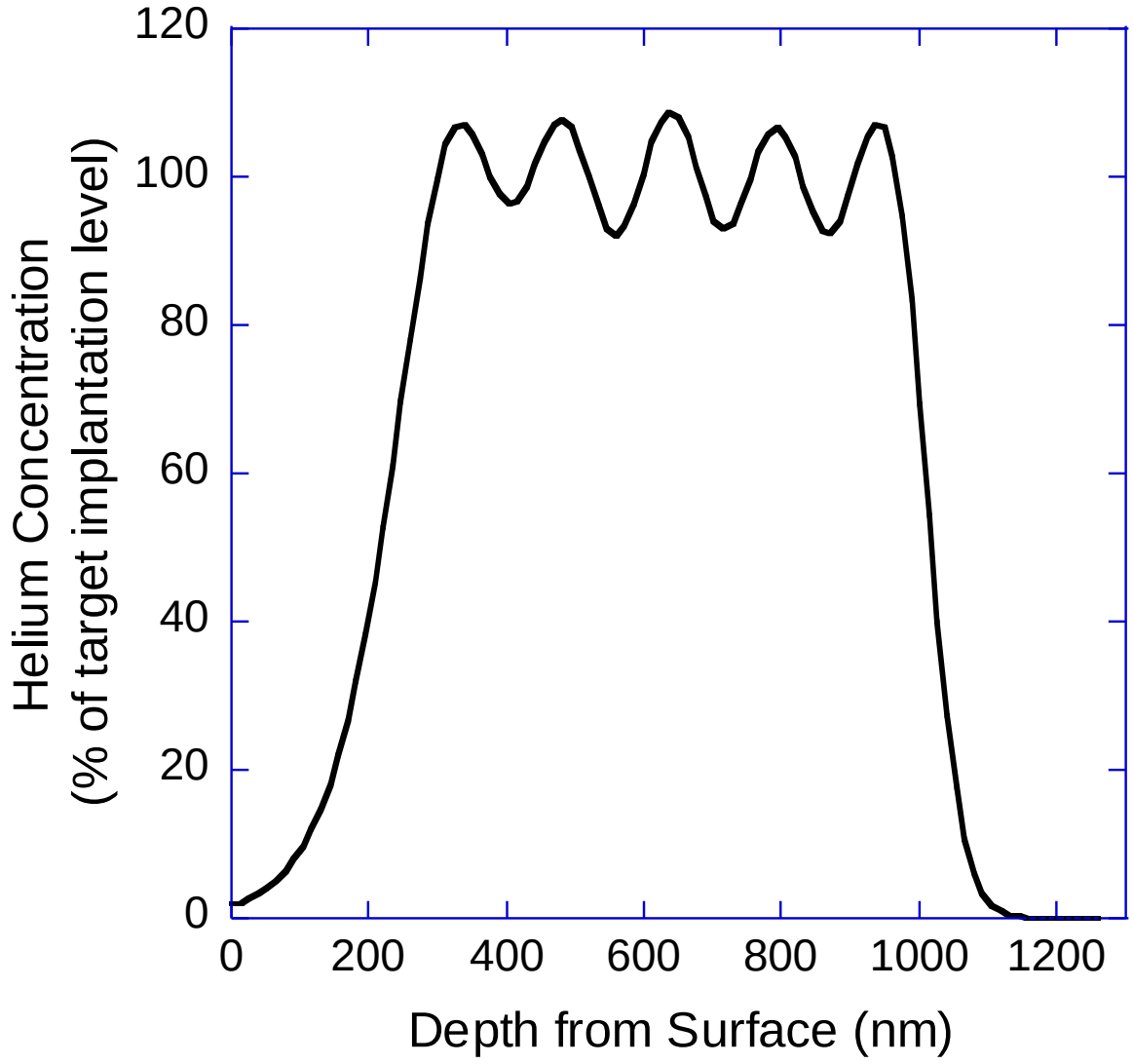

Figure 4.5 The helium profile as a function of depth in T91 as estimated by SRIM calculation as a result of implantation at various energies.

The 1 appm pre-implantation was performed at a damage rate of approximately 8 x 10^{-7} dpa/s, as estimated by SRIM. For the higher helium levels, the current (and consequently the damage rate) was increased by approximately an order of magnitude for each level to keep the pre-implantation time roughly constant. At the highest helium level (1000 appm), the damage caused by pre-implantation was estimated to be 0.02 dpa. At this low damage level and at room temperature, no significant changes to the pre-existing microstructure were expected, aside from the presence of helium. The 1000 appm He condition was implanted using a current density of about 0.5 μA/cm^2, which does not result in measurable beam heating over the course of a 10 minute implant. This determination was made using a reference experiment that was conducted at a power density 5 times that of the 1000 appm He implant experiment. In the reference experiment, the temperature was observed to rise a maximum of 55°C only after 3 h of irradiation [65]. **Figure 4.6** shows the microstructure of T91 pre-implanted with 1000 appm prior to ion irradiation. No helium bubbles were observed, even at very high magnifications using either conventional or scanning transmission electron microscopy. However, some damage from the focused-ion beam liftout technique is observed, especially near the sample surface.

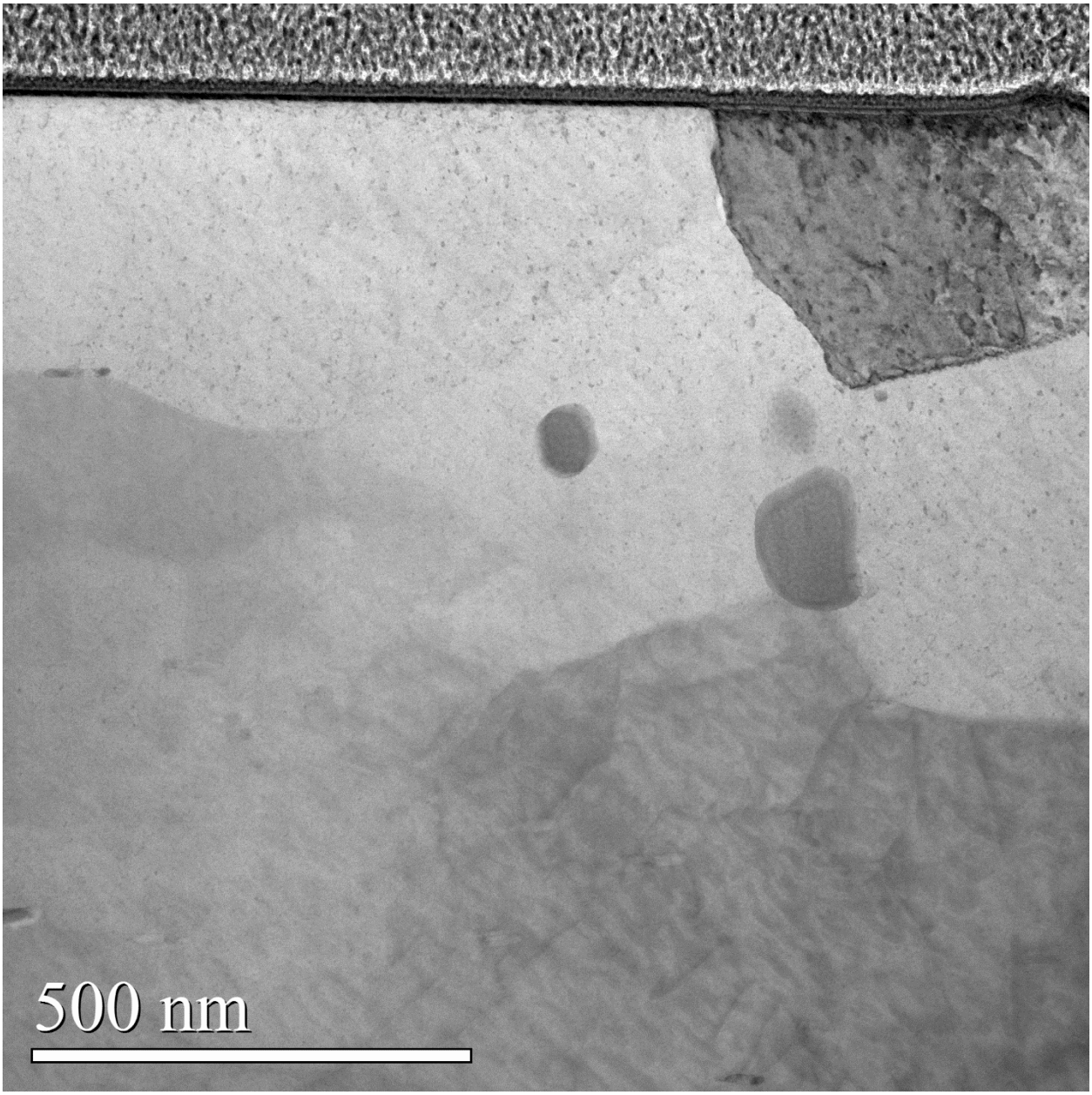

Figure 4.6 Bright Field STEM cross-sectional image of T91 microstructure implanted with 1000 appm helium at room temperature.

4.3. Fe^{2+} Irradiations

4.3.1 Experiments and Characterization Performed

For clarity, the first irradiation campaign, with uncoated samples, will be referred to as the Excess Carbon Campaign and the second irradiation campaign, with alumina-coated samples will be referred to as the Nominal Carbon Campaign.

A total of six irradiation experiments were performed for this thesis. Each irradiation was performed at 460°C and contained five helium implantation conditions (0, 1, 10, 100 and 1000 appm). Three separate sets of samples were used to obtain a damage dependence, with multiple irradiations being performed a single set.

The first irradiation campaign consisted of one set of samples which was irradiated without an alumina coating. Since no anti-contamination measures were used, these samples were susceptible to carbon uptake. The first irradiation utilizing these samples was performed up to a nominal damage level (at 600 nm depth) of 150 dpa. After the irradiation was performed, at least two TEM specimens were extracted for characterization and the samples were further irradiated. In the next experiment, an additional 150 dpa, to a total of 300 nominal dpa. The samples were characterized and the process was repeated at 150 dpa for a final damage level of 450 dpa. **Table 4.2** summarizes the experimental details of the irradiations performed in the first campaign and which microstructural features were characterized for each condition.

The second irradiation campaign consisted of two sets of samples, which were coated with a layer of 100 nm of alumina to prevent carbon uptake during irradiation. The first irradiation was performed to a nominal damage level of 300 dpa. The second irradiation was performed on a new set of samples to 50 dpa. The third irradiation in this campaign added 100 dpa to the 50 dpa samples to achieve 150 dpa. As before, at least two TEM specimens were extracted from each sample after each damage step. **Table 4.3** summarizes the experimental details and which microstructural features were characterized in the second irradiation campaign.

Table 4.2. The experimental details and microstructural characterization for the first irradiation campaign with uncoated samples.

Date of Completion	Beam Energy (MeV)	Damage added/total (Kinchin-Pease dpa)	He (appm)	Cavity Characterization	Dislocations	Carbide Precipitates
3/18/2016	5	150/150	0	✓	N.M.	N.M.
			1	✓	N.M.	N.M.
			10	✓	✓	✓
			100	✓	N.M.	N.M.
			1000	✓	N.M.	N.M.
4/28/2016	5	150/300	0	✓	N.M.	✓
			1	✓	N.M.	✓
			10	✓	✓	✓
			100	✓	N.M.	✓
			1000	✓	N.M.	✓
6/16/2016	5	150/450	0	✓	N.M.	✓
			1	✓	N.M.	✓
			10	✓	N.M.	✓
			100	✓	N.M.	✓
			1000	✓	N.M.	✓

Table 4.3 The experimental details and microstructural characterization for the second irradiation campaign with coated samples.

Date of Completion	Beam Energy (MeV)	Damage added/total (Kinchin-Pease dpa)	He (appm)	Cavity Characterization	Dislocations	G-phase Precipitates
9/29/2016	5	300/300	0	✓	N.M.	N.M.
			1	✓	N.M.	N.M.
			10	✓	✓	✓
			100	✓	N.M.	N.M.
			1000	✓	N.M.	N.M.
11/2/2016	4.4	50/50	0	✓	N.M.	N.M.
			1	✓	N.M.	N.M.
			10	✓	✓	✓
			100	✓	N.M.	N.M.
			1000	✓	N.M.	N.M.
12/2/2016	4.4	100/150	0	✓	✓	✓
			1	✓	✓	✓
			10	✓	✓	✓
			100	✓	✓	✓
			1000	✓	✓	✓

The samples were irradiated using a 3 MV NEC Pelletron accelerator at the Michigan Ion Beam Laboratory. The accelerator, along with a series of diagnostic instruments allowed for the performance of well-controlled experiments. Irradiations in this thesis were performed using either 5.0 MeV or 4.4 MeV Fe^{2+} ions. 5.0 MeV ions from the NEC Pelletron provided an adequate penetration depth to analyze the irradiated microstructure using a focused ion beam lift out technique (detailed later in **Section 4.4.1**). 4.4 MeV ions were used in some cases, as it was a practical limit when using the 1.7 MV accelerator instead of the 3.0 MV Pelletron accelerator.

4.3.2 SRIM Damage Calculations

During the experiment, the beam current hitting the samples was measured using periodic Faraday cup insertions. To calculate the damage induced during the ion experiments, a conversion needed to be made from the measured current in a Faraday cup to dpa (displacements per atom). Damage in ion irradiation experiments is typically measured in dpa. For ion irradiation experiments, dpa depends on many factors, including irradiating ion, ion energy, target composition, and depth of examination.

SRIM was used to provide a depth-dependent estimation of the damage caused by an ion, given its energy and the target material composition. The SRIM damage calculations were performed using the "quick" Kinchin-Pease mode [66,67]. The composition of the target material was detailed in **Table 4.1**. The simulation was run for 100,000 ions to obtain smooth damage and implantation curves and adequate counting statistics. **Figure 4.7** shows a schematic taken from SRIM of how the damage rate and injected interstitials change with depth for 5 MeV Fe^{2+} ions in T91 with a 100 nm thick alumina coating. As is clear in image, the damage varies with depth. The damage level at 600 nm depth was used as the nominal damage level for any given experiment. That is, if an experiment was said to be performed to 300 dpa, then it was irradiated until the damage at 600 nm reached 300 dpa. 600 nm was chosen because it lies in a relatively linear portion of the damage curve and avoids the peak and near-surface regions. The damage rates provided by SRIM for the relevant experiments performed (5.0 or 4.4 MeV, with or without alumina coatings) are tabulated in **Table 4.4**. A significant difference was not observed in the shape of the profile when the coating was or was not present, so both coated and uncoated samples could be included on the same stage while still achieving the same damage level. The addition of 100 nm of alumina

to the surface does not significantly change the shape of the SRIM profile other than off-setting the profile within the metal by 100 nm relative to the uncoated case.

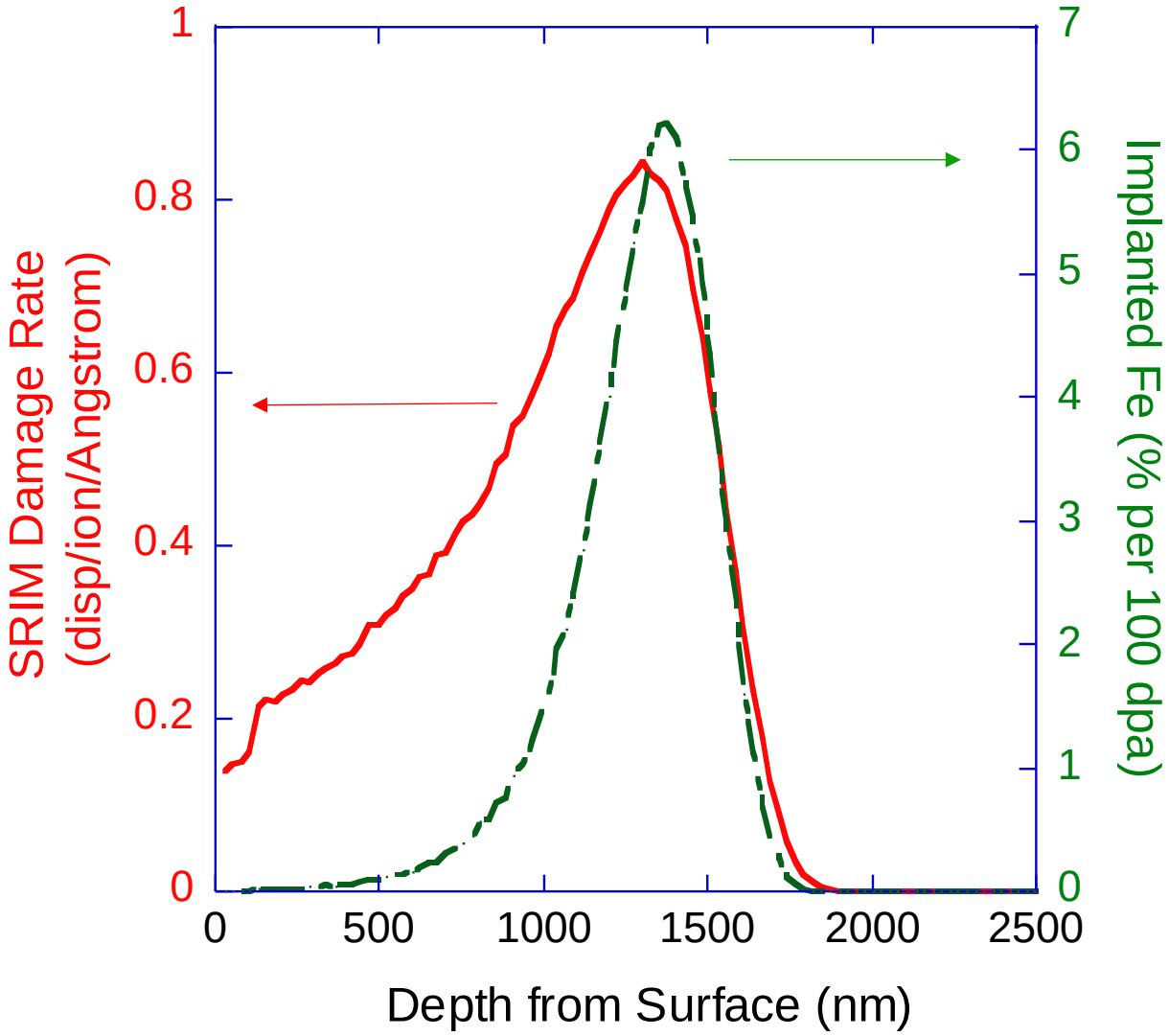

Figure 4.7 The damage rate and implanted ion concentration as a function of depth for 5 MeV Fe^{2+} in alumina coated T91 as calculated by SRIM.

Table 4.4 The calculated SRIM damage rates at a depth of 600 nm for relevant experimental conditions.

Condition	SRIM Damage Rate (disp/ion/Å)
5.0 MeV no alumina coating	0.344
5.0 MeV alumina coating	0.344
4.4 MeV alumina coating	0.372

The SRIM damage rate was used to estimate the total irradiation time required to reach any given damage level. By making periodic measurements of the beam current, and integrating it over the time of irradiation, an estimation of the total ion fluence was made. The equation below estimated the total irradiation time for a given condition (the units for each input and appropriate conversions are also given):

$$\frac{(Desired\ DPA)(Number\ Density)(Ion\ Charge)(Specimen\ Area\ Irradiated)}{(Time\ Averaged\ Current\ on\ Specimens)(SRIM\ Damage\ Rate)} = Irr.Time$$

$$\frac{\left(\frac{disp}{atom}\right)(atom/cm^3)(C/ion)(10^6 \mu C/C)(cm^2)}{(\mu A)(\frac{disp}{ion \cdot Å})(\frac{10^8 Å}{cm})}$$

4.3.3 Beam Raster-Scanning

In the above calculation, the *time-averaged current on specimens* was simply the current measurement made directly by the Faraday cup in front of the stage. However, not all of the current measured in the Faraday cup contributed to damage in the region of interest. This was due to the fact that the beam was over-scanned across the desired area in order to achieve uniform irradiation. Two techniques commonly used to to uniformly irradiate samples are raster-scanning and defocusing of a focused-beam. Several studies [68,69] have shown that raster-scanning of the beam tends to suppress microstructural evolution relative to a defocused beam. That is, densities and sizes of microstructural features such as voids and dislocations are relatively lower in the raster-scanned condition relative to the defocused condition. The Fully Dynamic Rate Theory model suggests that in-cascade annealing of defects between pulses results in suppressed microstructural features. However, the overall suppression of microstructural features due to raster-scanning is a minor effect, especially at high scanning speeds. With regards to cavities, the diameter was within experimental error, and the densities and swelling were different by less than a factor of 2.

Raster-scanning of the beam was used in all experiments in this thesis. The beam carries a roughly Gaussian profile, and the raster-scanning of the beam eliminates the effect of the Gaussian profile, but requires over-scanning of the target area. Before beginning an irradiation, the beam size was measured in a beam profile monitor (BPM) and it was ensured the FWHM (full-width at half maximum) was no larger than 2.5mm. The beam was raster-scanned at a frequency of 255Hz

in the x-direction and 2061Hz in the y-direction, which yielded cycle times of 3.92 and 0.48ms, respectively. **Figure 4.8** shows the diagram of the raster-scanned path over the irradiated area and the aperture system.

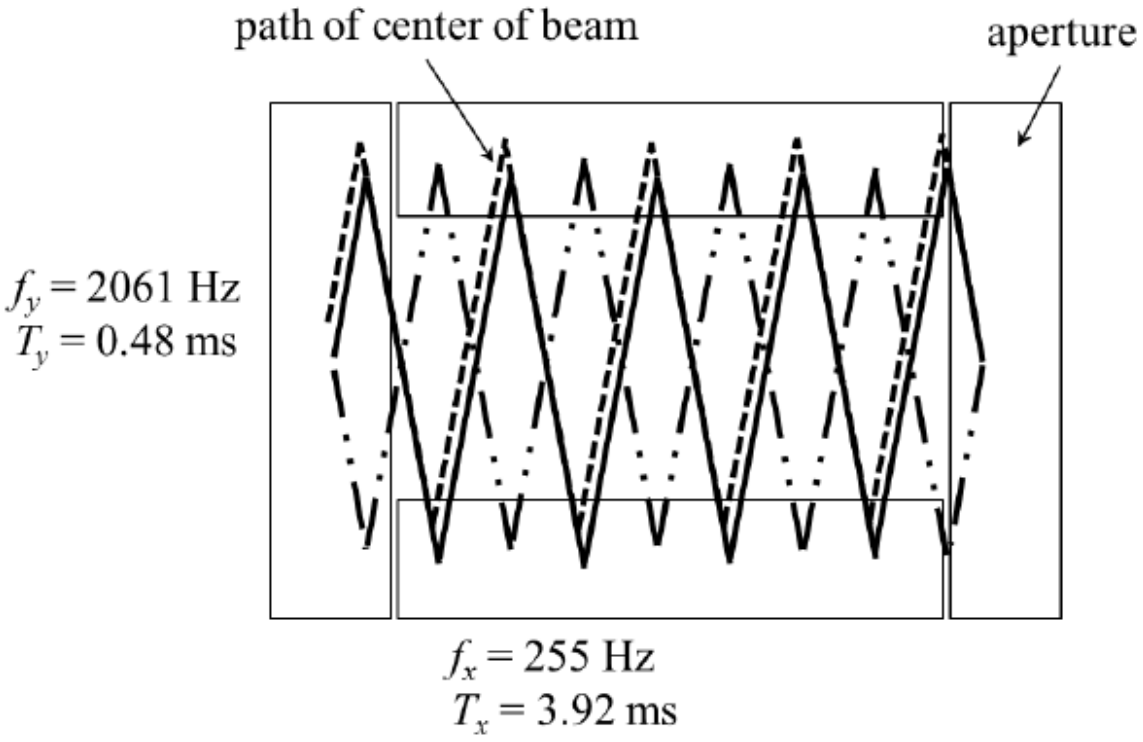

Figure 4.8 The path of the raster-scanned beam over the irradiated area and aperture.

To define the irradiated area, a slit aperture system was used. The aperture system consisted of four independently controlled and electrically isolated slits that could be moved into and out of the beam path via digital control. The slit apertures also measured the unsuppressed current incident on each individual slit. With this system, the area of irradiation was directly determined. For example, if a 5mm x 6mm irradiation area was desired, both X slits were set to a distance of 2.5mm and the Y slits were set to a distance of 3mm, resulting in a total area between the slits of 5mm x 6mm. To achieve a uniform damage profile, the beam needed to raster-scanned such that it completely passed through each point of the irradiated area. Therefore, the beam was raster-scanned an entire beam-width off of the irradiation area (and on to the apertures) in both the x and y directions. With a beam width of 2.5mm, the total raster-scanned area would then be 10mm x 11mm. **Figure 4.9** and **Figure 4.10** show the typical geometry and intensity profile achieved by raster-scanning the beam to fully irradiate a 5mm x 6mm area.

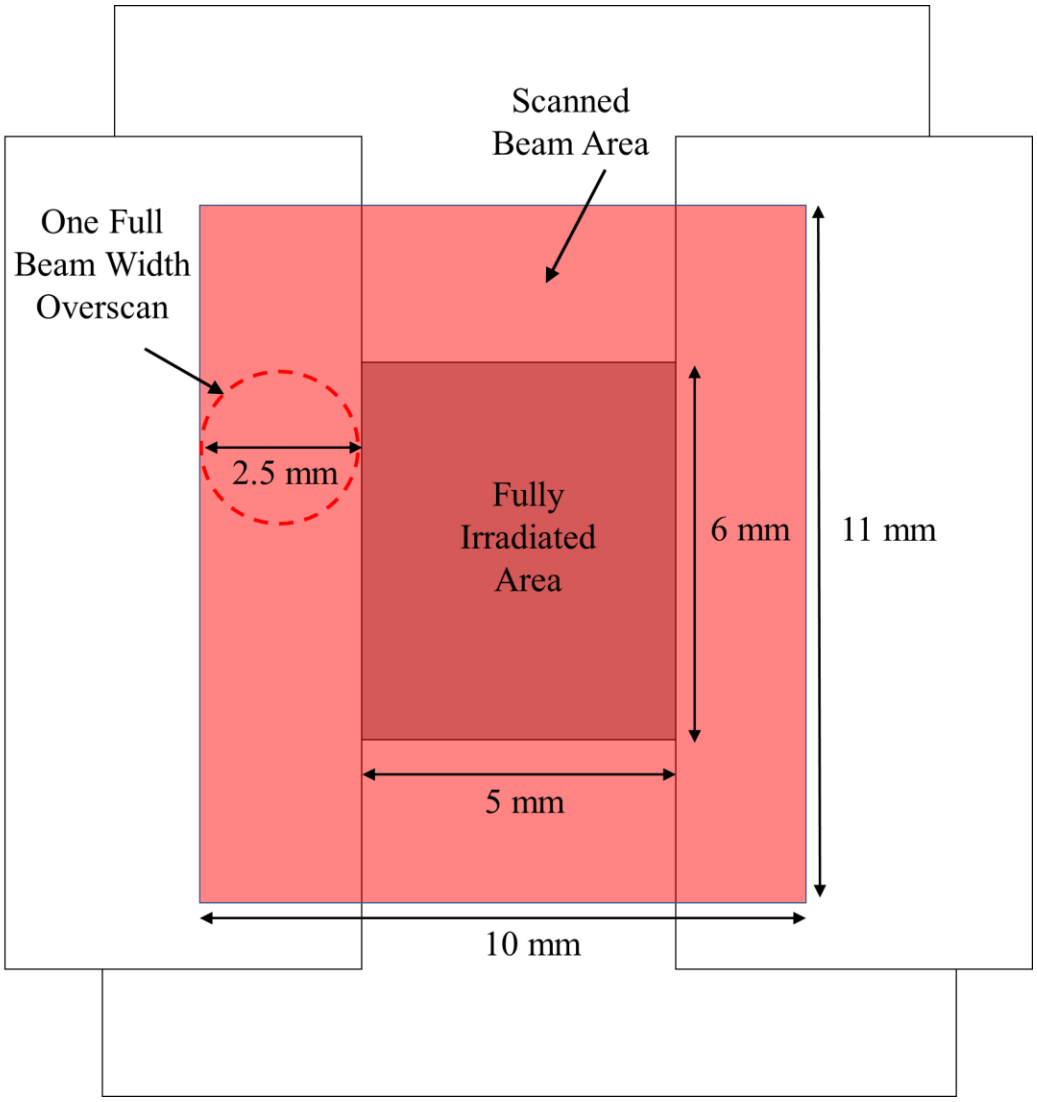

Figure 4.9 A schematic of the raster-scanned area with overscanning the beam by a full beam width to fully irradiate a 5 x 6mm area.

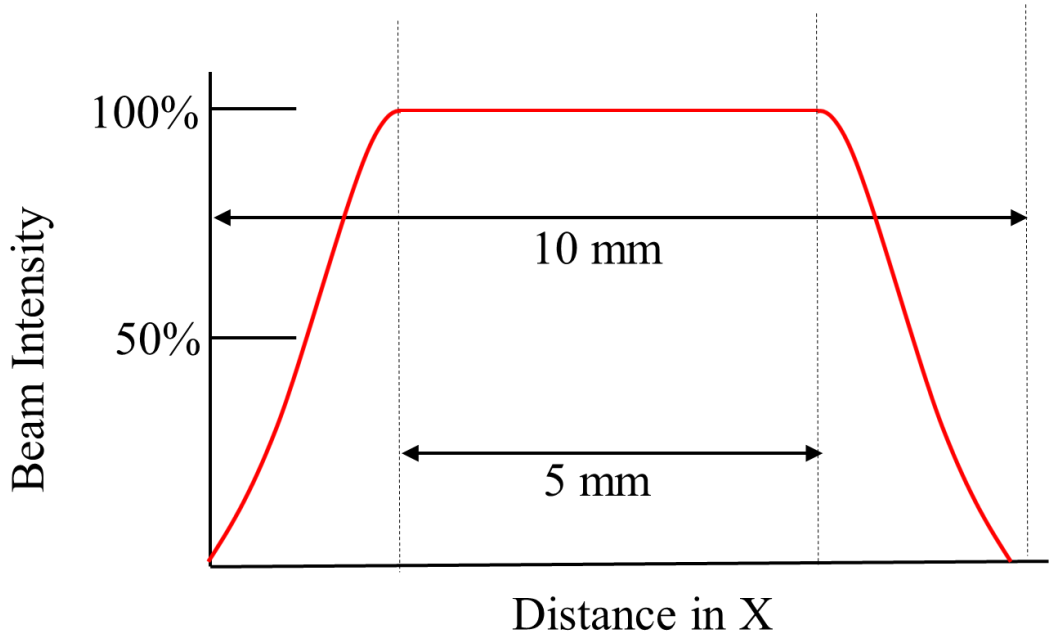

Figure 4.10 The beam intensity profile in the x-direction due to overscanning a full beam width.

As can be seen in **Figure 4.10**, a uniform profile is achieved over the desired area with the intensity falling off as the beam moves on to the slit apertures. This profile can be used to help determine how much of the beam should fall on the slits versus pass through them. If the beam intensity was equivalent across the entire area, then a simple ratio of the "fully irradiated area" compared with the "scanned beam area" could be used to determine the appropriate current partitioning. However, because of the Gaussian profile of the beam, less than 100% beam intensity falls on the slits. For calculational purposes, this intensity fall-off can be accounted for by reducing the effective overscan area by half a beam width on each slit. For example, for a 2.5mm beam, 1.25mm would be taken from each slit, reducing each dimension by 2.5mm. For the case shown in **Figure 4.9**, the "effective" scanned beam area is then 7.5mm x 8.5mm (the actual area being hit by beam is still 10mm x 11mm). To ensure that the beam is completely raster-scanned at least one beam width off of the target area, the following must be satisfied:

$$i_{stage} \leq \frac{X \cdot Y}{(X + beam\ width)(Y + beam\ width)} i_{total}$$

Where i_{stage} is the current measured in the faraday cup right before the stage, X and Y are the x and y dimensions defined by the slits, and i_{total} is the total current in the beamline before the slits. For the case when a 5mm x 6mm fully irradiated area is desired with a 2.5mm beam width, less than 47% of the total beamline current (i_{total}) must pass through the slits to the stage faraday cup (i_{stage}). When this condition is met, the beam is being raster-scanned at least one beam width off the stage. Any amount less than 47% of i_{total} would also suffice, but would result in a lower damage rate in the fully irradiated region. This method assumed that any divergence of the beam caused by the slit apertures was negligible.

4.3.4 The Irradiation Stage

After helium implantation, the samples were readied for Fe^{2+} irradiation. An irradiation stage was used to hold the samples in place, and provide the necessary heating and cooling avenues. A schematic of the stage is shown in **Figure 4.11**. The stage consisted of 6-inch long head composed of Hastelloy X (nominally Ni-20Cr-8Mo) welded to a flange, which would be mounted on the end of the beamline. A 0.25mm thick square of copper foil was placed on the nickel head to facilitate heat conduction from the back of the stage to the samples. The samples, along with

the guide bars, were then arranged on the copper foil side-by-side with the helium (and to-be-irradiated) side facing upward. The samples were held in place using a pair of hold-down bars and a shim which tightened into the stage using screws.

Two J-type thermocouples were spot welded on the upper and lower portions of each guide bar. The thermocouples were custom built for each experiment using 0.001mm iron and constantan wires. These wires were threaded through ceramic insulator pieces which could be split into pieces of any desired length. The junction was created by spot welding on to the guide bars. The wires were connected to a feedthrough which led to the back of the stage and would eventually be connected to the cold junction (digitally controlled). **Figure 4.12** shows an image of a completely built stage.

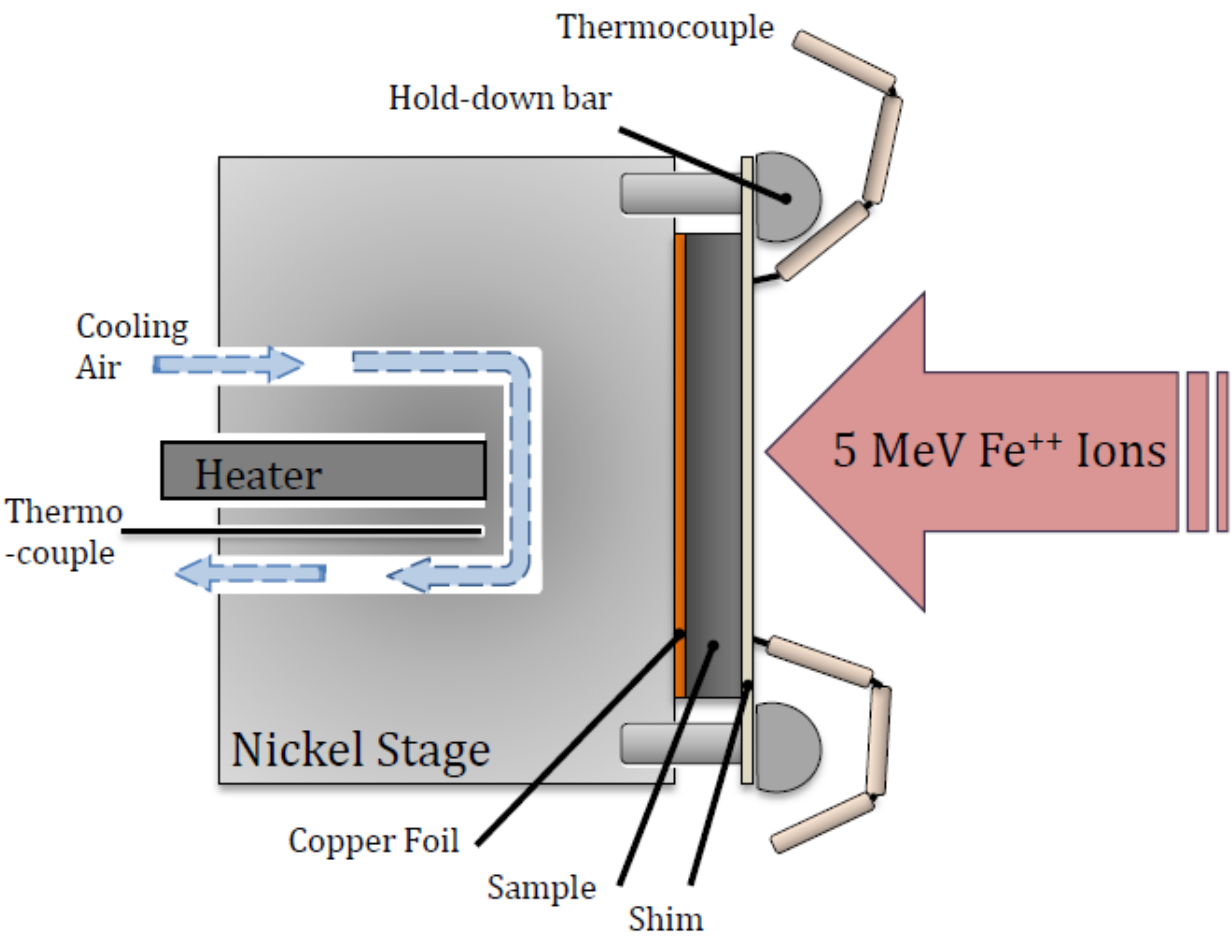

Figure 4.11 A side-view schematic of the Hastelloy X irradiation stage.

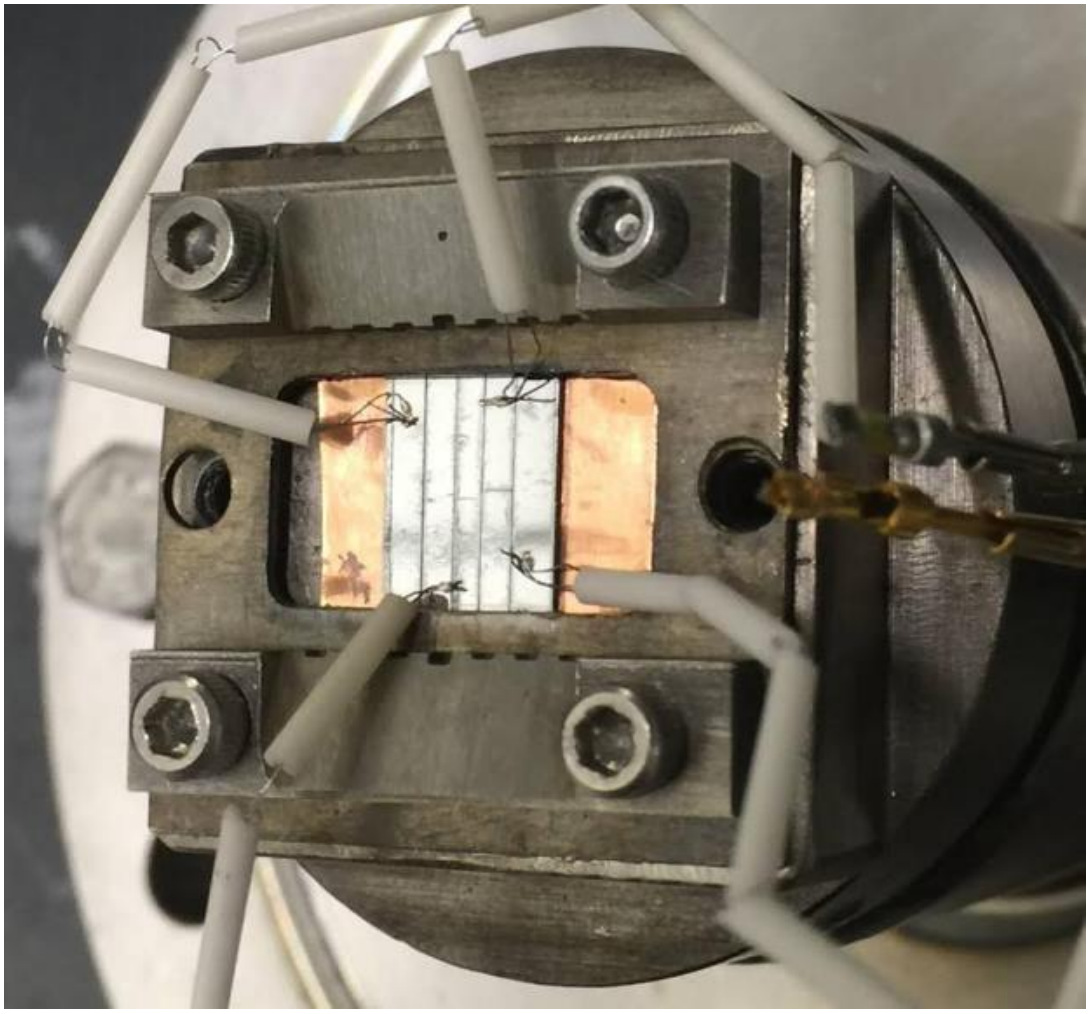

Figure 4.12 An image of a fully constructed irradiation stage.

4.3.5 The Irradiation Beamline

Once the stage construction was complete, it was mounted on the beamline. The stage was mounted to the end of the ion irradiation beamline using a copper gasket and tightened down with nuts and bolts. A schematic of the beamline end-station with the stage mounted is shown in **Figure 4.13.** Once mounted, a resistive cartridge heater was inserted into the back of the stage. The cartridge heater was approximately 4cm long and 1cm in diameter, with a temperature rating of up to 760°C. Additionally, a contact thermocouple was inserted into the back of the stage into an approximately 1mm diameter hole to monitor the temperature close to the heater. Cables from a computer readout were attached to thermocouple feedthroughs, and the airlines for cooling the stage were also attached.

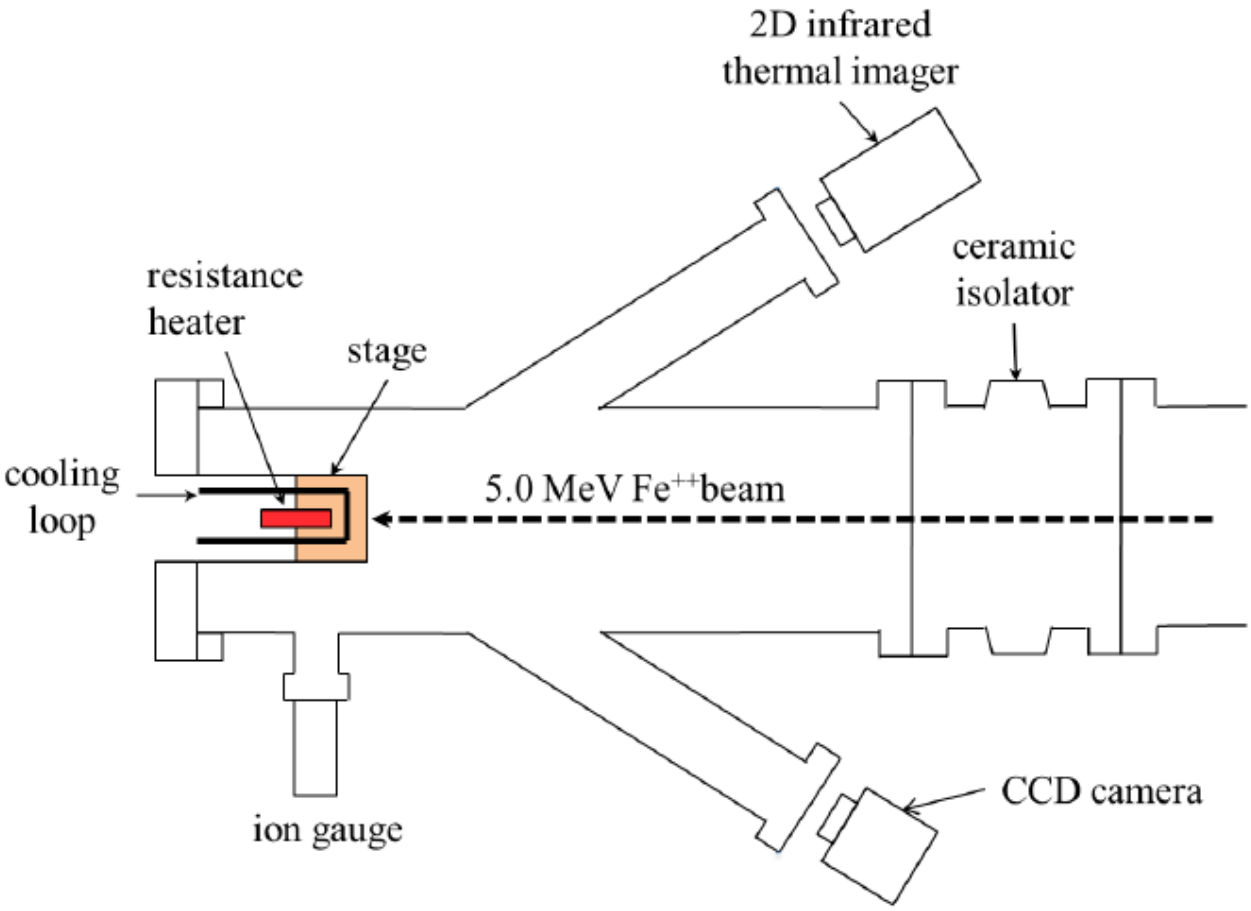

Figure 4.13 A schematic of ion irradiation end-station detailing key components.

The end station itself contained many diagnostic tools to monitor the status of the irradiation chamber before and during the irradiation experiment. An Inficon ion gauge was used to read the pressure. A CCD camera was available through a windowed port for a live view of the irradiation stage. In addition to the thermocouple system, a FLIR 2D infrared thermal imager was mounted to a port to provide *in situ* temperature measurements of the surface of the samples. All of these diagnostics provided digital outputs to computer systems, which recorded and displayed the information using custom built LabView™ programs.

After the appropriate diagnostic connections were made, the slit aperture system discussed in section 4.3.2 was set to the desired area. The alignment of the stage was then checked with a laser which had been previously aligned with the beam path. The laser was mounted at the end of a bending magnet near the accelerator. A plastic film was placed in front of the laser to diffuse the beam and simulate the effect of raster-scanning. The alignment of the laser illuminated area was checked via the CCD camera. If needed, minor adjustments were made with alignment screws at the end station of the beamline. **Figure 4.14** shows an image of samples mounted on the beamline and aligned with the laser.

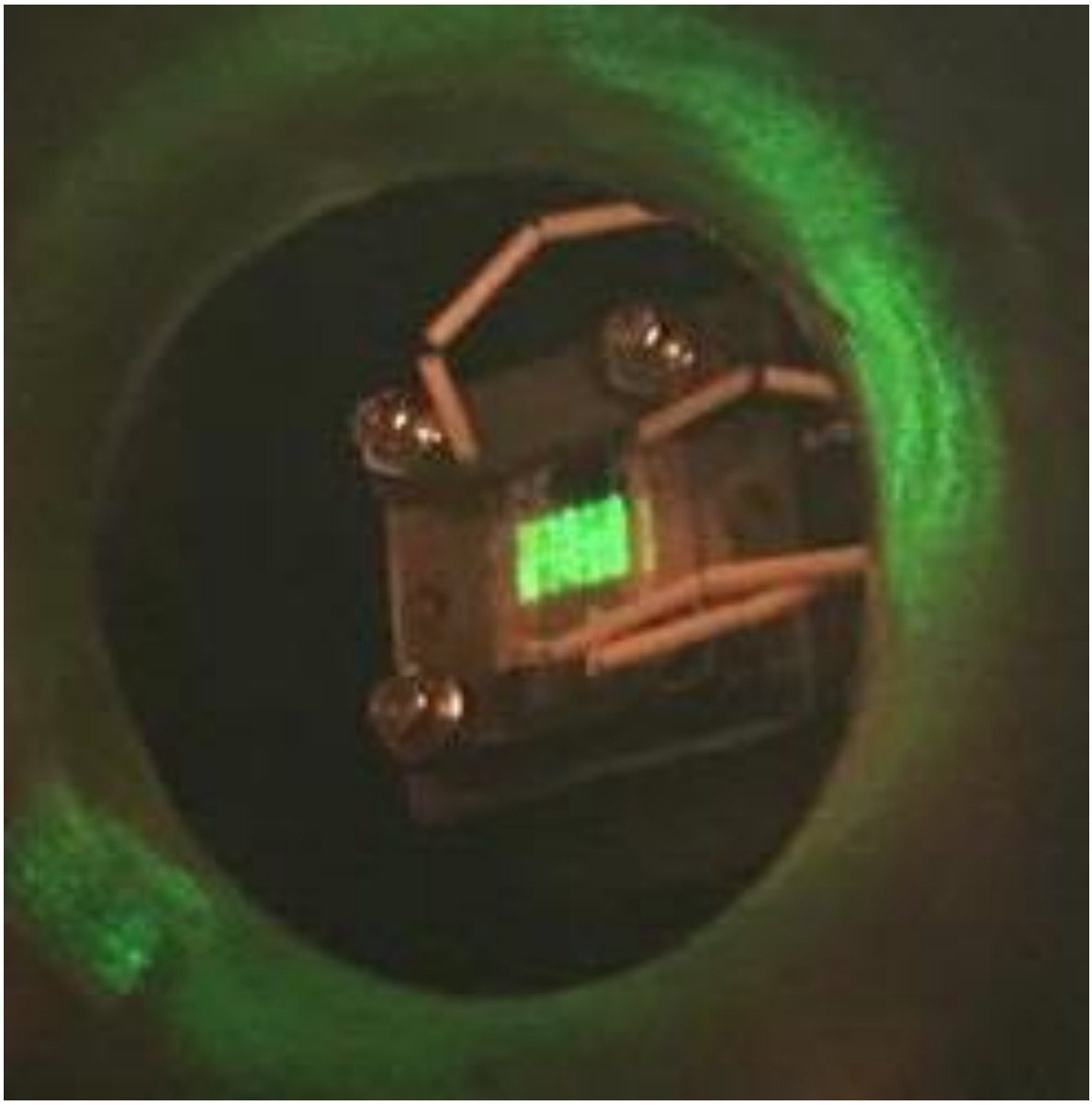

Figure 4.14 Samples aligned with the laser.

Once appropriately mounted and aligned, the irradiation chamber was pumped down, starting with a rough pump. Pumping with the rough pump for about 15 minutes allowed the chamber to reach a pressure of approximately $1x10^{-2}$ torr, at which point a turbo pump was turned on. The turbo pump was allowed to spin up to full speed and pumped the chamber further until a pressure of about $1x10^{-4}$ torr was reached, which took approximately 30 minutes. The gate valve to a cryopump directly underneath the stage was then opened. This cryopump almost immediately brought the chamber pressure to about $1x10^{-6}$ torr. The ion irradiation chamber was then opened up to the rest of the beamline, which was maintained at $1x10^{-8}$ torr, to provide additional pumping power. The stage was then left to pump for at least 12 hours, usually overnight, to achieve a pressure in the range of $1x10^{-8}$ - $1x10^{-7}$ torr.

The beam was prepared as described in Section 4.3.2, with a FWHM of at most 2.5mm. The total current in the beamline typically ranged from 600nA to 1μA of Fe^{2+} ions, targeting a damage rate of $1x10^{-3}$ dpa/s. Steering elements in the beamline were used to ensure the beam was properly aligned and that the currents on the slit apertures were evenly balanced. Although the slits were unsuppressed, a calibration factor was determined for each slit to estimate the actual value of current. This calibration factor was typically around 12. That is, the currents read by the slits were approximately 12 times higher than the same current in a suppressed faraday cup.

When the beam was confirmed ready, the stage was heated to the irradiation temperature by applying a voltage to the cartridge heater in the back of the stage. For all experiments in this thesis, the irradiation temperature was 460°C. To preserve the integrity of the room temperature helium pre-implantations, no outgassing was performed on the samples and the heat up to temperature was done as quickly as possible. This resulted in a temporary increase in the pressure near the stage to about 9×10^{-7} torr. The thermocouples were carefully monitored during heat-up to ensure that the samples exhibited uniform heating behavior. To reach 460°C, the entire heat up process typically took about 15-20 minutes. As soon as 460°C was reached on the thermocouples, (typically a spread of ~5 degrees on the thermocouples was observed, so an average was taken) the FLIR thermal imager was calibrated. In the thermal imaging program, three Areas of Interest (AOIs) were placed on each sample in the irradiated region. These areas defined the spots which would be monitored *in situ* throughout the entire length of the irradiation. The emissivity of these

spots was calibrated such the temperatures read by the thermal imager matched those of the thermocouples. **Figure 4.15** shows a typical thermal image with square AOIs on a heated irradiation stage. The hotter regions appear brighter. This calibration could be performed in under five minutes. As soon as the irradiation stage was at temperature and calibrated, the beam was allowed pass to the samples to begin the experiment.

Figure 4.15 An image taken from the FLIR 2D imager of a heated irradiation stage with three square AOIs on each sample.

4.3.6 Running the Irradiation

While the experiment was running, it was monitored 24/7 to ensure all of the irradiation parameters remained within specifications. The target temperature for all irradiations was 460°C, and was maintained within ±10°C. While the thermocouples were still monitored, the AOIs from the FLIR imager were used to monitor the temperature throughout the experiment. It provided a spatial dependence on temperature, and could be used to see if all samples were experiencing uniform temperature behavior. The LabView™ program would sound an alarm if any of the AOIs strayed beyond 10°C of the target temperature. If fluctuations were observed, changes were made to the voltage on the cartridge heater to compensate and keep the temperature as close to 460°C as possible. For an Fe^{2+} beam, only a small amount of beam heating was observed, ranging from 5-10°C depending on the current. The cooling lines for air flow were not typically used during the experiments, since the heater cartridge could stably maintain the temperature on its own.

The pressure near the stage and in the beamlines was also monitored digitally during irradiation using Inficon ion gauges. The target starting pressure before heat up was below $1x10^{-7}$ torr. With the combination of heating up and putting the beam on the samples, the stage pressure at the very beginning of irradiation spiked to high 10^{-7} range, but quickly recovered to below $1x10^{-7}$ within a couple of hours. It was important to always make sure the pressure was below 10^{-6} torr during irradiation to prevent the possibility of oxidizing the samples.

The current was also monitored at all times during the experiment. As mentioned in Section 4.3.2, the beam was raster-scanned such that a calculated proportion irradiated the samples and the slits. A suppressed faraday cup was periodically (every 30-40 min) inserted in front of the stage to measure the current that was impacting the samples. A continuous current measurement was not possible because the entire stage and irradiation chamber could not be suppressed. However, the slit apertures were used to continuously measure the presence of current and the alignment of the beam. If the balance of current the slits shifted, the bending magnet could be used to realign the beam. Additionally, while the current values on the slits were not quantitatively accurate, they could still be used to measure the relative stability of the beam (i.e. if the beam was increasing or decreasing in current). They would therefore provide an indication of whether the stage faraday cup needed to be inserted to capture a change in current.

If at any point during the irradiation the pressure, current, or temperature were compromised (due to a power outage, accelerator or source malfunction, etc.) priority was given to maintain the integrity of the samples. If for example, the beam was lost for a period longer than 20 minutes, the samples would be quickly cooled to room temperature. This would be achieved by shutting off the cartridge heater voltage and opening up the air cooling lines and applying a high air pressure. Typically, this would allow the samples on the stage to reach below 100°C within 10 minutes. Once the issue had been resolved, the samples would be heated up similar to start-up, the AOIs for the thermal imager would be recalibrated, and the irradiation would resume.

Once the target damage level was achieved, the irradiation was complete. The irradiation was terminated by blocking the beam with the Faraday cup and rapidly cooling the stage. The heater voltage was turned off and the air cooling lines were opened to high pressure. The stage was cooled to room temperature and the irradiation chamber was vented before the stage and samples could be removed.

4.4 Post Irradiation Characterization Methods

The following section details the preparation and analysis methods used to examine the microstructure of T91 after it was irradiated. It consists of TEM sample prep, TEM imaging, and the characterization of the images. In some cases, NRA (nuclear reaction analysis) was used to profile carbon content with depth.

4.4.1 TEM Specimen Preparation

Due to the shallow penetration depth of the Fe^{2+} ions (see **Figure 4.7**), the FIB (focused ion beam) lift-out method needed to be used to prepare TEM samples. This method allowed for the extraction of cross-sectional slices of material just a few microns into the surface. Additionally, T91 is highly magnetic, and large samples would cause magnetic distortion in the electron beam during TEM imaging. The FIB lift-out method allowed for microstructural analysis and avoided magnetic issues during imaging.

The TEM foils were prepared using a dual beam FIB. This instrument utilizes an electron beam (normal to a horizontal surface) for imaging, and a gallium ion gun (52° from the electron beam) for imaging and milling. The currents and energies of these beams could be varied. The ion beam operated at energies up to 30keV and currents of about 10nA. Energies of 30keV were used for most preparation steps. The specific instruments used in this thesis were FEI Helios

NanoLab™ Dual Beam™, Nova NanoLab™ DualBeam™, and Quanta™ 200 3D Focused Ion Beam Workstation. The FIB liftout method was utilized as follows.

The irradiated bar was mounted irradiated-side up using copper tape on an SEM mount and placed in the FIB chamber, which was then pumped down. The stage was tilted 52° to be perpendicular to the ion beam. An appropriate area on the sample was chosen in the irradiated (and potentially helium implanted) region. A gas injector was inserted and the gallium beam was used to deposit a small layer of platinum on the target surface, in dimensions of approximately 20 x 5 x 5 microns, using a current of about 0.2 nA. Using a higher current (~7nA), the gallium beam was used to create trenches about 4 microns deep on three sides of platinum deposition. The long sides of the deposition were cleaned up using lower current (~3nA). The stage was then tilted back to 0° so that the gallium beam could provide an undercut of the sample so that it was held only by one edge. A micromanipulator (called an Omniprobe™ needle) was inserted and slowly positioned such that it made contact with the corner of the platinum deposition. A small amount of platinum (~0.5 microns) was used to weld the Omniprobe™ needle to the sample. The final connecting edge was then cut with the gallium beam to free the specimen from the metal bulk. The Omniprobe™ needle was then carefully raised a safe distance away from the irradiated sample and the stage was moved to the location of a mounted Omniprobe™ grid (or the SEM chamber was evacuated and a mounted grid was placed inside). The needle with the attached sample was lowered to a position where it was just in contact with one of the Omniprobe™ grid posts. The gallium beam was used to weld the specimen to the post with about 1 micron of platinum. The needle was then cut free from the sample and retracted from the chamber. At this point, the specimen was still ~2 microns in thickness. To achieve the target thickness of 100 nm, successive thinning needed to be done. The sample was tilted to 52° and the current was lowered to 80 pA. The sample was alternately tilted ±2° about 52° to thin the sample in a wedge shape. This method was used to minimize the amount of material milled from the top of the sample to preserve the surface, while still thinning the entire specimen. The current was successively lowered as needed, while alternating the angle until the specimen was measured in the SEM to be less than 100nm thick. The chamber was then vented and the sample attached to the grid was placed in a labelled membrane box for safe keeping. **Figure 4.16** highlights the key steps summarizing the FIB lift-out process.

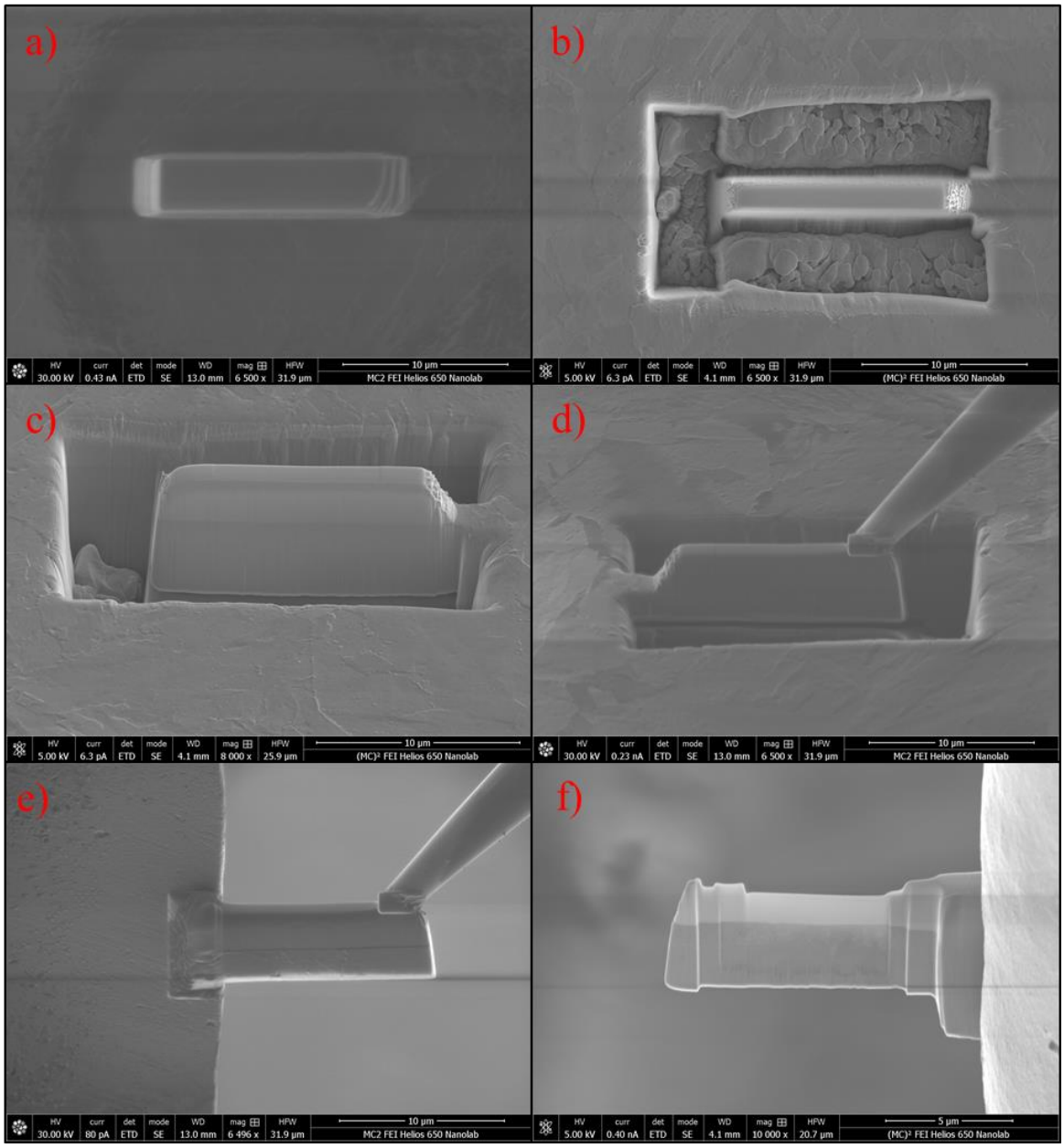

V

Figure 4.16 A schematic of the FIB process, showing a) platinum deposition on the surface, b) trenching around the platinum deposition, c) undercut of the sample at 52°, d) attaching of the Omniprobe to the sample, e) attaching of the sample to the copper grid and f) a thinned FIB specimen.

4.4.2 Cavity Imaging

Imaging for all of the TEM specimens in this thesis was performed using a JEOL 2100F Cs Corrected Analytic Electron Microscope (AEM) at the Michigan Center for Materials Characterization $(MC)^2$. The JEOL 2100F is a 200keV microscope that operates mainly in scanning TEM (STEM) mode. This microscope also maintained the capability for XEDS using an EDAX® detector, with EDAX® acquisition software. Additionally, a Gatan® Imaging Filter (GIF) allowed for the capability to perform electron energy loss spectroscopy (EELS). A software suite called DigitalMicrograph® was used to acquire the images. The TEM specimen was mounted on a JEOL Single-tilt or Double-tilt stage and inserted into the microscope.

Imaging of the entire liftout was performed using STEM mode, capturing a high angle annular dark field (HAADF) image and a bright field (BF) image simultaneously. Typically, convention TEM (CTEM) images have been used to image cavities. However, while using CTEM some cavities may appear in focus while others appear out of focus. Because of this variation in focus, the sizing of these cavities may not be accurate while using CTEM. Therefore, STEM HAADF images are used. The contrast in STEM HAADF images arises mainly from thickness and "Z-contrast," which is dependent on the atomic number of the material. Cavities, which lack both thickness and any atomic number appear as distinct, dark areas under these imaging conditions with well defined boundaries. The HAADF images are typically free from contrast caused by dislocation networks and FIB damage allowing for accurate and convenient imaging of cavities. Example images of a typical HAADF image and its corresponding BF image is shown in **Figure 4.17**.

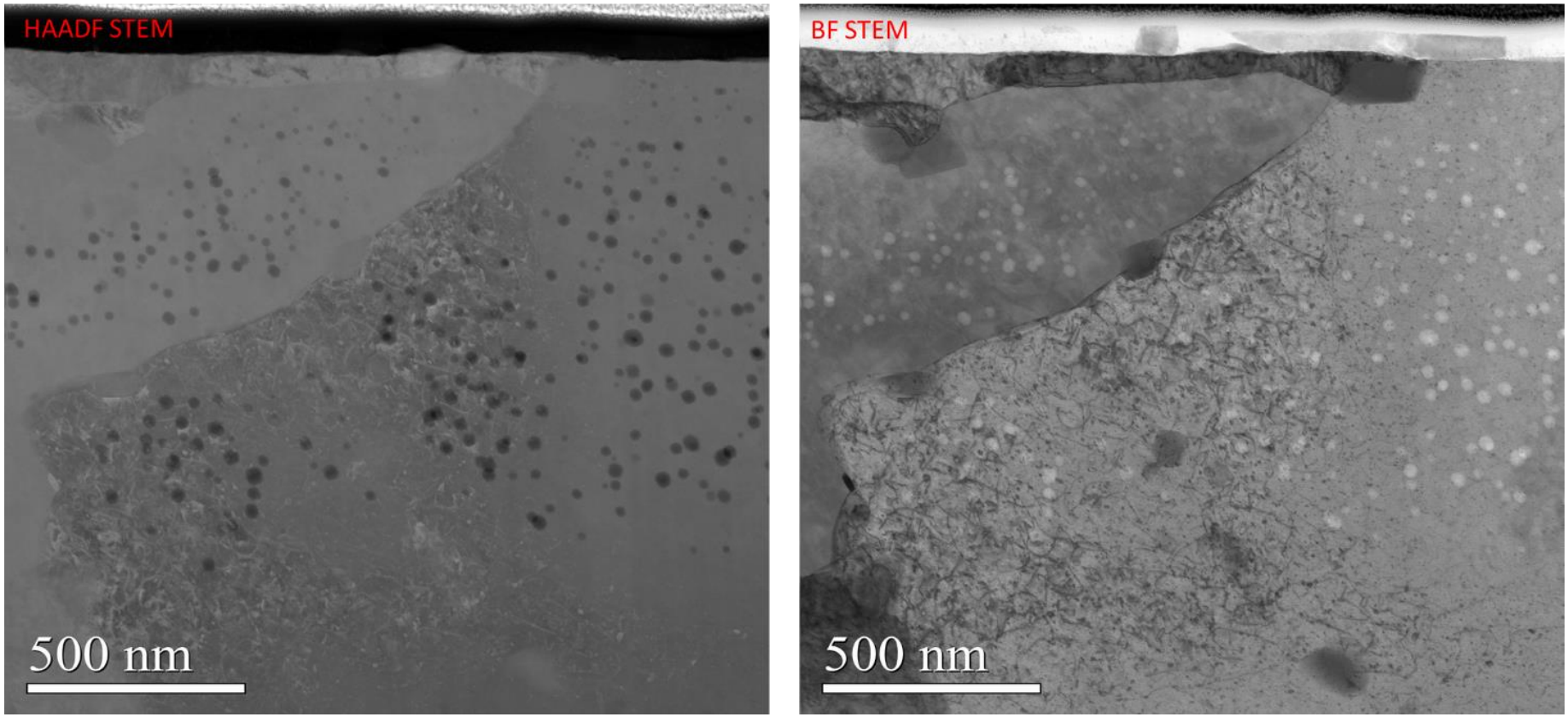

Figure 4.17 HAADF STEM (left) and BF STEM (right) micrographs of the same area on a T91 specimen irradiated to 150 dpa at 460°C using 4.4 MeV Fe^{2+} ions.

A standard procedure for consistent imaging across all samples was used. Images were taken at approximately 500kx magnification, which allowed for a field of view of about 2 x 2 microns. Successive images were taken across the length of the sample with minimal overlap until a complete set of HAADF and BF images covering the entire specimen were taken. In many cases, higher magnification images were taken to acquire more detailed views smaller cavities and microstructural features.

The thickness of the TEM specimen was measured using EELS (electron energy loss spectroscopy). This method estimated the thickness of the sample by measuring the amount of electron energy loss as the beam passed through the sample. The electron beam was set to probe size of ~1nm and the camera length was set to 2cm (for a corresponding collection angle of about 38mrad). A zero-loss spectrum was taken in an area without going through the sample to calibrate the beam. Then an EELS spectrum map was taken on at least six areas of the sample (within the 500-700nm depth region). The DigitalMicrograph® software included an algorithm to calculate the thickness by calculating the error in a logarithmic fit of the inelastic mean free path of the electrons through the sample. The error in this calculation is estimated to be around 10% [70]. The average of these thickness measurements taken from the EELS map was used as the nominal thickness of the TEM Specimen.

4.4.3 Cavity Characterization

Characterization of the cavities after the images were taken was performed using a freely available ImageJ software. Each HAADF image was divided into 100nm depth bins, starting with the surface of the sample. The cavities in each bin were counted and measured, the results stored separately. During counting, the HAADF images were cross-referenced with the BF images to ensure that the cavities being counted were indeed cavities and not precipitates or other microstructural features. After the counting of an image was complete, the next sequential image was examined for any overlapping regions and marked off. This ensured that no cavities would be double-counted. When the entire TEM specimen was counted, the lengths of all the counted regions (excluding overlapping regions) was tallied for the total length of the specimen. Taking this length into account, the 100nm depth of the bin, and the average thickness of the specimen a total volume of the bin, V_{bin}, was calculated. The volume of each individual cavity was calculated,

assuming each cavity was a sphere. The sum of the volume of each cavity was tallied for each bin. This value was effectively the change in volume, ΔV, of the bin. Swelling is calculated as the change in volume divided by the original volume, so the swelling of any particular bin in %, could be expressed as:

$$\text{Swelling (\%)} = \frac{\Delta V}{V_{bin} - \Delta V} * 100 = \frac{\frac{\pi}{6}\sum_{i=1}^{N} d_i^3}{l * w * \delta - \frac{\pi}{6}\sum_{i=1}^{N} d_i^3} * 100$$

where l is the length of the liftout, w is the width of the bin, δ is the thickness of the TEM specimen, N is the number cavities in the bin, and d_i is the diameter of the ith cavity. For the nominal swelling value within the 500-700 nm depth region, the volume change calculation included cavities from both the 500-600 nm and the 600-700 nm bins. Average cavity diameter and number densities were also determined as a function of depth. Additionally, a cavity size distribution with number density plotted as a function of size was also determined.

The sink strength of any particular bin was determined by summing over the size distribution of that bin:

$$k_v^2 = 2\pi \sum_{l=0}^{L} l\rho_l$$

where d is the diameter of the cavity, ρ_l is the density of cavities with a diameter of l, and L is the maximum cavity size observed. Density bins in the size distribution were calculated with a resolution of at least 2 nm.

An example of the results of depth profiling cavities with size, number density, and swelling is shown in **Figure 4.18**.

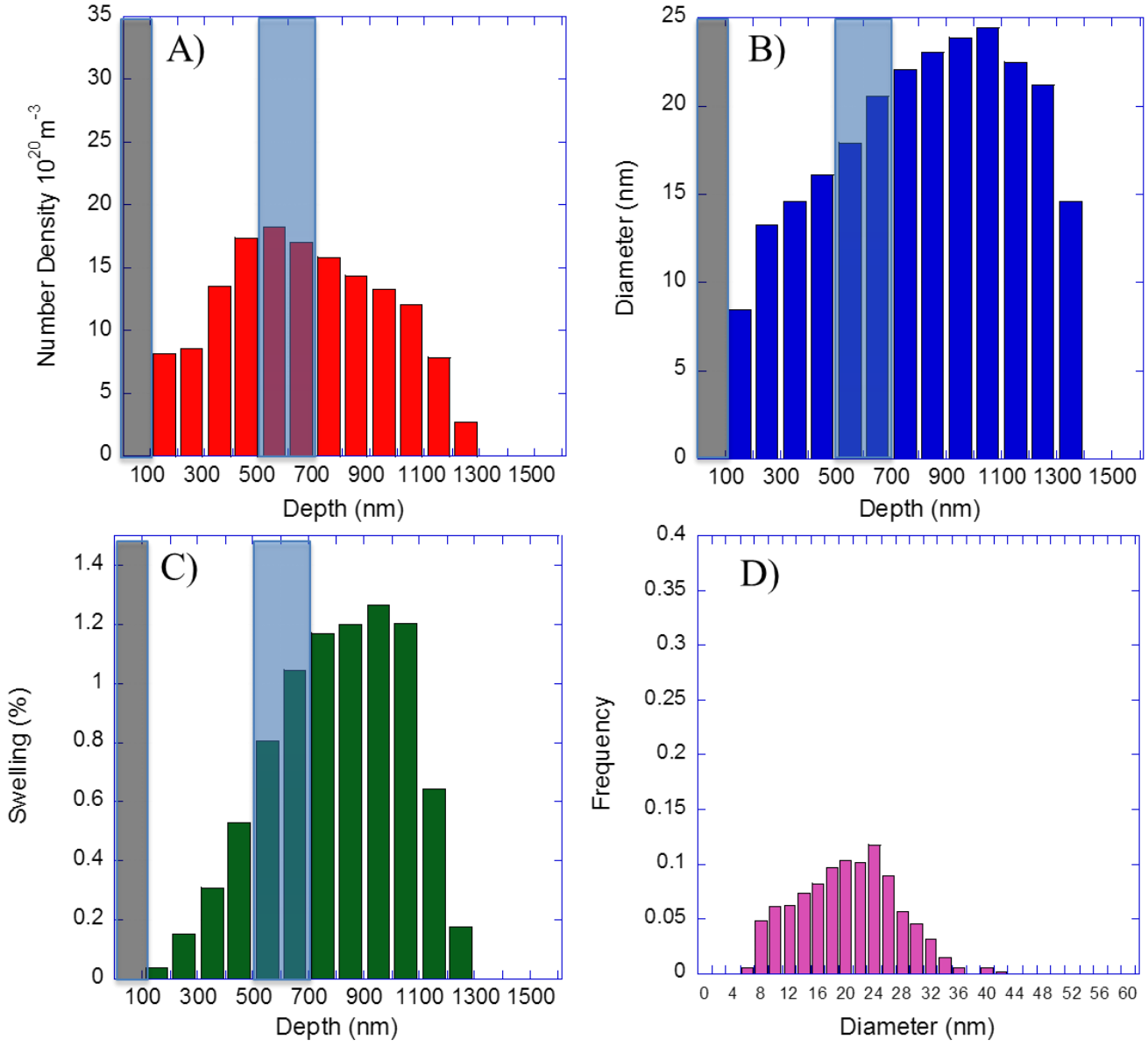

Figure 4.18 An example of profiling cavities through depth in 150 dpa T91 for A) number density B) average diameter and C) swelling. The resulting size distribution from the 500-700 nm region is shown in D).

4.4.4 Nominal Damage Level and Valid Depth of Analysis

As seen in the SRIM profile in **Figure 4.7**, the damage rate changes as a function of depth, so the calculation of a damage level for a particular experiment is not straightforward. As mentioned previously, a depth of 600 nm in the SRIM profile was used as the nominal damage level for each experiment. This depth was chosen as it adequately avoids the effects of injected interstitials at the higher depths, and avoids any surface effects at the lower depths. Zinkle [3] determined the valid depths of analysis for a Fe-10Cr system for 5 MeV ions, which takes into account diffusion of interstitials from higher depths and the void-denuded surface effects. For the T91 system at 450 dpa and 460°C, the valid depth regions remain within a range of 300 – 800 nm, which adequately avoids surface and interstitial effects. A similar depth range was determined as valid by Getto [8] in HT9. For the coated samples in this study, the surface is effectively adds 100 nm to depth of the surface effect, so the valid analysis region becomes 400-800 nm. Partitioning within the 400-800 nm depth region was performed to obtain data from multiple damage levels from a single experiment. However, the nominal damage level for a particular experiment was calculated at the 600 nm depth.

As seen in **Table 4.4**, the damage rate at 600 nm depth does not change if the sample is coated or uncoated. To remain consistent between samples which are coated and uncoated, this constant SRIM profile depth of 600 nm was used as the nominal damage level for all experiments. In this thesis, all depths are referred to in reference to the SRIM profile, unless stated otherwise.

4.4.5 Error Calculations

For all conditions in this thesis, an effort was made to minimize the error due to counting statistics, to ensure the accuracy of the swelling measurements. At least two TEM specimens for each condition were extracted, which was nominally equivalent to 2 μm^2 of material about 100nm thick (for the 500-700nm region). However, errors due to instrument limitations, such TEM resolution needed to be taken into account. The two types of error that needed to be accounted for were error due to TEM resolution, and error due to EELS thickness measurements.

The resolution for the images taken was 0.7nm/pixel. This would mean that the error on each end of a measurement would be less than 1nm, regardless of the size of the measurement. The error in the measurement of the size of the feature (cavity, precipitate, or dislocation), would then depend on the size of the measurement. The fractional error could then be represented by:

$$\mu_{res} = \frac{1nm}{L}$$

Where L is the length of the measurement. **Figure 4.19** shows how the error due to TEM resolution changes as a function of cavity size. This measurement error would also contribute to any calculation which depends on the cavity size, such as the calculation of swelling.

As mentioned previously, the fitting of the EELS zero loss method exhibits an error of 10%. This thickness measurement affects the calculation of number density, but is not dependent on any other factors. Therefore, error in number density at all times is estimated to be 10%. This is depicted as a flat line in **Figure 4.19**.

The calculation of swelling includes both diameter and thickness measurements, therefore the contributions of error in both TEM resolution and EELS thickness measurements both contribute to the swelling error. Void swelling is directly proportional to the number density and proportional to the cube of the diameter, as shown below:

$$\frac{\Delta V}{V} \propto N_V \propto \left(\frac{D}{2}\right)^3$$

The propagation of error for multiplicative quantities and quantities raised to a power is shown below:

$$\mu_{mult} = \frac{\sigma_u}{u} = \sqrt{\left(\frac{\sigma_x}{x}\right)^2 + \left(\frac{\sigma_y}{y}\right)^2}$$

$$\mu_{power} = n * \left(\frac{\sigma_x}{x}\right)$$

Where n is the exponent. For swelling, these two propagations can be combined, resulting in the following calculation for swelling error:

$$\mu_{swelling} = \sqrt{\left(\frac{\sigma_{N_D}}{N_D}\right)^2 + \left(n * \frac{\sigma_D}{D}\right)^2} = \sqrt{\left(\mu_{N_D}\right)^2 + \left(3 * \mu_D\right)^2}$$

Where N_D is the number density, D is the diameter, and μ_{N_D} and μ_D are the fractional errors in number density and diameter, respectively. The swelling error therefore depends on errors in the number density and diameter. The dependence of the error with swelling on cavity size is also shown in **Figure 4.19**.

It is also important to consider the high degree of homogeneity inherent to ferritic-martensitic steels. Grain-to-grain variation in the microstructure contributes additional uncertainty to the swelling measurements, as cavity nucleation and growth can vary extensively in adjacent grains. In an effort to minimize this uncertainty, multiple TEM specimens were extracted for each condition from different regions of the irradiated sample. At least two TEM specimens were made per condition, encompassing an area of approximately 2 μm^2, with foil thicknesses less than 100 nm. Unless cavity nucleation was significantly suppressed, over 150 voids were characterized for each damage level (200 nm wide depth bin).

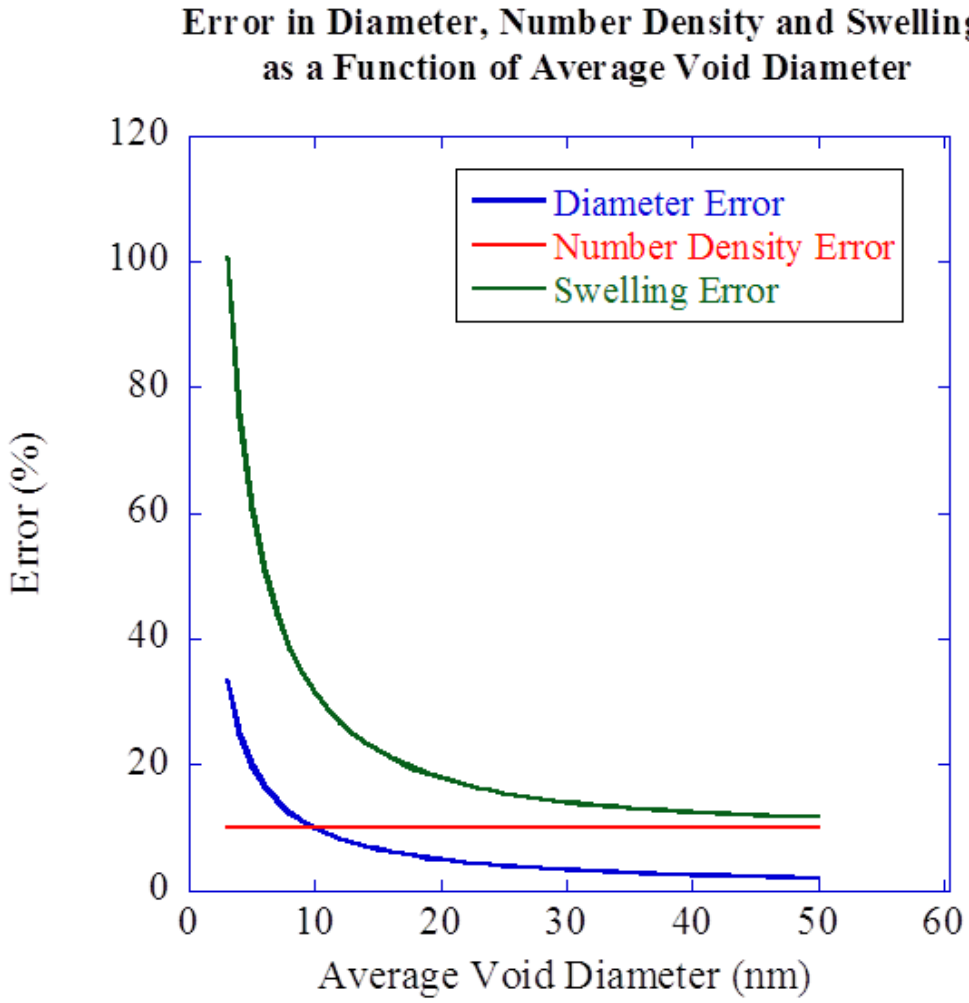

Figure 4.19 The error in diameter, number density and swelling is plotted as a function of cavity diameter.

4.4.6 Dislocation Imaging and Characterization

Imaging of dislocation loops in ferritic-martensitic steels requires careful imaging conditions and sample preparation. The TEM specimens which were used for cavities were also used for dislocations. Two types of loops exist in FM alloys: sessile **b**<100> loops aligned on the [100] planes and glissile ½ **b**<111> loops. The ratio between these loops typically favors a higher population of **b**<100> loops. Typically, CTEM has been used to investigate the presence of these loops using the weak two-beam condition. However, such a method requires a sequence of images in the same area using varying diffraction vectors **g** to satisfy the dislocation loop **g·b** invisibility criterion. This is especially difficult in ferritic-martensitic steels which typically exhibit small grains with limited orientations. Methods to image dislocation loops using STEM mode have been used to more easily characterize these loops [71]. STEM imaging of loops also smears out thickness-dependent contrast that may be present in CTEM, resulting in a cleaner image. On-zone STEM imaging allows for the simultaneous imaging of all possible diffraction vectors, allowing for viewing of **b**<100>, ½ **b**<111> loops and dislocation lines all in the same image. When imaging along the [100] zone axis, b<100> loops appear circular or as perpendicular lines aligned with the [002] directions, while the ½ b<111> loops appear as ellipses aligned with the [011] direction. A schematic of loop orientations when imaged along the [100] zone axis is shown in **Figure 4.20**.

In practice, the loops were imaged in STEM mode just slightly off of the [100] zone axis so that perpendicular loops did not appear as lines, and the inside-outside contrast was seen. An example micrograph showing **b**<100> loops, ½ **b**<111> loops, and dislocation lines of T91 irradiated to 150 dpa is shown in **Figure 4.21**.

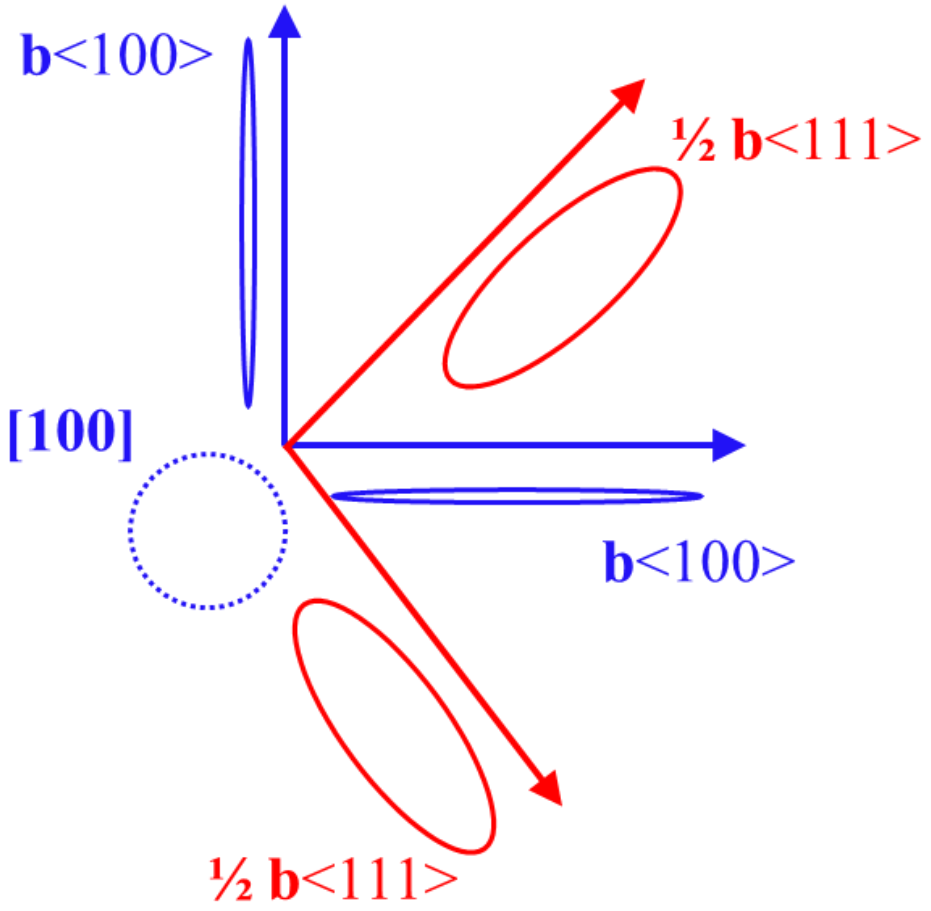

Figure 4.20 Schematic of what b<100> and ½ b<111> loops look like when imaged down the [100] axis.

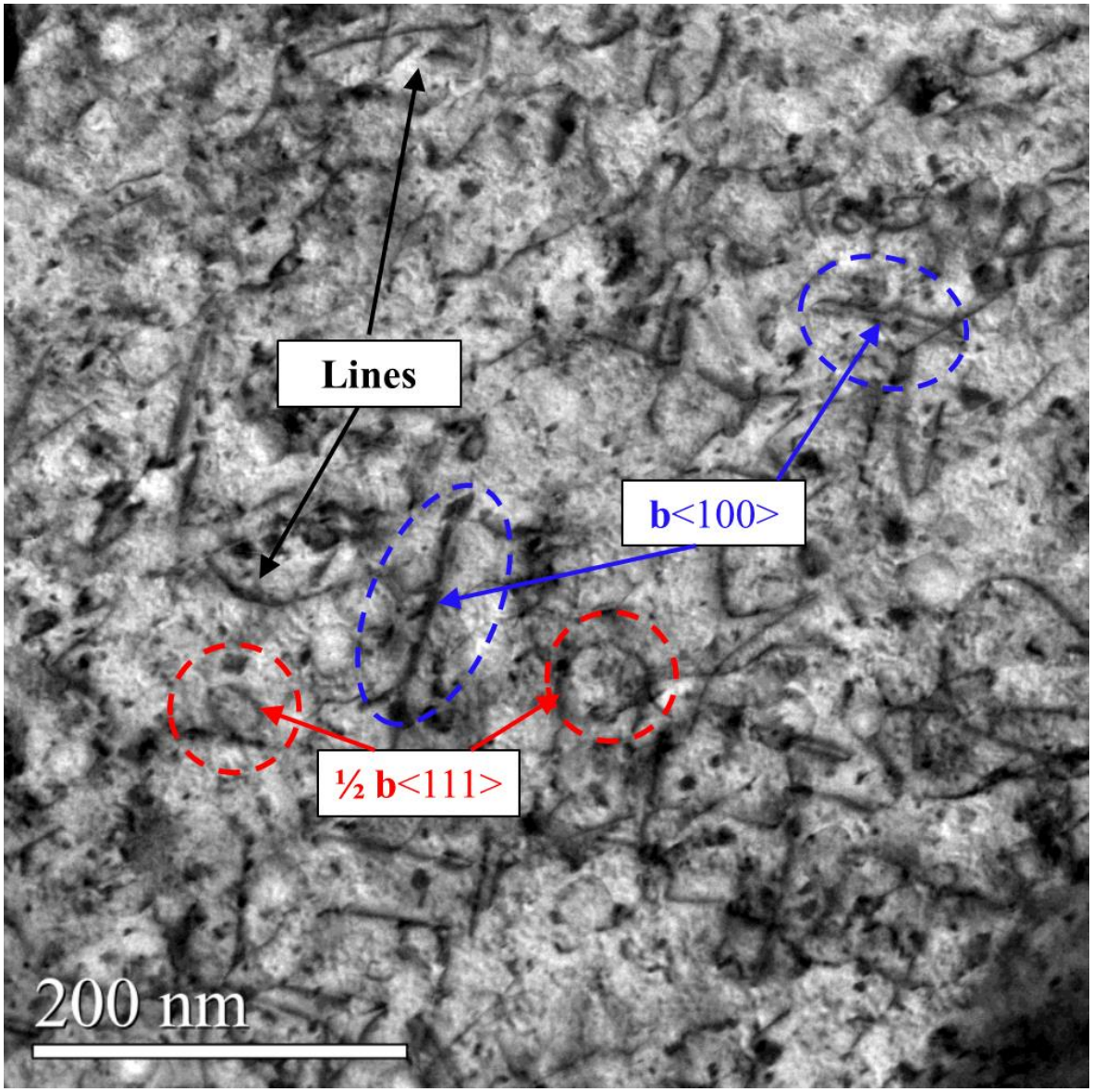

Figure 4.21 BF STEM image taken down the [100] zone axis showing b<100> loops, ½ b<111> loops and dislocation lines in T91 irradiated to 150 dpa.

Images of loops were taken from at least three different grains for every condition within the 500-700nm depth region. Using ImageJ, loops were counted and sized in a single orientation (for examples along the [001] direction for **b**<100> loops). EELS thickness measurements were used as before to calculate a loop density. The density was then multiplied by 3 to account for the loops in the two other directions which were not counted. From the values of diameter and density a total loop line length (or sink strength) was also calculated. The sink strength of the dislocation loops was calculated using the following equation:

$$k_{loop}^2 = 2\pi \frac{d_{loop}}{2} \rho_{loop}$$

Where d_{loop} is the average loop diameter and ρ_{loop} is the loop density.

The dislocation network density was calculated using a method established by Smith *et al*. [72] This method utilizes an equidistant circular grid, and counts the number of intersections of dislocation lines with the grid. The following equation was used to calculate the network dislocation density, or sink strength (in units of m^{-2}):

$$\rho_{net} = \frac{N\pi}{4n_c^2 d_c t}$$

Where n_c is the number of concentric lines, d_c is the spacing of the concentric lines, t is the thickness of the TEM specimen, and N is the total number of intersections counted. **Figure 4.22** shows an example of the intersections counted using the concentric circle method.

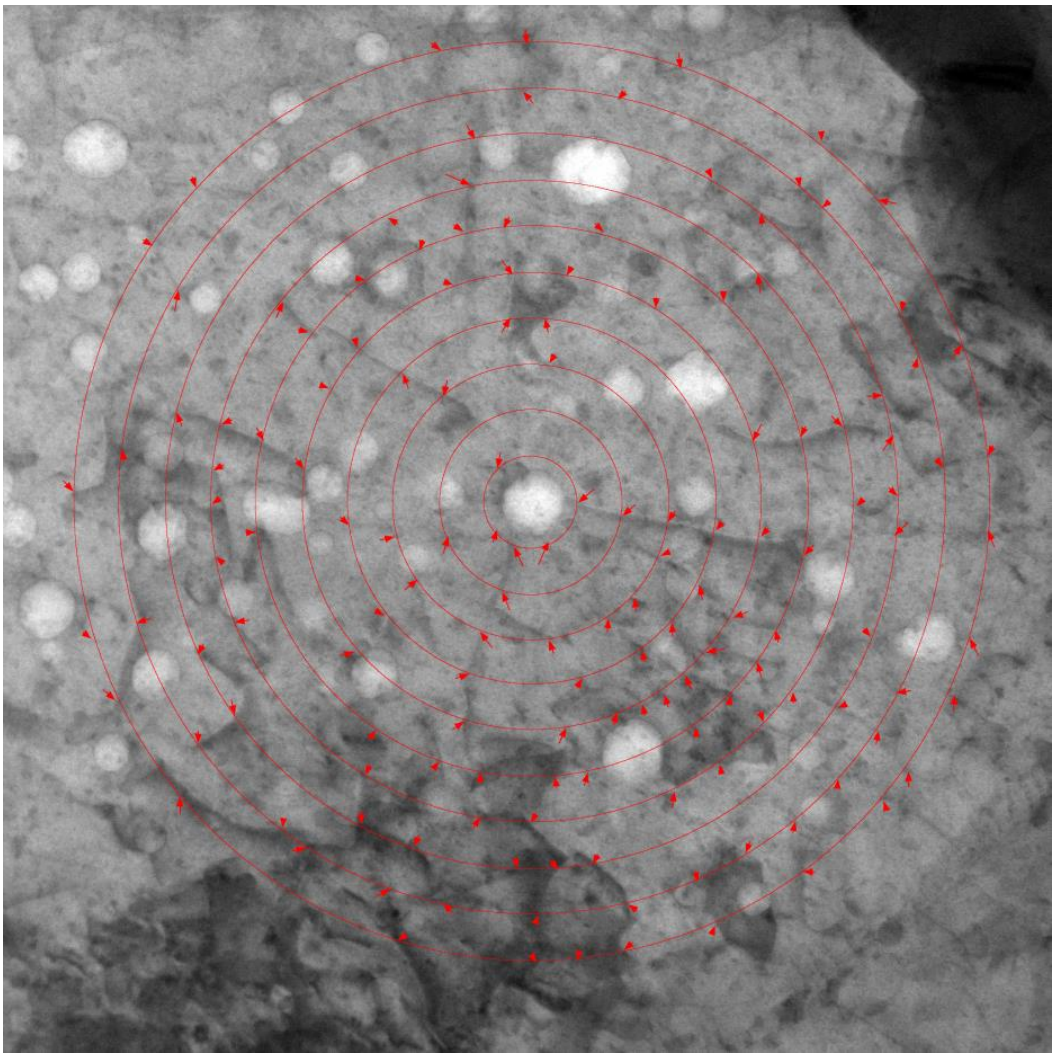

Figure 4.22 BF STEM image with a concentric circle grid used to count intersections with dislocation lines.

4.4.7 Precipitate Imaging and Characterization

Two different types of precipitates were characterized in this thesis: G-phase and M_2X carbides. Images of precipitates were taken primarily in BF STEM. Magnification depended on the size of the precipitates, but typically ranged between 500kx and 1Mx. Thickness of the samples were estimated with EELS as before.

The presence of the G-phase was verified using XEDS and BF STEM imaging. G-phase is a complex FCC silicide which typically exhibits stoichiometry of $Ni_6Mn_{16}Si_{17}$. This exact stoichiometry was not confirmed, however spheroidal clusters shaped like G-phase and heavily enriched in Ni and Si under XEDS were observed. Similar clusters have been observed in other ion-irradiated ferritic-martensitic steels confirmed to be G-phase so it is not unusual to expect its appearance in T91. The calculation for sink strength of this Ni-Si clusters assumed a spherical geometry and was determined using the following equation:

$$k_{ppt}^2 = 4\pi \frac{d_{ppt}}{2} \rho_{ppt}$$

Where d_{ppt} is the diameter of the cluster, and ρ_{ppt} is the number density.

As beam-induced carbon contamination caused the uptake of carbon in many cases, characterization of the carbides formed as a result was very important. In samples that did not have a 100 nm coating of alumina on the surface, a high density of carbides was typically observed. These carbides were imaged primarily in BF STEM, but also using LAADF (low angle annular dark field), which is the STEM equivalent of CTEM dark field imaging. Magnification of the images varied between about 300kx and 600kx. XEDS and diffraction patterns were used to help identify these carbides as M_2X. Additionally, these carbides were rod-like and grew along the [100] directions as ion-irradiated carbides in other ferritic-martensitic steels have been observed [5,73,74]. These carbides have also been identified as M_2X with M=Cr and X=C. Since these carbides are not spherical, calculating their sink strength is more complex. The sink strength for an acicular precipitate with l>>w can be calculated using the following formalism, taken from [75]:

$$k_{ppt}^2 = 4\pi r_p \frac{\kappa}{r_p} \rho_{ppt} = 4\pi\kappa\rho_{ppt}$$

Where r_p is the effective radius and κ is the capacitance for a precipitate where $w \approx t$. The values of r_p and κ are defined as follows:

$$r_p = \sqrt[3]{lwt}$$

$$\kappa = \frac{\sqrt{l^2 - t^2}}{\ln\left[\left(\frac{l}{t}\right)^2 - \sqrt{\left(\frac{l}{t}\right)^2 - 1}\right]}$$

Where l is the length, w is the width, t is the thickness of the precipitate. The widths and lengths of the precipitates were correlated with each other. Measurements of the thickness of the precipitates were taken from precipitates oriented perpendicular relative to those with length measurements. An average density, length, and sink strength was determined for each condition which contained M_2X precipitates.

4.4.8 NRA Measurements

To more completely characterize the amount of carbon taken up during irradiation, nuclear reaction analysis (NRA) was used to profile the carbon concentration with depth through several samples. NRA utilizes a set of detectors to collect a spectrums from a known nuclear reaction, in this case the reaction $^{12}C(d,p_0)^{13}C$. The counts collected from this reaction are compared to a known standard without C and fit to simulation provide an estimate of the amount of carbon at various depths.

The NRA experiment used the 1.7MV accelerator and ion beam analysis chamber at the Michigan Ion Beam Laboratory. The samples to be analysed were mounted on a holder which held the sample face perpendicular to the beam. This holder was attached to an electrically controlled goniometer which could translate and rotate the sample. Mounted along with the sample was a dummy sample of the same height, covered with a mylar sheet. This allowed for the beam to be imaged on the dummy sample via a CCD camera in the chamber so that the beam position could be precisely recorded. A 1.5 MeV deuterium beam was collimated using a 1mm diameter aperture about 3m from the sample and by a double slit system approximately 30cm from the sample. The position of the holder was adjusted such the beam was centered on the sample, without hitting any of the edges. A beam current of about 10 nA was used, and spectra were acquired for 6-12 hours.

The spectra were acquired using a silicon surface barrier detector positioned at a scattering angle of 170° with a solid angle of 3.2msr. The detector collected the Rutherford Backscattering (RBS) and NRA events.

The spectra acquired consisted of counts collected within particular energy channels. They were analyzed using SimNRA software [76], with the cross-section of the $^{12}C(d,p_0)^{13}C$ reaction calculated using the SigmaCalc 2.0 library [77]. This reaction has been shown to provide high depth resolution, with the capability to separate a surface layer of carbon from any near-surface distributions [78]. This program was used to fit the high energy edge of the RBS events by inputting the number of ions and the solid angle of the detector. Carbon was profiled to a maximum depth of about 3µm with a resolution of about 200nm and 360nm at 3µm of depth. SimNRA was used to create layers that matched with the depth resolution. The carbon profile was determined by adjusting the concentration in each layer so that the SimNRA spectrum matched that of the experiment. An example of typical energy spectrum (with a carbon contaminated T91 sample) is shown in **Figure 4.23**.

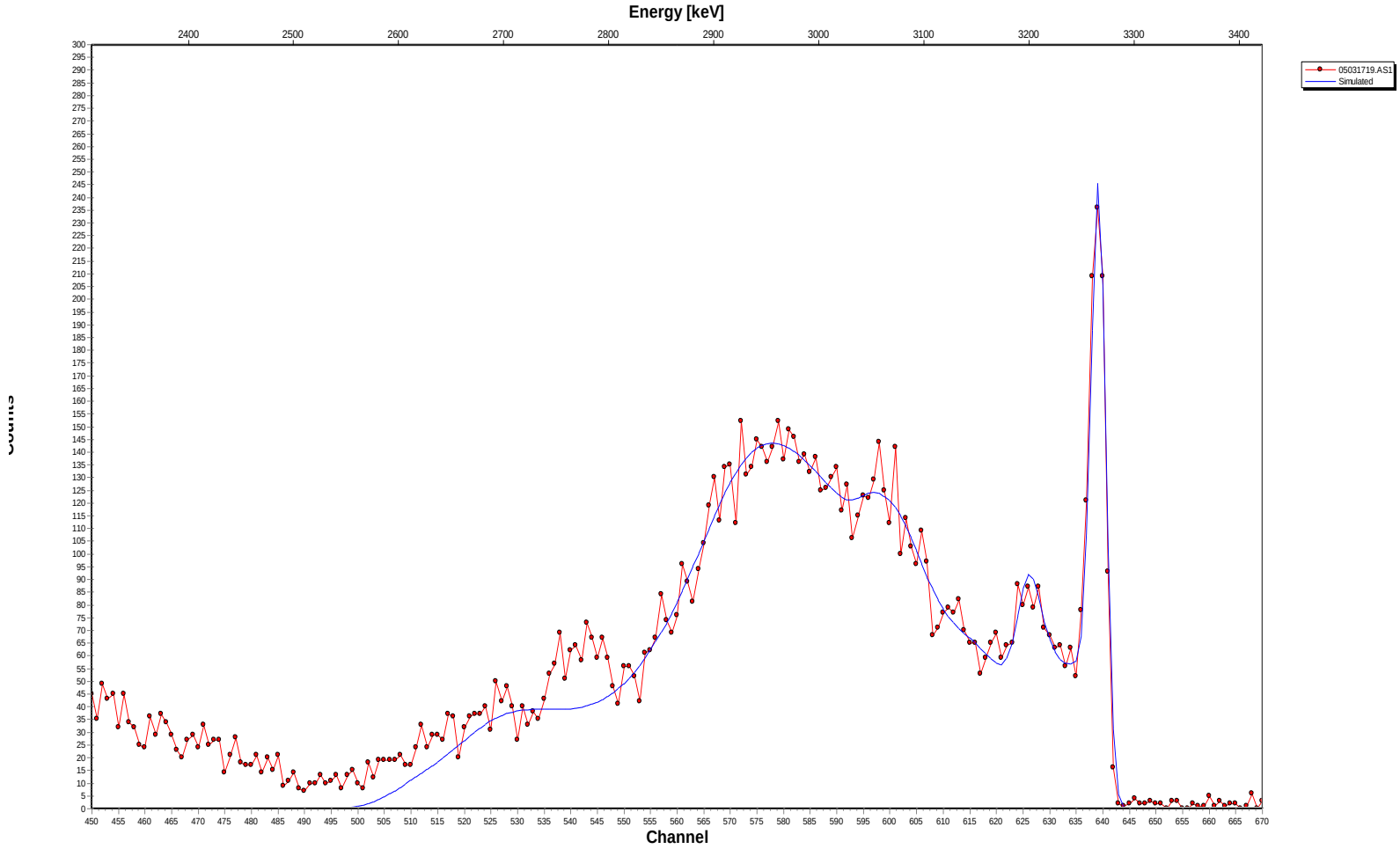

Figure 4.23 A typical NRA spectrum obtained from an unirradiated sample of T91 overlaid with the fit simulated with SimNRA.

CHAPTER 5: EXPERIMENTAL RESULTS

This chapter presents the results from the characterization of the ion irradiation experiments detailed in Chapter 4. The results are divided between the characterization acquired pertaining to two irradiation campaigns. The first irradiation campaign (**Table 4.2**), utilized samples which were not coated with alumina, and the second irradiation campaign (**Table 4.3)** used alumina-coated samples. The purpose of this coating was to prevent the uptake of carbon. For clarity, the first irradiation campaign, with uncoated samples, will be referred to as the Excess Carbon Campaign and the second irradiation campaign, with alumina-coated samples will be referred to as the Nominal Carbon Campaign. Chronologically, the Excess Carbon Campaign occurred before the Nominal Carbon Campaign, however the results for the Nominal Carbon Campaign are presented first as the results are less complex than the Excess Carbon Campaign results.

5.1 Nominal Carbon Campaign Cavity Results

As mentioned previously, the Nominal Carbon Campaign utilized samples with the surface coated with 100 nm of alumina. Cavities were observed at all damage and helium levels within the analysis regions. The cavities were profiled through the depth. As mentioned in Chapter 4, the valid regions of interest were limited to 400-800 nm from the surface. Divisions with a width of 200 nm consisted of 400-600, 500-700, and 600-800 nm. The nominal damage levels (600 nm depth) for the Coated Irradiation Campaign were 50, 150, and 300 dpa. Considering the three 200 nm depth widths for each of these experiments resulted in a total of nine valid damage levels: 45, 50, 58, 134, 150, 175, 276, 300, and 356 dpa.

Figure 5.1 shows representative HAADF STEM images of the T91 microstructure at 300 dpa and at all levels of helium pre-implantation. A generous population of cavities is evident within

the helium-implanted and ion-damaged region. **Figure 5.2** and **Figure 5.3** show how the cavity size, density, and swelling in T91 evolve at various damage and helium pre-implantation levels. Increasing the amount of helium from 0 to 1000 appm at any damage level resulted in an increase in cavity density and a decrease in diameter. The 0 appm He condition always exhibited the largest cavity size, which decreased monotonically with He up to 1000 appm. Swelling was highest in the low helium conditions (0, 1, and 10 appm), and was considerably suppressed in the 100 and 1000 appm conditions. **Table 5.1** summarizes the results of the cavity characterization, including the average size, densities, swelling, and sink strength at all damage levels and helium levels of 0, 1, 10, 100, and 1000 appm.

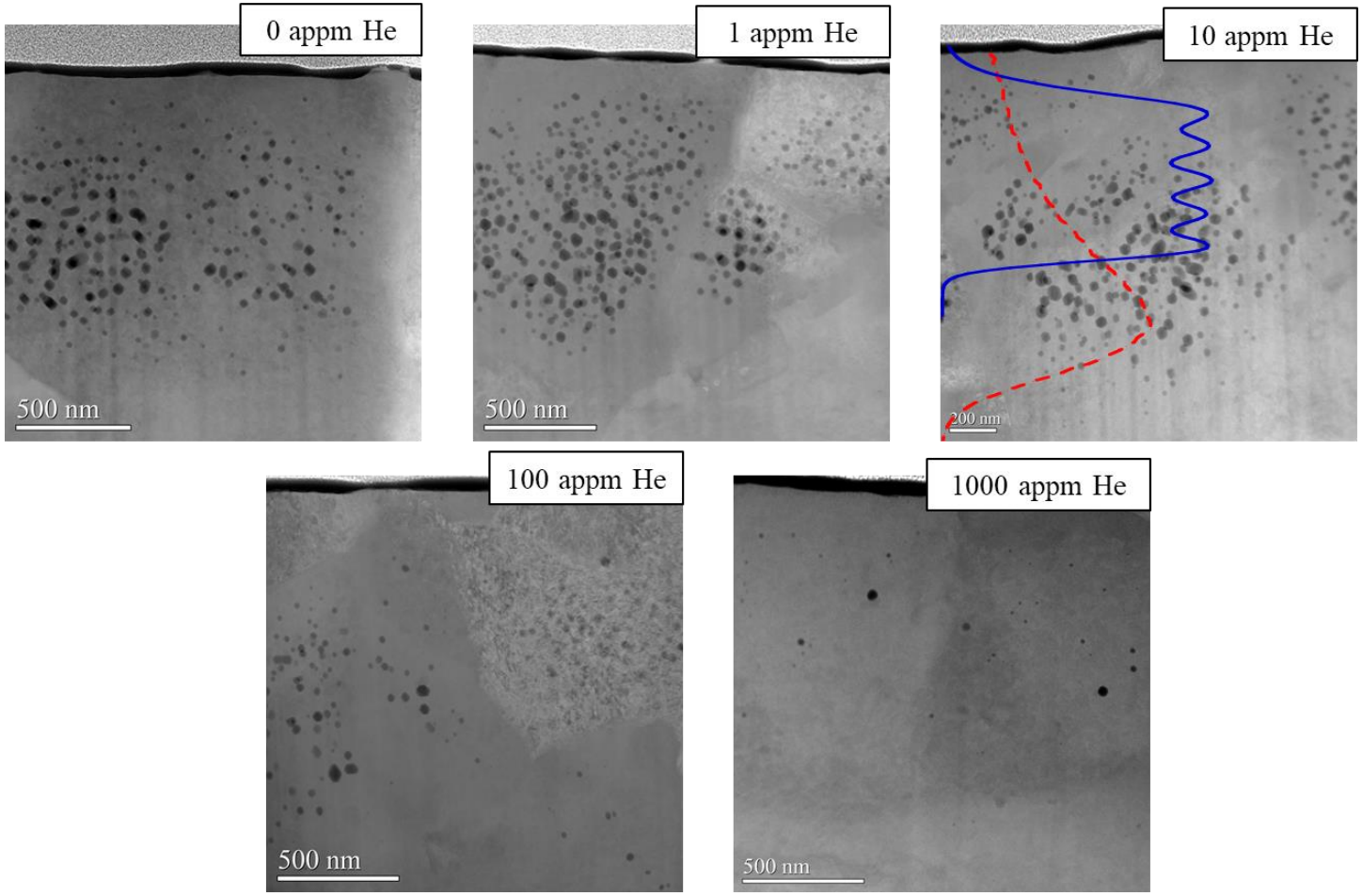

Figure 5.1 HAADF STEM images of T91 irradiated to 300 dpa with pre-implanted helium levels of 0, 1, 10, 100, and 1000 appm. The damage (dashed) and helium (solid) profiles are overlaid on the 10 appm He image.

Table 5.1 Summary of cavity results in T91 samples in the Nominal Carbon Campaign after ion irradiation for various combinations of damage and helium levels.

Damage level (dpa)	Depth of Analysis	Pre-Implanted He (appm)	Average Diameter (nm)	Cavity Density (10^{20} m^{-3})	Swelling (%)	Cavity Sink Strength (10^{14} m^{-2})
45	400-600nm	0	9.7	11.5	0.079	0.70
		1	8.6	19.5	0.098	1.05
		10	8.5	25.5	0.124	1.36
		100	3.2	85.7	0.048	1.72
		1000	1.6	904.0	0.061	9.09
50	500-700nm	0	10.1	11.7	0.091	0.74
		1	8.72	20.1	0.107	1.10
		10	8.5	24.2	0.124	1.29
		100	3.3	87.8	0.052	1.82
		1000	1.56	907.0	0.062	8.89
58	600-800nm	0	10.3	11.5	0.094	0.74
		1	8.9	19.9	0.114	1.11
		10	8.8	24.8	0.147	1.37
		100	3.3	87.2	0.051	1.81
		1000	1.6	908.0	0.065	9.13
134	400-600nm	0	17.0	17.8	0.67	1.90
		1	13.9	17.6	0.37	1.54
		10	13.3	23.6	0.44	1.97
		100	4.9	70.4	0.17	2.17
		1000	2.09	657.7	0.10	8.64
150	500-700nm	0	19.2	17.6	0.92	2.12
		1	15.3	20.7	0.58	1.99

		10	14.3	24.0	0.56	2.16
		100	5.07	72.4	0.20	2.31
		1000	2.1	658.6	0.11	8.69
175	600-800nm	0	21.2	17.7	1.1	2.36
		1	16.6	21.9	0.76	2.28
		10	15.5	23.0	0.65	2.24
		100	5.1	72.7	0.21	2.33
		1000	2.08	655.7	0.11	8.57
276	400-600nm	0	26.0	18.5	2.6	3.02
		1	25.5	21.3	2.9	3.41
		10	24.1	16.4	1.8	2.48
		100	4.8	61.6	0.44	1.86
		1000	1.79	757.7	0.12	8.52
300	500-700nm	0	29.3	20.1	3.9	3.70
		1	28.2	21.6	3.9	3.83
		10	26.4	18.9	2.7	3.14
		100	5.3	62.3	0.61	2.07
		1000	1.79	757.0	0.13	8.51
356	600-800nm	0	31.8	19.8	4.8	3.96
		1	30.3	19.7	4.2	3.75
		10	28.8	19.3	3.5	3.49
		100	5.7	63.3	0.78	2.27
		1000	1.80	755.8	0.15	8.55

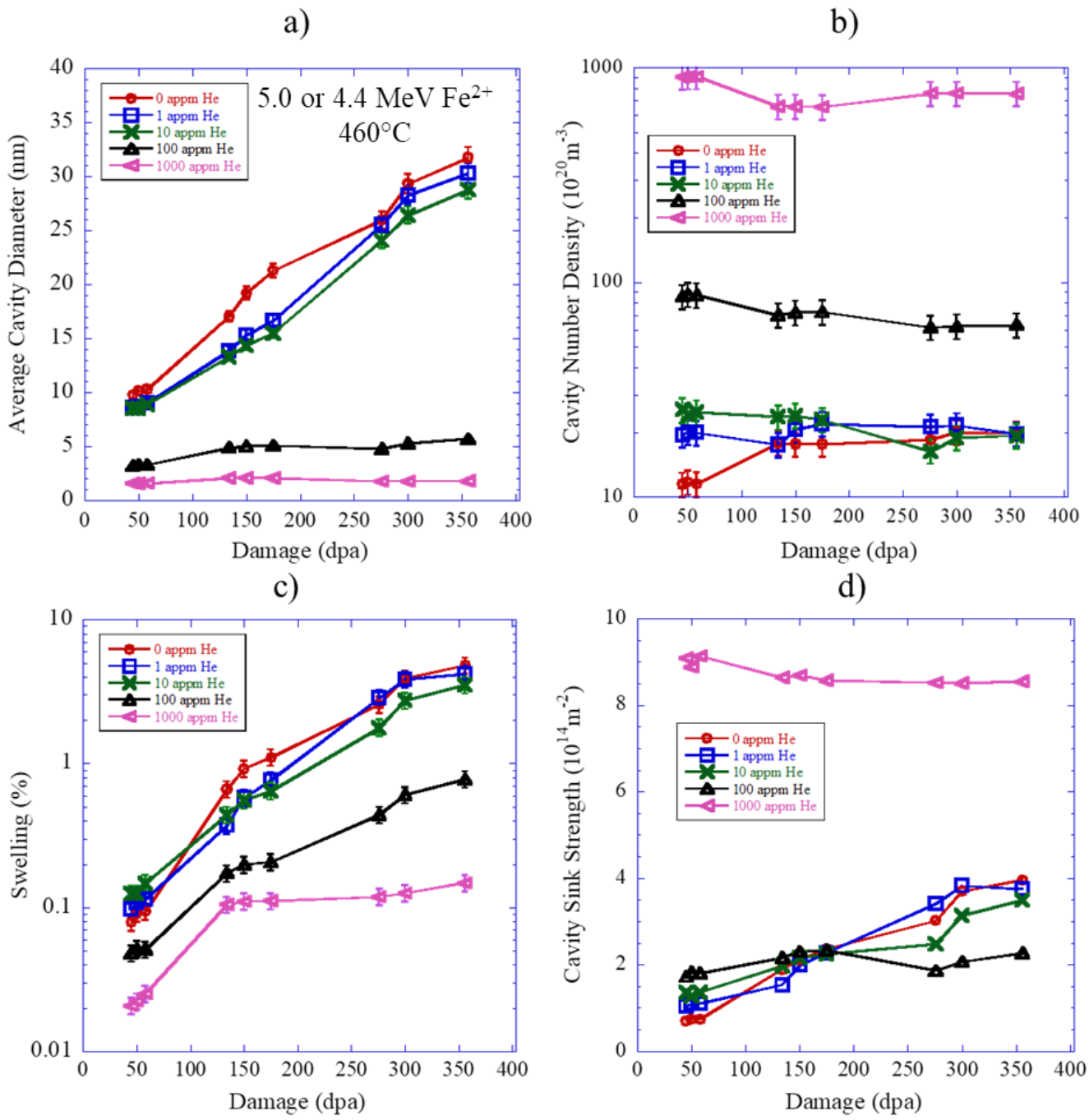

Figure 5.2 a) Average cavity diameter b) number density, c) swelling and d) cavity sink strength as a function of damage in T91 for pre-implanted He levels of 0, 1, 10, 100, and 1000 appm.

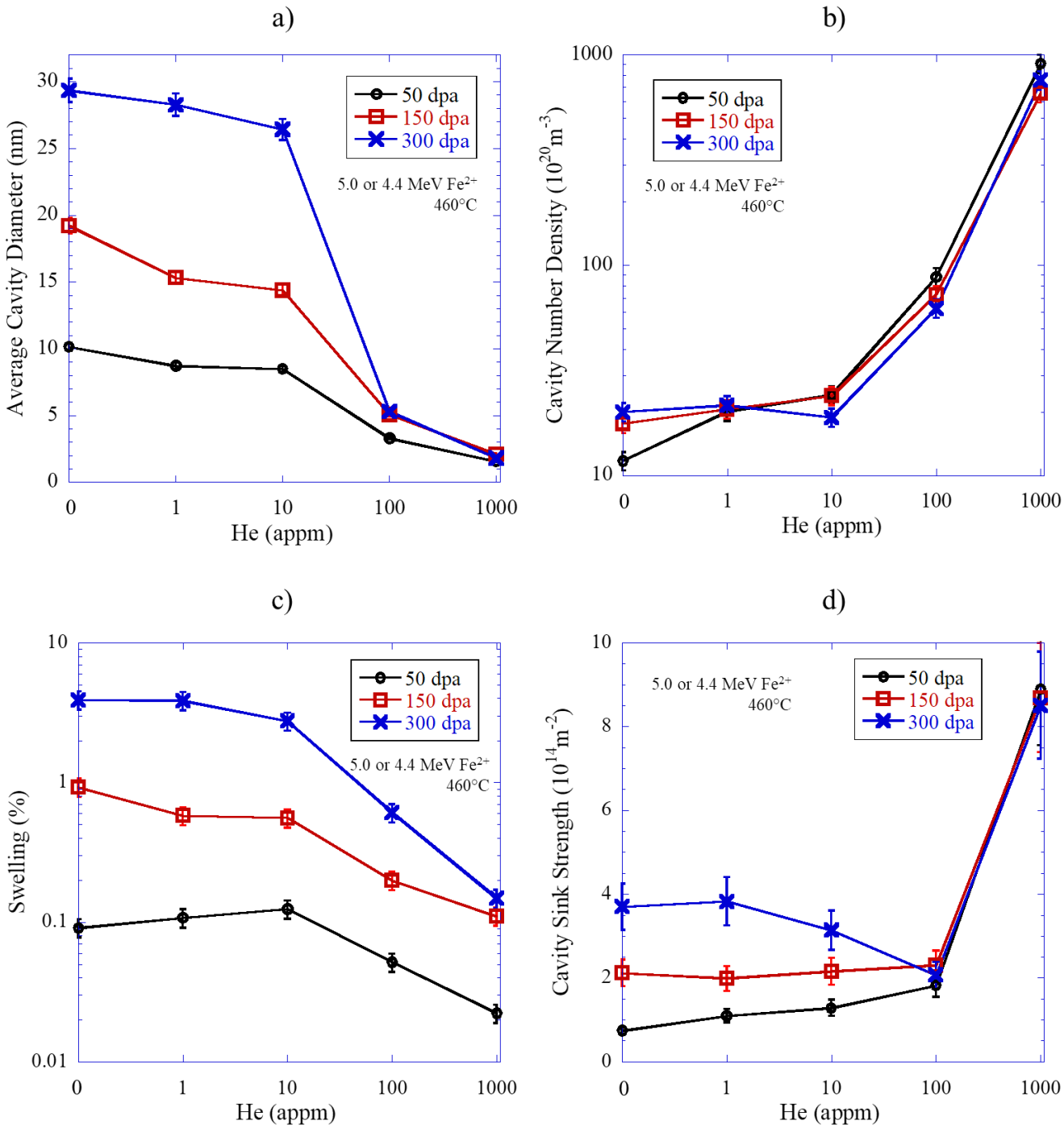

Figure 5.3 a) Average cavity diameter b) number density, c) swelling and d) sink strength as a function of helium concentration for 50, 150, and 300 dpa.

5.1.1 Low Damage, Low Helium Regime

At low damage (50 dpa) and low helium levels (0, 1, 10 appm He), similar cavity sizes were observed. The 0 appm He condition had the highest size at about 10.3 nm, closely followed by the 1 and 10 appm conditions (8.9 and 8.8nm, respectively). The main difference between these helium conditions at low damage levels was in the cavity density. Density increased with helium content, with the biggest difference occurring between the un-implanted case, and the 1 appm He case. The 10 appm He condition exhibited a density of ~25 x 10^{20} m^{-3}, the 1 appm a slightly lower density of ~20 x 10^{20} m^{-3}, and then the 0 appm He case had the lowest value of ~11.5 x 10^{20} m^{-3}.

5.1.2 High Damage, Low Helium Regime

As the damage level was increased to the high damage regime (150 and 300 dpa), the cavity size distributions for the 0, 1, 10 appm He conditions began to converge. **Figure 5.4** shows how the cavity distributions evolved with damage. The size distributions of these three helium conditions all followed a single, roughly Gaussian profile. Differences between the helium levels are noticeable at low damage (50 dpa), but by 300 dpa the distributions appear very similar. Despite having different helium levels, very similar final cavity densities and sizes were observed between the 0, 1, and 10 appm conditions at 300 dpa (20.1, 21.6, and 18.9 x 10^{20} m^{-3}, and 29.3, 28.2, and 26.4 nm, respectively). **Figure 5.5** shows representative images of the cavity evolution of the 0, 1 and 10 appm He conditions. Differences in the cavity densities are apparent in the 50 dpa condition, however by 300 dpa, the microstructures and distributions were almost indistinguishable (**Figure 5.4**).

Throughout the entire damage range, the 0 appm He condition maintained a slightly larger cavity size (**Figure 5.2a**). However, by 150 dpa the cavity density in the 0 appm He case caught up to that of the 1 and 10 appm conditions (**Figure 5.2b**), confirming that it was still in the nucleation phase at 50 dpa. Beyond 150 dpa, no significant increases in cavity density were observed for the 0, 1, and 10 appm helium conditions. In fact, over the entire damage range studied, only the 0 appm helium condition showed any sign of cavity density dependence on dpa, and this was between 50 and 150 dpa. For any amount of He, there was no significant change in density with damage (**Figure 5.2b**), indicating that in any pre-implantation condition, the final cavity density was determined very early in the irradiation (< 50 dpa).

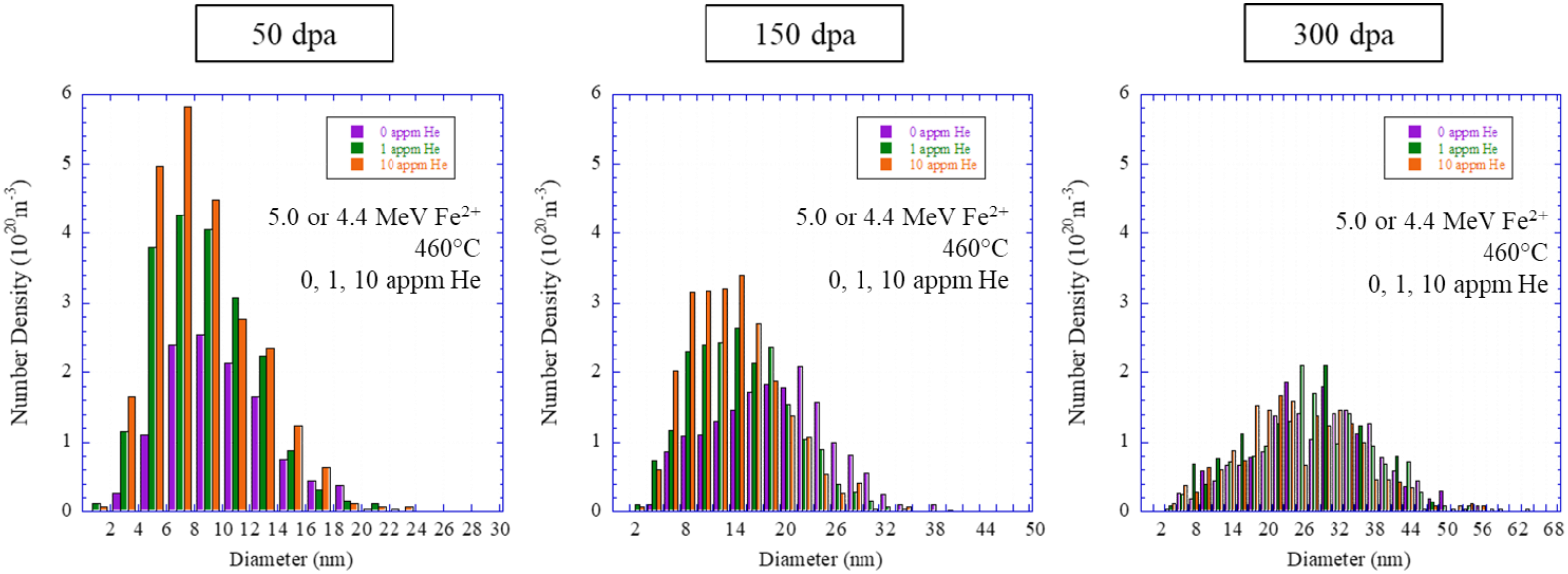

Figure 5.4 Cavity size distributions for the 0, 1, and 10 appm He conditions in T91 at 50, 150, and 300 dpa (500-700 nm depth).

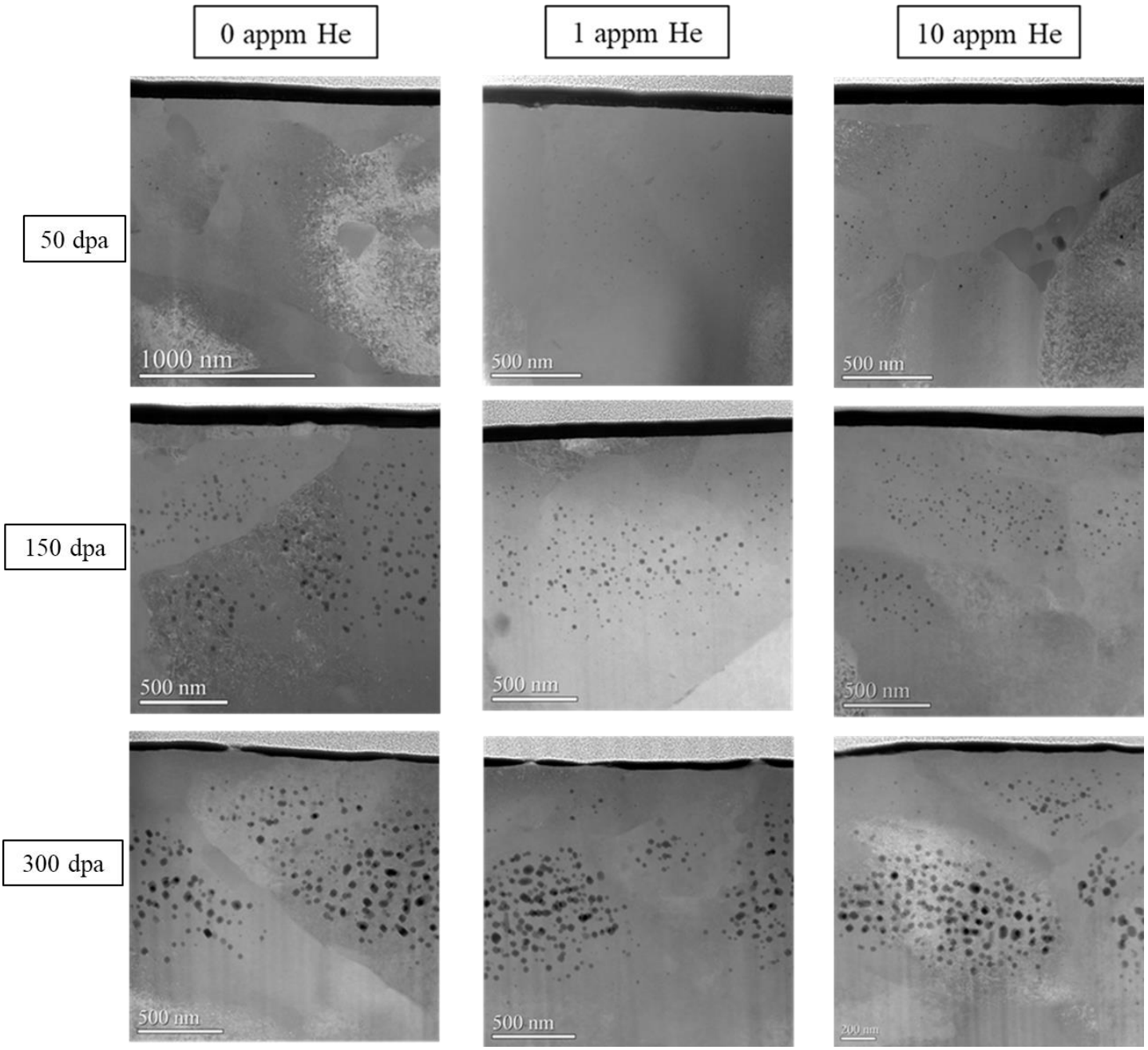

Figure 5.5 HAADF STEM images showing the evolution of the T91 microstructure with damage for the 0, 1, and 10 appm He conditions at 460ºC.

5.1.3 High Helium Regime

Inspection at high magnifications revealed the presence of an extremely high density of very small cavities in the 100 and 1000 appm He conditions at all damage levels. **Figure 5.6** shows high magnification images of T91 irradiated at 150 dpa for all helium levels. The 100 appm He condition contained some very small cavities (< ~4nm), and the 1000 appm He condition shows the highest density of these cavities. Cavities in this size range were not observed in any helium condition lower than 100 appm. Because of local variation, characterization of these small cavities in the 100 and 1000 appm conditions was difficult to perform as a function of depth. Therefore, measurements of the maximum observed cavity densities in the 500-700nm region were used to estimate the maximum swelling contribution of the small cavities. The resulting densities and swelling values are summarized in **Table 5.1** for the 100 and 1000 appm conditions.

The presence of these small cavities in the 100 and 1000 appm He conditions resulted in bimodal cavity distributions. The evolution of these distributions with damage is shown in **Figure 5.7**. Both 100 and 1000 appm He conditions exhibit high cavity densities of sizes < ~4 nm, with the 1000 appm He condition having a noticeably higher density than that of the 100 appm He. These small cavities appeared to be insensitive to damage, as their densities remained relatively unchanged from 45 to 356 dpa (**Figure 5.2b**). At the larger sizes, it is evident that a small amount of growth occurred, as the tails of the distributions in **Figure 5.7** extended to higher sizes at higher damage levels. The limited growth was slightly higher in the 100 appm He condition increasing from 3.2nm to 5.7nm, while the 1000 appm He only increased from 1.2 nm to 1.8 nm with the addition of ~300 dpa. These very low amounts of growth resulted in minimal swelling, even at high damage levels (**Figure 5.2c**).

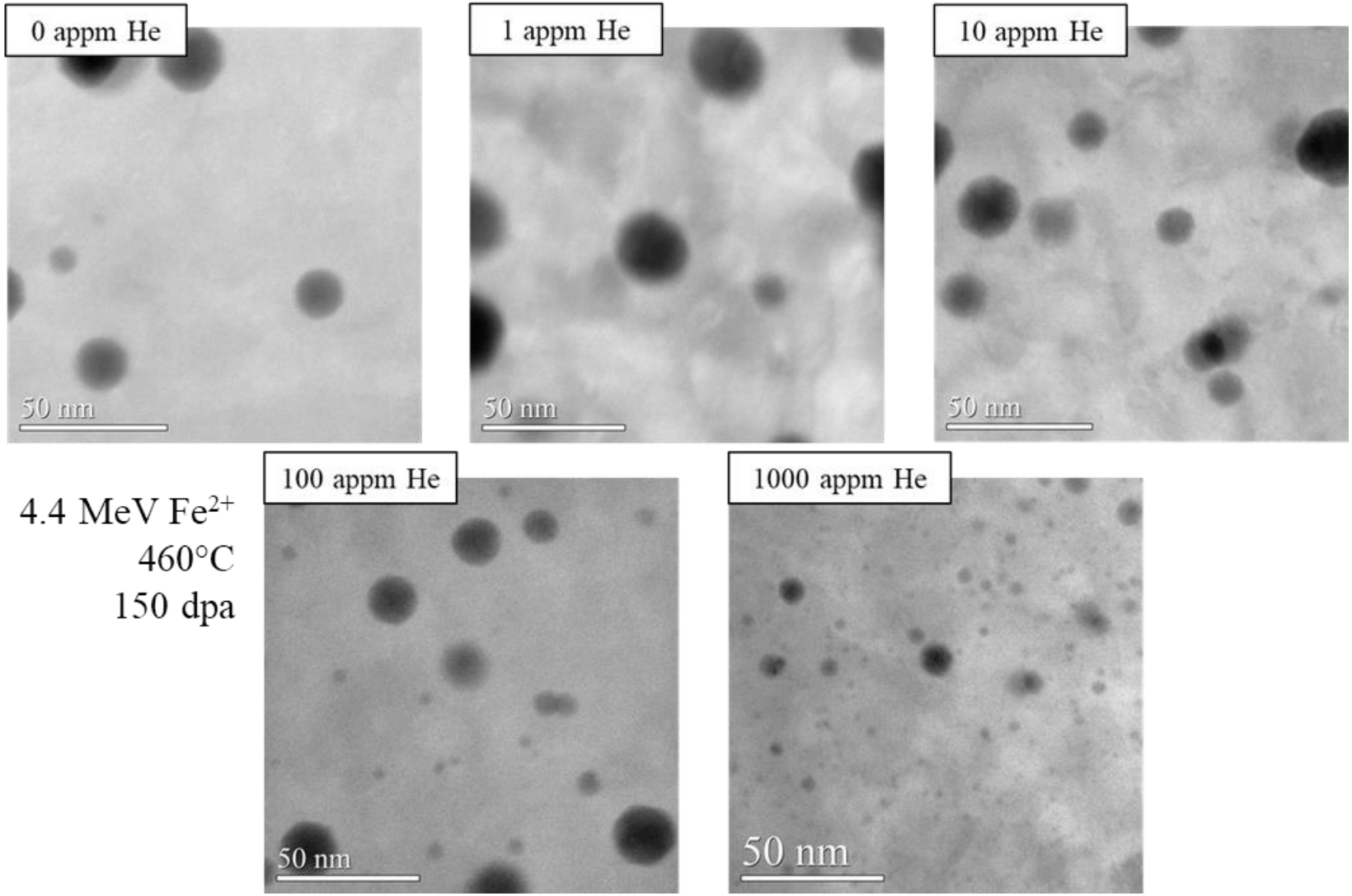

Figure 5.6 High magnification (1Mx) HAADF STEM images of T91 irradiated to 150 dpa (500-700 nm depth) with pre-implanted helium levels of 0, 1, 10, 100, and 1000 appm.

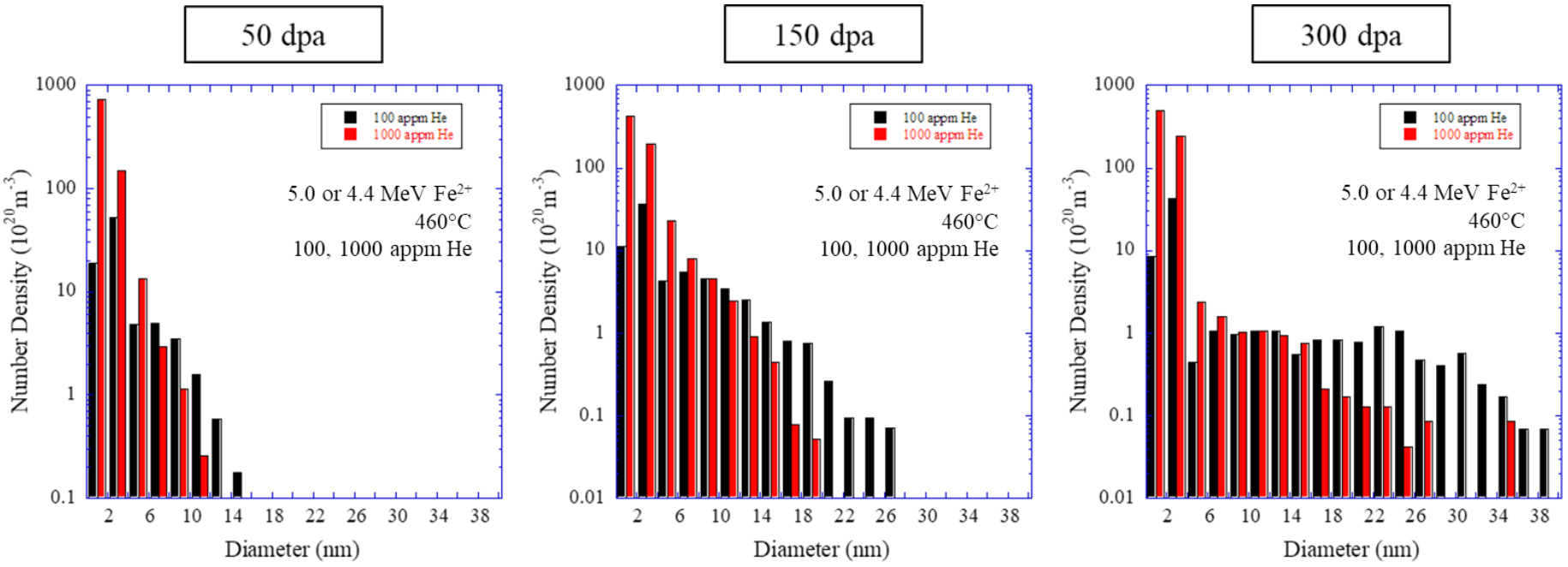

Figure 5.7 Cavity size distributions for the 100 and 1000 appm He conditions at 50, 150, and 300 dpa (500-700 nm depth).

5.3 Nominal Carbon Campaign Dislocations and Precipitates

The loop diameter and densities, along with representative images, at 50, 150, and 300 dpa are shown in **Figure 5.8** for the 10 appm He condition. For both **b**<100> and ½ **b**<111> loops, a higher density was observed at 50 dpa, which dropped by 150 dpa and stabilized through 300 dpa. Both types of loops also experienced a small amount of growth from 50 to 300 dpa. Overall, **b**<100> loops were observed in a higher density by 3-4 times, and about twice the size of ½ **b**<111> loops at any given damage level.

<100> loops were also measured as a function of helium content. **Figure 5.9** shows how the loop diameter and density varied with helium content at 150 dpa. For all of the pre-implanted cases, the loop diameter ranged between 21 and 29 nm at 150 dpa, with no obvious trend appearing as helium content was increased. A similar case was seen with the loop density, which ranged between 19 and 25 x 10^{20} m^{-3}. The un-implanted (0 appm He) condition exhibited a slightly larger loop size of 36.3 nm.

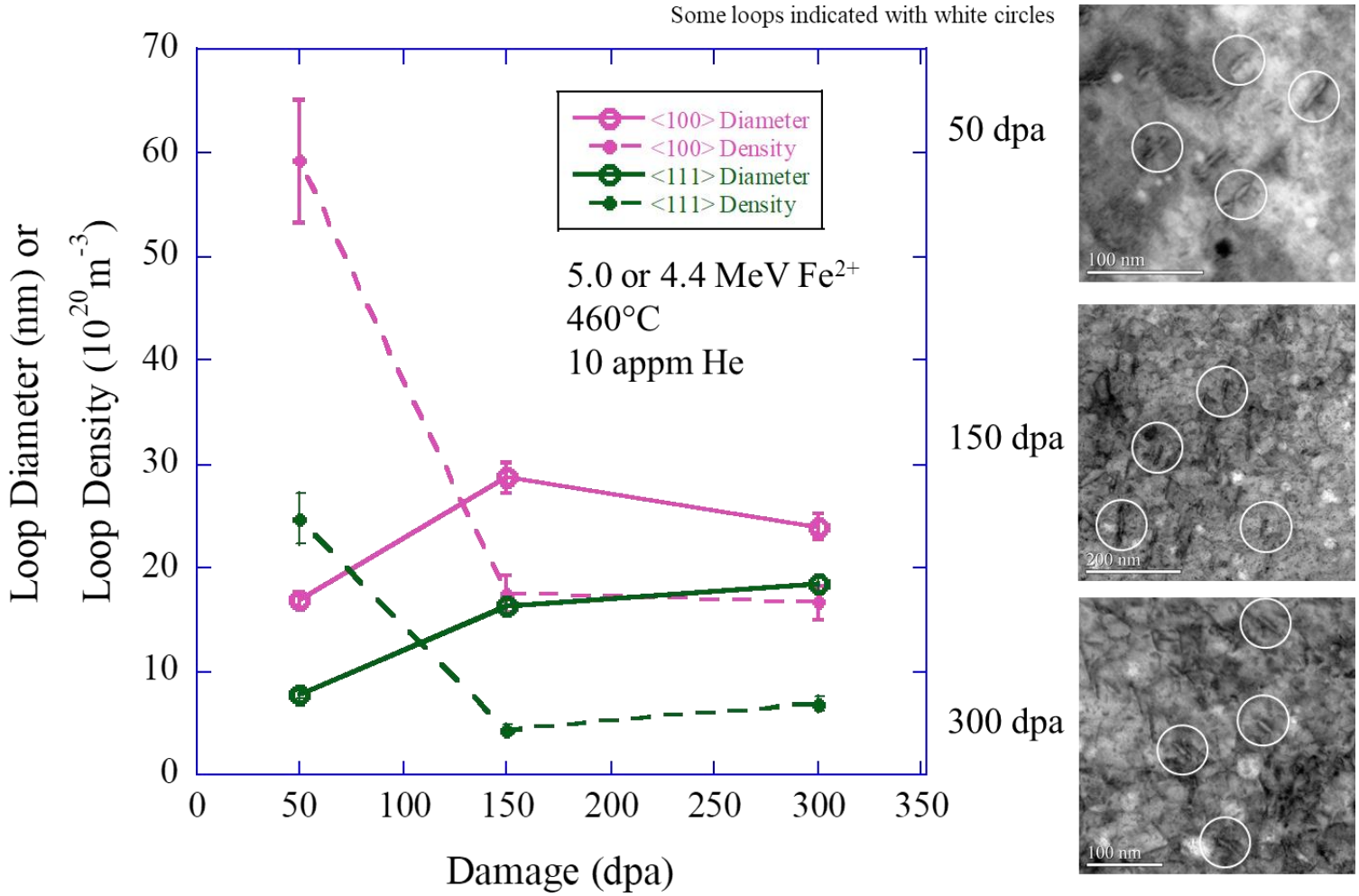

Figure 5.8 Dislocation loop densities and diameters for b<100> and ½ b<111> loops are plotted as a function of damage for the 10 appm He condition. Some loops are indicated in the images with white circles

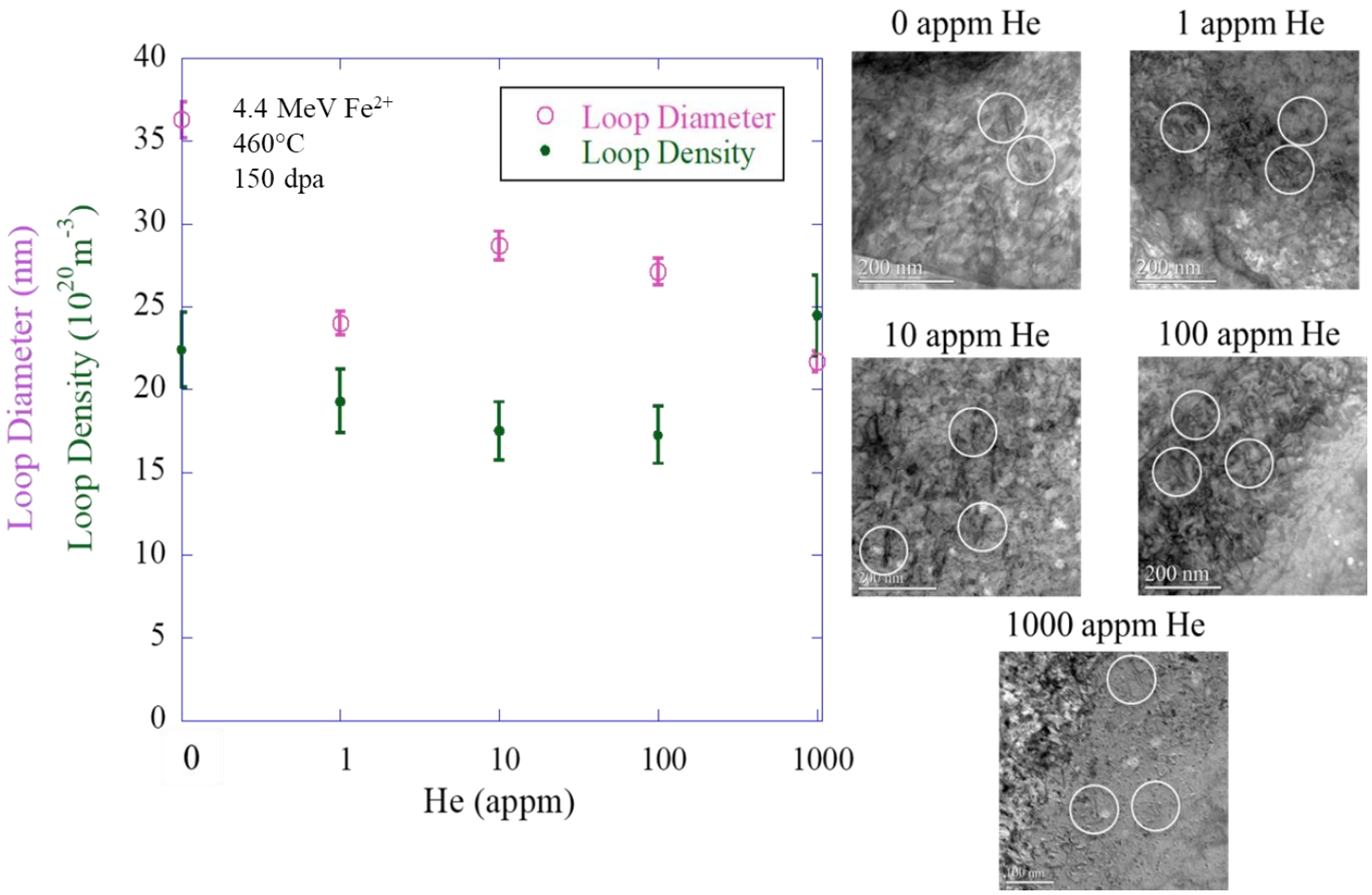

Figure 5.9 Densities and diameters for b<100> dislocation loops are plotted as a function of helium content at 150 dpa. Some loops are indicated in the images with white circles.

The dislocation network showed an even lower sensitivity to helium. Across the full spectrum of helium concentration, the dislocation network density ranged from 2.2 to 4.2 x 10^{14} m^{-2}, well within any measurement error.

Figure 5.10a shows how <100> loop line length, dislocation network, and total line length varied with helium content at 150 dpa. The total line length remained insensitive to He content and varied between 6-7 x $10^{14}m^{-2}$ for the pre-implanted cases, and was slightly higher for the 0 appm He condition. A comparison of the total line length to the cavity sink strengths at 150 dpa for all helium levels is shown in **Figure 5.10b**. The ratio of sink strengths falls above 1 for the 0-100 appm He conditions, indicating a dislocation dominant microstructure. For 1000 appm, the ratio falls slightly below 1, suggesting a cavity dominant microstructure. All of the results for the dislocation loops and network are summarized in **Table 5.2**.

The evolution of Ni-Si rich clusters (G-phase) with damage and 10 appm He implanted is shown in **Figure 5.11**. **Table 5.2** summarizes the measured size, density, volume fraction, and sink strength of G-phase. As the damage level increased, the precipitates experienced an increase in size and decrease in density. In addition to this coarsening effect, addition Ni and Si segregated to the clusters, resulting in an increase in the total volume fraction up to about 0.04% by 300 dpa. The sink strength for G-phase remained low, ranging from 0.36 to 0.58 x $10^{14}m^{-2}$.

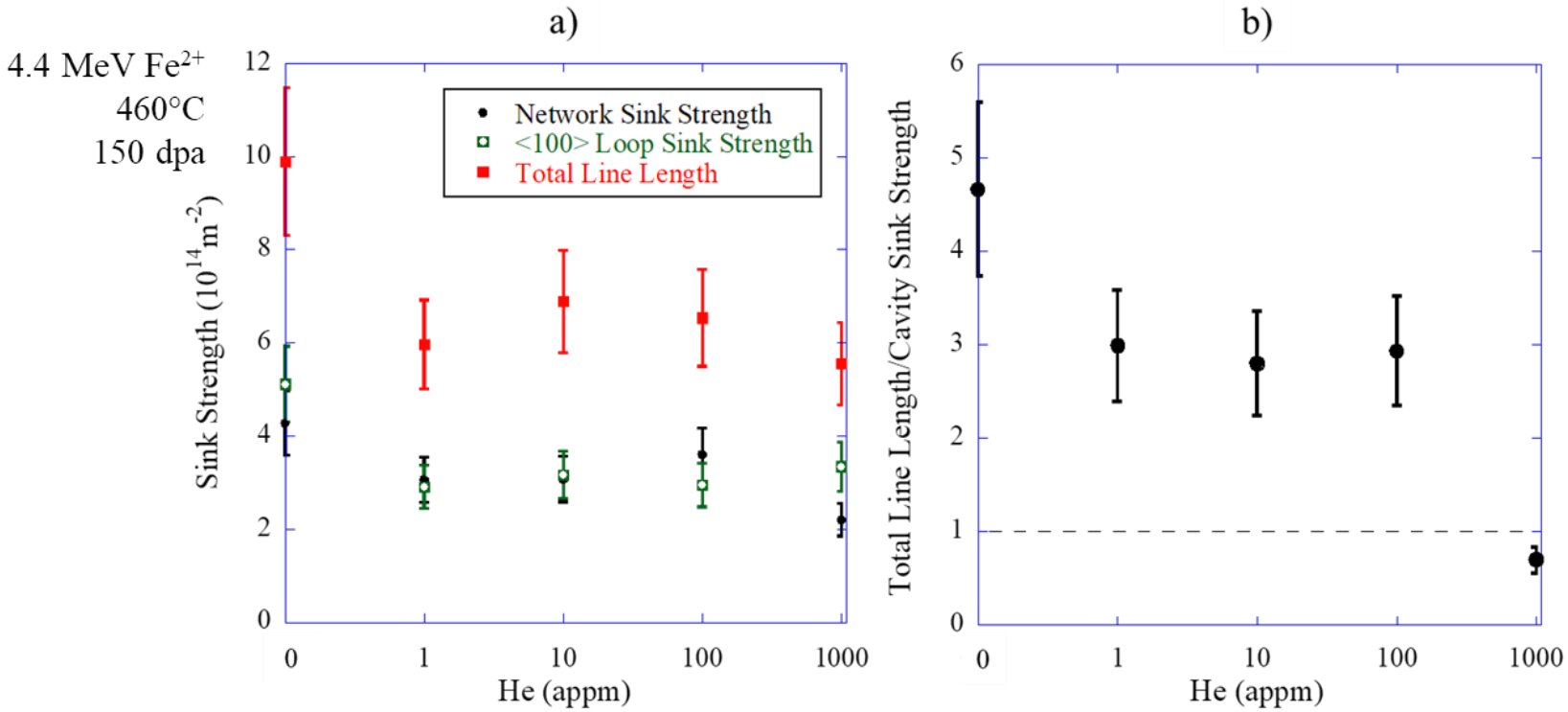

Figure 5.10 a) Network and <100> loop sink strength are plotted along with the total line length and b) ratio of total line length to cavity sink strength as a function of helium content at 150 dpa.

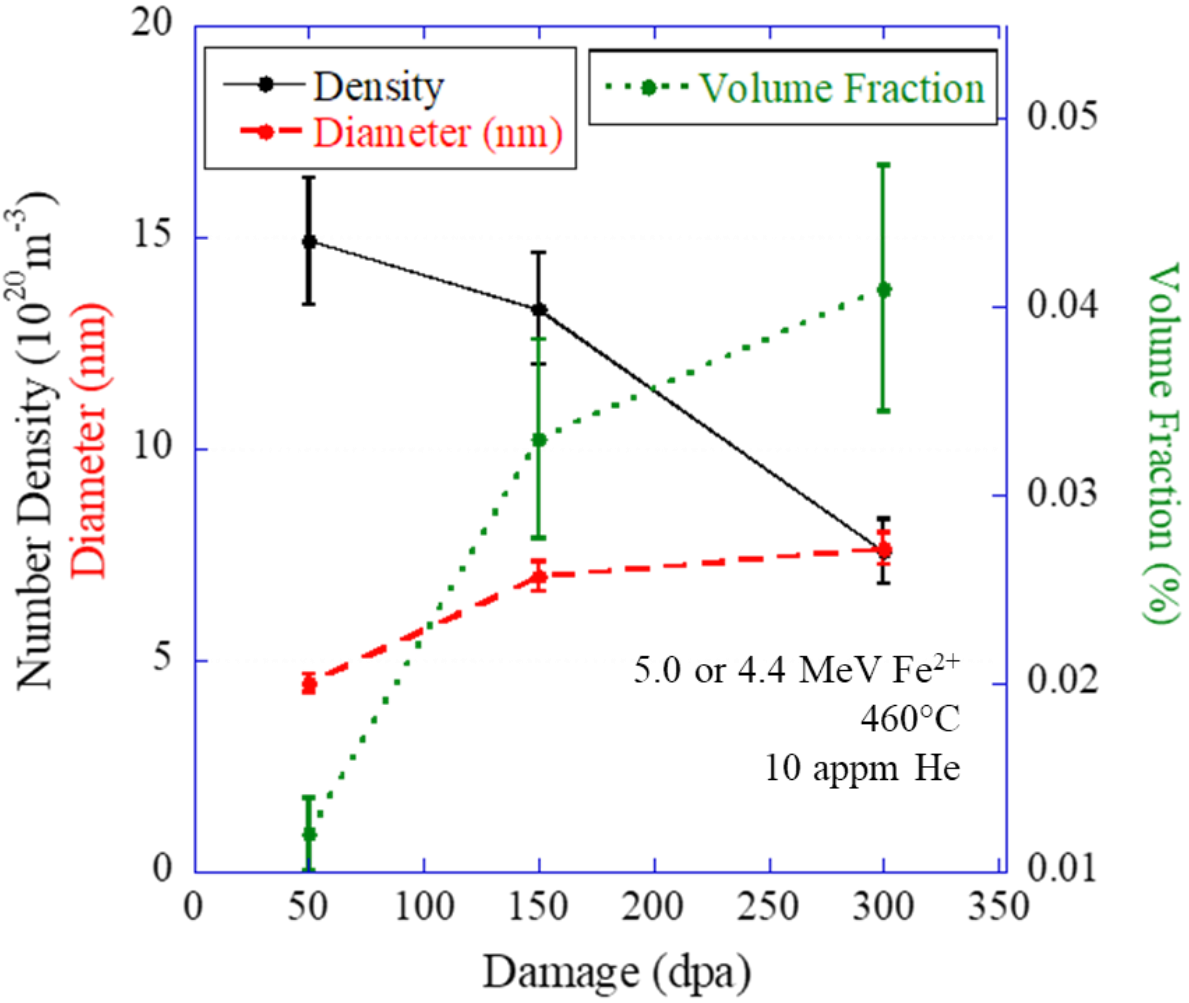

Figure 5.11 Number density, diameter, and volume fraction of G-phase plotted as a function of damage with 10 appm He pre-implanted in ion-irradiated T91.

Table 5.2 A summary of dislocation loops, dislocation network, and G-phase.

Damage level (dpa)	Pre-Implanted He (appm)	<100> Loop Diameter (nm)	<100> Loop Density (10^{20} m^{-3})	<111> Loop Diameter (nm)	<111> Loop Density (10^{20} m^{-3})	Network Density (10^{14} m^{-2})	Total Dislocation Sink Strength (10^{14} m^{-2})	G-phase Diameter (nm)	G-phase Density (10^{20} m^{-3})	G-phase Volume Fraction (%)	G-phase Sink Strength (10^{14} m^{-2})
50	10	16.9	59.3	7.9	24.8	3.04	10.6	4.5	14.9	0.012	0.42
150	0	36.3	22.4	N.M.	N.M.	4.27	9.88	N.M.	N.M.	N.M.	0.45
	1	24.0	19.2	N.M.	N.M.	3.05	5.96	N.M.	N.M.	N.M.	0.55
	10	28.7	17.5	16.4	4.4	3.07	6.88	7.0	13.3	0.033	0.58
	100	27.1	17.2	N.M.	N.M.	3.59	6.53	N.M.	N.M.	N.M.	0.42
	1000	21.6	24.4	N.M.	N.M.	2.2	5.54	N.M.	N.M.	N.M.	0.35
300	10	24.0	16.7	18.4	6.9	2.45	5.67	7.6	7.57	0.041	0.36

5.4 Excess Carbon Campaign

As mentioned previously, the Excess Carbon Campaign utilized uncoated, or bare samples which were susceptible to carbon uptake. The details of the irradiation and the conditions characterized are presented in **Chapter 4** in **Table 4.3**. Cavities were characterized for all conditions. As before, the three depth regions within the sample were characterized 400-600, 500-700, and 600-800 nm. The nine damage levels characterized for cavities in this campaign were: 134, 150, 175, 276, 300, 356, 414, 450, and 534 dpa. Carbide precipitates were characterized with 10 appm He implanted (at all nominal damage levels, 150, 300, and 450 dpa), and at all helium levels at 300 and 450 dpa (0, 1, 10, 100, and 1000 appm He) to achieve both a helium and damage dependence. Dislocations were characterized for only the 10 appm He condition and for damage levels of 150 and 300 dpa. A very high density of carbides made dislocation imaging at 450 dpa extremely difficult and accurate measurements could not be made. For the same reason, G-phase or G-phase precursors could not be characterized in the excess carbon conditions.

5.5 Excess Carbon Campaign Cavity Results

Cavities were observed at all damage and helium levels. Higher levels of pre-implanted helium resulted in higher cavity densities and lower cavity sizes. The swelling increased with increasing He content up to 10 appm He, after which the swelling decreased with further increases in He content. The evolution of cavity size, density, swelling, and sink strength as a function of damage and helium are shown in **Figure 5.12** and **Figure 5.13**, respectively. These values, along with the cavity sink strengths are summarized in **Table 5.3**. The cavity sink strengths were calculated as described in **Chapter 4**.

Table 5.3 Summary of cavity results in T91 in excess carbon samples after ion irradiation for all damage levels and helium levels.

Damage level (dpa)	Depth of Analysis	Pre-Implanted He (appm)	Average Diameter (nm)	Cavity Density (10^{20} m^{-3})	Swelling (%)	Cavity Sink Strength (10^{14} m^{-2})
134	400-600nm	0	15.6	1.84	0.047	0.36
		1	15.6	9.0	0.23	1.76
		10	13.2	19.2	0.29	3.18
		100	9.8	9.6	0.063	1.18
		1000	1.44	511	0.018	9.25
150	500-700nm	0	15.8	2.2	0.056	0.44
		1	16.5	8.64	0.250	1.79
		10	14.2	18.0	0.34	3.21
		100	10.3	11.7	0.095	1.51
		1000	1.44	511	0.018	9.25
175	600-800nm	0	16.7	3.27	0.099	0.69
		1	17.0	9.90	0.32	2.11
		10	14.9	17.6	0.39	3.30
		100	10.4	12.2	0.103	1.59
		1000	1.44	510.0	0.016	9.23
276	400-600nm	0	24.1	2.77	0.26	0.84
		1	23.0	5.74	0.45	1.66
		10	21.6	12.5	0.88	3.39
		100	16.2	10.6	0.33	2.16
		1000	2.29	146	0.036	4.20
300	500-700nm	0	26.6	3.42	0.43	1.14
		1	25.6	6.58	0.73	2.12
		10	22.3	13.2	1.02	3.70
		100	17.3	10.7	0.41	2.33

		1000	2.30	147	0.043	4.25
356	600-800nm	0	27.9	3.98	0.58	1.40
		1	26.5	7.53	0.95	2.51
		10	23.0	14.3	1.24	4.13
		100	18.0	11.3	0.49	2.56
		1000	2.30	147	0.044	4.25
414	400-600nm	0	24.6	2.29	0.24	0.71
		1	28.3	9.04	1.47	3.21
		10	26.0	9.50	1.25	3.10
		100	23.0	7.92	0.67	2.29
		1000	13.9	0.28	0.004	0.05
450	500-700nm	0	27.8	2.63	0.42	0.92
		1	30.5	9.35	1.88	3.58
		10	28.0	10.3	1.65	3.62
		100	23.4	8.37	0.80	2.46
		1000	16.9	0.46	0.013	0.10
534	600-800nm	0	28.6	3.21	0.58	1.15
		1	31.8	10.6	2.50	4.24
		10	28.5	10.3	1.76	3.69
		100	25.2	9.48	1.14	3.00
		1000	16.4	0.51	0.014	0.11

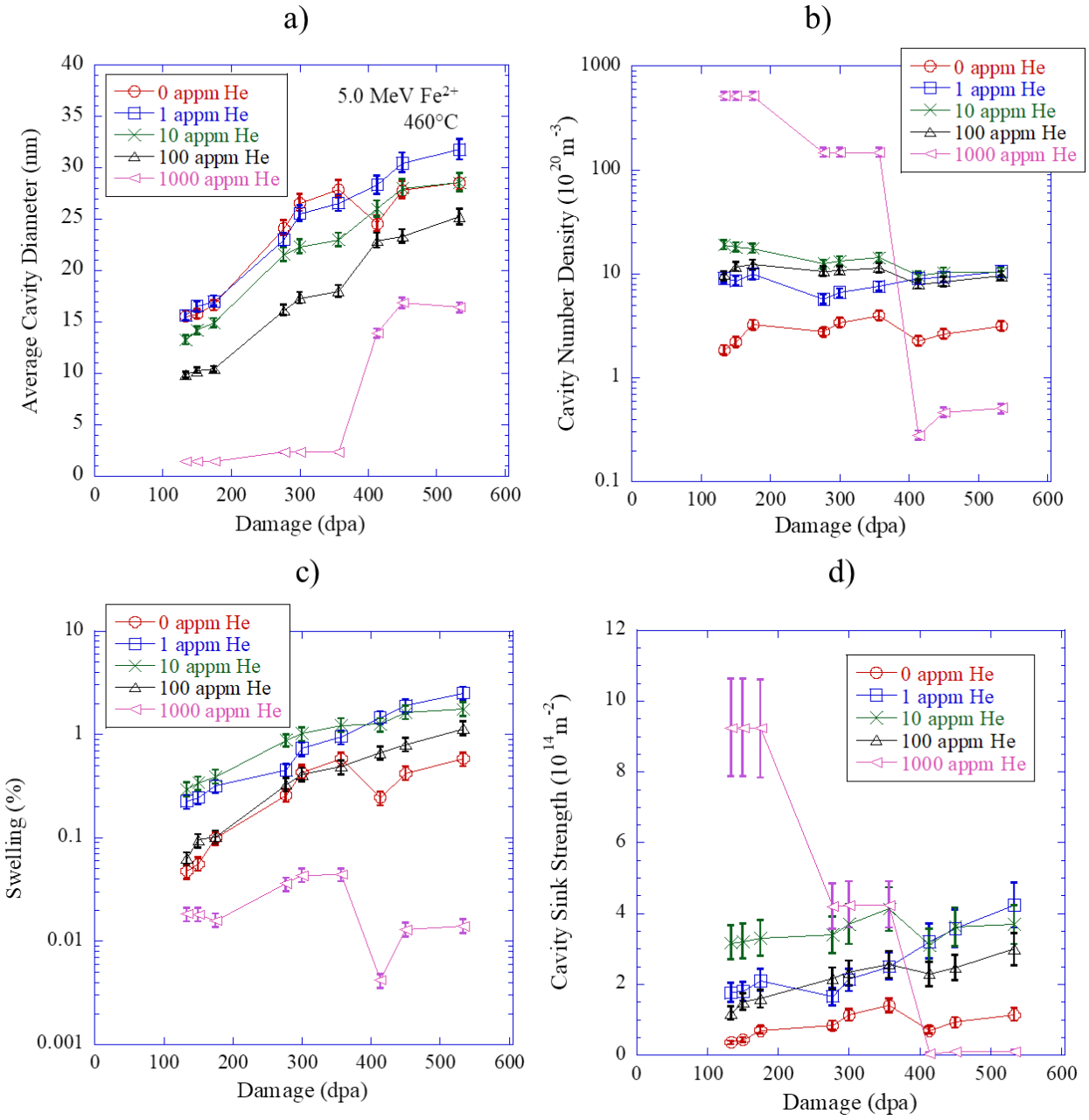

Figure 5.12 a) Average cavity diameter b) number density, c) swelling and d) cavity sink strength as a function of damage in T91 for pre-implanted He levels of 0, 1, 10, 100, and 1000 appm irradiated with 5 MeV Fe2+ ions at 460°C.

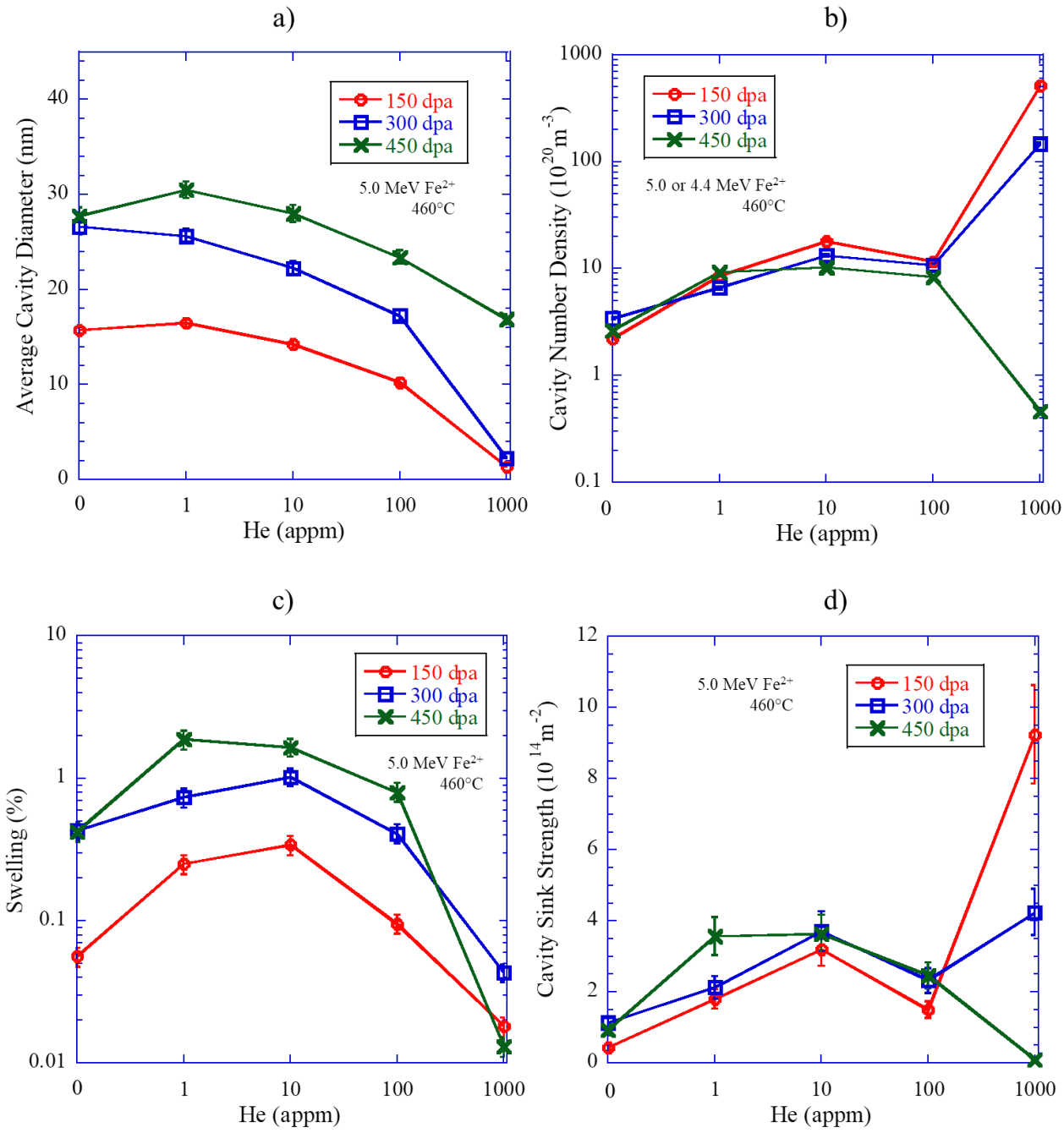

Figure 5.13 a) Average cavity diameter b) number density, c) swelling and d) cavity sink strength as a function of helium content in T91 for damage levels of 150, 300, and 450 dpa.

Figure 5.14 shows representative HAADF STEM images of the cavity evolution for all of the implanted He conditions. The resulting cavity distributions are plotted in **Figure 5.15** for the 0, 1, and 10 appm He conditions, and in **Figure 5.16** for the 100 and 1000 appm He conditions. As seen in **Figure 5.13b**, the cavity densities for all of the helium conditions, except for the 1000 appm condition, did not dramatically change in the entire observed damage range, from 134-534 dpa. The 0 appm He condition exhibited the lowest cavity density at all damage levels, ranging from ~2-3 x 10^{20} m^{-3} over the entire damage range. The cavity density increased with increasing helium content, with the 1 appm He cavity density ranging between 6-10 x 10^{20} m^{-3} and the 10 appm He density ranging between 9-19 x 10^{20} m^{-3}. The 100 appm He condition did not exhibit significantly higher cavity densities than the lower helium levels, ranging between 9-12 x 10^{20} m^{-3}.

In general, all He conditions exhibited increases in the average cavity size with increasing damage. From 150 to 300 dpa, cavity sizes were the largest for the 0 and 10 appm He conditions (**Figure 5.13a**), however, the 0 appm He condition did not exhibit significantly increased growth from 300 to 450 dpa, and thus experienced a stagnation in swelling behavior (**Figure 5.12c**).

The 1000 appm He condition exhibited extremely high densities of small cavities up to ~300 dpa. The high density of small cavities (<~4 nm) was only visible at high magnifications. Cavities of this size were not observed in any other helium condition. These cavities resulted in the formation of a bimodal distribution in the 1000 appm He condition, seen in **Figure 5.16**. **Figure 5.17** shows high magnification images of the 1000 appm He condition at 150, 300, and 450 dpa. The presence of these very small cavities was observed at 150 and 300 dpa, but not at 450 dpa. The sudden loss of the population of small cavities resulted in a dramatic drop in cavity density (**Figure 5.12b**) and a corresponding increase in the average cavity size (**Figure 5.12a**). The swelling in the 1000 appm He condition remained very low at all damage levels (**Figure 5.13c**).

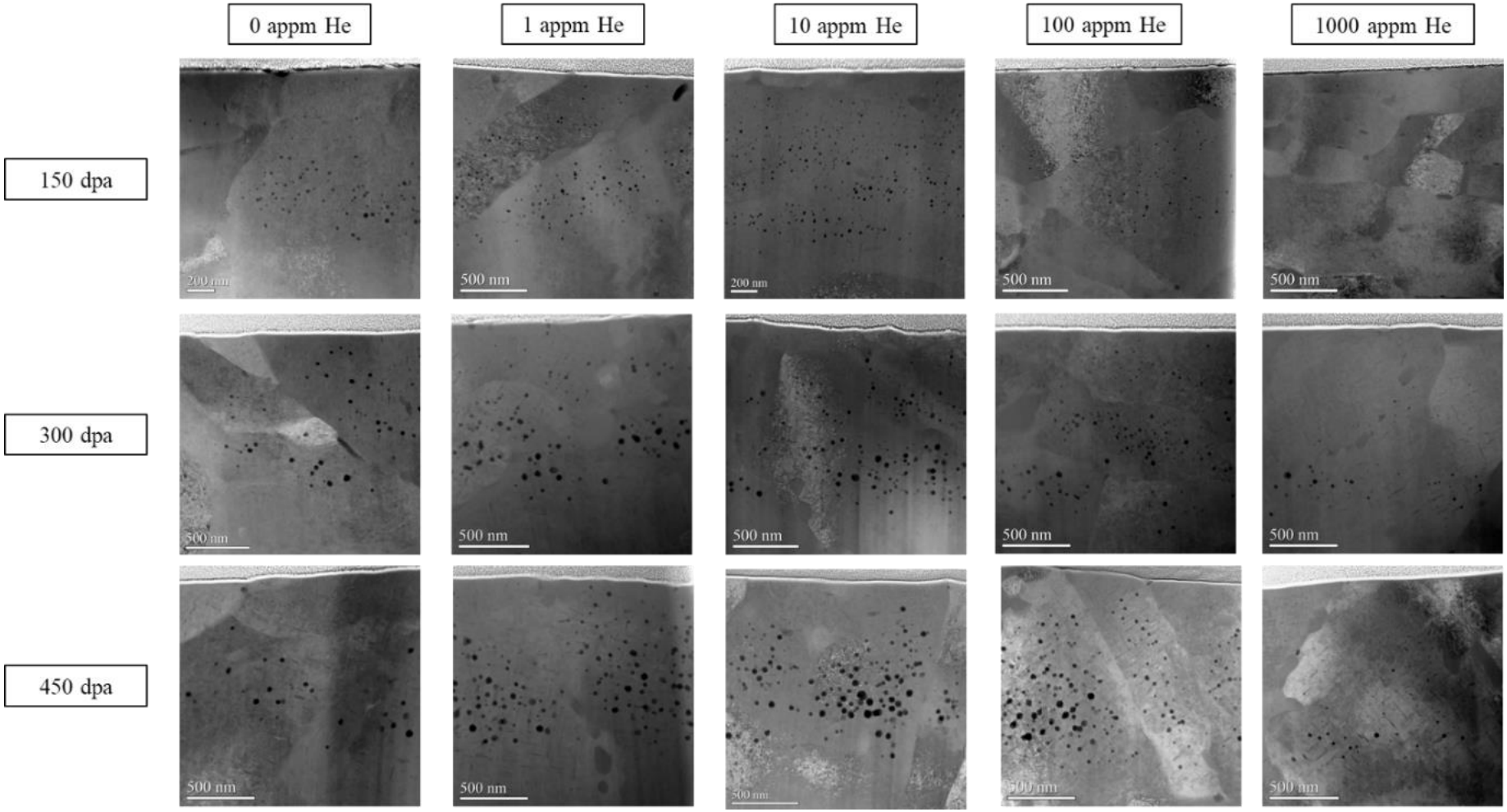

Figure 5.14 HAADF STEM images showing the evolution of the T91 microstructure with damage for the 0, 1, 10, 100 and 1000 appm He conditions irradiated at 460°C with 5 MeV Fe^{2+} ions.

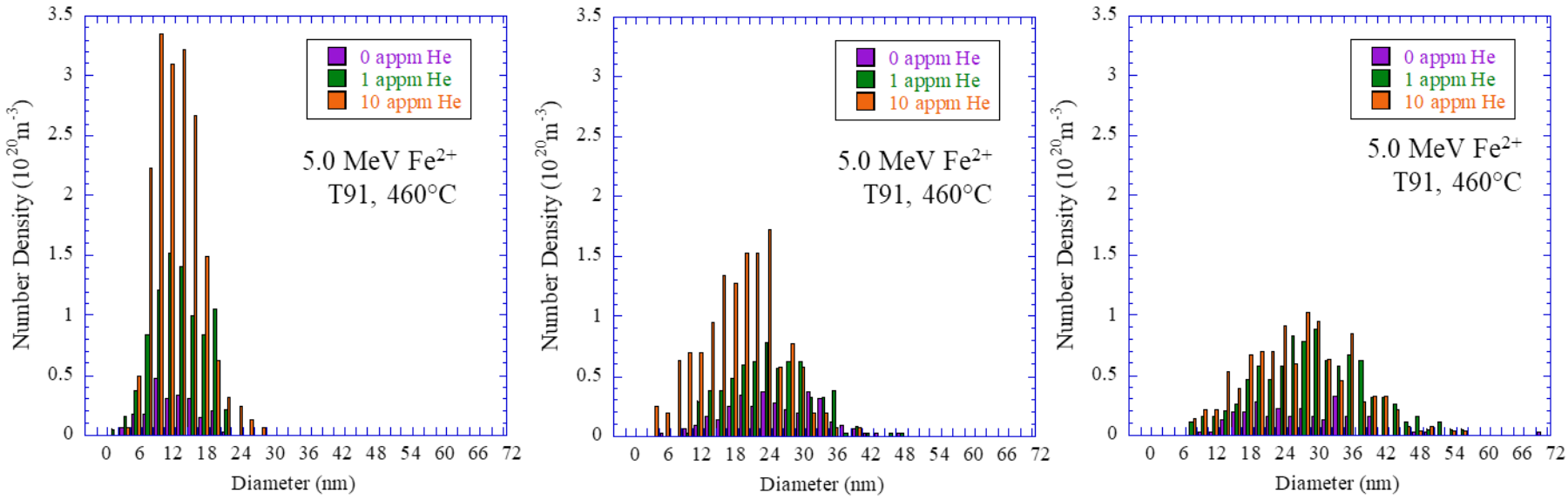

Figure 5.15 Cavity size distributions for the 0, 1, and 10 appm He conditions at 50, 150, and 300 dpa (500-700 nm depth).

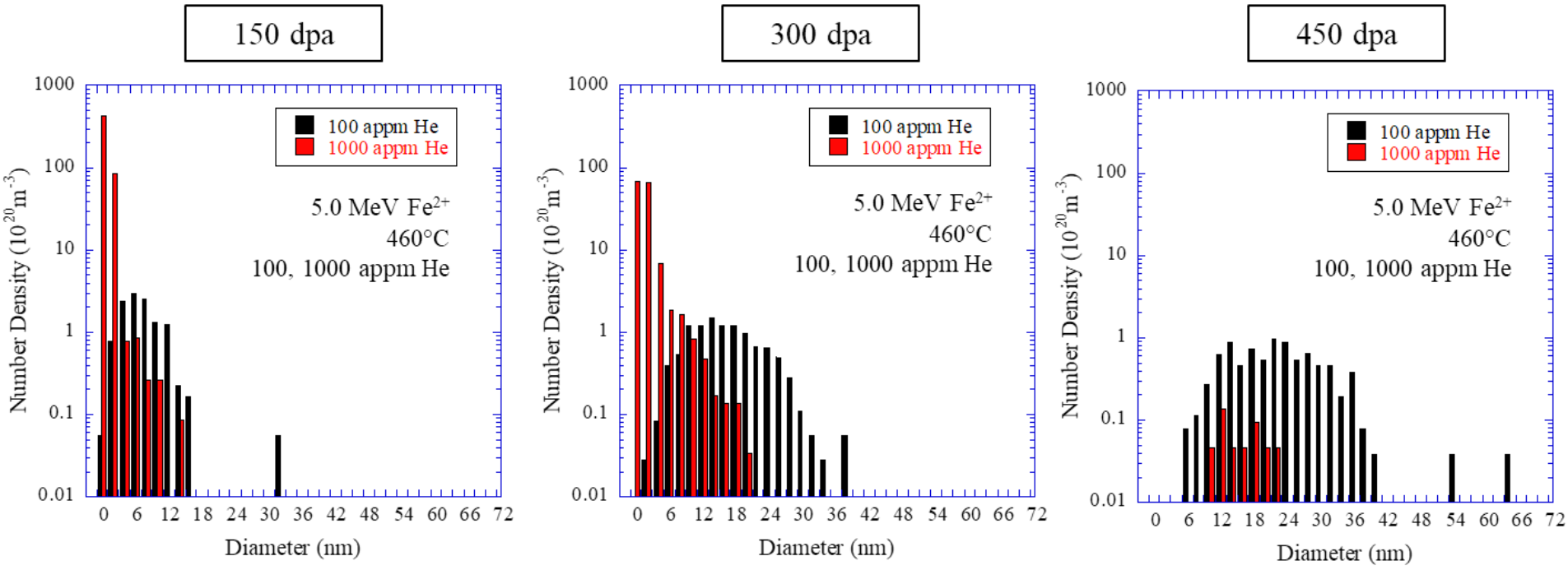

Figure 5.16 Cavity size distributions for the 100 and 1000 appm He conditions at 50, 150, and 300 dpa (500-700 nm depth).

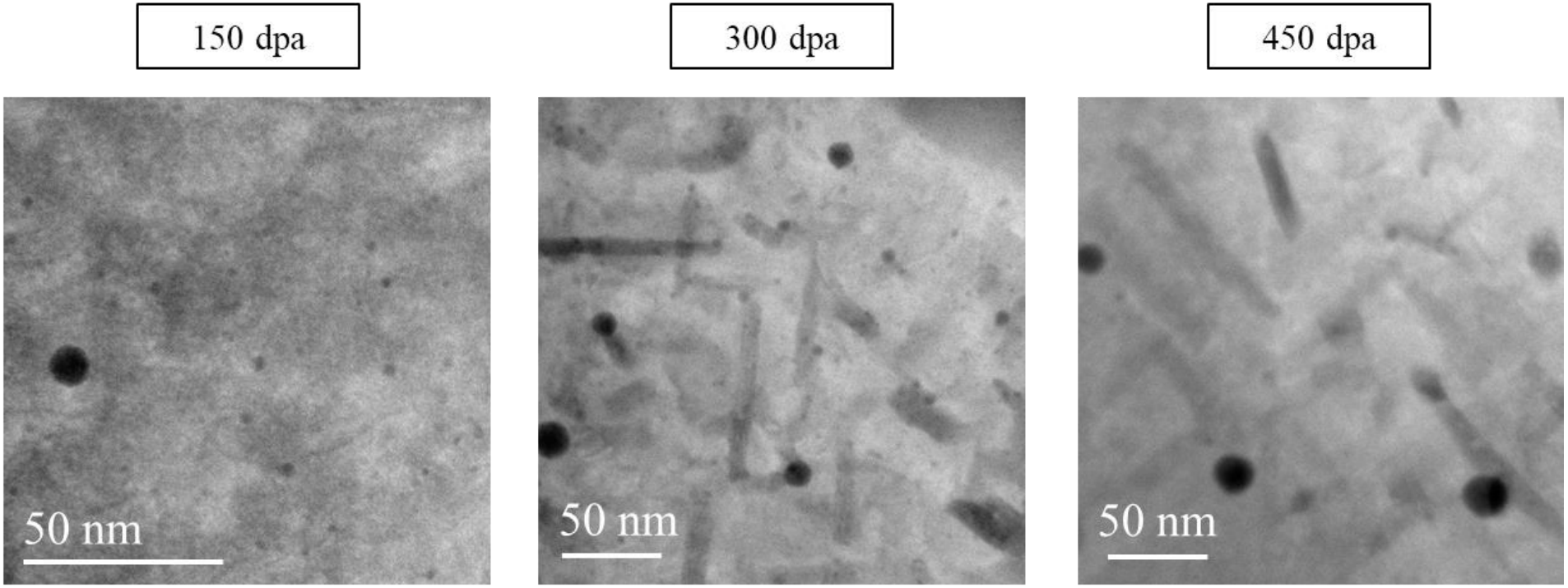

Figure 5.17 High magnification HAADF STEM images of T91 implanted with 1000 appm He at damage levels of 150, 300, and 450 dpa (500-700 nm depth) irradiated with 5.0 MeV Fe^{2+} at 460°C.

5.6 Carbon Content of Samples in Excess Carbon Campaign

A high density of precipitates was observed throughout the irradiation region at all damage levels of the excess carbon samples. These precipitates were typically rod-like aligned along the [100] direction. Carbides with identical morphology and alignment consistent with M_2X carbides observed in HT9 and other irradiated ferritic-martensitic steels [73,74,79–81]. These studies have identified the carbides as M_2X, with M=Cr and X=C, in both HT9 and CNSI and CNSII. HRTEM and XEDS was used to confirm the identity of the carbides in this work as M_2X as well. The XEDS map in **Figure 5.18b** shows that the carbides are Cr-rich. Indexing of the Fast Fourier Transform pattern from HRTEM imaged along the [001] axis of the carbide (**Figure 5.18c**) confirmed the identity as M_2X, with a hexagonal structure with a = 2.8 Å and c = 4.4 Å.

These carbides were characterized for their damage dependence in the 10 appm He condition. **Figure 5.19** shows images of the evolution of the carbides with damage using LAADF (low angle annular dark field) STEM in which the carbides appear in lighter contrast. As damage was increased, the carbides grew both in density and size. **Figure 5.20** plots the dependence of the carbide length, density, volume fraction, and sink strength as a function of damage. From 150 to 450 dpa, the carbide length increased from 52 nm to 67 nm (**Figure 5.20a**), and the density increased from 5.8 x 10^{20} m^{-3} to 18.8 x 10^{20} m^{-3} (**Figure 5.20b**). This resulted in a corresponding increase of volume fraction from 0.15% to 2.12% (**Figure 5.20c**) and increase of sink strength from 2.9 x 10^{14} m^{-2} to 13.5 x 10^{14} m^{-2} (**Figure 5.20d**).

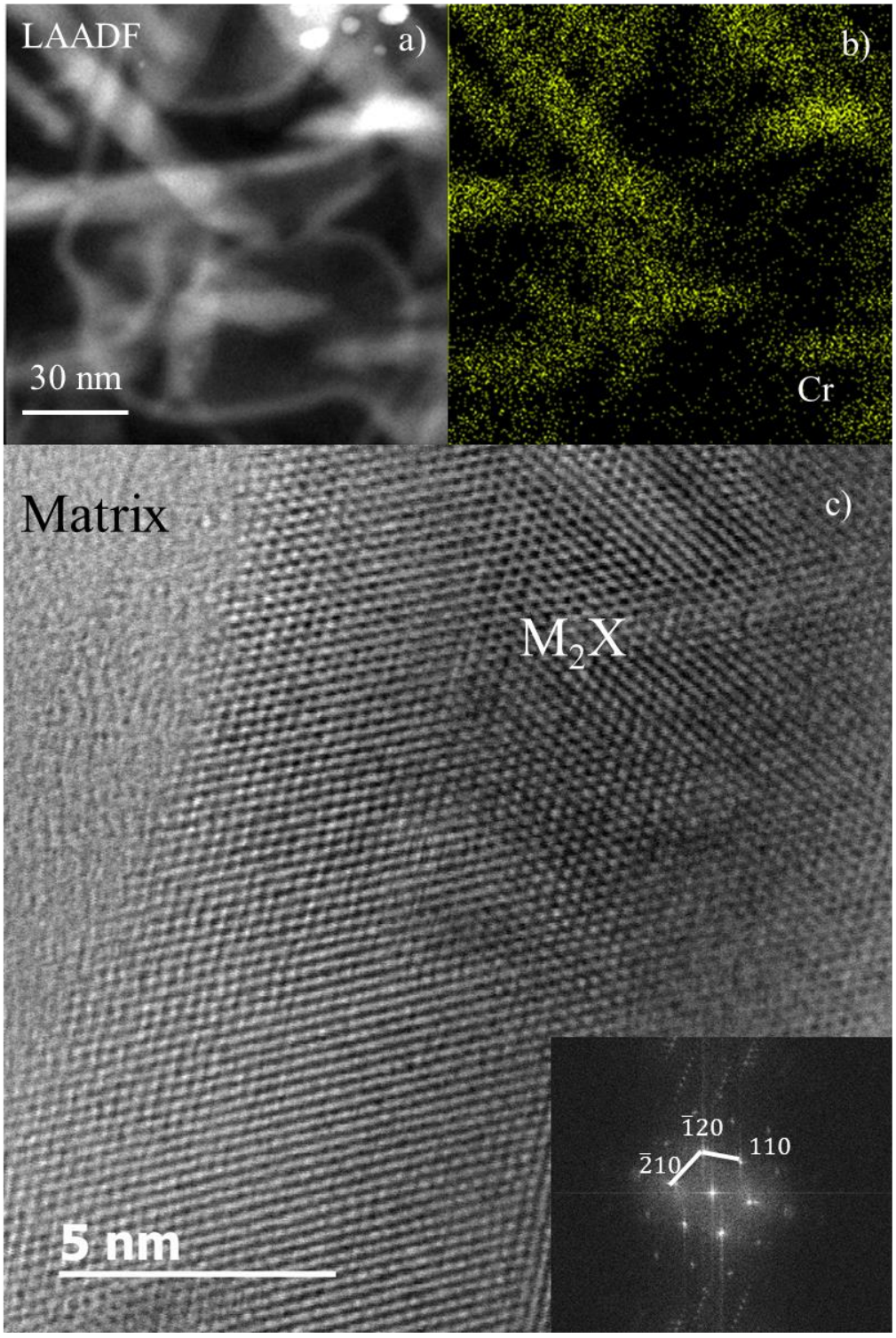

Figure 5.18 a) LAADF image, b) and a corresponding Cr XEDS along with c) HRTEM image of an M_2X carbide in T91 imaged along [001] with inlaid FFT taken from a sample irradiated to 450 dpa with 1 appm He.

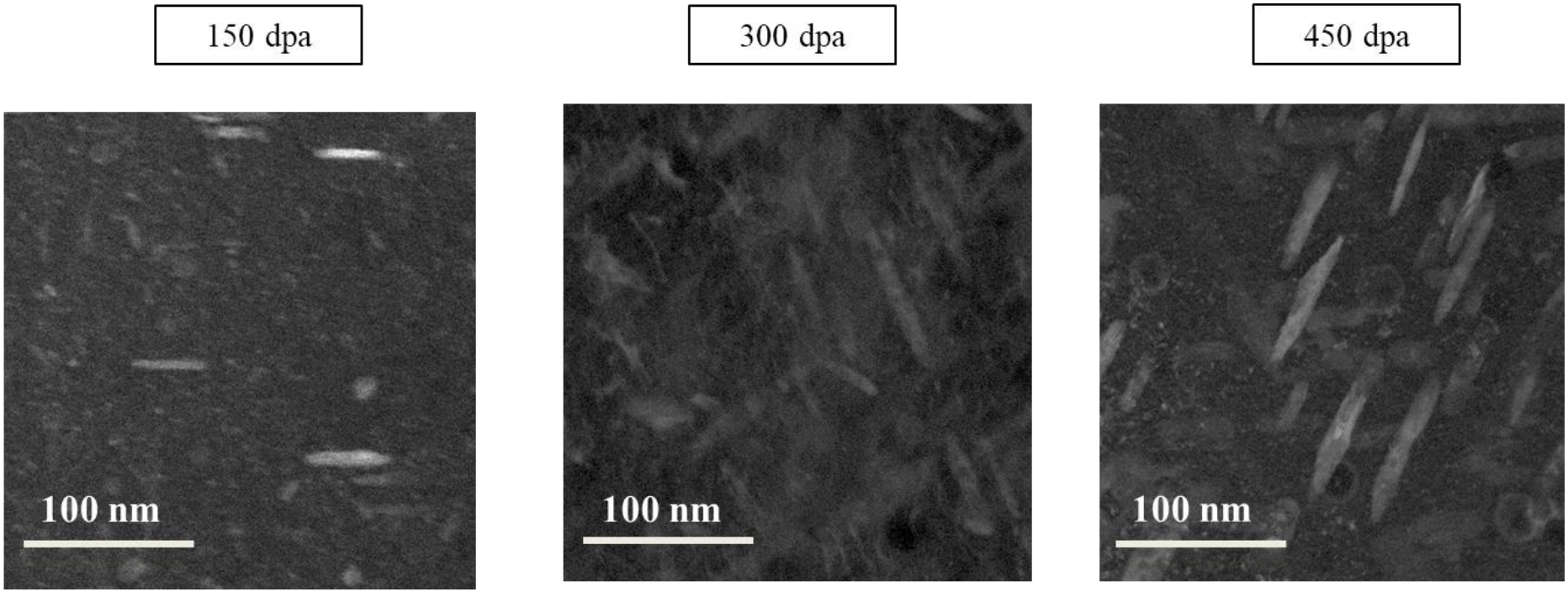

Figure 5.19 LAADF (Low Angle Angular Dark Field) STEM images of carbides taken at 150, 300 and 450 dpa (500-700 nm depth) in T91 with 10 appm He implanted and irradiated with 5 MeV Fe^{2+} at 460°C.

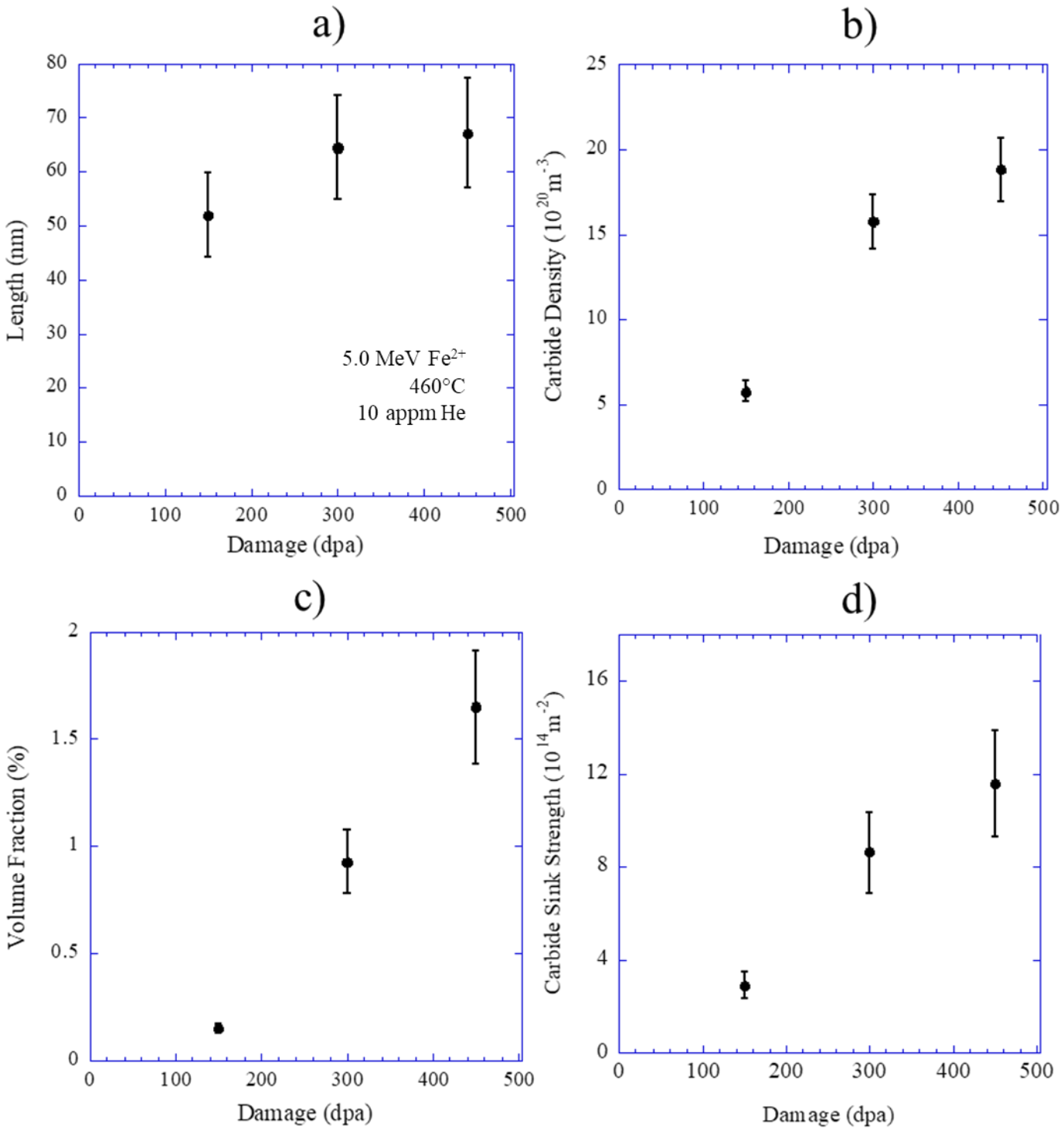

Figure 5.20 The a) length, b) density, c) volume fraction, and d) sink strength evolution of carbides in T91 implanted with 10 appm He as a function of damage at 460°C.

The carbides were also characterized as a function of helium at 450 dpa. **Figure 5.21** shows BF STEM images of the microstructure at 450 dpa, where a high density of carbides is visible regardless of helium content. **Figure 5.22** plots the dependence of carbide length, density, volume fraction and sink strength for implanted helium concentrations of 0, 1, 10, 100, and 1000 appm. No significant trend was seen across helium levels with carbide size, with most ranging between 45 and 50 nm (**Figure 5.22a**). The carbide densities for the low helium levels of 0, 1, and 10 remained between 15-20 x 10^{20} m^{-3}, but increased at 100 appm He to 28.5 x 10^{20} m^{-3} and again at 1000 appm He to 33.1 x 10^{20} m^{-3} (**Figure 5.22a**). The highest volume fraction was observed in the 10 appm condition at 2.12%, but no significant trend with helium and volume fraction was observed (**Figure 5.22b**). Similarly, no obvious trend was observed with carbide sink strength with the overall the sink strength remaining between 8-14 x 10^{14} m^{-2} (**Figure 5.22b**). A summary of the characterized carbides is provided in **Table 5.4.**

To further quantify the carbon and carbides, the depth profiles of carbon were taken from several conditions using NRA. **Figure 5.23** shows the depth profiles of the 450 dpa condition (with 10 appm He implanted) along with an unirradiated profile. The unirradiated profile remained at 0.5% C throughout the depth, which is the nominal concentration of the alloy. The 450 dpa profiles exhibited uptake of excess carbon, with a peak of about 2.5% C at the surface and through the irradiated region. The 2.5% C through 1000 nm fell to about 0.5% by about 1500 nm depth.

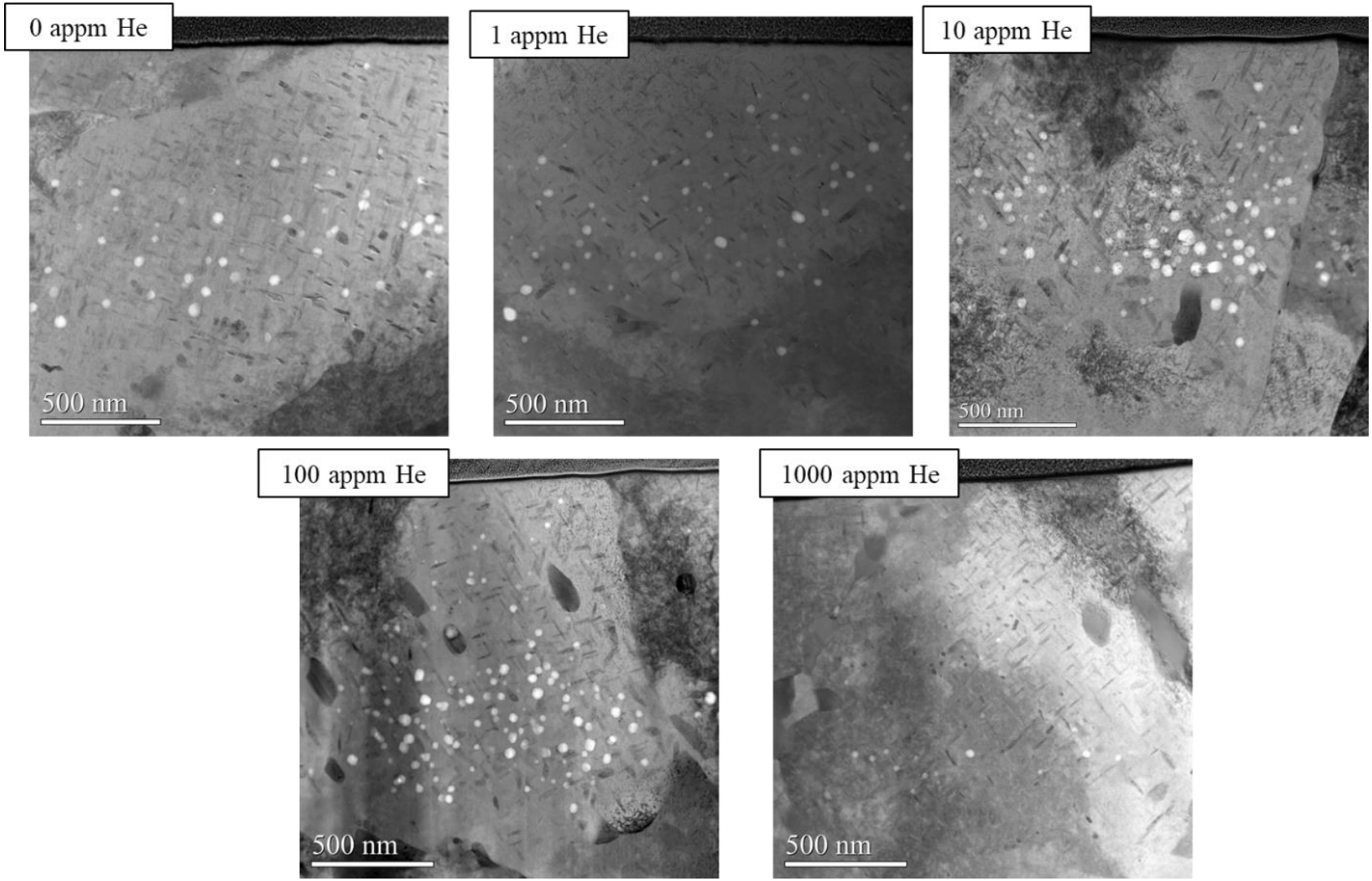

Figure 5.21 BF STEM images showing the presence of a high density of carbides in T91 in all helium conditions at 450 dpa irradiated with 5.0 MeV Fe^{2+} at 460°C.

Table 5.4 Summary of carbide length, density, volume fraction and sink strength in excess carbon T91 following irradiation with Fe^{2+} at 460°C.

Damage level (dpa)	Pre-Implanted He (appm)	Carbide Length (nm)	Carbide Density (10^{20} m^{-3})	Carbide Volume Fraction (%)	Carbide Sink Strength (10^{14} m^{-2})
150	10	52	5.8	0.15	2.92
300	0	33.2	18.5	0.22	6.67
	1	40.7	16.35	0.26	6.49
	10	65	15.8	0.93	8.64
	100	36	19.2	0.53	8.26
	1000	28.8	19.1	0.15	6.19
450	0	45.3	17	0.56	9.59
	1	47.9	18.7	0.46	7.94
	10	67.2	18.8	1.65	11.6
	100	44.7	28.5	0.8	9.8
	1000	49.3	33.1	1.64	14.4

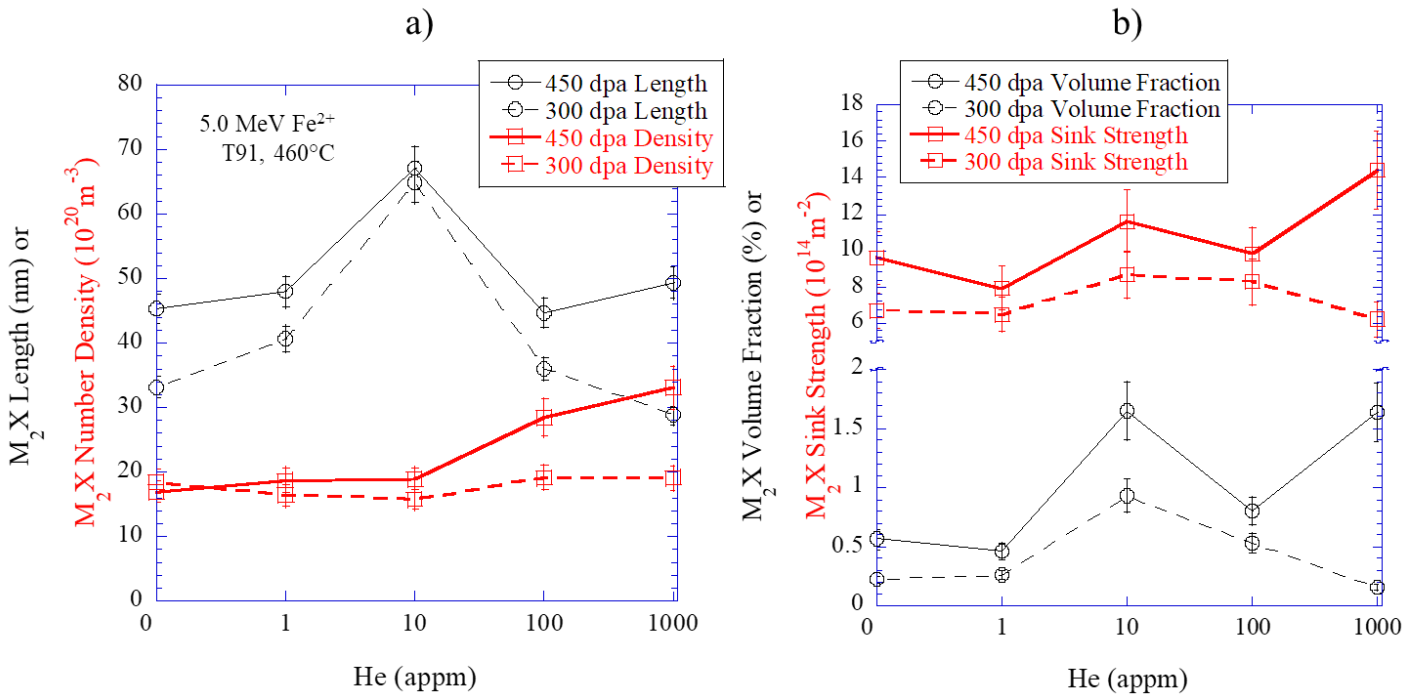

Figure 5.22 The a) length and density and b) volume fraction, and sink strength evolution of carbides in T91 at 300 and 450 dpa at 460°C as a function of He content.

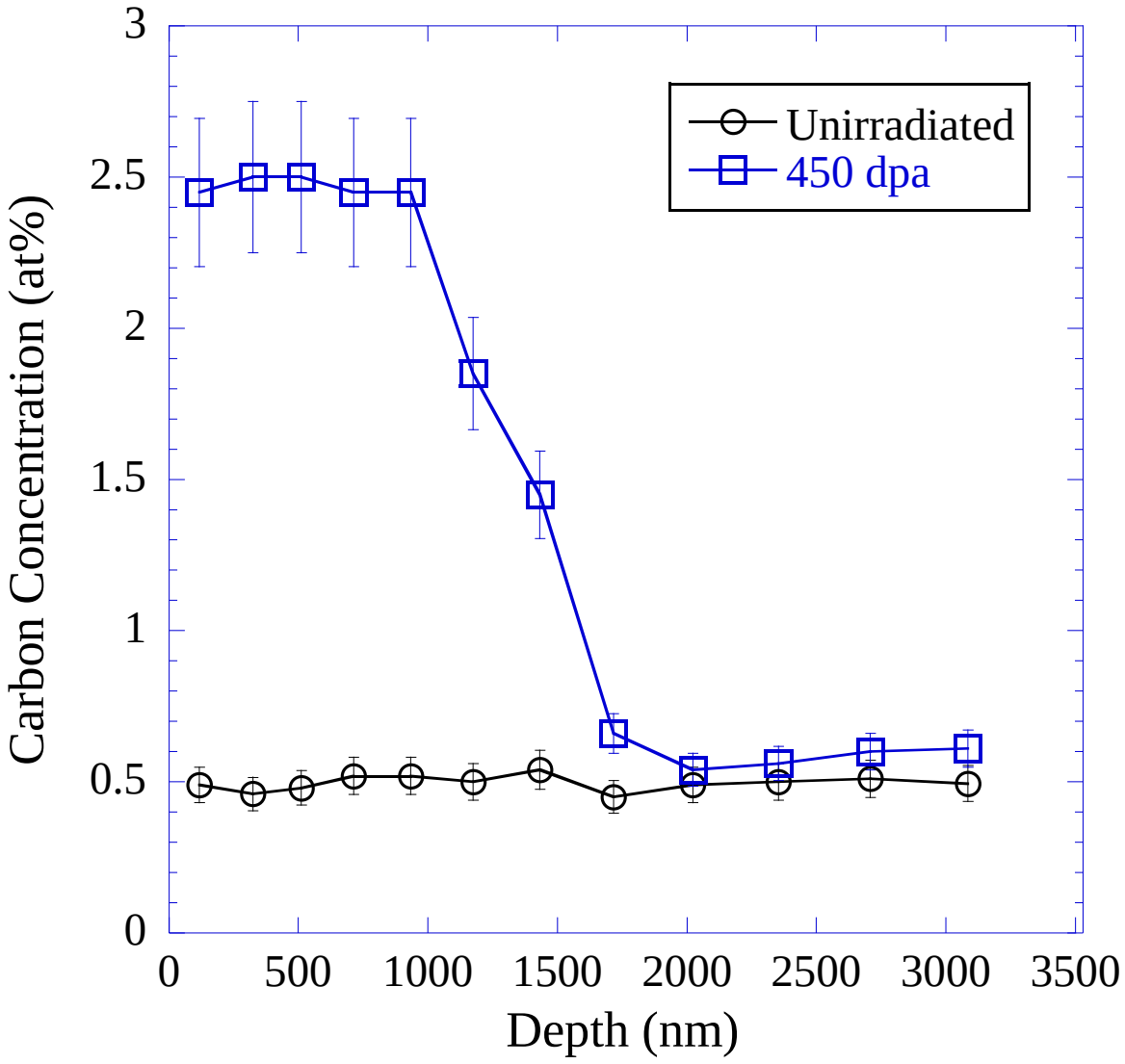

Figure 5.23 The NRA carbon profiles through the depth in T91 in the 450 dpa (460°C) excess carbon condition and in the unirradiated condition.

5.7 Excess Carbon Campaign Dislocations and Precipitates

The density of carbide precipitation in the excess carbon conditions made dislocation imaging and characterization very difficult. The dislocations and the carbides both habit the same [100] family of planes. Additionally, in bright field STEM imaging, both features exhibit a similar contrast. Therefore, it can become exceedingly difficult to differentiate between lines that correspond to loops and thin carbides on the same plane. As such, dislocation characterization could only be performed in the 150 and 300 dpa conditions of the excess carbon conditions—the extremely high density of carbide precipitation in the 450 dpa condition prevented accurate characterization of dislocation loops. The results for the dislocations in the excess carbon condition are shown in **Table 5.5.** When increasing damage from 150 dpa to 300 dpa, an increase in both loop density and diameter is seen.

The difficulty in imaging in the presence of carbides also applied to G-phase. Sharing similar contrast with G-phase in BF-STEM, accurate distinctions could not be made between carbides and G-phase, especially at high damage levels.

Table 5.5 Dislocation density, diameter and line length are shown for the conditions characterized in excess carbon T91.

Damage level (dpa)	Pre-Implanted He (appm)	<100> Loop Diameter (nm)	<100> Loop Density (10^{20} m^{-3})	<111> Loop Diameter (nm)	<111> Loop Density (10^{20} m^{-3})	Network Density (10^{14} m^{-2})	Total Line Length (10^{14} m^{-2})
150	10	29.4	10.6	15.6	5.6	3.69	5.69
300	10	41.3	19.8	16.5	15.2	5.84	10.97

CHAPTER 6: DISCUSSION

The discussion of the results in the Chapter 5 will be divided into three main components—the influence helium on cavity evolution, the influence of carbon on cavity evolution, and finally the combined effects of helium and carbon on cavity evolution. To determine the influence of helium on cavity evolution, only the results from the Nominal Carbon Campaign are considered. The results from the both the Nominal and Excess Carbon Campaigns are used to determine the influence of carbon. Lastly, the results of both irradiation campaigns are discussed to determine the influence of the combined effects of helium and carbon on cavity evolution. The effect of both helium and carbon on other microstructural features (precipitates, dislocations) are discussed where relevant.

6.1 The Influence of Helium on Cavity Evolution

The cavity evolution in the Nominal Carbon Campaign samples depended highly on both the amount of implanted helium and the damage level. The following discussion addresses the influence of helium in causing sink strength-moderated behavior at low helium levels (0-10 appm), and on the formation of a bimodal distribution and suppression of growth at high helium levels (100 and 1000 appm). Lastly, it is shown that other microstructural features such as dislocations loops and network, and G-phase precipitates had a negligible influence on the cavity evolution.

6.1.1 Sink strength-moderated cavity evolution

At low helium levels (0, 1, and 10 appm), the cavity behavior was controlled by the cavity sink strengths. The effect of helium in promoting cavity nucleation is clearly seen in **Figure 5.2b**. At the lowest damage level, the swelling and cavity sink strengths were dominated by the cavity density. Therefore, an increase in cavity volume occurred with increasing He from 0, to 1, to 10 appm He, (0.091%, 0.107%, and 0.124%, respectively at 50 dpa). At 50 dpa, the sink strength of the 10 appm He condition was almost double that of the 0 appm He condition. **Figure 6.1** shows

how the cavity sink strengths varied with He content at different damage levels. The slightly higher size of cavities in the 0 appm He case was not large enough to overcome the ~2x density for the 1 and 10 appm He conditions.

The presence of pre-implanted helium served to create nucleation sites such that a high density of cavities was established early on in the irradiation. However, the 0 appm He condition did not have the aid of helium to assist nucleation, thus the formation of cavities (or voids in this case), occurred purely by vacancy agglomeration. The 0 appm He condition experienced a much slower nucleation rate such that at 50 dpa it was still in the nucleation-dominant regime.

By 150 dpa, the 0 appm condition achieved the highest swelling of any of the helium levels studied. Cavities in the 0 appm He case grew at a faster rate, as seen by the larger cavity sizes (**Figure 5.2a**), while simultaneously nucleating new cavities over a longer period (**Figure 5.2b**). The same number of vacancies produced by irradiation were distributed over a higher number of cavities in the pre-implanted cases, resulting in lower growth rates compared to the 0 appm He case. This difference in growth rates resulted in a cross-over point in swelling between 50 and 150 dpa (**Figure 5.2c**), where the 0 appm He case achieved a similar cavity sink strength as in the 1 and 10 appm conditions (**Figure 6.1**). At 150 dpa, cavity sink strengths for the 0, 1, and 10 appm He conditions were essentially the same.

After 150 dpa, no further increases in cavity density occurred, suggesting that vacancies were being absorbed into cavities at nearly the same rate across the three helium levels. Nucleation of new cavities was suppressed, and the sink strength of the established cavity microstructure was strong enough to assure a net absorption of vacancies causing growth in cavity size. Ultimately, similar sink strengths at 150 dpa with no further increases in density resulted in similar growth behavior and a convergence of the 0, 1, and 10 appm cavity distributions by 300 dpa. **Figure 5.4** shows how very different size distributions between the 0, 1, and 10 appm He conditions at 50 dpa converged to nearly identical distributions by 300 dpa. Small additions of helium did not change the final distribution or total amount of vacancies in cavities, rather, it only provided more sites for the cavities to nucleate.

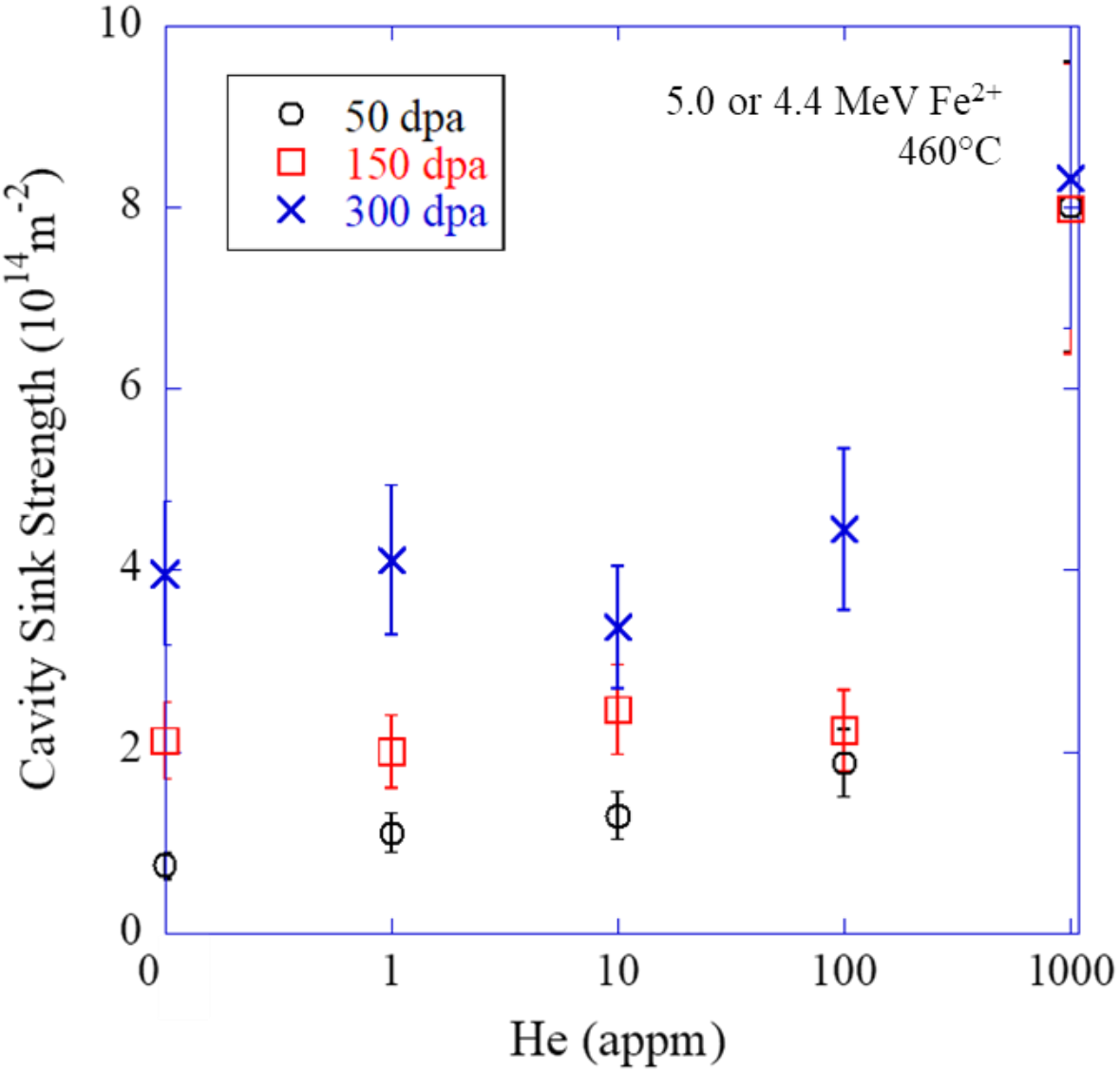

Figure 6.1 Cavity sink strength is plotted as a function of helium content at damage levels of 50, 150, and 300 dpa in ion irradiated T91.

Only a small distinction could be made between additions of 1 and 10 appm helium, as both had achieved their highest densities by the lowest damage level. However, it is suspected that the 10 appm He condition nucleated more quickly than the 1 appm condition due to a higher density of nucleation sites. This difference in nucleation was not significant enough to result in different sink strengths, and thus the cavity evolution of the 1 and 10 appm conditions remained largely the same.

Overall, the role of small additions of helium was simply to accelerate cavity nucleation, but not to alter the final cavity microstructure. The difference in cavity microstructure was largest at low damage levels, where the swelling behavior was dominated by nucleation. However, similar cavity sink strengths between the 0, 1, and 10 appm He conditions ultimately led to nearly identical size distributions by 300 dpa.

6.1.2 Formation of bimodal cavity distributions

The cavity behavior in the high helium conditions (100 and 1000 appm) was fundamentally different than that of the low helium conditions. Bimodal distributions (**Figure 5.7**) and a clear suppression of growth resulting in low swelling (**Figure 5.2c**) were observed at all damage levels. The presence of a bimodal distribution suggests that helium levels were high enough to induce the formation of helium bubbles. Hishinuma and Mansur [82] postulated that the formation of a bimodal distribution is due to a reduction in the critical radius in the presence of helium. Bubbles below the critical radius are able to remain relatively stable and insensitive to damage as long as they retain a particular number of helium atoms.

The analysis from [82] can be applied to the T91 system to create a map in which a bimodal distribution would be expected to be stable. The critical radius of a cavity, r_c^{crit}, as a function of its helium gas pressure can be expressed as:

$$r_c^{crit} = 2\gamma / \left\{ p_g + \frac{kT}{\Omega} \ln \left[\left(1 - \frac{Z_i^c Z_v^d}{Z_v^c Z_i^d} \right) \frac{C_v}{C_v^o} + \frac{Z_i^c Z_v^d}{Z_v^c Z_i^d} \right] \right\}, \tag{6.1}$$

where γ is the surface energy, p_g is the helium gas pressure of the cavity, k is Boltzmann's constant, T is irradiation temperature, Ω is the atomic volume, Z_i^c is the cavity capture efficiency

for interstitials, and Z_i^d is the dislocation capture efficiency for interstitials, and Z_v^c and Z_v^d are the capture efficiencies for vacancies and lastly, C_v / C_v^o is the vacancy super saturation. The gas pressure in the cavity, p_g , can be expressed by the number of helium atoms in the cavity:

$$p_g = n_g kT / \left(\frac{4}{3} \pi r_c^3 - n_g B \right), \tag{6.2}$$

where n_g is the number of helium atoms, r_c is the cavity radius, and B is the Van der Waals coefficient for helium. For a given cavity size, Eq. (6.2) predicts that the pressure within a cavity will increase as the number of gas atoms in the cavity increases. With increases in helium pressure, Eq. (6.1) predicts that the critical cavity radius will decrease. Eq (6.1) can also be used to calculate the critical radius for a gas-free cavity (void), by setting the gas pressure to zero. The gas-free critical cavity radius for the T91 system is calculated as 1.8 nm, using the parameters listed in **Table 6.1**. The effect of adding helium to the cavity on the critical radius is shown in **Figure 6.2**, which plots the critical radius as a function of the number of helium atoms in the cavity. For a given cavity size, the critical cavity radius decreases as the number of helium atoms in the cavity increases. Additionally, for smaller cavity sizes, the addition of helium has a much more dramatic effect on lowering the critical cavity radius. This makes sense, since the pressure of smaller cavities increases more easily than larger cavities when adding a set number of helium atoms. It is important to note that while **Figure 6.2** predicts that the critical cavity radius will eventually approach zero, with increasing helium content, only values above the actual cavity radius are relevant. That is, for a 1 nm radius cavity, the critical cavity radius below 1 nm would not be achieved as the cavity will achieve bias-driven growth by 1 nm.

The effect of helium lowering the critical cavity radius is essential in describing how a bimodal cavity distribution may form in T91. By substituting the expression for p_g in Eq. (6.2) into Eq. (6.1), a cavity stability map (**Figure 6.3**) was created that shows the dependence of the critical cavity radius on the actual cavity radius and the number of gas atoms in the cavity. The key parameters used for this calculation are summarized in **Table 6.1**. Calculation of the vacancy supersaturation was required for both **Figure 6.2** and **Figure 6.3**. This calculation is detailed in Appendix D.

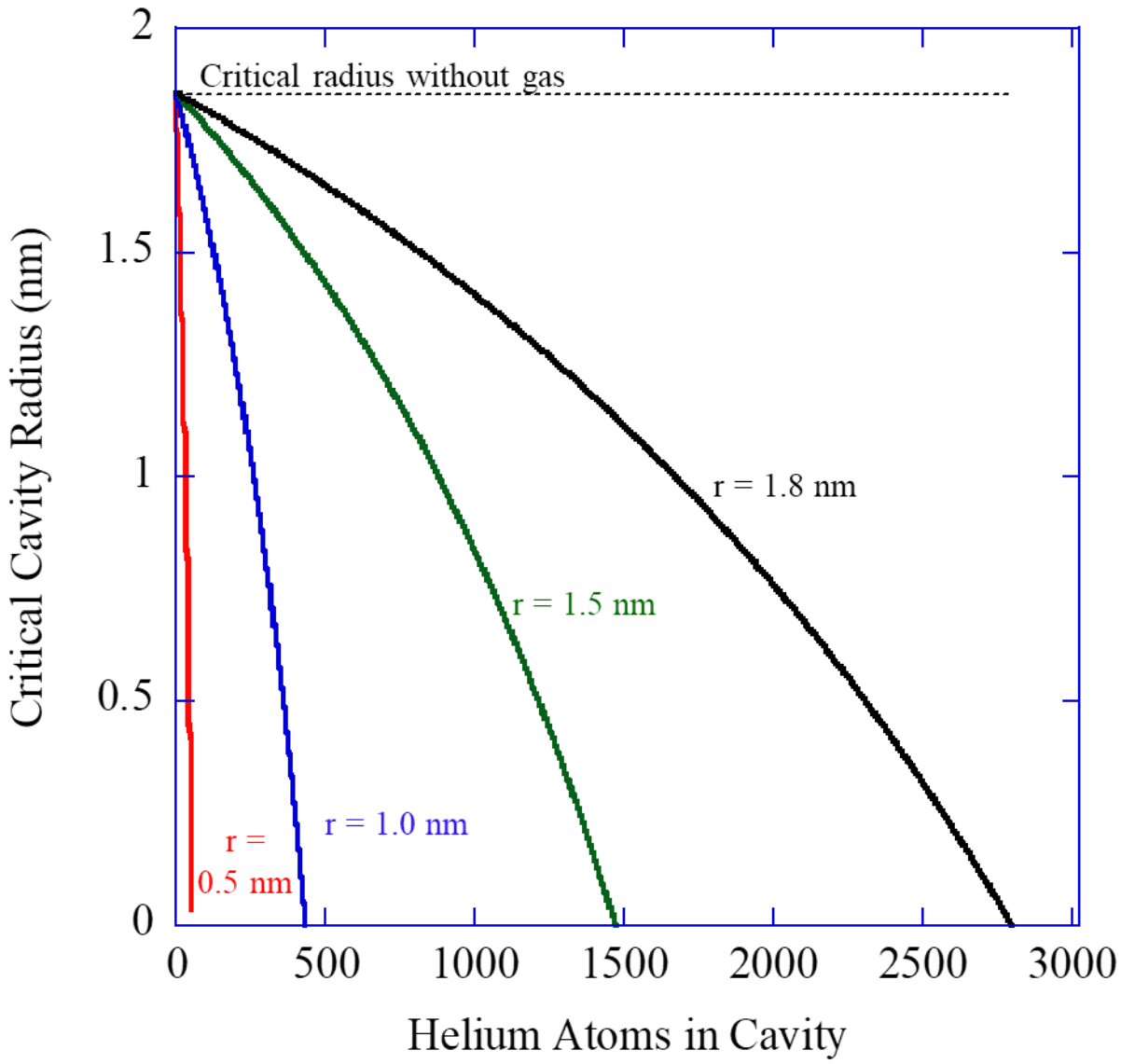

Figure 6.2 The critical cavity radius for a cavity plotted as a function of the number of helium atoms in the cavity for cavity sizes of 0.5, 1.0, 1.5, and 1.8 nm.

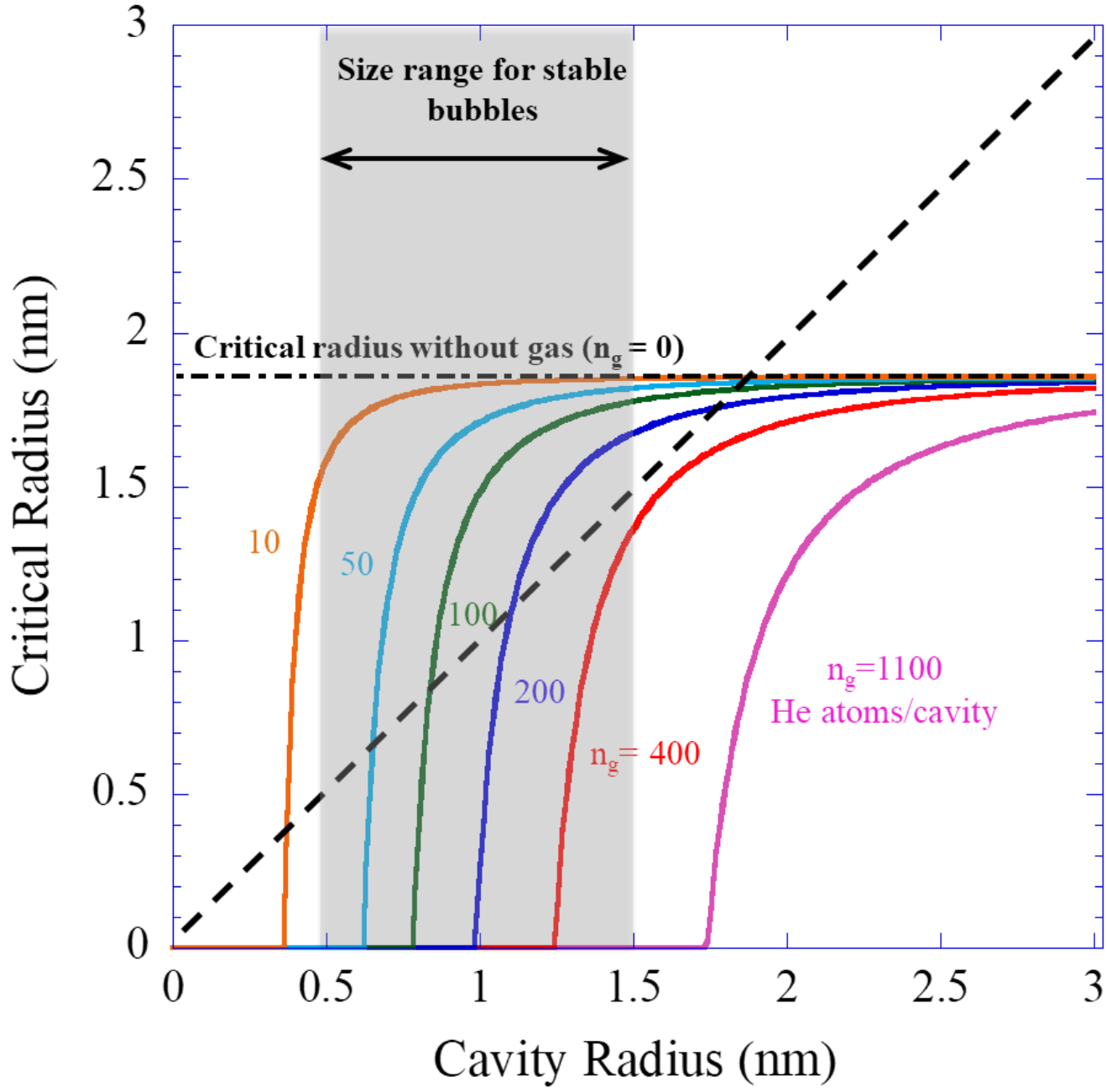

Figure 6.3 Cavity stability map for T91 showing dependence of the critical radius on the actual cavity radius for various numbers of contained gas atoms. The highlighted grey area shows the possible size range for the presence of stabilized bubbles.

Table 6.1 Key parameters for calculating the T91 cavity stability map.

Symbol	Definition	Value	Ref.
T	Irradiation Temperature	460°C	-
γ	Surface Energy	1.7 J/m^2	[82]
Ω	Atomic Volume	2.38 x 10^{-29} m^{-3}	-
B	Van der Waals Coefficient for He	0.0096 L/mol	[82]
$\frac{Z_i^c Z_v^d}{Z_v^c Z_i^d}$	Capture Efficiency	0.95	[82]
*K_o	Damage Rate	1 x 10^{-3} dpa/s	-
* E_v^m	Vacancy Migration Energy	0.63 eV	[14]
* E_v^f	Vacancy Formation Energy	1.6 eV	[14]
* E_i^m	Interstitial Migration Energy	0.22 eV	[14]

*used to determine vacancy supersaturation, C_v / C_v^o

In **Figure 6.3**, the estimated critical radius when no gas is present ($n_g = 0$) is shown by the horizontal dashed line at approximately 2 nm. When helium gas atoms are added to a cavity, the critical radius falls below this 2 nm line, indicating that the presence of helium results in a smaller critical radius than with no gas. As higher amounts of helium are added to the cavity, the effect of lowering the critical radius extends to larger cavity sizes.

The diagonal dashed line in **Figure 6.3** denotes the equality of the critical radius and the actual cavity radius. The intersection point of any of the curves with the diagonal line indicates a point of stability. At any point below the diagonal line, a cavity with a given number of helium atoms will grow along its respective curve until it reaches the diagonal. At that point, the cavity cannot grow any further because at all points above the diagonal line, the critical radius is greater than the actual cavity radius. This results in a relatively stable bubble at a size lower than the critical radius without gas (~2 nm). For the T91 system, curves describing cavities with less than ~400 He atoms contain intersection points with the diagonal line, indicating that < 400 He atoms/cavity are required to form a bimodal distribution. In practice, cavities with radius smaller than 0.5 nm were not observed or could not be resolved reliably under STEM. Using this 0.5 nm lower limit, a more realistic threshold for the creation of a bimodal distribution would be a range of ~50-400 He atoms/cavity. The greyed area in **Figure 6.3** highlights this range.

To determine whether a bimodal distribution is reasonable to expect in the 100 and 1000 appm He conditions, an estimation of the total amount of He in bubbles was made. Assuming that the smaller size groups (< 4 nm) were entirely equilibrium pressurized bubbles, **Eq 6.2** was set equal to the cavity surface energy of an equilibrium bubble, $2\gamma/r$, and integrated over the size distribution to determine the possible total number of gas atoms. The size distribution of bubbles in the size range of 0 to 4 nm was assumed to follow a Gaussian distribution. For the 1000 appm He case at 50 dpa, a mean bubble radius of 0.8 nm, a standard deviation of 0.23 nm and total bubble density of ~885 x 10^{20} m^{-3} was used to approximate the bubble size distribution as shown in **Figure 5.7**. Assuming each bubble was at equilibrium, **Eq. 6.2** was solved for the number of gas atoms at each size and integrated over the size distribution to obtain the total amount of gas in the distribution. For the 1000 appm He condition the distribution could accommodate ~400 appm of He or an average of ~380 He atoms per cavity. For the 100 appm condition at 50 dpa, a mean bubble size of 1.1 nm, a standard deviation of 0.23 nm and total bubble density of ~70 x 10^{20} m^{-3} was used to approximate the bubble size distribution, resulting in a total of ~84 appm He in the

distribution, or ~1000 He atoms per cavity. Thus, both the 100 and 1000 appm He conditions are capable of satisfying the required He threshold (~50-400 He atoms/cavity) to form a stable bimodal cavity distribution. Increasing the amountof helium in a given cavity reduces the critical cavity radius to establish a bubble-dominated microstructure. It should be stressed that the analysis presented here and inherent in the calculations for **Figure 6.2** and **Figure 6.3** are for increases in helium for a given cavity, not necessarily for increases in helium in the system as a whole. The calculations assume that helium is not changing the sink microstructure. In practice, higher levels of helium may result in a high cavity sink strength, which would reduce the vacancy super-saturation, and in turn would increase the critical radius of system as a whole. However, for a given cavity, increases in the amount of helium within that bubble would lower its critical radius.

The 1 appm and 10 appm He cavity distributions could theoretically accommodate ~40 He atoms/cavity and ~350 He atoms/cavity, respectively, which is in the viable range for a bimodal distribution. However, since the cavities are much larger in the 1 and 10 appm He conditions, the cavities would be extremely underpressurized and do not behave as equilibrium bubbles. In fact, for the 1 appm He distribution, an additional 1100 appm He (or ~40,000 He atoms/cavity) would be required to convert the existing distribution into an equilibrium bubble distribution. Similarly, for the 10 appm He cavity distribution, an additional 2000 appm He (or ~70,000 He atoms/cavity) would be required to achieve an equilibrium bubble state. Since the cavities in the 1 and 10 appm He conditions are far removed from the equilibrium bubble state, the cavity stability map in **Figure 6.3** cannot describe their behavior.

It is very likely that at the low helium content of 1 and 10 appm, there is not enough helium to readily achieve significant clustering. Clustering of helium atoms in these low helium cases remains below the visible range of 1 nm cavities. Increasing the amount of helium from 1 to 10 appm only increases the number of sites available for nucleation, but does not achieve an observable difference in helium clustering. The low amount of clustering does not provide for a significant reduction in the critical cavity radius, so a bimodal distribution cannot form in the 1 and 10 appm He conditions.

6.1.3 Helium-suppressed cavity evolution

In the 100 appm and 1000 appm conditions, a suppression of total swelling was observed. Suppression of swelling with high helium levels has often been attributed to the development of a

very high cavity sink strength [17,47,50]. At a sufficiently high cavity sink strength, it is expected that both vacancies and interstitials would annihilate in equal numbers, thus resulting in a suppression of growth. However, based on **Figure 6.1**, the 100 appm condition exhibits a very similar cavity sink strength as the 0, 1, and 10 appm conditions, which did not experience significant suppression of growth, suggesting that sink strength alone cannot account for the suppression of swelling. In fact, such suppression would only occur if cavities were the dominant sink in the system. For the 100 appm He condition at 150 dpa, dislocations are still the dominant sink as shown in **Figure 5.10b** where the dislocation sink strength is ~3x higher than the cavity sink strength. Similar cases were reported in stainless steel [6,83] where cavity sink strength alone was not sufficient to account for swelling suppression. Therefore, other mechanisms must contribute to swelling suppression in the presence of helium.

Hishinuma [82,83] suggested that the presence of helium could lower the bias of the system and result in reduced growth. Small cavities or helium clusters could serve as obstacles for dislocation climb, thus reducing their effectiveness in capturing interstitials and reducing vacancy supersaturation. Since growth is bias-driven, this effect would preferentially influence the larger size group. Alternatively, elasticity theory, kinetic Monte Carlo and molecular statics models have demonstrated that cavities of very small size do not behave as neutral sinks, and instead are biased toward interstitials [84–87]. This bias is strongest at small cavity sizes, decreasing as cavity size increases. For the size range observed in T91 (< 2 nm), the cavity bias can be significant, with a net interstitial bias ranging between 10-25%. If this is the case, then the role of helium is to create a distribution of small cavities whose growth is restricted (stabilized) by this cavity bias and remain relatively insensitive to damage. Because of the bias toward interstitials, these small cavities reduce the net vacancy flow to cavities, and result in a suppression of swelling.

While the interstitial biases discussed above were mostly calculated for voids, it is possible that the presence of gas in a bubble may counter-act the effect and reduce the interstitial bias. Kohnert and colleagues [87] studied the effect of helium gas on the cavity bias and found that the bias was not significantly affected unless the bubble was over-pressurized. Addition of helium to a cavity did not change the capture radius for interstitials, but beyond equilibrium pressure was found to increase the vacancy capture radius linearly with increasing helium content. Since the bubbles in this work are likely at or below equilibrium, a significant cavity bias would still apply.

A helium trapping mechanism has also been proposed [26,40,47,88–90] as a possible method of swelling suppression. High levels of helium may trap vacancies within the matrix and enhance recombination. As mentioned before, the small size group of the 1000 appm He distribution could accommodate at most ~400 appm of He. This means that ~600 appm He is elsewhere in the lattice. Even with the assumption that all cavities observed in the 1000 appm He condition at 50 dpa were equilibrium bubbles, only ~800 appm He could be accommodated in the entire cavity distribution. No bubbles were observed at grain boundaries or at precipitates, so it is very likely that small invisible helium clusters remain in the matrix, either bound with dislocations or solute atoms. These helium sites could serve to immobilize the vacancies, enhancing recombination and preventing cavity growth.

As mentioned previously, the dislocation sink strength in the 100 appm He condition at 150 dpa was approximately 3x higher than the cavity sink strength (6.5 $x10^{14}$ m^{-2} and 2.5 $x10^{14}$ m^{-2} for dislocations and cavities, respectively). In order for the cavity sink strength to begin to contribute to swelling suppression, the invisible clusters would have to add an additional sink component to make up for the difference, or about 4 x 10^{14} m^{-2}. Assuming the cavities are just below the resolution limit of 1 nm, they would need to be present at a density of ~3 x 10^{22} m^{-3} to produce 4 x 10^{14} m^{-2} of sink strength. If these unresolvable cavities are assumed to be equilibrium bubbles, they would accommodate an additional ~11 appm He. Adding this to the 84 appm already accounted for by the rest of the distribution results in about 95 appm He. Therefore, there is enough helium available in the 100 appm He system to begin to experience an effect of helium trapping.

The high cavity sink strength of the 100 and 1000 appm conditions was not sufficient to explain the observed suppression in swelling. Therefore, an alternative mechanism, such as helium trapping, or helium-induced alteration of cavity and dislocation bias are the likely causes of the reduction in swelling.

6.1.4 Influence of dislocations and precipitates on cavity evolution

The behavior of dislocations with damage (**Figure 5.8**) was not unusual and similar behavior has been reported in previous high damage irradiations on HT9 [81], which showed that loop diameter was relatively insensitive to damage beyond 200 dpa. A total sink strength of ~3-6 x 10^{14} m^{-2} was reported in HT9, which is slightly lower than that observed in this study of T91 (5-7 $x10^{14}$ m^{-2}, **Figure 5.10a**) due to a higher density of <100> loops observed in T91. At 300 dpa

with 10 appm He implanted, the <100> loops exhibited a higher sink strength when compared to the <111> loops (3.3 x $10^{14}m^{-2}$ versus 0.5 x $10^{14}m^{-2}$). Therefore, the <100> loops would be expected to be a much stronger sink over the <111> loops.

The dislocation behavior was very similar across helium levels, suggesting that it did not influence the cavity evolution differently across the various helium levels, as seen in **Figure 5.9**. The 0 appm He condition experienced the biggest deviation in loop size, which was slightly larger than the other helium conditions at 36 nm versus about 21-28 nm for the pre-implanted conditions at 150 dpa. It is possible that the lack of helium in this condition allowed the loops to grow to larger sizes. Small pre-implanted helium clusters may have served as pinning sites for dislocation loops, restricting their growth. However, this trend did not continue with addition of helium beyond 1 appm. The 0 appm He condition exhibited similar loop densities as the pre-implanted cases, suggesting that the presence of helium had little to no effect on the nucleation of dislocation loops. Irradiation with helium has been shown to increase the dislocation density [48], however, the implantation was performed at room temperature and ferritic-martensitic steels naturally contain a high dislocation density. Furthermore, any effect on the dislocations by irradiation with helium was insignificant compared to the high damage induced by the 5 MeV Fe^{2+} ions. The dislocation density of the 1000 appm He implanted condition measured 3.71 x 10^{14} m^{-2}, which was well within the measurement error of the unirradiated condition of 3.0 x 10^{14} m^{-3}.

To determine any possible effect the dislocations may have had on cavity behavior, their sink strengths need to be considered. **Figure 5.10a** plots the sink strengths of the <100> loops, the dislocation network, along with the total line length at 150 dpa. The sink strengths ranged between 6–7 x 10^{14} m^{-2}, with the exception of the 0 appm He case, which exhibited a sink strength of about 1 x $10^{15}m^{-2}$ due to the aforementioned larger loop size, and a slightly higher network dislocation sink strength. These sink strengths are reasonable, considering typical values for ferritic-martensitic steels reported in the literature range from ~1 x 10^{14} – 1 x 10^{15} m^{-2} [13,40,42]. Previous work on HT9 [91] showed that changes in the dislocation sink strength within this range would not dramatically alter the swelling rate. **Figure 5.10b** compares the dislocation sink strengths at 150 dpa with the cavity sink strengths across all helium levels. At every helium level except 1000 appm, the ratio between sink strengths was above 1, signifying that the sink balance and relative importance of dislocations did not change across helium levels. **Figure 5.10a** shows that the total line length did not change significantly with helium content, therefore the dislocations did not

influence the sink structure differently across helium levels. Considering the consistency of the dislocation sink strength across four magnitudes of pre-implanted helium content, changes in the cavity microstructure cannot be attributed to changes in the dislocation microstructure.

Ni-Si clusters (G-phase) experienced an increase in size and a decrease in density as damage level was increased (**Figure 5.11**). A similar behavior was also observed in high damage irradiation on HT9 [81]. It was determined that G-phase in this alloy would have a negligible effect on the swelling behavior up to 650 dpa [91]. G-phase in the HT9 study was observed to have a sink strength of ~1 x $10^{14}m^{-2}$. By 300 dpa, the Ni-Si clusters in T91 in this study achieved a sink strength of only 0.3 x 10^{14} m^{-2}, or a factor of 20 less than that due to dislocations. Therefore, even less of an effect on cavity evolution would be expected.

In summary, <100> loops and network dislocations appear to be insensitive to implanted He content, and G-phase and <111> loops exhibit very low sink strengths which are not expected to influence cavity evolution. Therefore, changes in the cavity microstructure cannot be attributed to changes in other microstructural features. The determining factor in the differences in cavity evolution was the concentration of implanted helium.

6.2 The Influence of Carbon on Cavity Evolution

The effect of carbon on cavity evolution was determined by analyzing the results of the Excess Carbon Campaign as a function of damage, and comparing them with the results from the Nominal and Excess Carbon Campaigns. The shared conditions between these series irradiations were 150 and 300 dpa with all helium contents. These irradiations can be used as a direct comparison to evaluate the effect of carbon on cavity evolution. The following discussion focuses on explaining the suppression of cavity evolution and the loss of helium bubbles.

6.2.1 Carbon-induced suppression of cavity nucleation

The main effect of excess carbon on cavity evolution was to inhibit cavity nucleation. This behavior is clear when comparing the microstructure between the excess and the nominal carbon conditions. **Figure 6.4** shows bright field STEM images comparing the microstructure of T91 nominal carbon and excess carbon conditions following irradiation to 300 dpa. The excess carbon

conditions show a very high density of carbides and a noticeably lower density of cavities. **Figure 6.5** shows that there is a dramatic difference in the magnitude of the swelling between excess and nominal carbon conditions in the 0 appm He condition. This difference in swelling is mainly due to differences in cavity densities, as seen in **Figure 6.6**, which shows only a slight difference in the size of cavities, but almost an order of magnitude difference in density. Since the presence of excess carbon is the only difference between these conditions, it must be the cause of the difference in nucleation between the two conditions.

Several studies [57,58,62,92] have suggested that higher amounts of carbon in solution could serve as trapping sites for vacancies, with a strong binding energy estimated at ~0.41 eV [93]. The trapping mechanism enhances recombination and reduces the supersaturation of vacancies which would inhibit cavity nucleation. While carbon could only be detected via the volume fraction of carbides, there is likely a high concentration of carbon in solution or associated with unresolvable carbon-defect clusters. At 460°C, the expected solubility of C in T91 is very low, approximately 0.05%, or 500 appm. Since precipitation occurred constantly from 150 to 450 dpa, carbon in solution is likely maintained at or above the saturation point—which would provide a high density of vacancy trapping sites within the matrix.

The NRA profiles in **Figure 5.23** suggest a total concentration of about 2.5% carbon after 450 dpa. A calculation of the amount of carbon in carbides can be used to estimate the amount of carbon accounted for by M_2X. It is assumed that the carbides are M_2X with a hexagonal crystal structure of a = 0.272 nm and c = 0.452 nm, and they have a regular parallelepiped shape with the same width and thickness. Utilizing the measured density and average volume of the carbides, the number of hexagonal unit cells and hence the average number of carbon atoms per precipitate was calculated, and yielded a concentration of 2.09 ± 0.42% C. Given that the initial carbon concentration in the alloy is approximately 0.5%, this calculation accounts for roughly all 2.5% of carbon measured by NRA.

Since precipitation is occurring, it is likely that the amount of carbon in solution is maintained at the saturation point. The uptake of excess carbon due to irradiation could increase the amount of trapping sites in a couple of ways. Either the carbon in solution is increased to a super-saturated, metastable state due to the irradiation process, or small M_2X precursors/carbon clusters not visible in TEM serve as traps for vacancies. However, given that almost all of the excess carbon was accounted for by visible M_2X carbides, the amount of super-saturated carbon

or carbon in small clusters cannot exceed the error of the carbon content calculation (0.42% or 4200 appm of C). Work on HT9 by Getto [94] suggested that carbon in solution was a much stronger suppressor of swelling than M_2X sink strength, and that significant swelling suppression would occur with 500 appm of carbon in solution. Therefore, the presence of up to 4200 appm of C in the form of super-saturation or small clusters would be expected to also have a significant suppressive effect on cavity nucleation in addition to any effect of the M_2X sink strength.

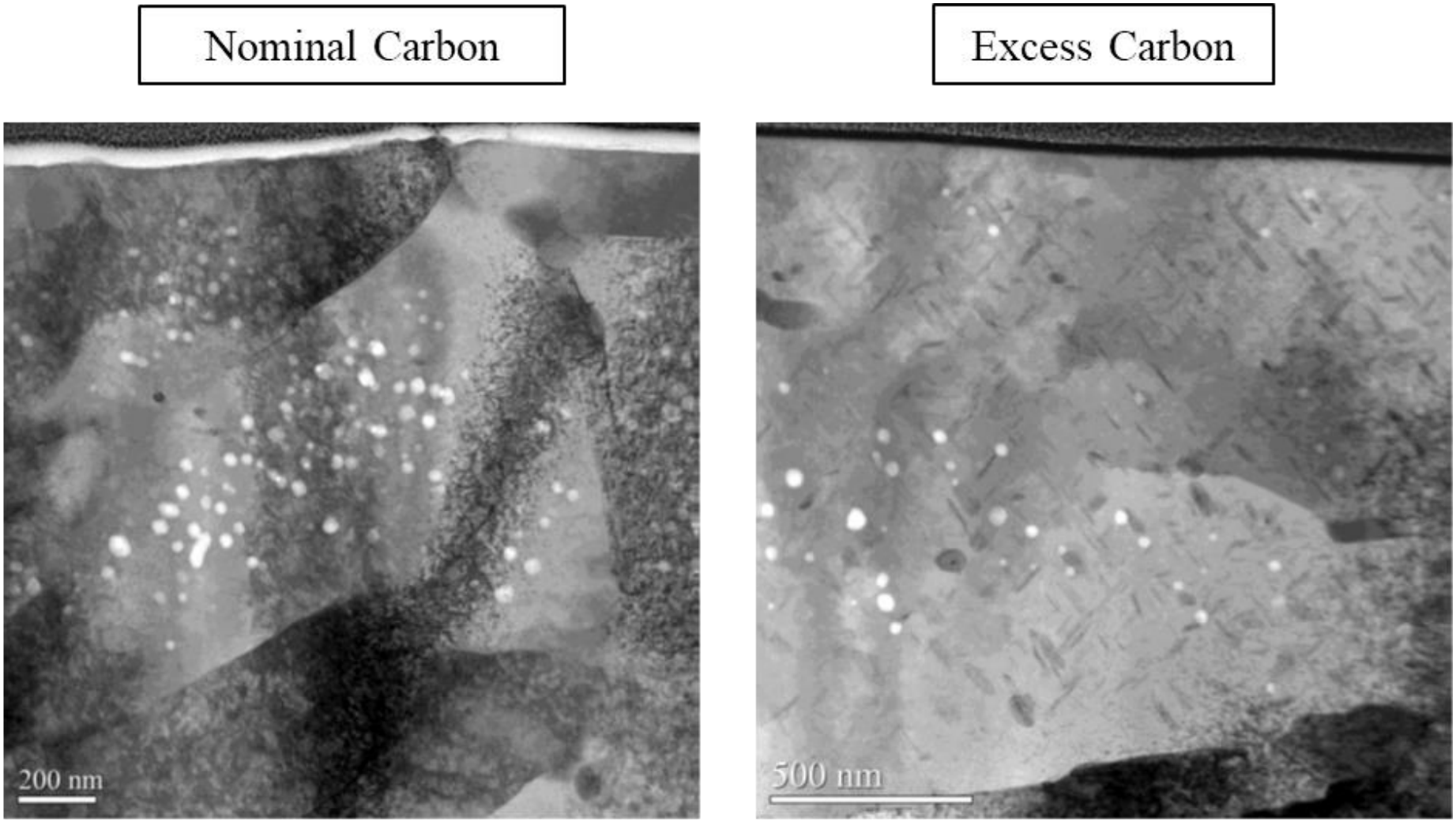

Figure 6.4. Bright field STEM images of T91 irradiated to 300 dpa with nominal and excess carbon levels using 5.0 or 4.4 MeV Fe^{2+} ions at 460°C.

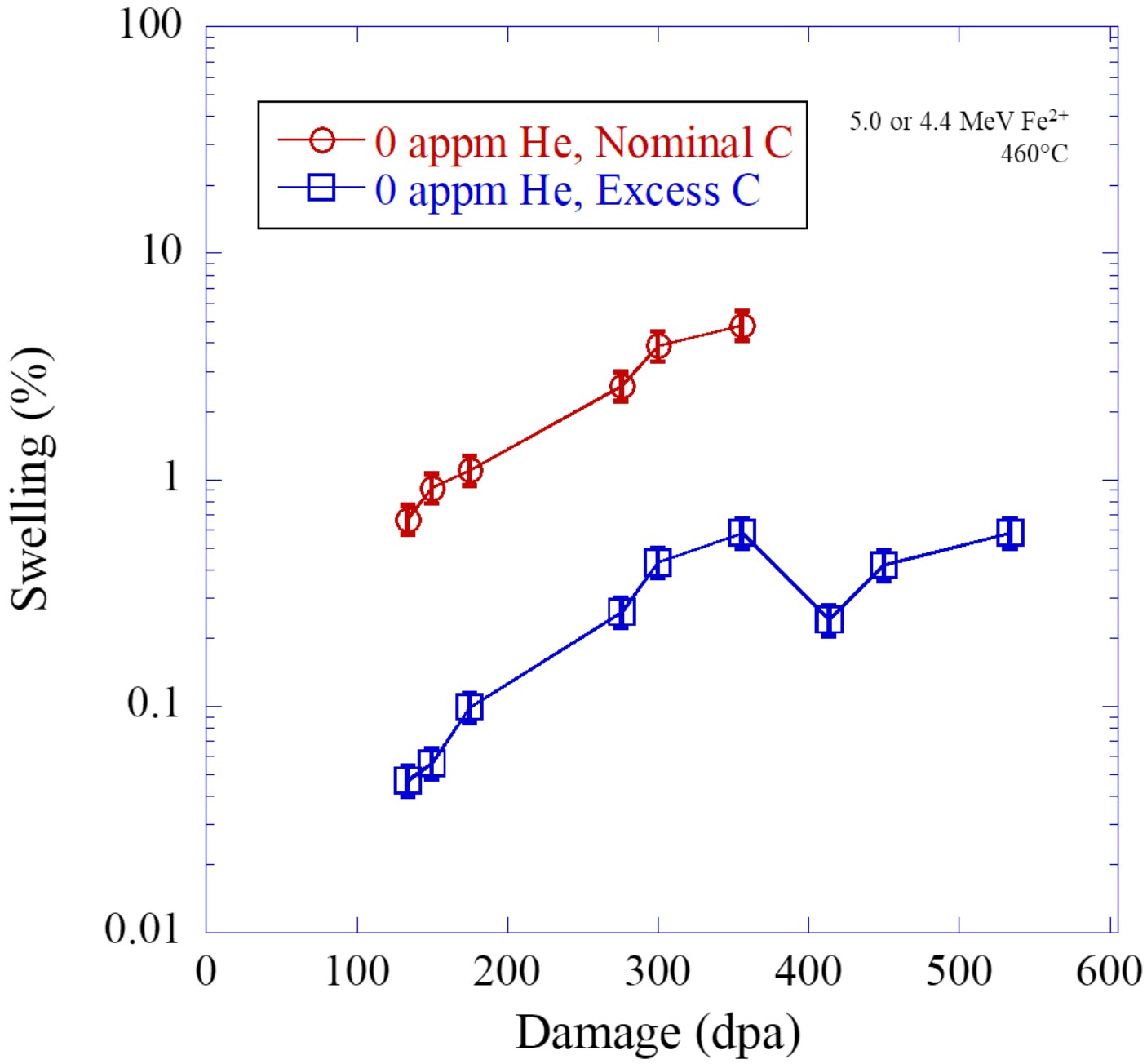

Figure 6.5 Swelling as a function of damage for nominal and excess carbon T91 with no helium implantation.

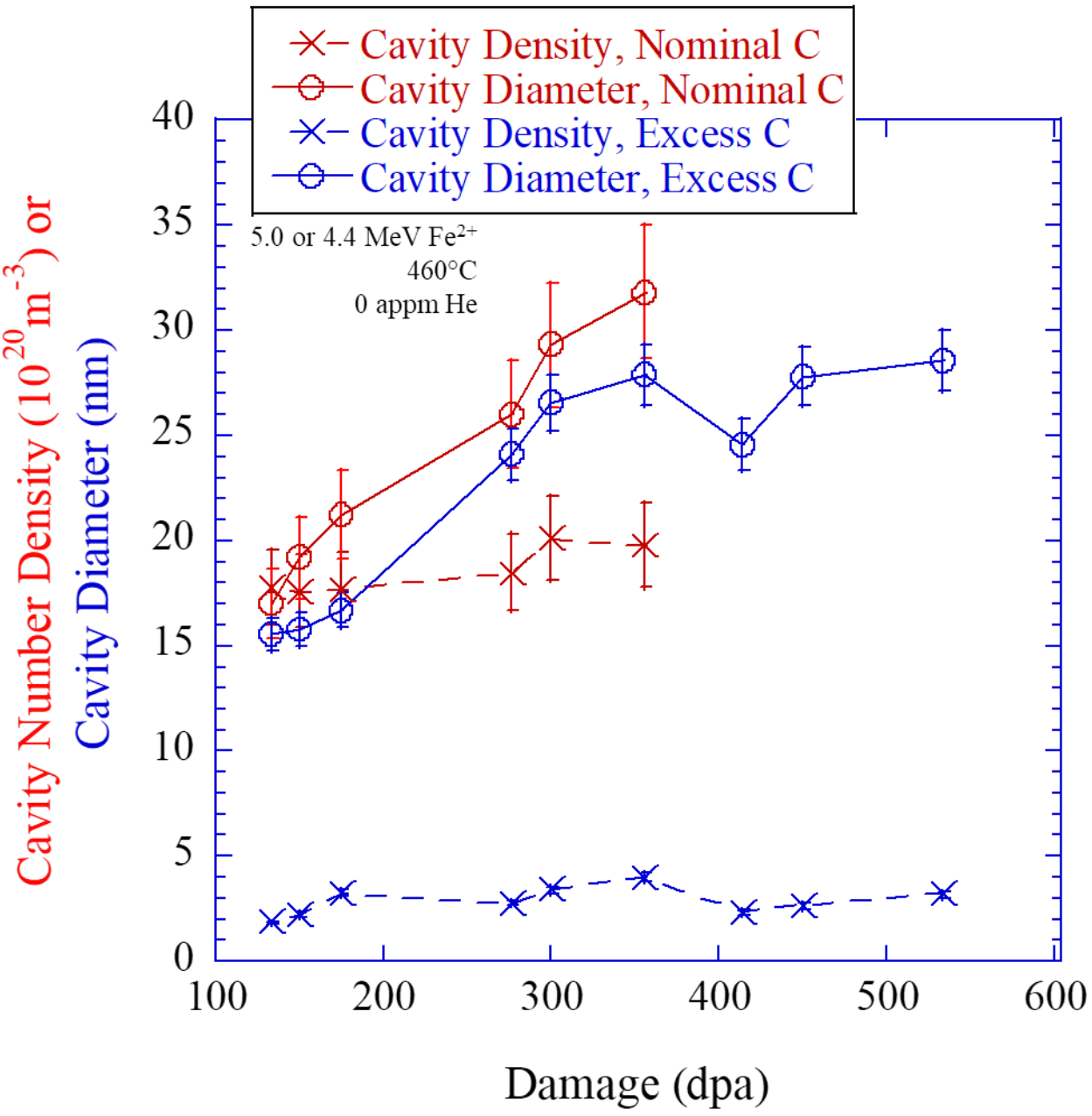

Figure 6.6 Cavity number density (red dashed) and cavity diameter (blue solid) as a function of damage for nominal and excess carbon samples of irradiated T91, implanted with no He.

6.2.2 Carbon-induced suppression of cavity growth

A significant carbide sink strength also likely contributed to suppression of cavity growth. **Figure 6.5** shows a slightly reduced cavity diameter in the excess carbon condition with 0 appm He, suggesting that the presence of carbides may only have a minor effect on growth. The diameters between the excess and nominal conditions track very well, with similar growth rates. However, the excess carbon conditions experienced a slightly lower diameter through 300 dpa. This may be due to the role carbon plays in inhibiting nucleation, which would serve to increase the incubation period relatively to the nominal carbon condition. Since it was more difficult for cavities to nucleate in the excess carbon condition, growth could not occur until a higher damage level, so the diameter in the excess carbon condition lags behind that of the nominal condition.

It is also possible that carbon begins to suppress the growth of cavities at 450 dpa due to a high carbide sink strength effect. The excess carbon samples were irradiated further to 450 dpa, where they experienced a complete arrest in swelling (**Figure 5.12c**). From 300 to 450 dpa, the swelling in the 0 appm He excess carbon condition essentially remained the same at ~0.43%, with the diameter increasing by only 1.2 nm and the density decreased from 3.4 to 2.6 x 10^{20} m^{-3}. The size distributions plotted in **Figure 5.15** also clearly show that growth in the 0 appm He condition was suppressed compared with the 1 and 10 appm He conditions. Both the 1 and 10 appm He conditions exhibit a noticeable shift in the size distribution to larger sizes when increasing from 300 to 450 dpa, while the 0 appm He condition does not.

This complete suppression of swelling in the 0 appm He condition can be explained by looking at the cavity and carbide sink strengths. **Figure 6.7** plots the ratio of carbide sink strengths to cavity sink strengths for all implanted helium levels at 300 and 450 dpa. At both damage levels, the 0 appm He condition exhibited the highest ratio of carbide to cavity sink strength of 5 at 300 dpa, which increased to ~10 at 450 dpa. The remaining helium levels (excluding 1000 appm at 450 dpa) exhibited sink strength ratios ranging between 1 – 3. The 0 appm helium condition was the only condition to exhibit a complete arrest in swelling, and it is likely due to the fact that the carbide sink strength was much higher compared to the cavity sink strength. In the 0 appm He condition, the carbides were clearly the dominant sink in the system, which left few excess vacancies to provide growth for the few existing cavities.

Swelling suppression in the presence of carbon is two-fold. Nucleation of cavities is suppressed, likely through a combination of carbide sink strengths and carbon in solution. The few cavities that do nucleate are subject to suppression of growth via the carbon trapping effect and a substantial sink strength of carbide precipitates.

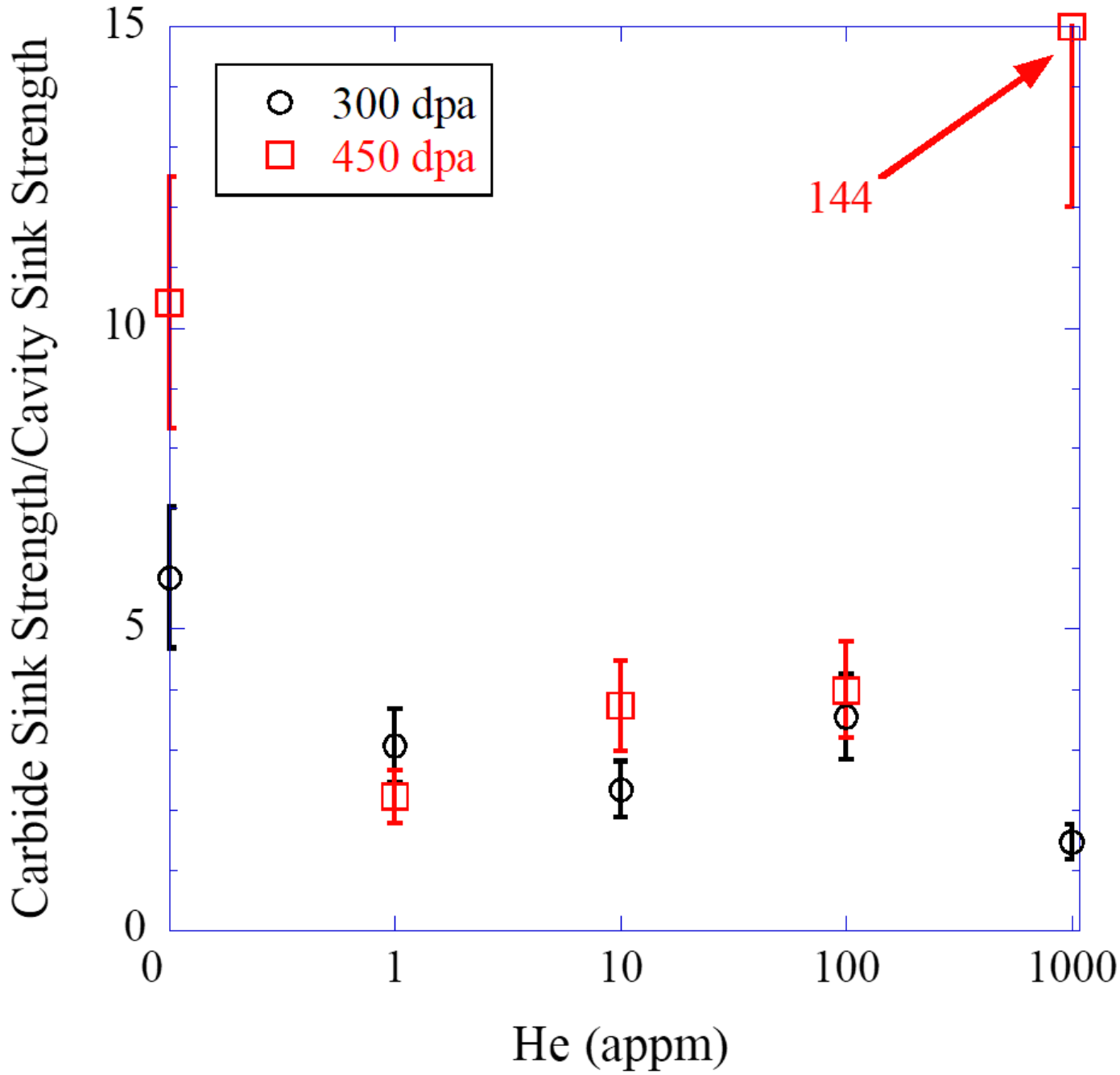

Figure 6.7 The ratio of carbide sink strength to cavity sink strength for the excess carbon T91 samples at 300 and 450 dpa are plotted as a function of He content.

6.3 Interaction of Carbon and Helium

In addition to suppressing overall swelling, the presence of carbon was also found to change the swelling behavior as a function of helium content. The study with nominal carbon samples showed that swelling tended to decrease monotonically with increasing helium content. Small additions of helium (1 or 10 appm) did not significantly alter the cavity distributions, and large additions of helium (100 or 1000 appm) resulted in the creation of a bimodal distribution and significant swelling suppression.

Figure 6.8 shows a comparison of the cavity size, density, and swelling behavior between the nominal and excess carbon conditions in T91 at 150 dpa as a function of helium content. At all helium levels, the swelling is lower in the excess carbon condition. Additionally, the trend of swelling with helium is different in the excess carbon samples. The excess carbon samples exhibit a peak in swelling at 10 appm He, whereas maximum swelling occurs at 0 appm He in the nominal carbon samples (**Figure 5.3c** vs **Figure 5.13c**). This peaked behavior as a function of helium in the excess carbon condition is fundamentally different than that of nominal carbon condition.

The peaked behavior in the excess carbon samples occurs due to competing effects on nucleation. As mentioned in the previous section, the main effect of excess carbon was to inhibit cavity nucleation, which can be clearly seen in **Figure 6.8b**. Addition of helium tends to counteract this effect to some degree and promote nucleation. Therefore, swelling increased with the addition of helium up to 10 appm. Conditions with helium levels lower than 10 appm suffered from cavity suppression due to excess carbon and lack of helium. Conditions with helium higher than 10 appm suffered from suppression due to excess carbon and high helium content.

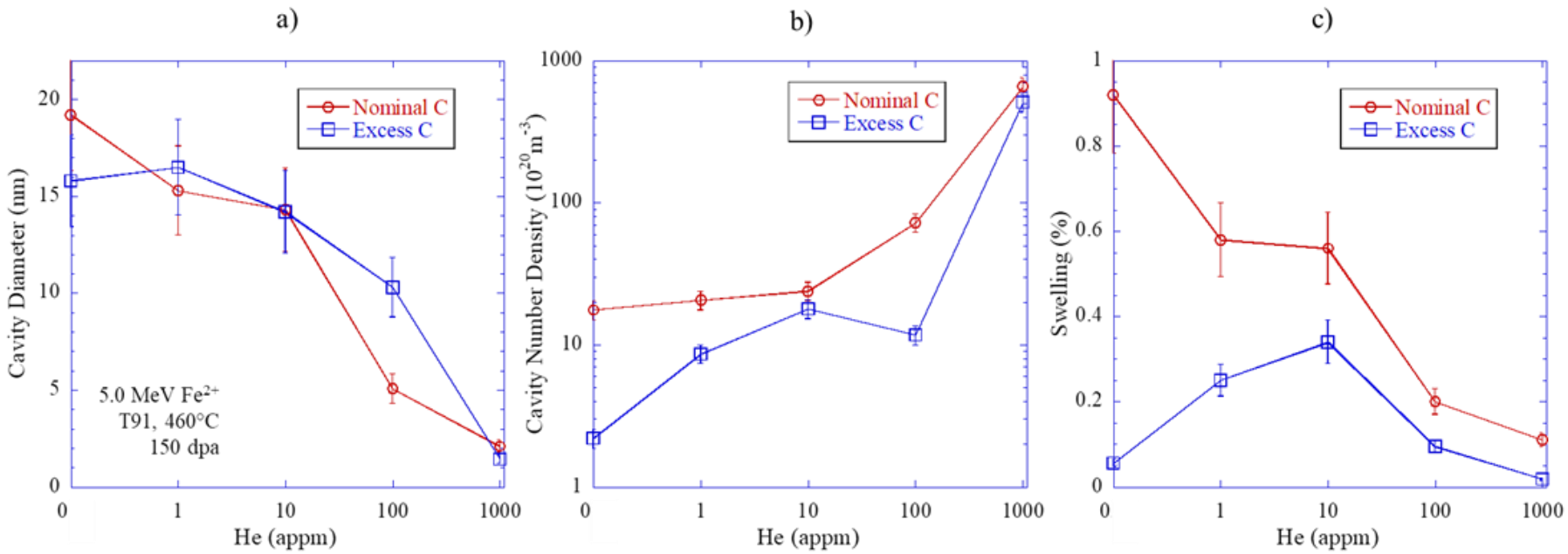

Figure 6.8 a) Cavity diameter, b) cavity number density, and c) swelling as a function of He content for the nominal and excess carbon conditions in T91 at 150 dpa.

6.3.1 Carbon-induced helium bubble dissolution

The most dramatic difference between the nominal and excess carbon conditions is the effect of carbon on the bubble populations in the highest helium condition. The 1000 appm He T91 nominal carbon condition exhibited a high density of bubbles that remained stable from 50 to 300 dpa and disappeared by 450 dpa, resulting in a unimodal distribution, a drop in cavity density and an increase in diameter (**Figure 5.12a** and **Figure 5.12b**). The disappearance of bubbles was only observed in the excess carbon condition at the highest damage level, whereas the nominal carbon condition bubble population maintained its density at all damage levels. Since the only difference between the two cases was the presence of excess carbon, it had to play an integral role in the dissipation of helium bubbles.

The loss of bubbles between 300 and 450 dpa (**Figure 5.16**) cannot simply be explained by sink strengths. While the carbide sink strength increased substantially (~3x) between 300 and 450 dpa, the cavity distributions in **Figure 5.16** show that the small bubbles were preferentially disappearing over the larger cavities. A strong carbide sink strength would mainly serve to reduce bias-driven growth, which would preferentially affect the larger cavities, not helium-stabilized bubbles. For carbides to be the factor influencing the disappearance of He bubbles, they must exert an effect not captured by the sink strength.

The HAADF STEM images in **Figure 5.17** show that many of the small bubbles appear to be decorating the carbides at 300 dpa, suggesting an association between the carbides and helium bubbles. Both carbon and chromium are known to segregate to cavity surfaces and form precipitates [62,95,96]. **Figure 5.22a** shows an increasing density of carbides in the 100 and 1000 appm He conditions going from 300 to 450 dpa, indicating the carbides may have preferentially nucleated on helium bubbles. It is very likely that the bubbles nucleated prior to the carbides, since bubbles were observed as early as 50 dpa in the nominal carbon condition.

For the helium bubbles to dissolve, helium atoms must be ejected from the bubbles. There are several mechanisms that could cause the disappearance of helium bubbles; resolution by displacement cascades, thermal emission, and bubble coalescence. Resolution of helium atoms from damage cascades has been predicted by several models [97–100] and has also been observed to occur experimentally in Fe-Cr alloys [101]. Thermal emission of helium is only observed at

very high temperatures. The He dissociation energy from bubbles is estimated from molecular dynamics studies [102,103] to be ~2.12 eV, which is high enough to prevent helium emission at 460ºC unless bubbles are extremely over-pressurized. Helium bubbles with high pressure (high He/vacancy ratios in the range of 4-5) are likely to emit helium atoms. However, since bubbles in this work are assumed to be at or below equilibrium pressure, thermal helium emission is very improbable.

Once free from a bubble, the helium atoms are free to migrate back to the bubble or diffuse elsewhere and possibly nucleate a second generation of bubbles. However, carbides can serve as a sink for emitted helium atoms. Further, the proximity of the carbides to the bubbles eliminated the need for long-range migration of He to reach the matrix-carbide interface.

Since the M_2X carbides grow to relatively large sizes (in excess of 50 nm by 450 dpa) and exhibit a high surface area, it is possible that helium emitted from bubbles disperses along the carbide interface rather than re-clustering into visible bubbles. M_2X has been previously characterized by Getto [73] as semi-coherent within the HT9 matrix. M_2X primarily grows in the [101] direction (length), which exhibits a 16% d-spacing mismatch with the matrix. This would result in misfit dislocations occurring along this direction approximately once every 1.4 nm. Misfit dislocation sites have been known to be the primary occupational site for helium at semi-coherent interfaces [104–107]. Given that the M_2X carbide length nearly doubled between 300 and 450 dpa and their density increased significantly as well (**Figure 5.22a**), the number of sites for the emitted helium atoms would also have increased. Dissipation of bubbles only occurred in the presence of significant M_2X precipitation at 300 dpa and above. At 150 dpa, the bubble density was similar to that of the nominal carbon condition (comparing **Figure 5.13b** with **Figure 5.3b**), indicating that carbides are yet to have an effect. However, once significant carbide densities formed by 300 dpa, the density of bubbles in the excess carbon condition decreased. The large drop in bubble densities between 300 and 450 dpa (seen in **Figure 5.16** distributions) occurred only because of the increase in carbide size and density.

Helium emitted by cascade displacement would find a preferential site at misfit dislocations along the matrix-carbide interface. Molecular dynamics calculations by Heinisch *et al*. [108] estimate that the binding energy of helium atoms at dislocations to be approximately 2.5 eV, which is strong enough to prevent helium emission up to temperatures of ~530°C. Therefore,

any helium emitted from bubbles will find energetically favorable sites to occupy at nearby misfit dislocations on the M_2X-matrix interface.

In addition to providing a site for helium atoms, the M_2X carbides may also influence helium bubble loss by decreasing the vacancy flux to bubbles. The M_2X carbides are oversized precipitates in the T91 matrix, and thus require a vacancy flux to grow. Since the precipitates grew significantly between 300 and 450 dpa (**Figure 5.22**), they must have served as strong vacancy sinks. The extremely high sink strength achieved in the 1000 appm He condition (14.4×10^{14} m^{-2} by 450 dpa) and the spatial proximity of the carbides to the bubbles would significantly reduce the vacancy flux to bubbles. Incoherent or semi-coherent precipitates have been known to serve as fast diffusion paths for point defects created during irradiation [15], which can channel defects along the surface to pre-existing bubbles. A similar mechanism could result in the coalescence of helium bubbles at the precipitate interfaces. From the images shown in **Figure 5.17**, it is not clear whether the larger cavities in the 450 dpa case were pre-existing or formed as a result of coalescence of helium bubbles. While the exact mechanisms for the disappearance of the helium bubbles cannot be determined by taking snapshots at coarse damage levels, the displacement cascade resolution and bubble coalescence at the matrix-precipitate interface offer two likely explanations.

The absence of bubbles in the excess carbon condition of the 100 appm He case also suggests He bubble dissolution. No bimodal cavity distribution was observed at any damage level for the 100 appm He excess carbon case. Since swelling suppression was still apparent in the 100 appm He condition (**Figure 5.13a**) relative to the lower helium conditions, it is possible that a bimodal distribution of cavities was present early in the irradiation, but by 150 dpa all of the bubble sites had been dispersed by carbide precipitation. Since the 100 appm He condition would exhibit a lower density of bubbles compared to the 1000 appm He condition, it is reasonable to expect that the bubbles were dispersed at a lower damage level.

It is clear through the evidence presented in the 100 and 1000 appm He excess carbon conditions that the formation of M_2X was responsible for the dissolution of helium bubbles.

6.5 Helium retention

In addition to enhancing the mobility of vacancies, higher temperature irradiations will also enhance the mobility of the helium atoms themselves. The high mobility of helium at temperature

becomes a concern of helium retention. As discussed in **Section 6.1.2**, all of the helium could not be accounted for in the observed bubble populations in the 100 and 1000 appm He conditions. It is possible that helium is capable of diffusing away from the irradiated/implanted region of the sample, or possibly escape through the surface.

There was no evidence that helium escape was occurring in the T91 samples of this work. Helium is known to be a very fast diffuser in iron with a migration energy of only ~0.06 eV [109]. However, under irradiation conditions and in ferritic-martensitic alloys, helium's mobility can be severely limited by the density of traps in the material. As mentioned previously, helium can be trapped at dislocations with a binding energy of ~2.5 eV, which is enough to prevent de-trapping up to 530ºC. High concentrations of vacancies, and the presence of Cr up to 10% have also been known to limit the mobility of helium in complex ferritic alloys [110]. Given that helium bubbles at grain boundaries were not observed in any condition in this work, it is likely that helium mobility was not high enough to escape trapping at dislocations or other features within the matrix.

Additionally, if helium made it to the surface, it would be expected to agglomerate at the interface of the alumina coating and the metal in the nominal carbon samples. However, no significant bubble formation was observed at this interface. In fact, alumina coatings have been shown to retain helium in spent nuclear fuel [111], and would actually serve a similar purpose for the alumina-coated T91.

In the excess carbon samples, there was a distinct effect on swelling with each increment in helium level. **Figure 5.15** shows significant differences in the cavity distributions between 0, 1, and 10 appm He. Even the addition of 1 appm of He had a dramatic effect on increasing the cavity nucleation. This suggests that if helium was escaping, it was less than 1 appm in all conditions. Furthermore, the bubble distributions of the 150 dpa, 1000 appm He excess and nominal carbon conditions are almost identical (**Figure 5.16** and **Figure 5.7**), suggesting that helium was distributed similarly in both cases. Therefore, the excess and nominal carbon conditions likely retained the same amount of helium. Lastly, the carbides formed in the excess carbon samples would also contribute to reducing the mobility of helium by trapping it at misfit dislocation sites.

Measurements of helium content and pressure contained in bubbles have been performed in martensitic steel EM10 using EELS techniques [112], however these measurements were only performed with extremely high helium levels (~5000 appm). While direct measurements of the helium content could not be made in the T91 samples, the lack of bubbles near the surface and at

grain boundaries, and the application of an alumina layer means that the majority of the helium was likely retained within the irradiated region. Even if a fraction of the helium escaped the irradiation region, the value of the results in this thesis remain, as it is the trends with varying helium content that are essential, rather than the actual helium values themselves.

6.6 Applications to reactor systems

Pre-implanted helium is several steps removed from in-reactor generation of helium, and it is essential to consider the differences and the effects on cavity evolution that may result from these differences.

Perhaps the most obvious difference is that in the pre-implanted helium case, the entire amount of helium is present from the beginning, whereas in-reactor the helium is slowly generated over time. This will generate a difference in the initial densities of the cavities. **Figure 5.2b** shows that the cavity densities for all pre-implanted conditions have essentially saturated by 50 dpa. The 0 appm He condition shows an increase in cavity density up to about 150 dpa, but thereafter stabilizing at similar cavity densities with the 1 and 10 appm He conditions. In a reactor situation, where the helium will be slowly generated, it is likely that cavities will evolve in a manner in between that of the 0 appm He condition and the 10 appm He condition. The extent to which the evolution is more similar to the 0 appm He condition or the 10 appm He condition will depend on the helium generation rate.

In the high damage regime (>150 dpa), the low helium cases and the 0 helium conditions all converged to similar cavity distributions (**Figure 5.4**). At this point, the growth process has become dominant and the swelling and cavity distributions become more and more similar. Initial differences in the nucleation behavior of the cavities become less important, so the differences between helium levels is less clear. In a reactor situation, this behavior for low helium generation rates would likely be the same. Small differences in He content do not seem to affect growth significantly, and therefore the cavity evolution would be governed by the cavity sink strengths, similar to the pre-implanted case.

The formation of bimodal distributions in reactor may result in somewhat different swelling behavior at high helium levels compared to the pre-implanted case. Because the bimodal

distributions in the pre-implanted case are present very early (< 50 dpa), their suppressive effect on growth is present the entire time. Conversely, in a reactor environment, it would require more time for the helium levels to build up to a point where bimodal distributions will form. By the time this occurs, it is possible to have cavities which have already grown significantly. Since the bimodal distributions may not necessarily be present from early on in irradiation, their suppressive effects will not be as substantial and higher swelling would be expected in a reactor condition relative to a pre-implanted condition. However, the final value of swelling would depend on when exactly a bimodal distribution forms relative to the growth of other cavities. Additionally, because some cavities were allowed to grow, the relative size difference between the small bubble distribution and the cavity distribution would be expected to be larger in a reactor environment as well.

The results of the nominal carbon samples from this thesis show that in general, swelling actually decreases with increasing helium content (**Figure 5.3c**). This result is counter-intuitive to the generally well accepted notion that helium tends to promote swelling. The results in this thesis show that helium's effect on cavity evolution is mostly relevant in the nucleation regime, at low damage levels. While helium may promote swelling at lower damage levels (see 50 dpa case in **Figure 5.3c**), the work performed in this thesis was the first to show the *lack* of a helium effect on cavity evolution at high damage levels. At high damage levels, the swelling is dominated by growth, so small differences in helium content become unimportant. If helium levels are high enough to form a bimodal distribution, suppression of growth will occur, and swelling will remain low overall.

Despite using ion irradiation and helium pre-implantation, this work highlights possible avenues to minimize swelling in reactor conditions. Swelling can be reduced either through minimizing cavity nucleation, or reducing cavity growth. For high damage applications, minimizing the growth of cavities will be the more effective strategy. Small amounts of helium do not result in significantly different growth rates compared to the 0 appm He condition. Additionally, very high amounts of helium early on will result in low swelling due to suppressed growth. Therefore, high helium concentrations may be beneficial for high damage applications. However, for reactor applications where low overall damage levels are expected, helium will tend to increase swelling, as nucleation will dominate the cavity evolution.

The excess carbon results highlight the importance of understanding the interaction between helium and the microstructure. Excess carbon creates a difficult nucleation environment and delays the onset of cavity growth. Adding helium (up to 10 appm) actually increases swelling since helium combats the nucleation suppression effect of carbon. However, the suppression effect due to high helium levels remains the same. The results from the excess carbon samples are relevant for conditions where cavity nucleation is difficult, such as high sink strength materials, ODS alloys, or materials with high impurity concentration. Small amounts of helium in these environments may increase the swelling by encouraging cavity nucleation.

The work performed in this thesis provides a map for different helium regimes, which can be used to evaluate the possible susceptibility of a system to swelling for reactor applications. With careful consideration of the material system, the damage level, and the amount of helium, this work can be used to guide efforts to minimize swelling. Additionally, this work also provides insight into the expected cavity evolution of other ion beam experiments, and the potentially deleterious effects of carbon contamination. The knowledge provided in this thesis will be useful to interpret both previous and future results for the ion beam and nuclear materials community.

CHAPTER 7: CONCLUSIONS

This chapter presents the significant conclusions gathered from the results and analysis presented in Chapters 5 and 6. These conclusions focus on addressing the objective discussed in Chapter 3: **To determine the role of pre-implanted helium and carbon on the cavity evolution in ion-irradiated T91**.

Regardless of carbon content, cavity density increased monotonically with increasing helium concentration.

In nominal carbon conditions, and with low helium content (0, 1, and 10 appm He), cavity evolution was controlled by cavity sink strengths.

In nominal carbon conditions, and with high helium content (100 and 1000 appm He), the creation of helium clusters reduced the critical cavity radius and resulted in the formation of a stable bimodal cavity distribution.

In nominal carbon conditions, and with high helium content (100 and 1000 appm He), a high cavity sink strength, helium trapping, and cavity bias resulted in a suppression of swelling.

In nominal carbon conditions, dislocation loops, dislocation network, and G-phase precipitates had no effect on cavity evolution.

In excess carbon conditions, cavity nucleation was suppressed due to carbon trapping of vacancies and the formation of carbides.

In excess carbon conditions, cavity growth was suppressed at the highest dose due to a high carbide sink strength.

At low He contents, excess carbon suppressed nucleation of bubbles and cavities.

In excess carbon conditions, formation of M_2X was responsible for the disappearance of the bubble population, likely with the aid of cascade resolution or bubble coalescence.

Helium content was retained within the irradiation region.

CHAPTER 8: FUTURE WORK

The results and findings of this work provided considerable insight into the role of both helium and carbon on cavity nucleation. However, there are still many unanswered questions and areas which merit further study.

The effect of helium implantation method on cavity evolution. The ultimate goal of ion irradiations to be able to accurately emulate the effects of neutron damage as seen in-reactor. The experiments performed in this study all utilized pre-implanted helium, while in a reactor, the helium is produced over time. Performing dual beam irradiations, with a He beam in addition to an Fe beam in theory would approach a more realistic emulation of reactor experiments. A rigorous series of dual beam experiments would provide additional insight into how cavities evolve in-reactor.

The effect of irradiation temperature on cavity evolution. All of the experiments in this thesis were performed at a single irradiation temperature. The behavior of helium, and its role on cavity evolution is no doubt sensitive to changes in temperature. Ion irradiation studies at various temperatures would help understand how temperature affects the formation of cavities and bubble populations.

The fate of helium atoms in the material. While it is obvious that helium had a significant role in cavity evolution, helium is very insoluble in metals and retains very high mobility. To fully understand its role in influencing cavity nucleation, it is important to know where the implanted helium atoms migrate to—whether they become trapped on dislocations, precipitates, or migrate to grain boundaries or the surface and how much is retained within cavities and bubbles. This is a

complex problem that would require advanced characterization techniques and would benefit from *in situ* experiments.

The effect of carbon in solution vs. in precipitates on cavity evolution. While this study was able to see a dramatic effect of carbon on the cavity evolution, the state of carbon could not be easily assessed. Techniques to further and accurately differentiate how much carbon was in solution and how much was in precipitates and how that evolved with damage would provide considerable insight into the mechanisms for carbon-induced cavity suppression.

Coupling of the results with modelling methods. The cluster dynamics modeling community will greatly benefit from the results presented in this thesis. However, the models currently available struggle to describe the behavior seen experimentally. As seen from the results presented in this thesis, the behavior of cavities with helium can be very complex. A comprehensive cluster dynamics model would serve to provide insight into how helium interacts with point defects at levels not observable with the microscope which ultimately result in the cavity distributions observed experimentally.

APPENDICES

APPENDIX A: TEMPERATURE HISTOGRAMS

The temperature histograms for each irradiation performed for this thesis are presented in this appendix.

NOMINAL CARBON CAMPAIGN: 50 DPA (50 DPA TOTAL), 460ºC IRRADIATION

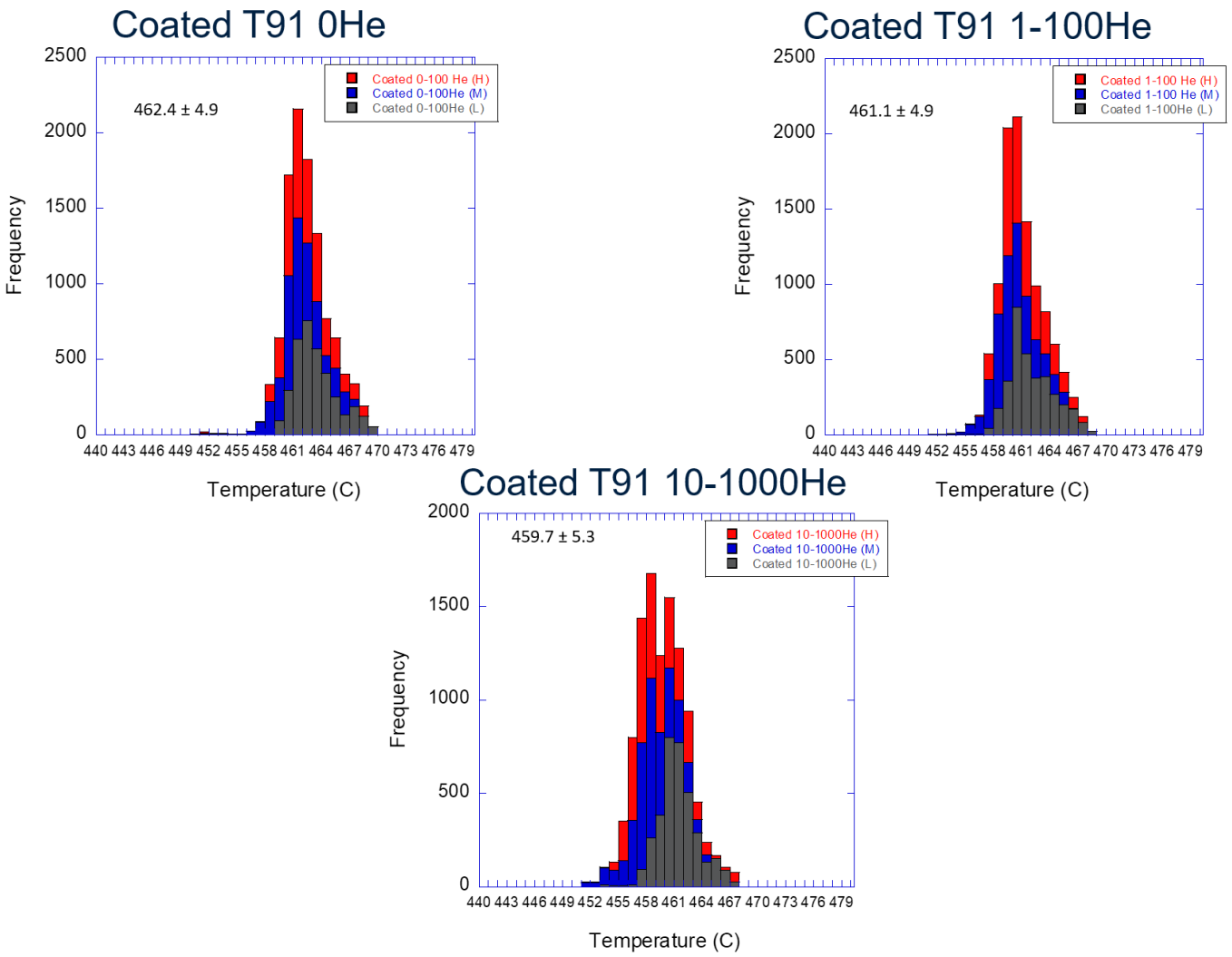

Figure A1. Temperature histograms for the 50 dpa, 460°C irradiation of alumina-coated T91 C2269 with 4.4 MeV Fe^{2+} ions for implanted He levels of 0, 1, 10, 100, and 1000 appm.

NOMINAL CARBON CAMPAIGN: +100 DPA (150 DPA TOTAL), 460ºC IRRADIATION

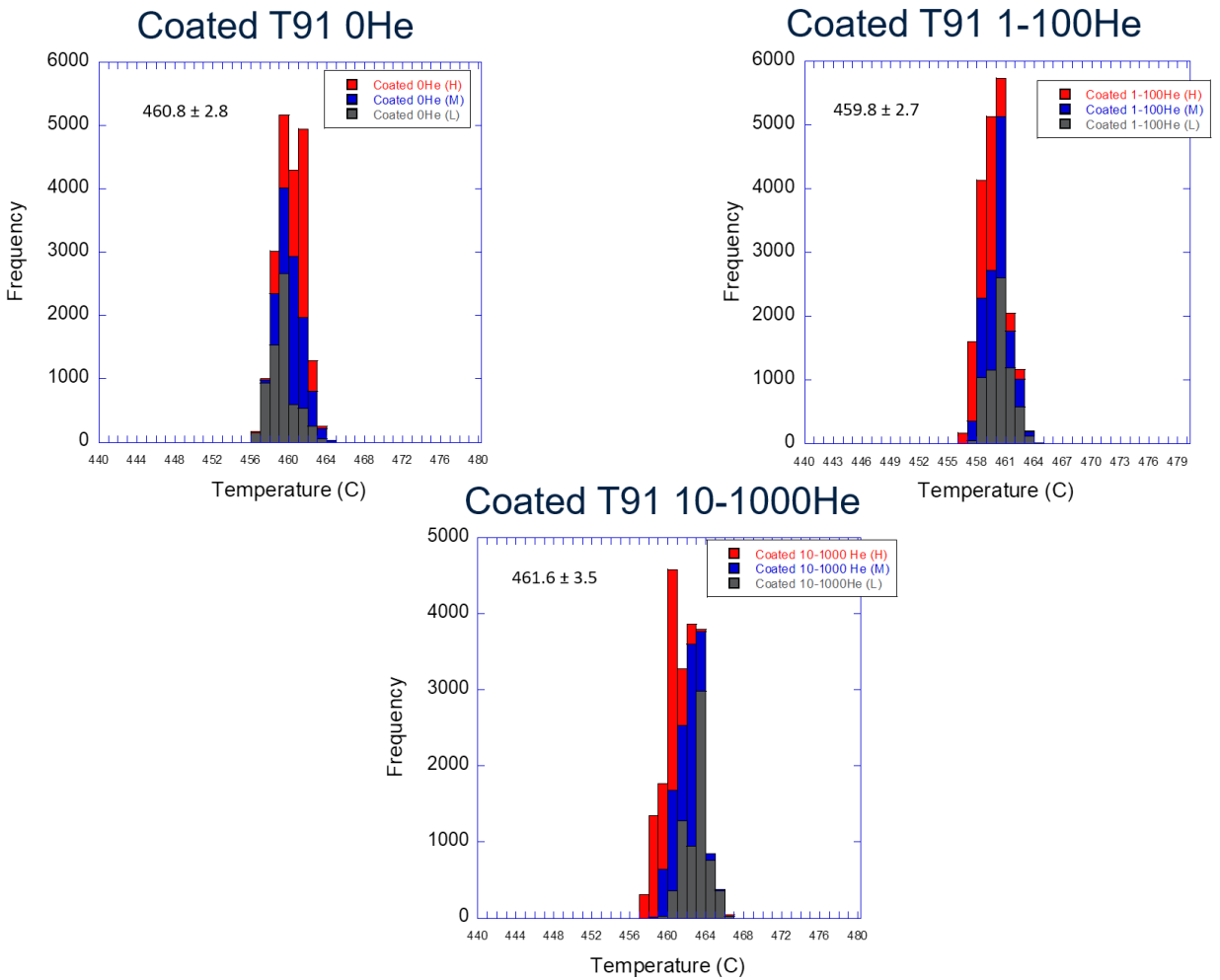

Figure A2. Temperature histograms for the +100 dpa (150 dpa total), 460°C irradiation of alumina-coated T91 C2269 with 4.4 MeV Fe^{2+} ions for implanted He levels of 0, 1, 10, 100, and 1000 appm.

NOMINAL CARBON CAMPAIGN: 300 DPA (300 D PA TOTAL), 460ºC IRRADIATION

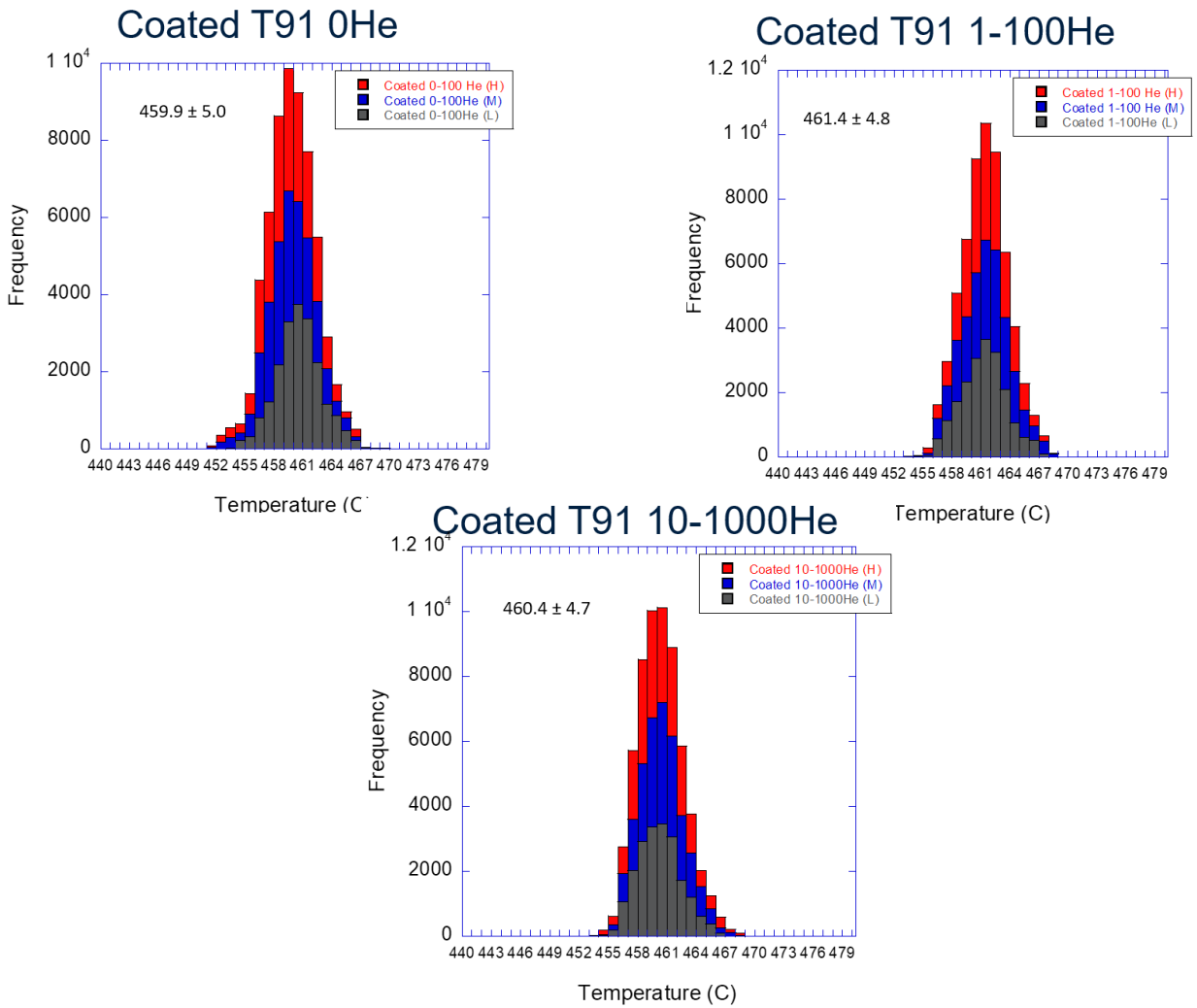

Figure A3. Temperature histograms for the 300 dpa, 460°C irradiation of alumina-coated T91 C2269 with 5.0 MeV Fe^{2+} ions for implanted He levels of 0, 1, 10, 100, and 1000 appm.

EXCESS CARBON CAMPAIGN: 150 DPA (150 DPA TOTAL), 460ºC IRRADIATION

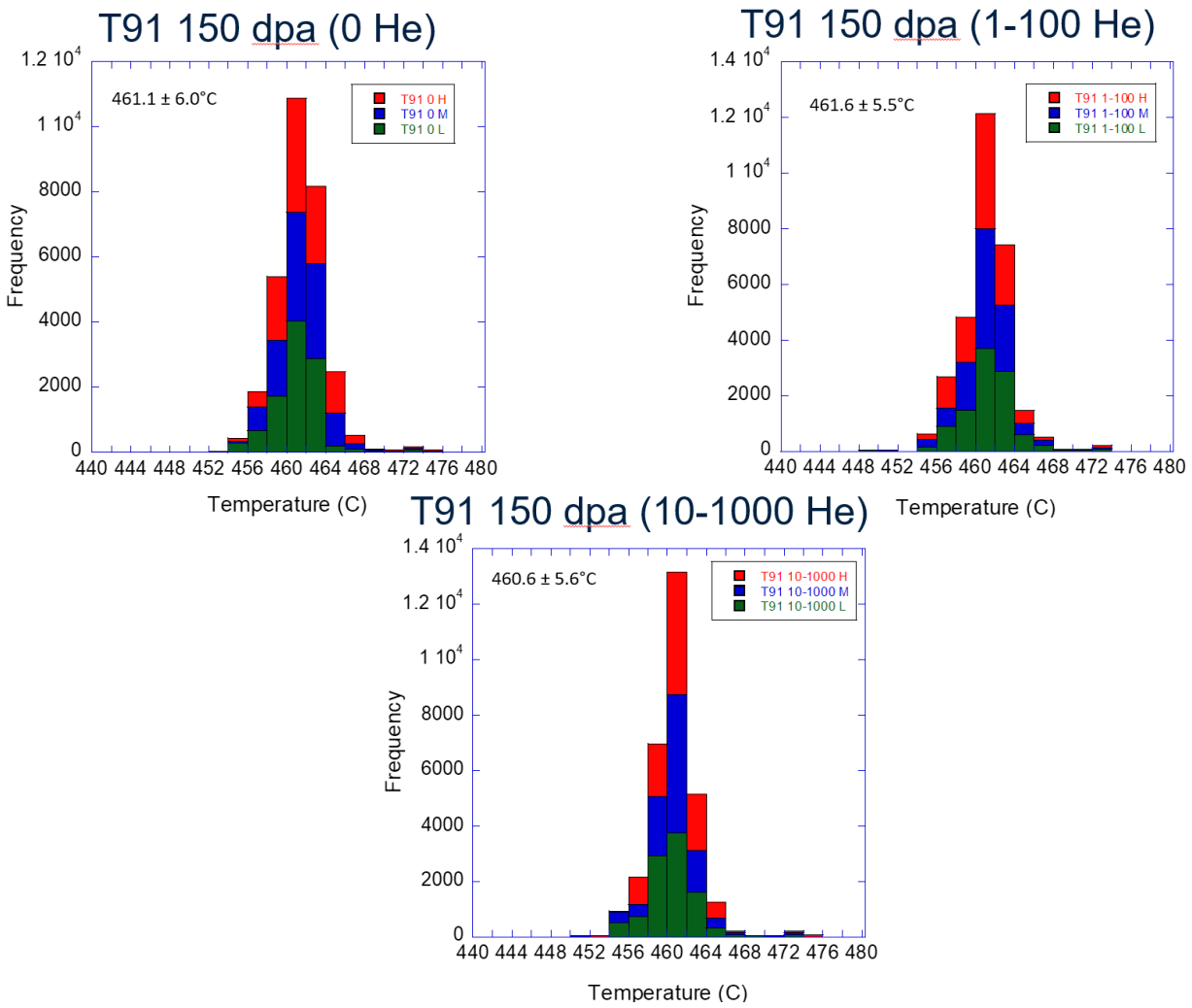

Figure A4. Temperature histograms for the 150 dpa, 460°C irradiation of uncoated T91 C2269 with 5.0 MeV Fe^{2+} ions for implanted He levels of 0, 1, 10, 100, and 1000 appm.

EXCESS CARBON CAMPAIGN: +150 DPA (300 DPA TOTAL), 460ºC IRRADIATION

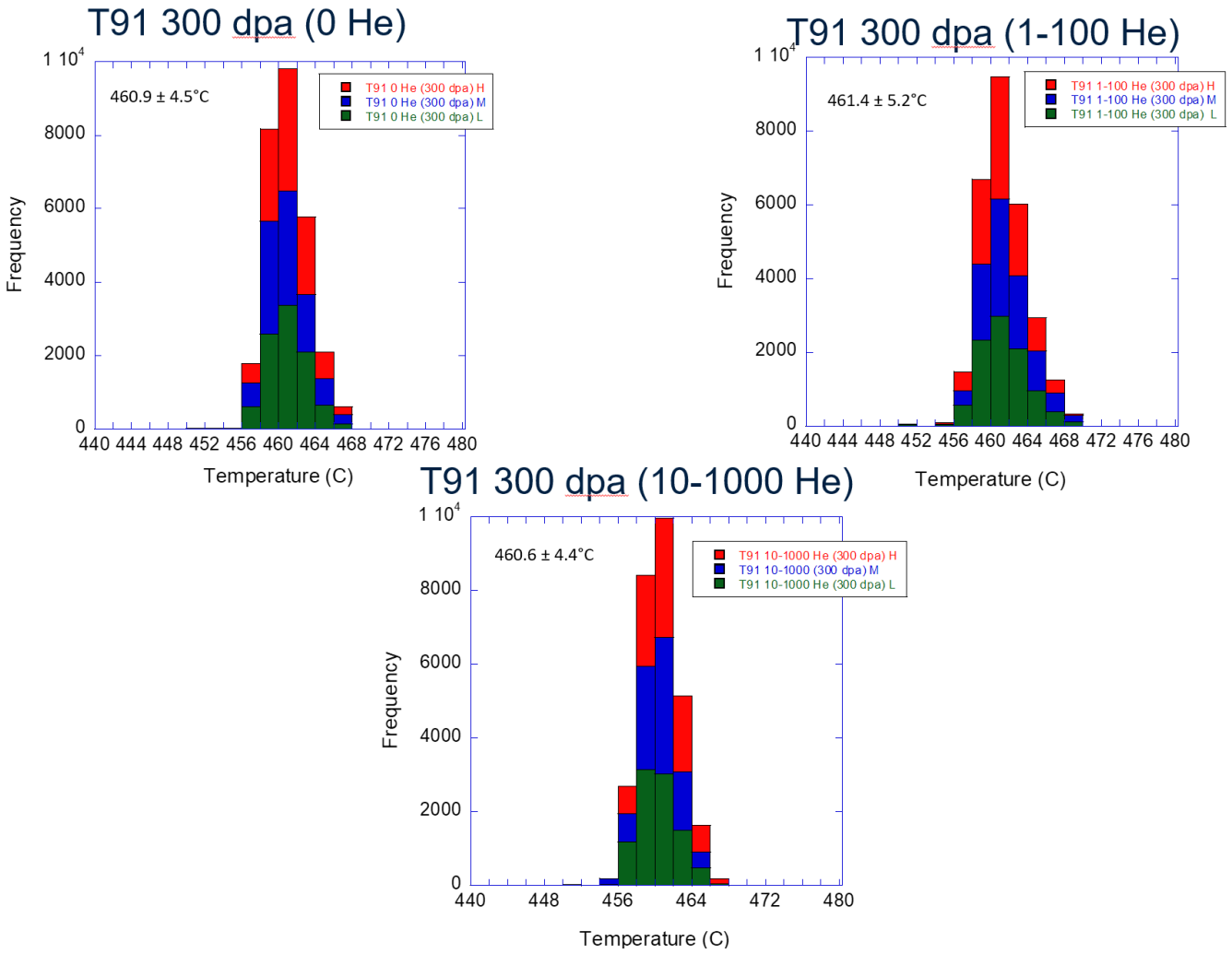

Figure A5. Temperature histograms for the +150 dpa (300 dpa total), 460°C irradiation of uncoated T91 C2269 with 5.0 MeV Fe^{2+} ions for implanted He levels of 0, 1, 10, 100, and 1000 appm.

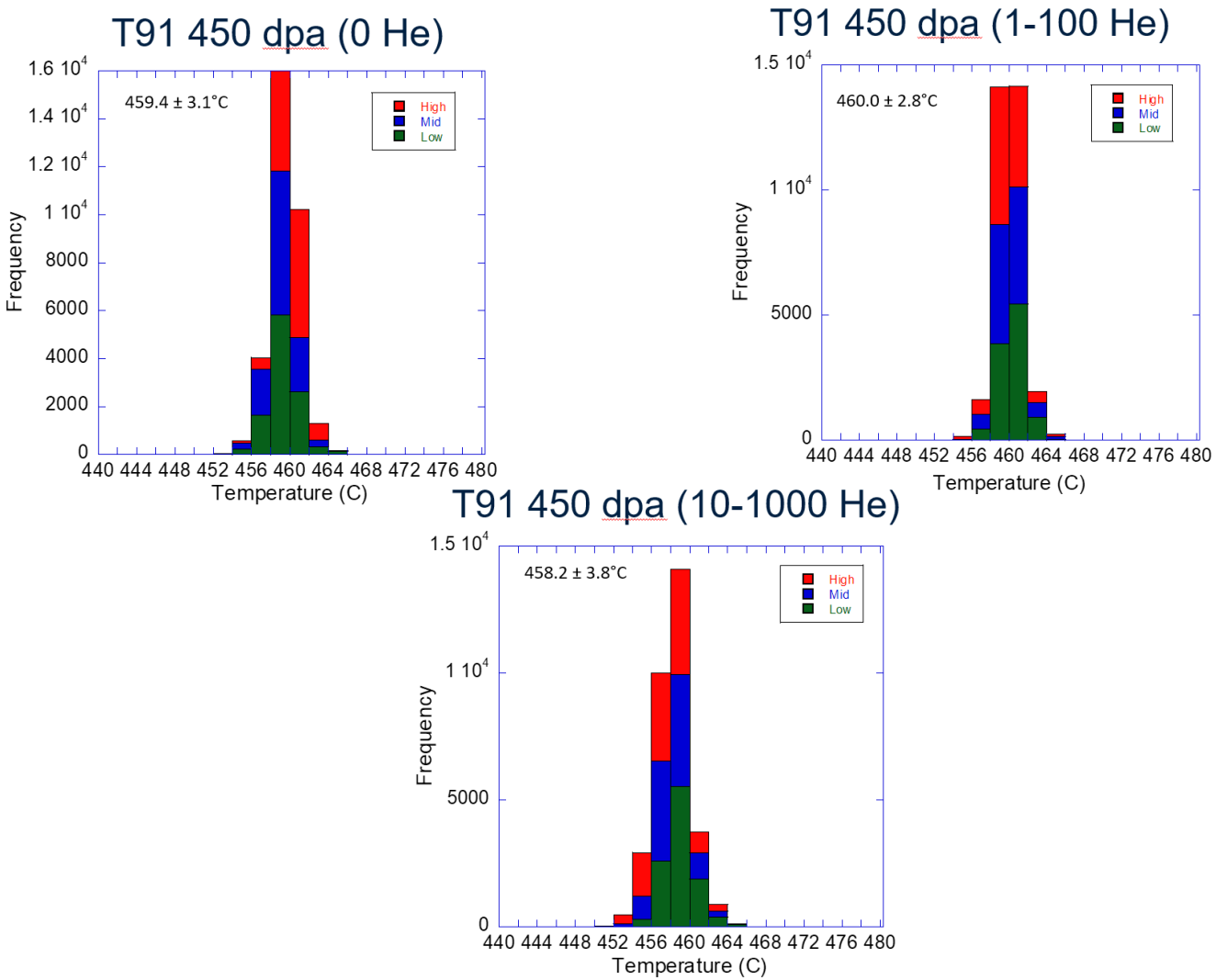

Figure A6. Temperature histograms for the +150 dpa (450 dpa total), 460°C irradiation of uncoated T91 C2269 with 5.0 MeV Fe^{2+} ions for implanted He levels of 0, 1, 10, 100, and 1000 appm.

APPENDIX B: LIFTOUT IMAGES

High angle annular dark field images (HAADF) and Bright field (BF) STEM images for each irradiated condition are presented in this appendix.

NOMINAL CARBON CAMPAIGN:50 DPA:460ºC:0 APPM HE

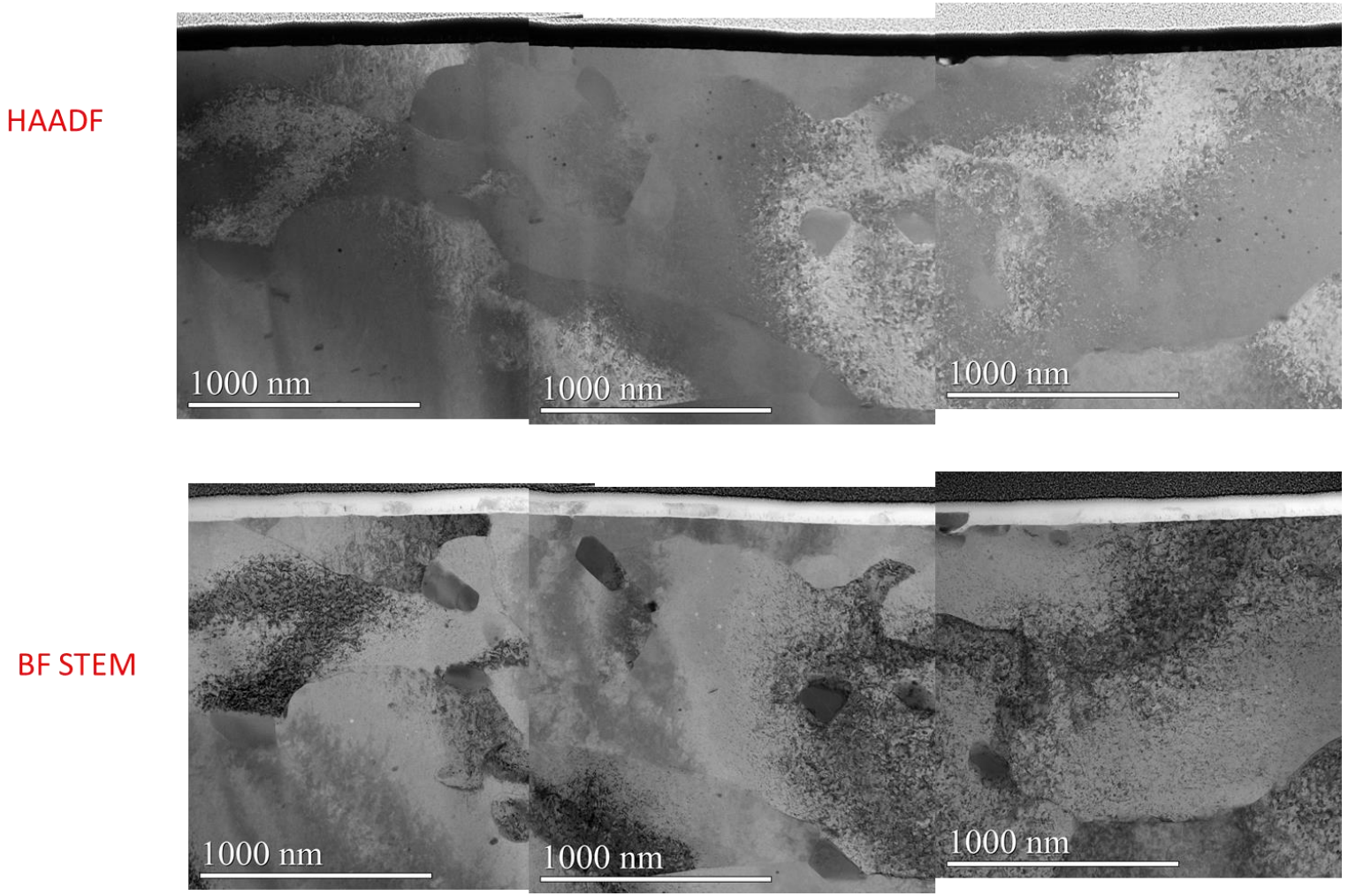

Figure B1. HAADF and corresponding BF STEM images for a liftout from the 50 dpa, 0 apppm He, nominal carbon condition.

NOMINAL CARBON CAMPAIGN:50 DPA:460ºC:1 APPM HE

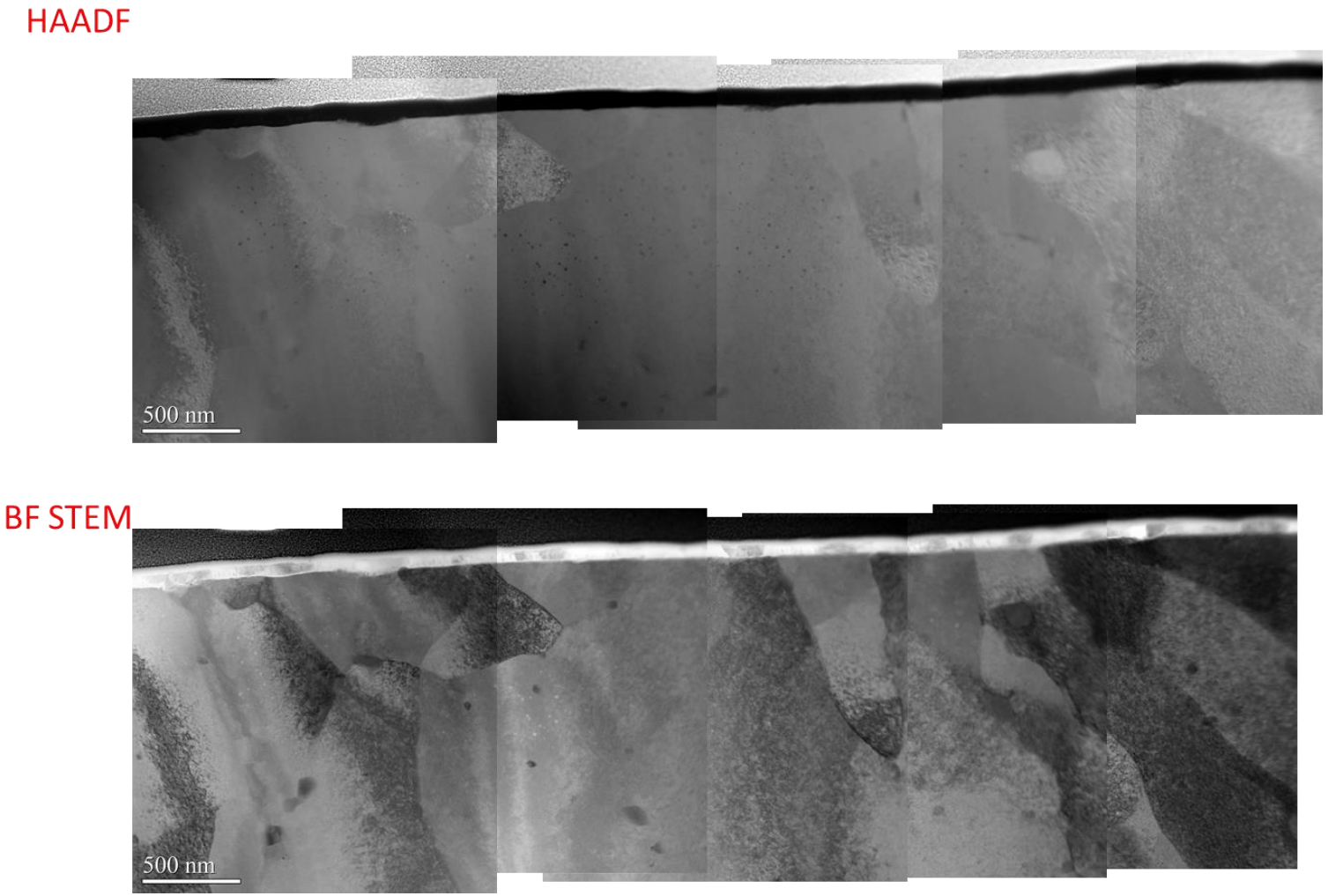

Figure B2. HAADF and corresponding BF STEM images for a liftout from the 50 dpa, 1 apppm He, nominal carbon condition.

NOMINAL CARBON CAMPAIGN:50 DPA:460ºC:10 APPM HE

HAADF

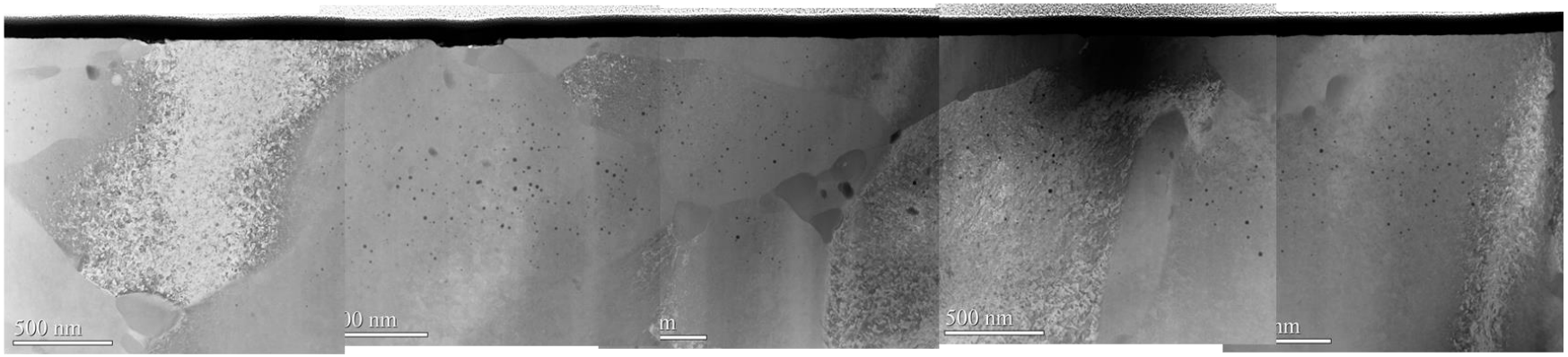

BF STEM

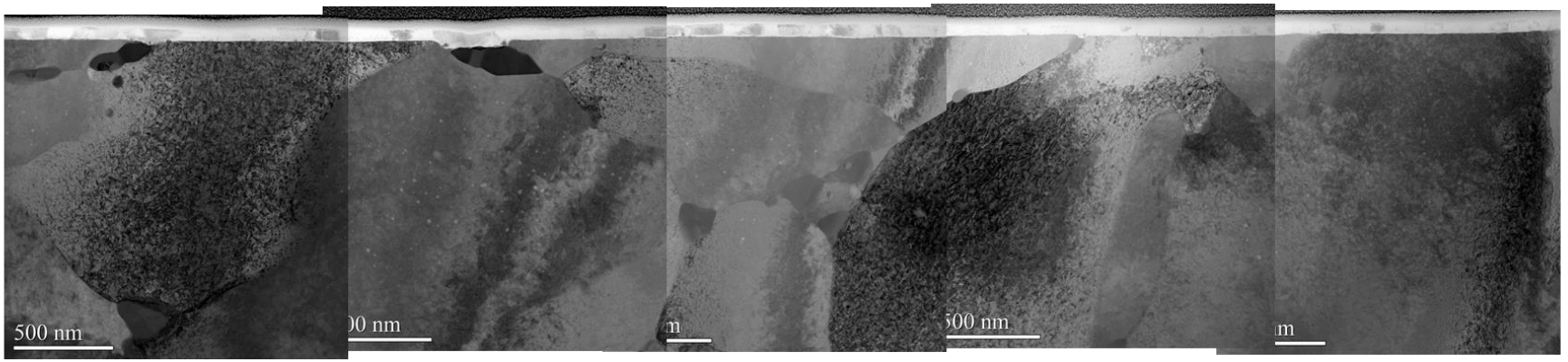

Figure B3. HAADF and corresponding BF STEM images for a liftout from the 50 dpa, 10 apppm He, nominal carbon condition.

NOMINAL CARBON CAMPAIGN:50 DPA:460ºC:100 APPM HE

HAADF

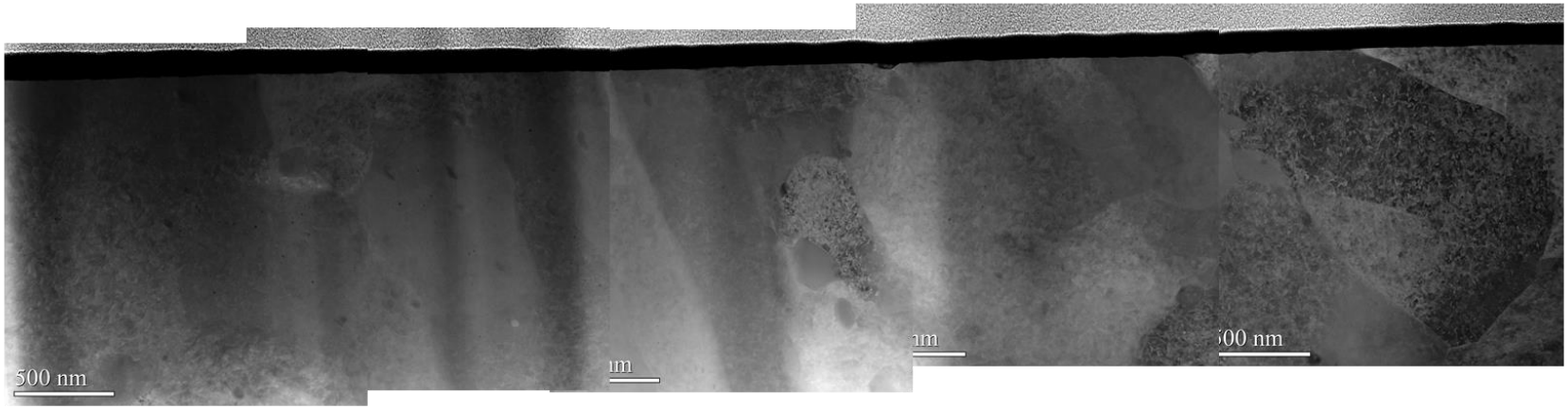

BF STEM

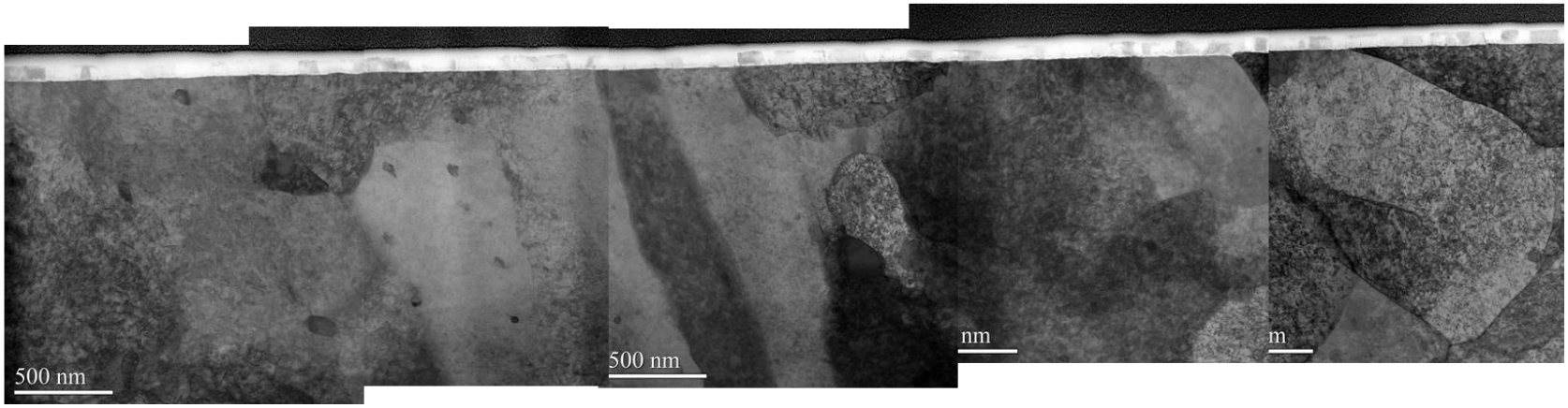

Figure B4. HAADF and corresponding BF STEM images for a liftout from the 50 dpa, 100 apppm He, nominal carbon condition.

NOMINAL CARBON CAMPAIGN:50 DPA:460ºC:1000 APPM HE

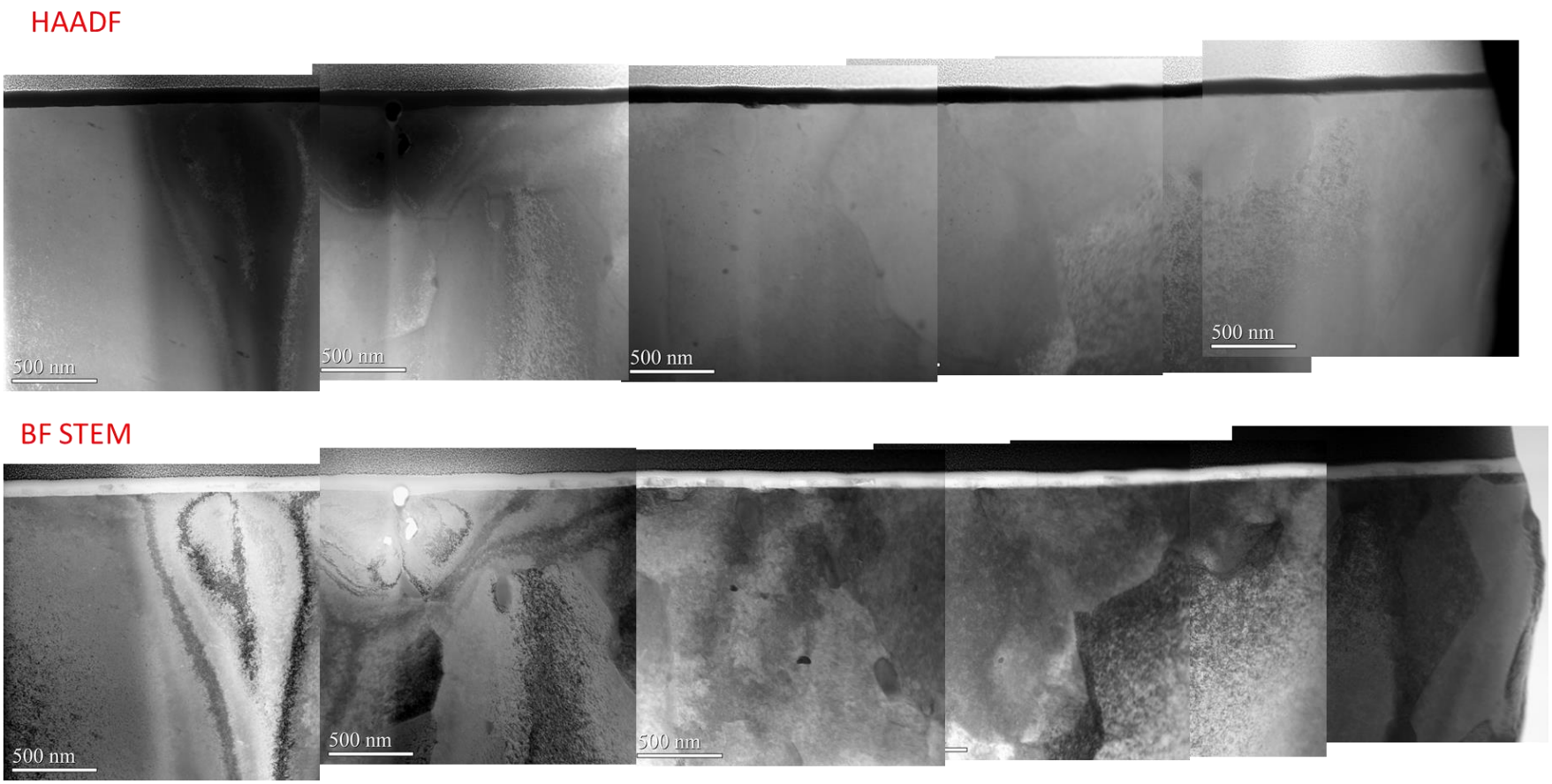

Figure B5. HAADF and corresponding BF STEM images for a liftout from the 50 dpa, 1000 apppm He, nominal carbon condition.

NOMINAL CARBON CAMPAIGN:150 DPA:460ºC:0 APPM HE

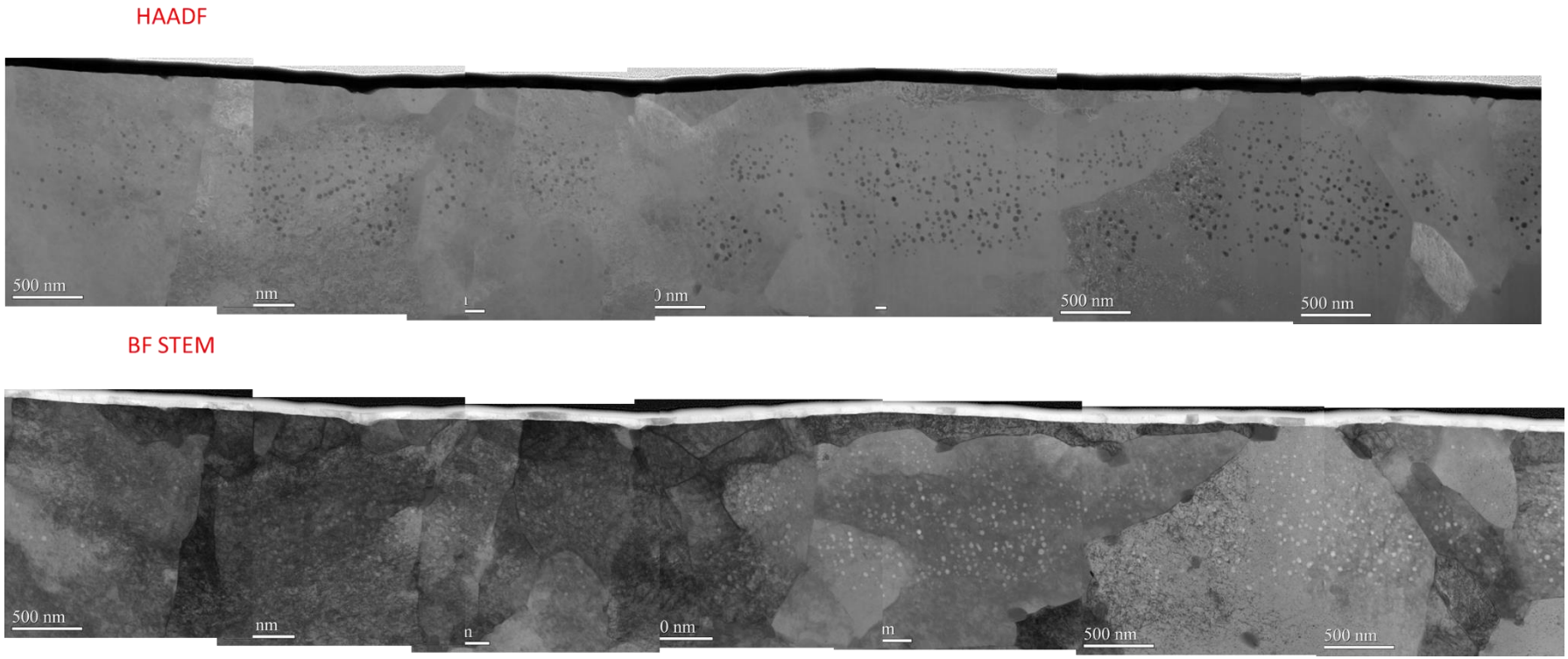

Figure B6. HAADF and corresponding BF STEM images for a liftout from the 150 dpa, 0 apppm He, nominal carbon condition.

NOMINAL CARBON CAMPAIGN:150 DPA:460ºC:1 APPM HE

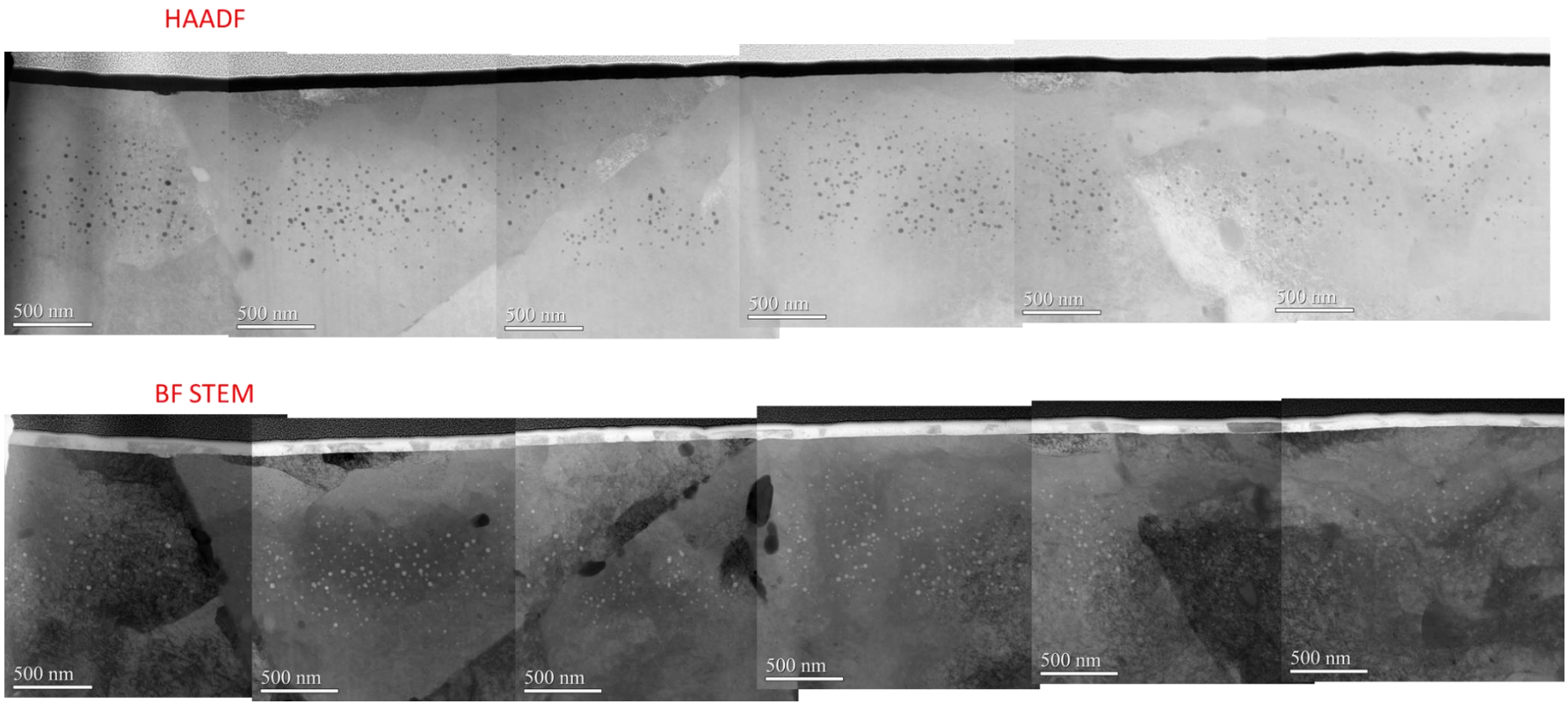

Figure B7. HAADF and corresponding BF STEM images for a liftout from the 150 dpa, 1 apppm He, nominal carbon condition.

NOMINAL CARBON CAMPAIGN:150 DPA:460ºC:10 APPM HE

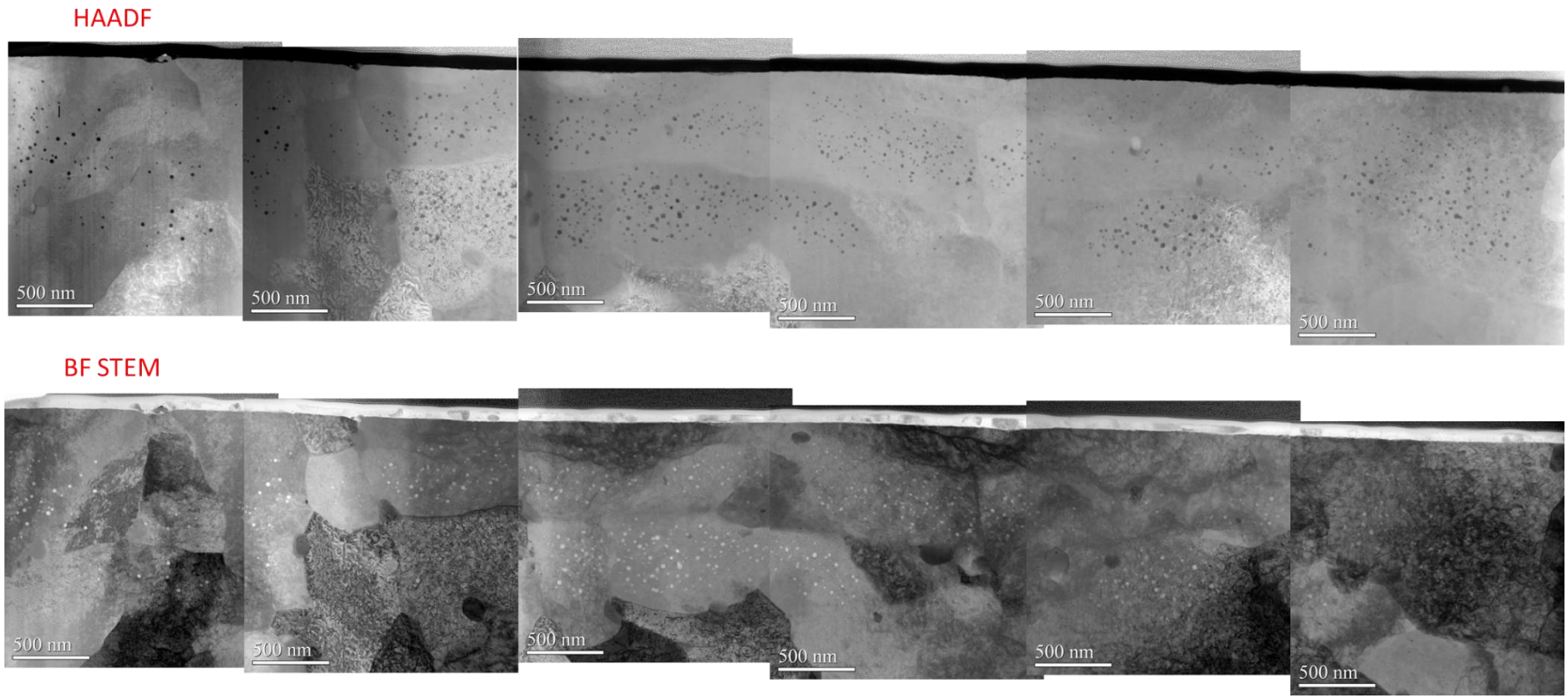

Figure B8. HAADF and corresponding BF STEM images for a liftout from the 150 dpa, 10 apppm He, nominal carbon condition.

NOMINAL CARBON CAMPAIGN:150 DPA:460ºC:100 APPM HE

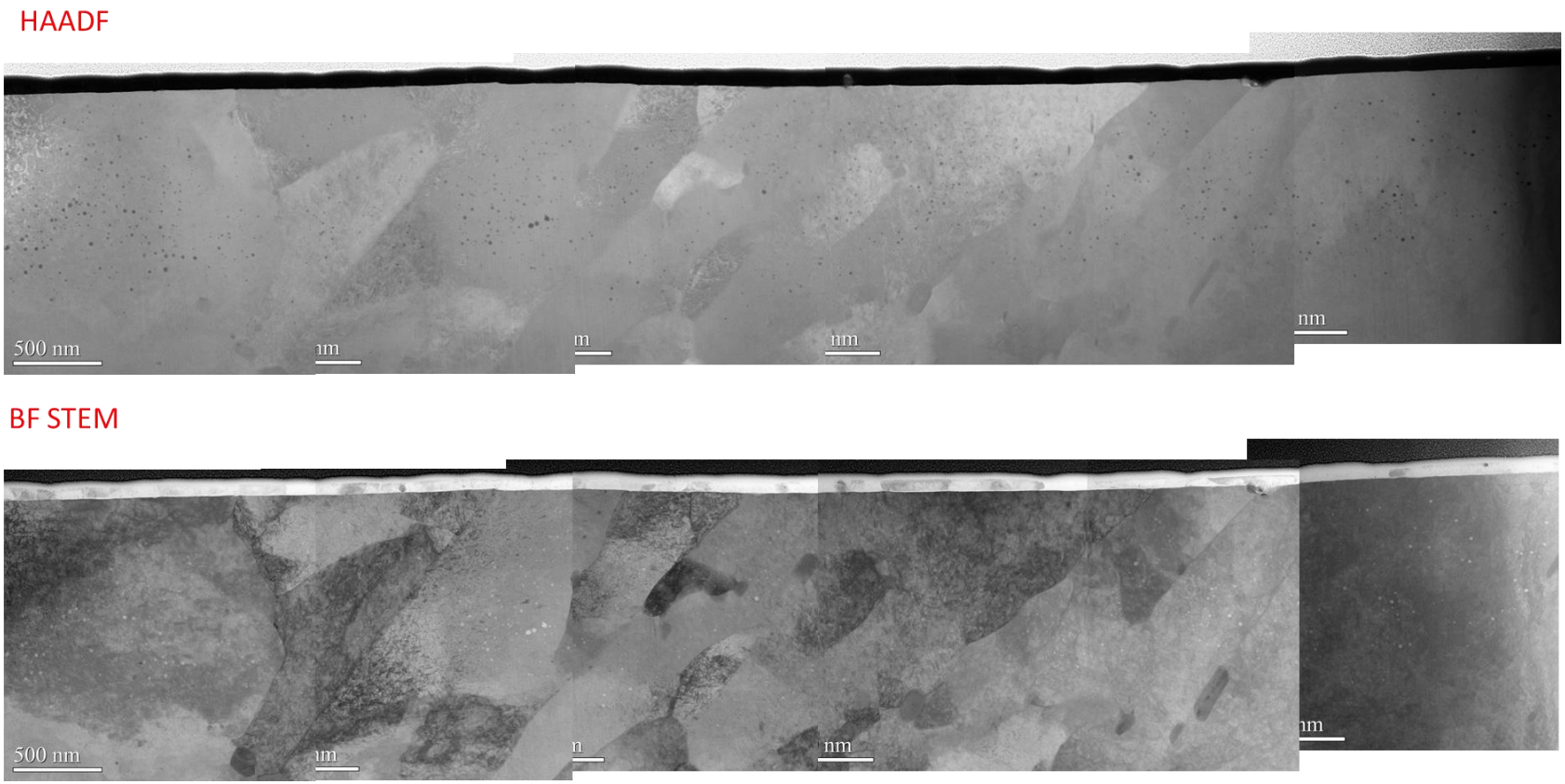

Figure B9. HAADF and corresponding BF STEM images for a liftout from the 150 dpa, 100 apppm He, nominal carbon condition.

NOMINAL CARBON CAMPAIGN:150 DPA:460ºC:1000 APPM HE

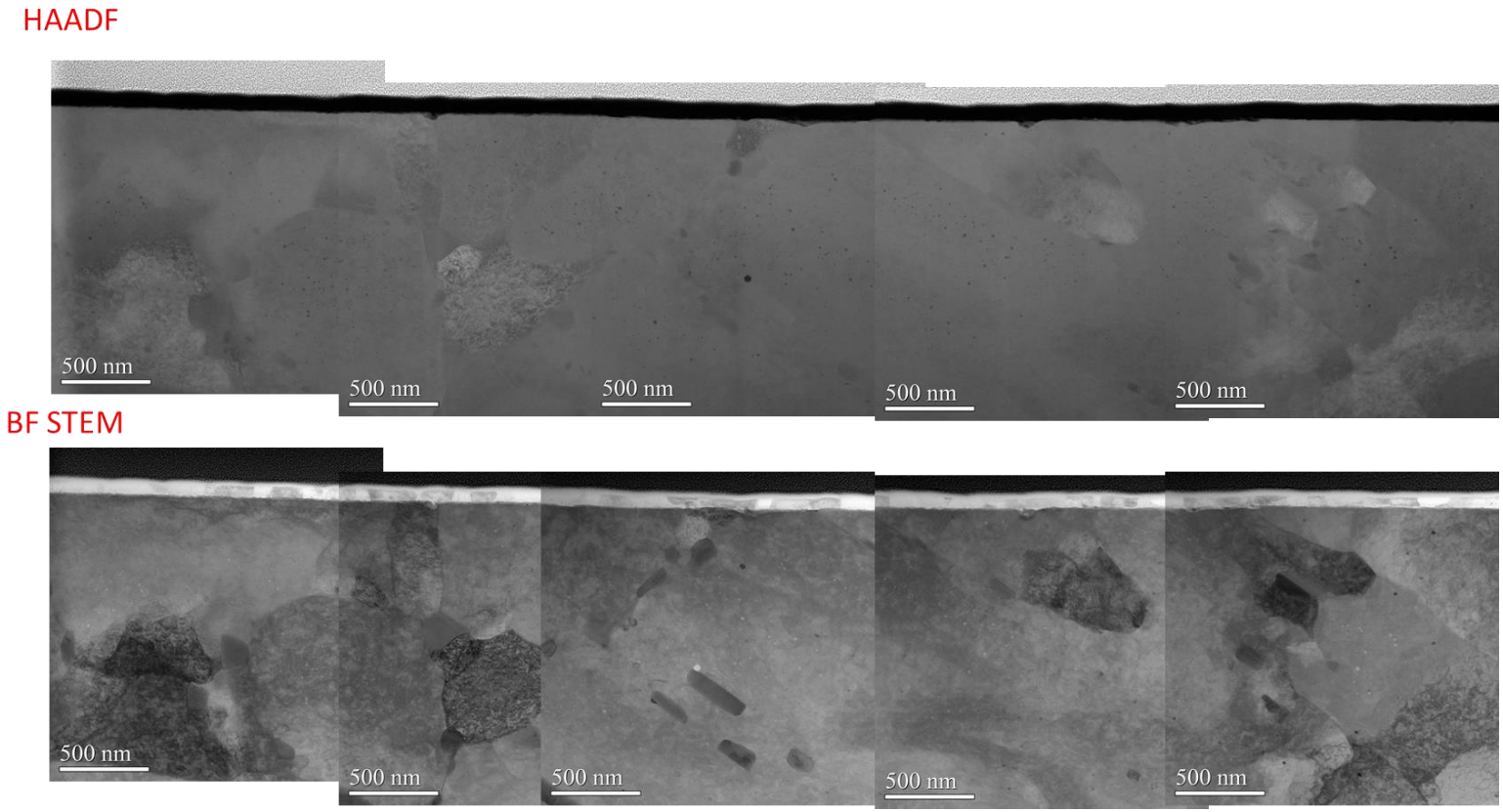

Figure B10. HAADF and corresponding BF STEM images for a liftout from the 150 dpa, 1000 apppm He, nominal carbon condition.

NOMINAL CARBON CAMPAIGN:300 DPA:460ºC:0 APPM HE

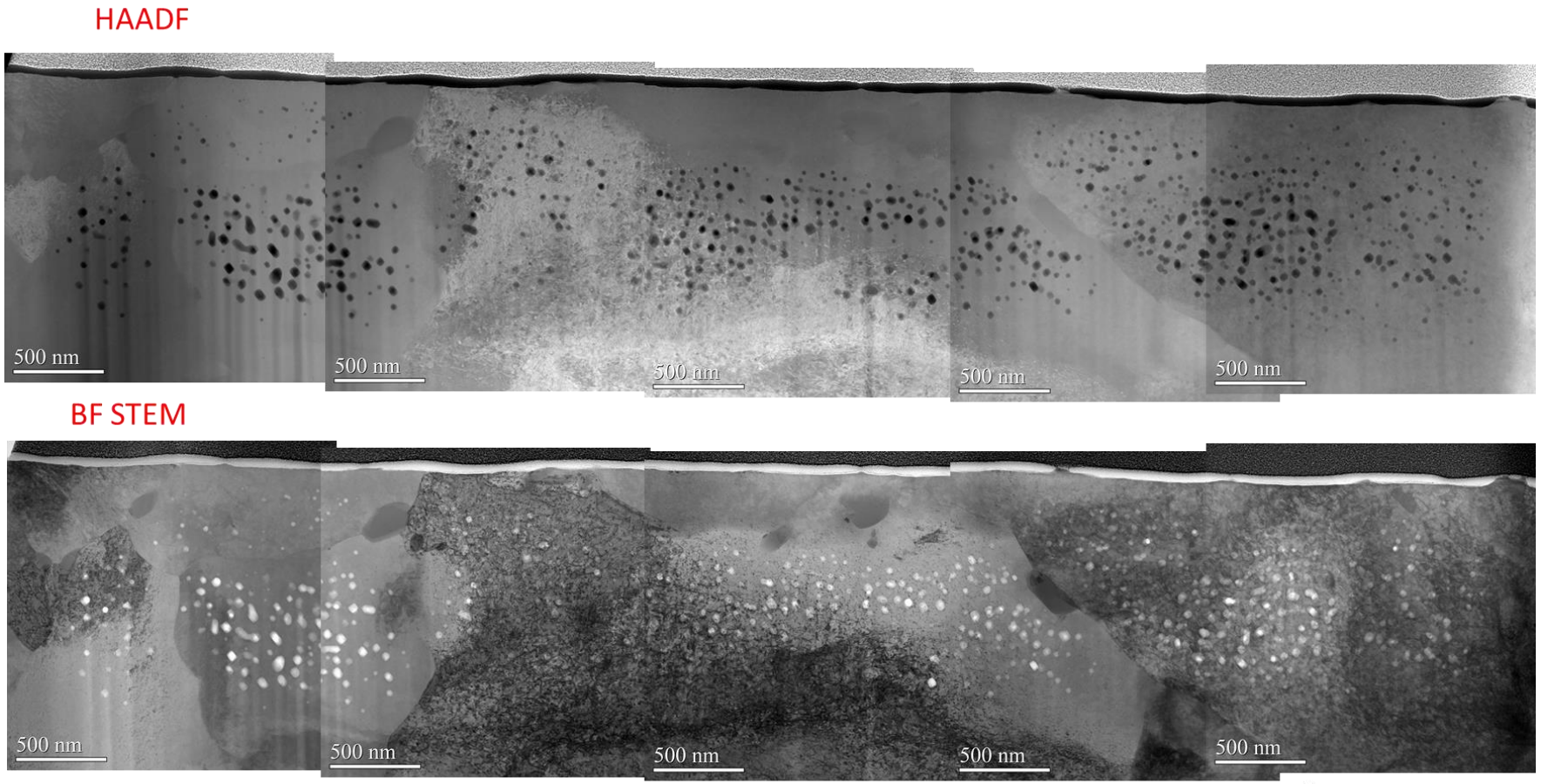

Figure B11. HAADF and corresponding BF STEM images for a liftout from the 300 dpa, 0 apppm He, nominal carbon condition.

NOMINAL CARBON CAMPAIGN:300 DPA:460ºC:1 APPM HE

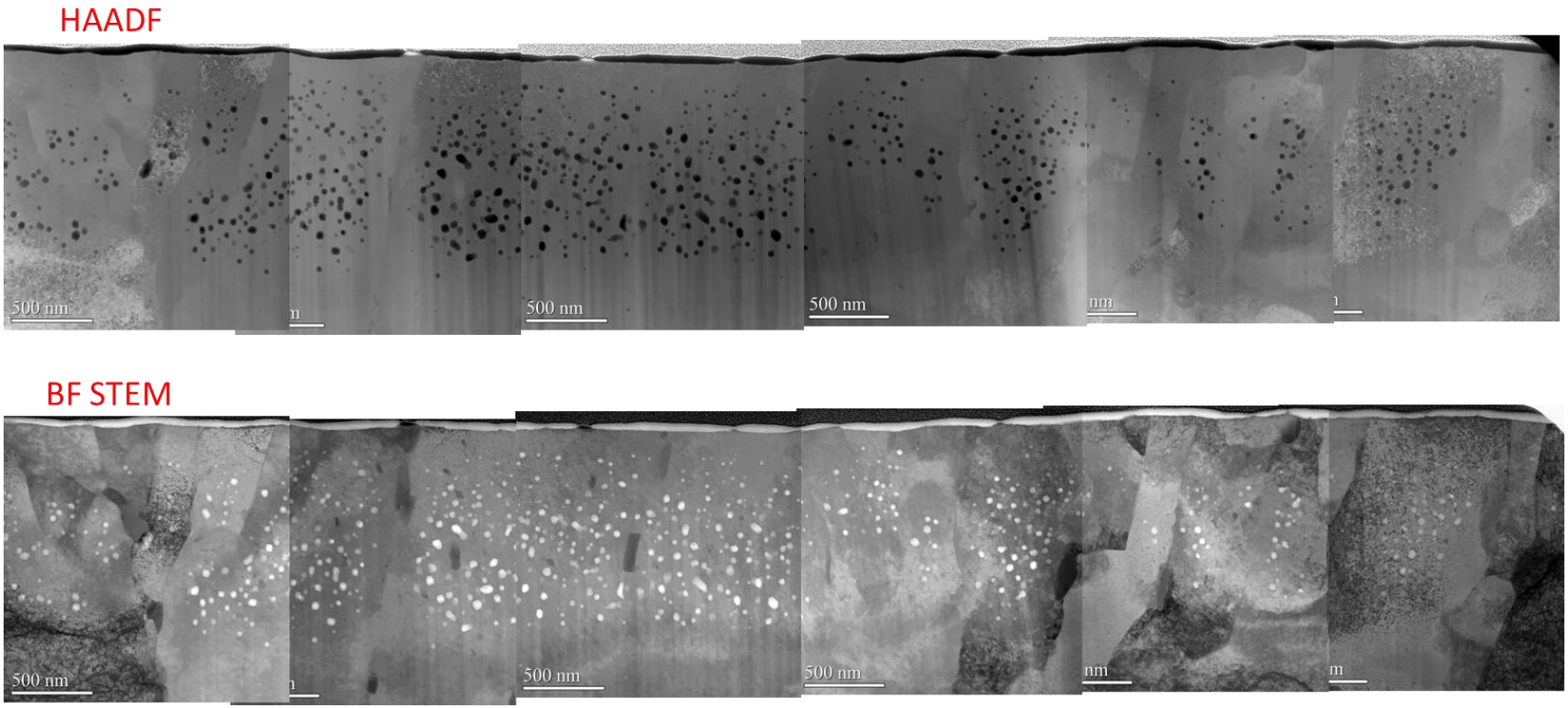

Figure B12. HAADF and corresponding BF STEM images for a liftout from the 300 dpa, 1 apppm He, nominal carbon condition.

NOMINAL CARBON CAMPAIGN:300 DPA:460°C:10 APPM HE

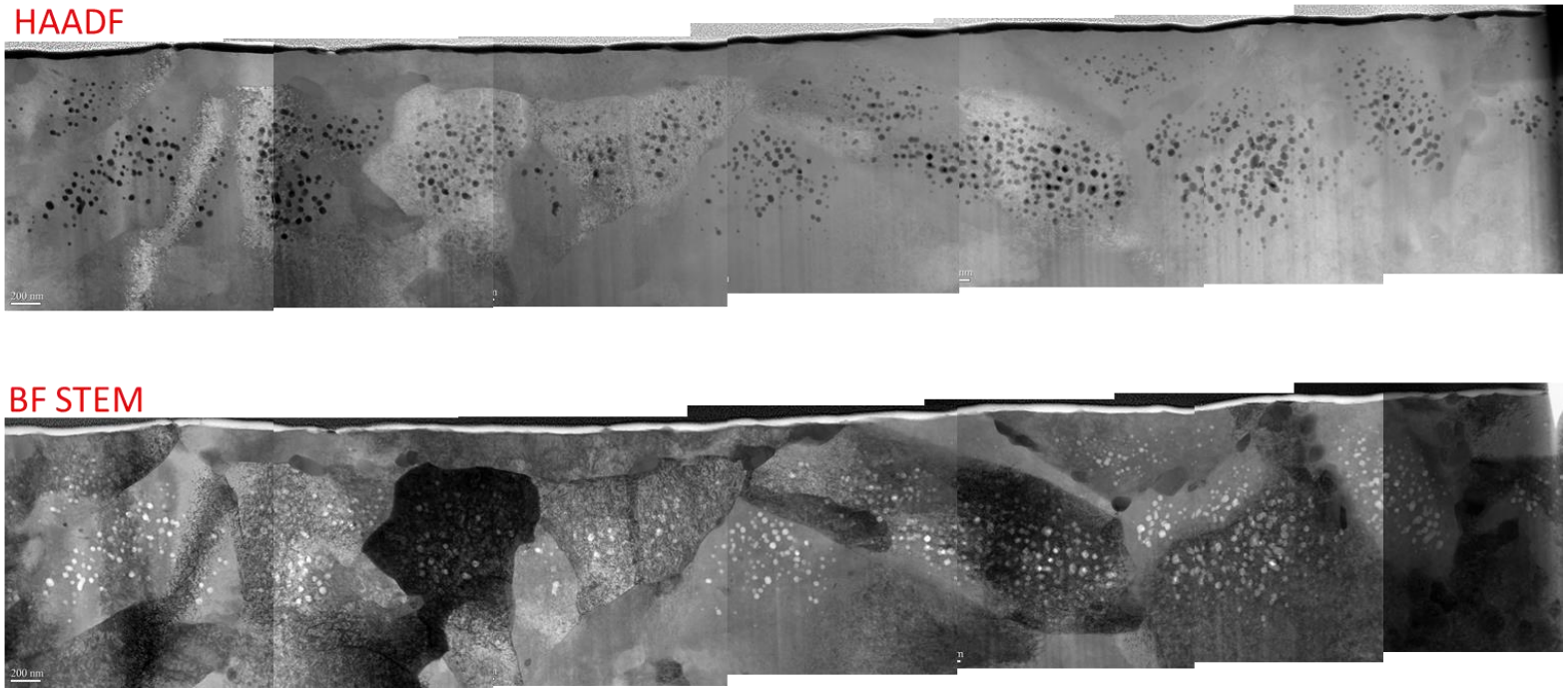

Figure B13. HAADF and corresponding BF STEM images for a liftout from the 300 dpa, 10 apppm He, nominal carbon condition.

NOMINAL CARBON CAMPAIGN:300 DPA:460°C:100 APPM HE

Figure B14. HAADF and corresponding BF STEM images for a liftout from the 300 dpa, 100 apppm He, nominal carbon condition.

NOMINAL CARBON CAMPAIGN:300 DPA:460ºC:1000 APPM HE

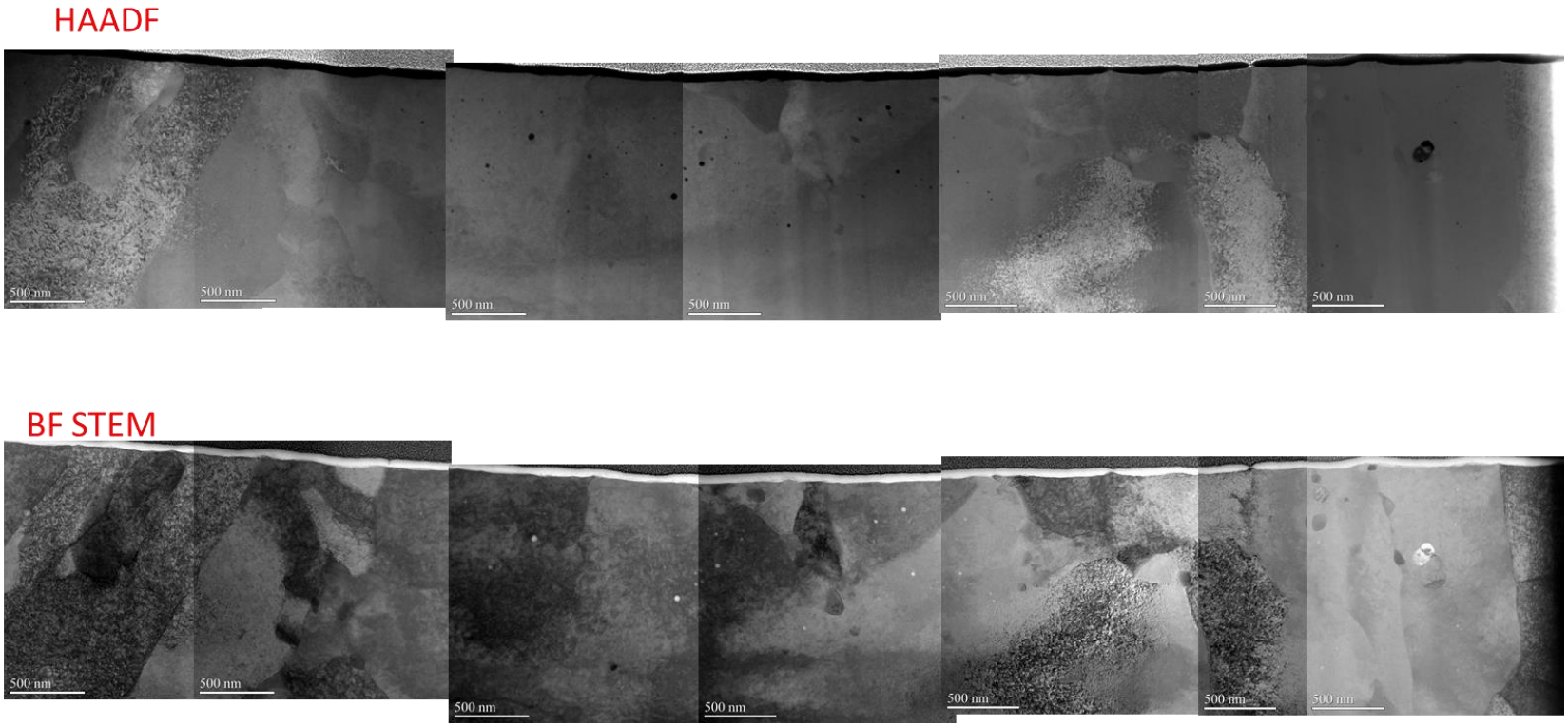

Figure B15. HAADF and corresponding BF STEM images for a liftout from the 300 dpa, 1000 apppm He, nominal carbon condition.

EXCESS CARBON CAMPAIGN:150 DPA:460ºC:0 APPM HE

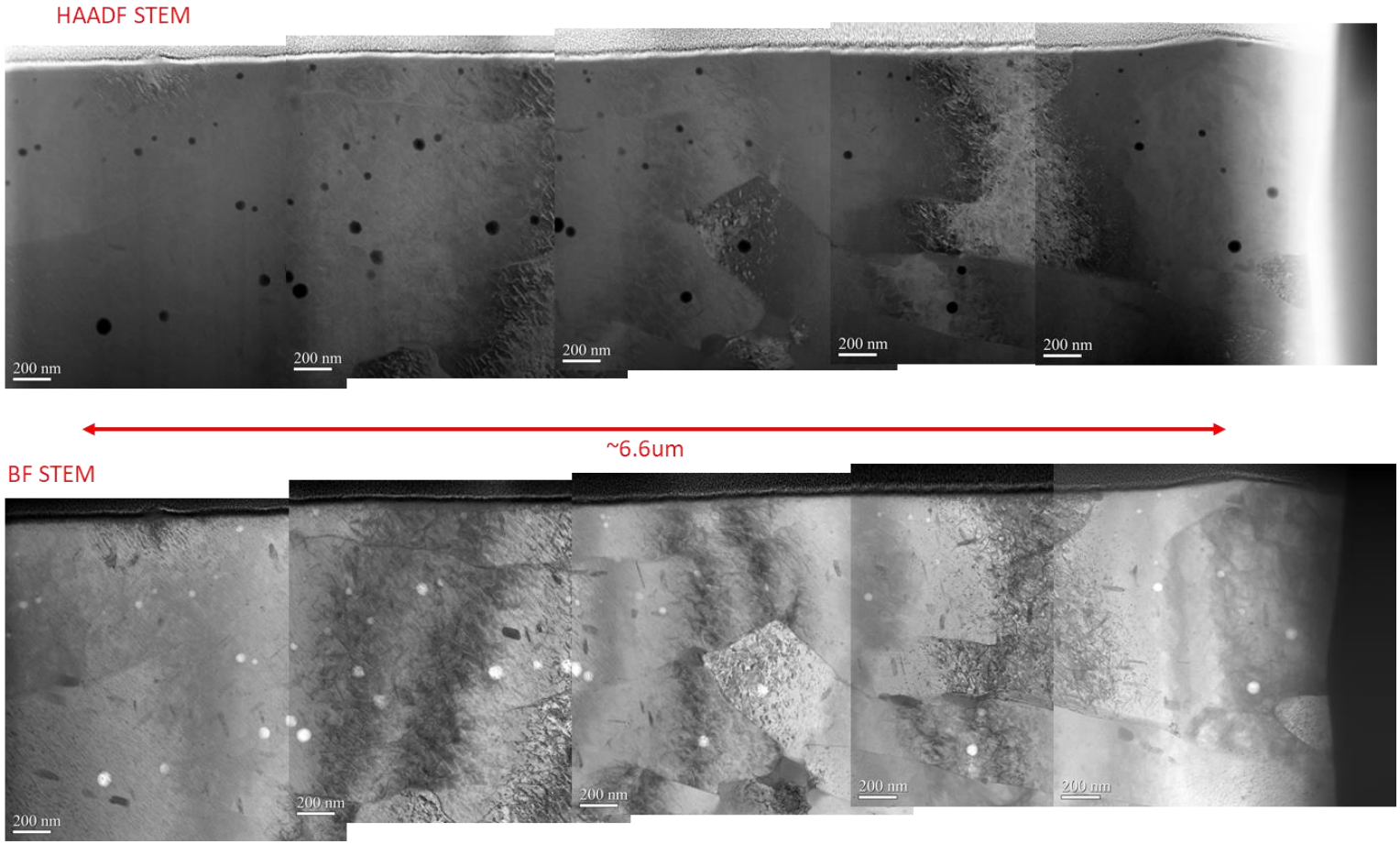

Figure B16. HAADF and corresponding BF STEM images for a liftout from the 150 dpa, 0 apppm He, excess carbon condition.

EXCESS CARBON CAMPAIGN:150 DPA:460ºC:1 APPM HE

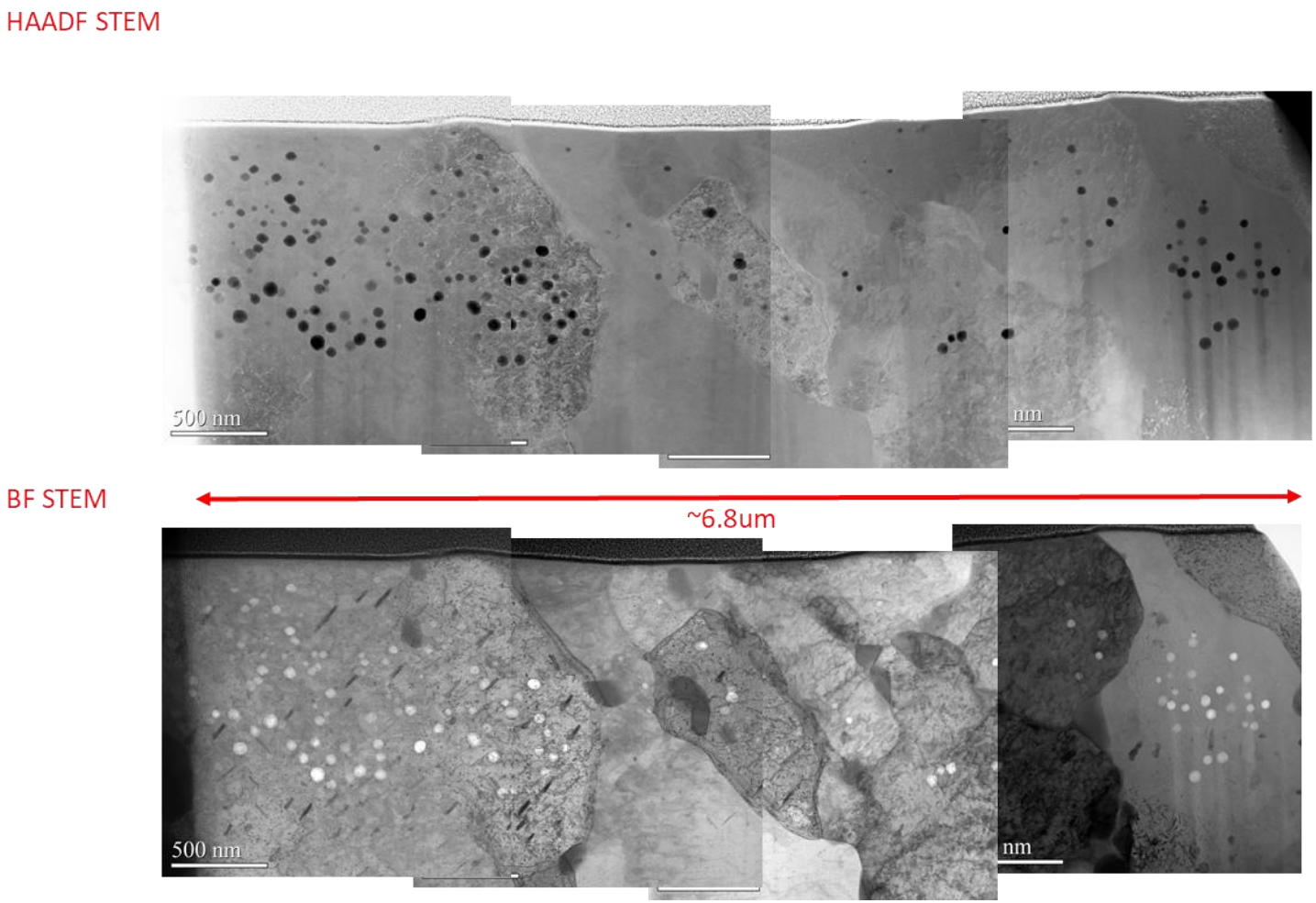

Figure B17. HAADF and corresponding BF STEM images for a liftout from the 150 dpa, 1 apppm He, excess carbon condition.

EXCESS CARBON CAMPAIGN:150 DPA:460ºC:10 APPM HE

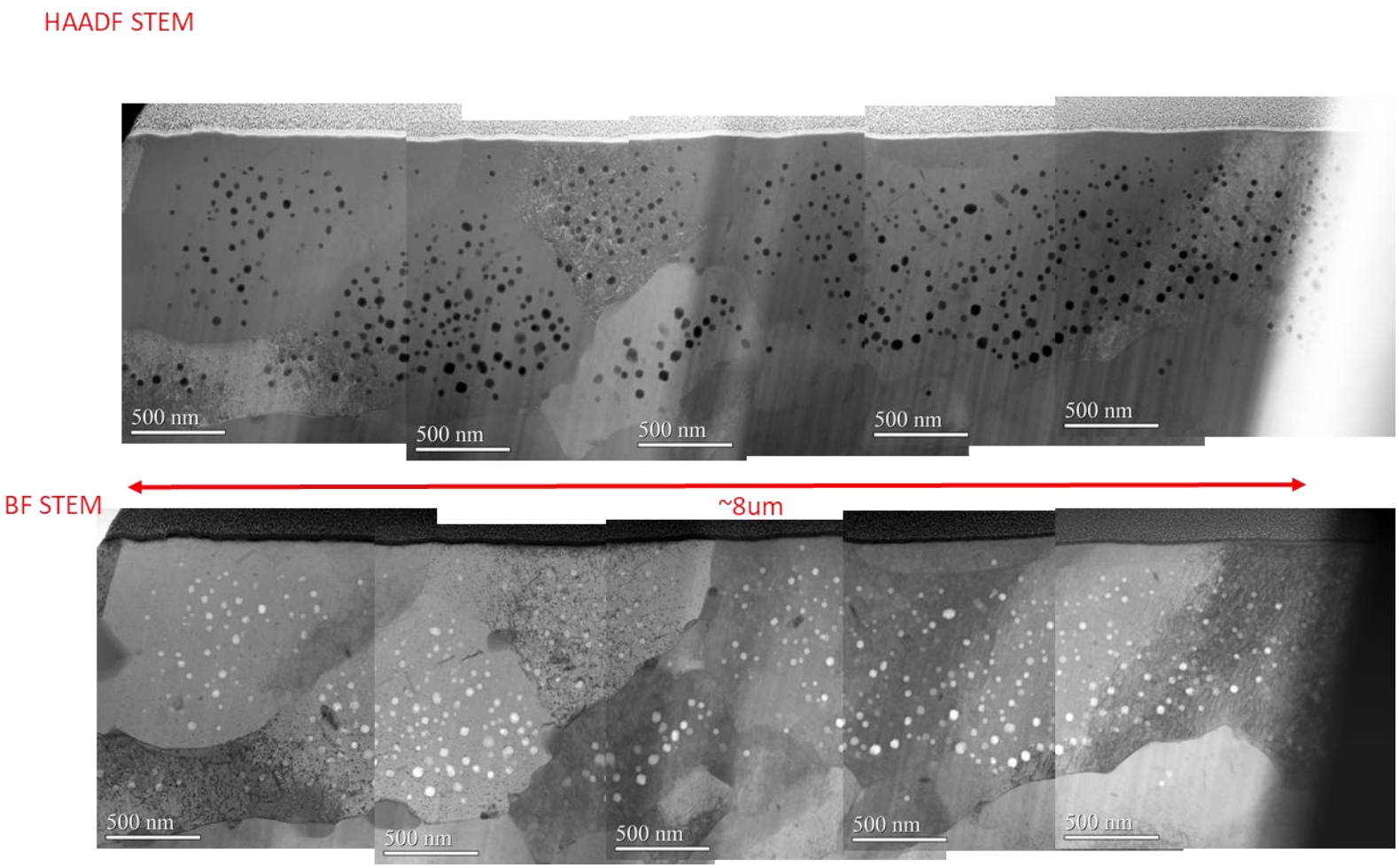

Figure B18. HAADF and corresponding BF STEM images for a liftout from the 150 dpa, 10 apppm He, excess carbon condition.

EXCESS CARBON CAMPAIGN:150 DPA:460ºC:100 APPM HE

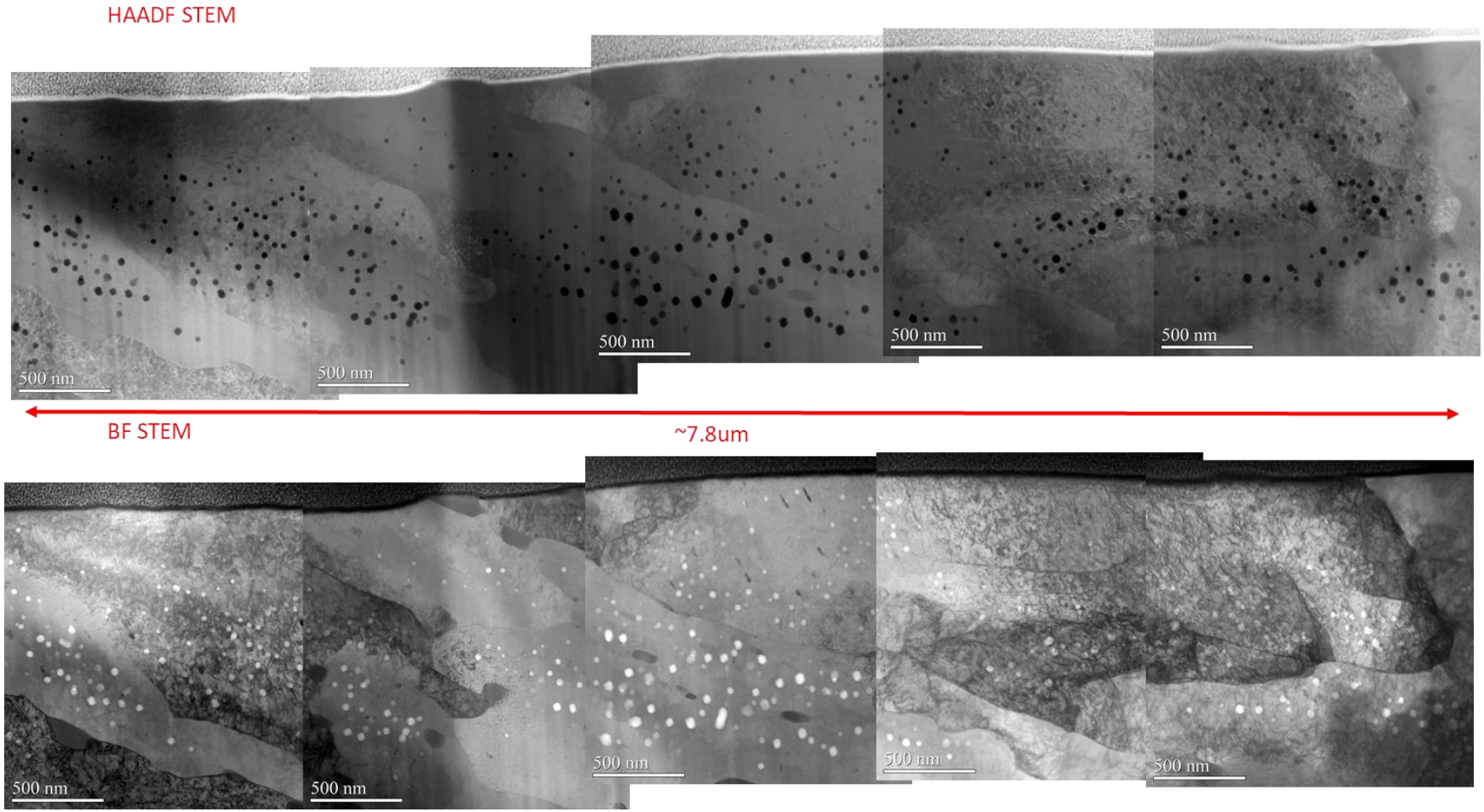

Figure B19. HAADF and corresponding BF STEM images for a liftout from the 150 dpa, 100 apppm He, excess carbon condition.

EXCESS CARBON CAMPAIGN:150 DPA:460ºC:1000 APPM HE

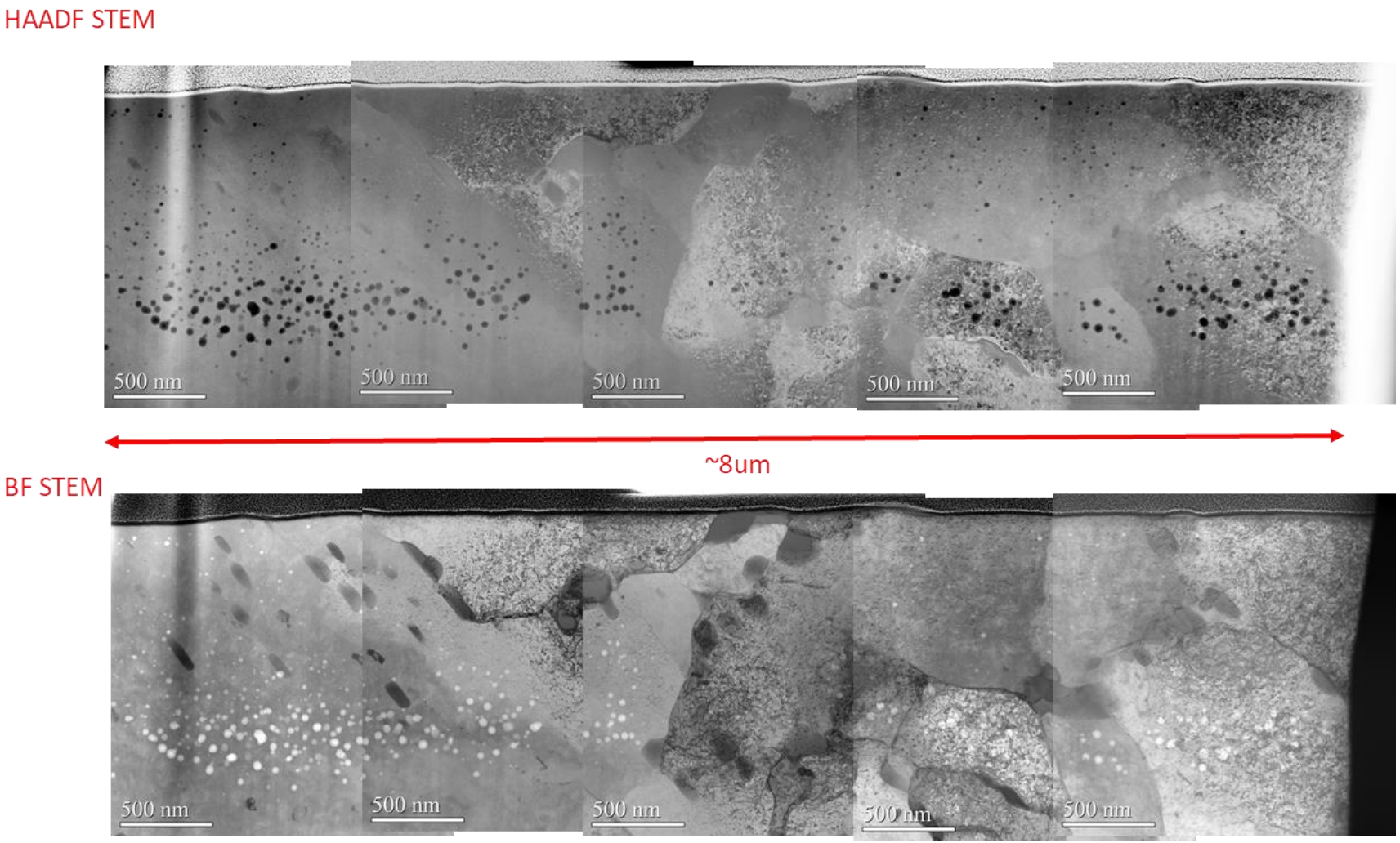

Figure B20. HAADF and corresponding BF STEM images for a liftout from the 150 dpa, 1000 apppm He, excess carbon condition.

EXCESS CARBON CAMPAIGN:300 DPA:460ºC:0 APPM HE

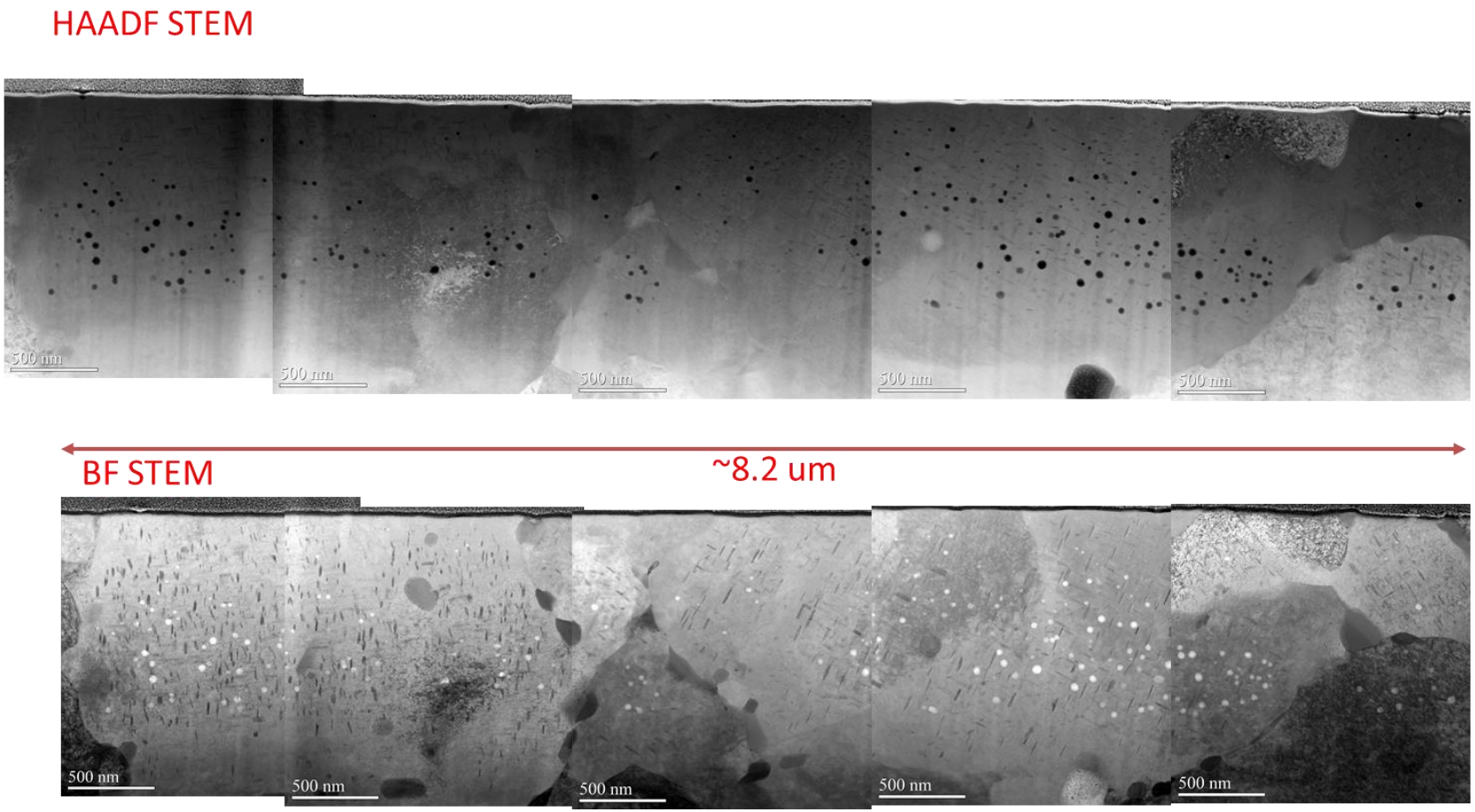

Figure B21. HAADF and corresponding BF STEM images for a liftout from the 300 dpa, 0 apppm He, excess carbon condition.

EXCESS CARBON CAMPAIGN:300 DPA:460ºC:1 APPM HE

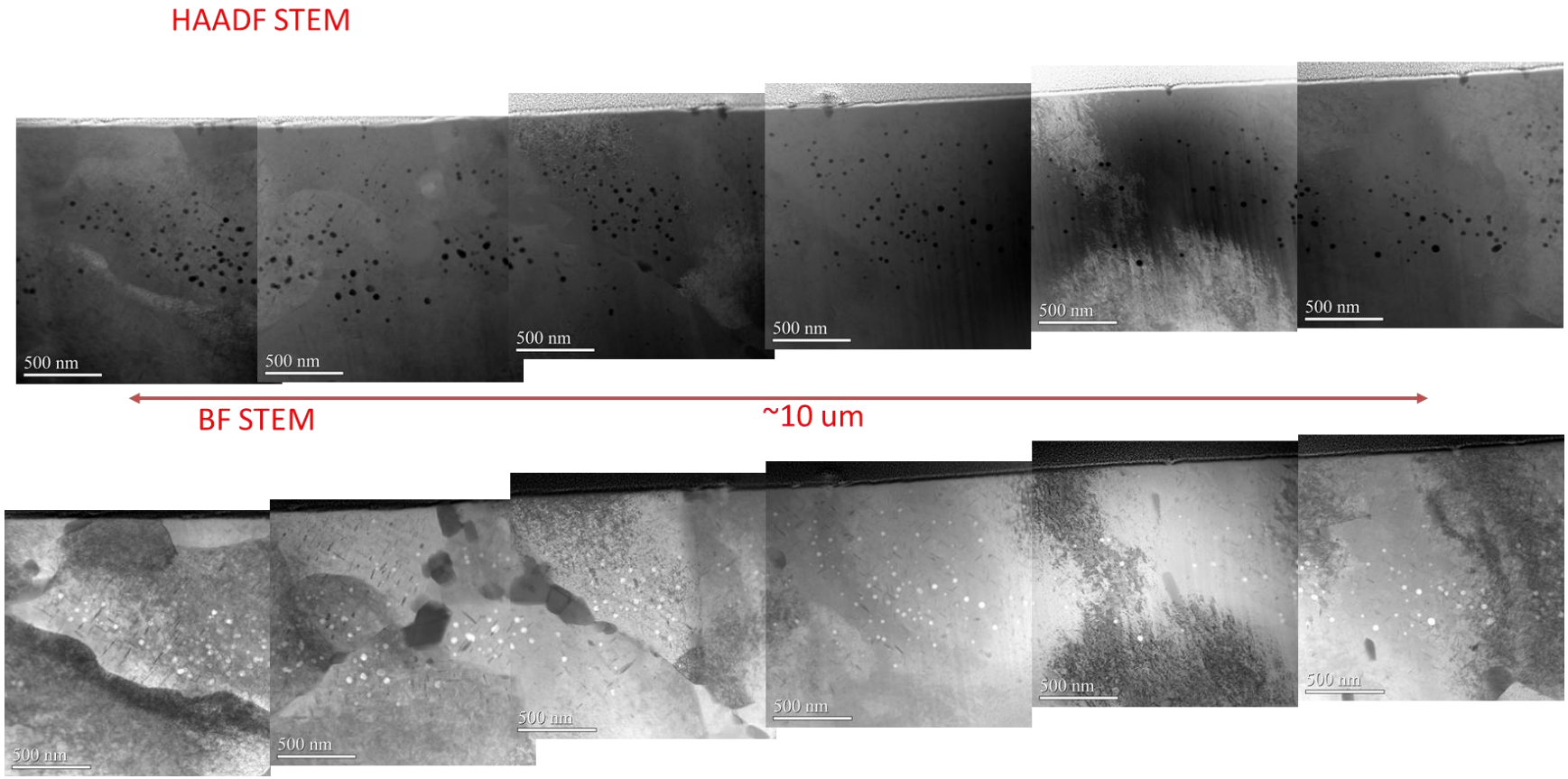

Figure B22. HAADF and corresponding BF STEM images for a liftout from the 300 dpa, 1 apppm He, excess carbon condition.

EXCESS CARBON CAMPAIGN:300 DPA:460ºC:10 APPM HE

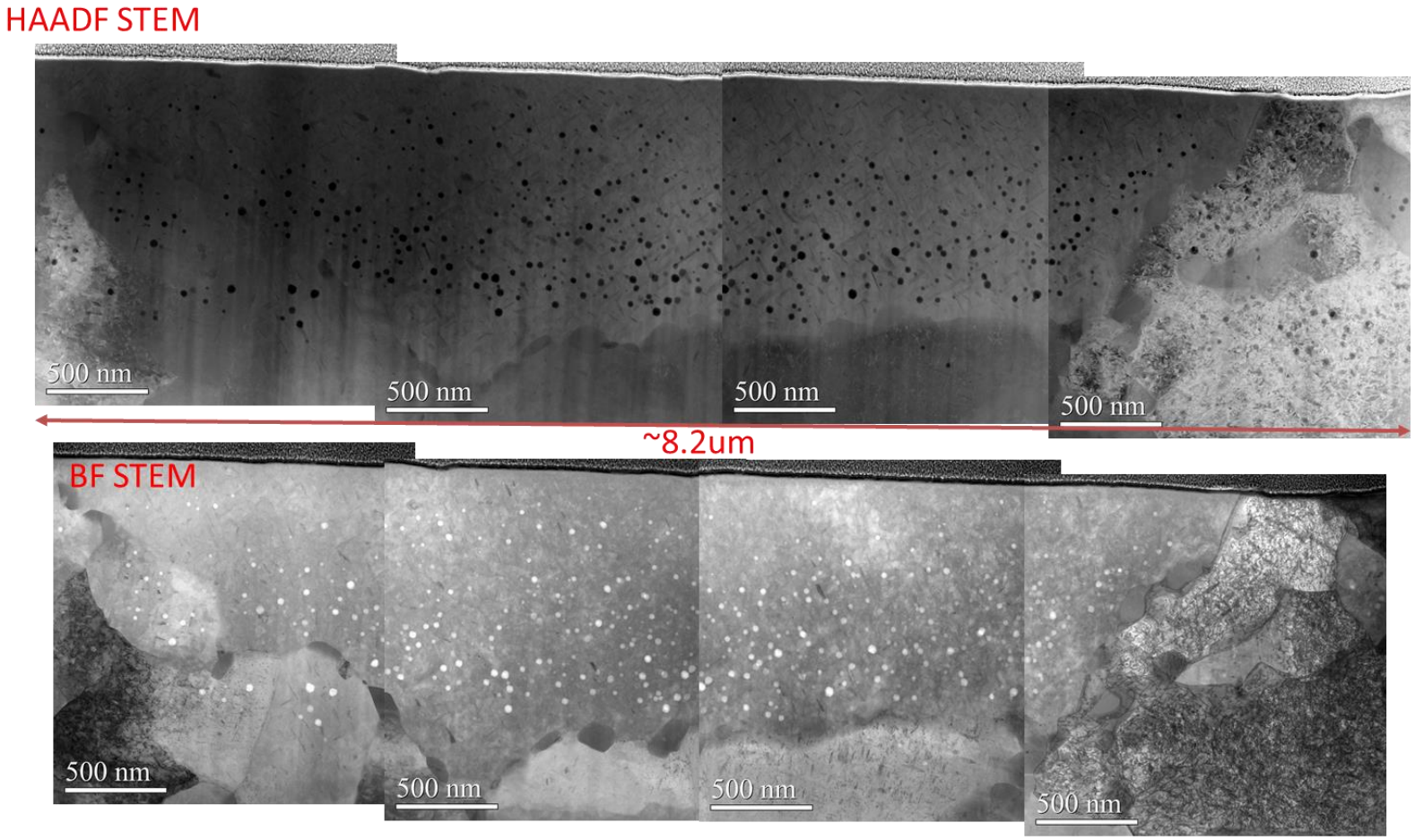

Figure B23. HAADF and corresponding BF STEM images for a liftout from the 300 dpa, 10 apppm He, excess carbon condition.

EXCESS CARBON CAMPAIGN:300 DPA:460C:100 APPM HE

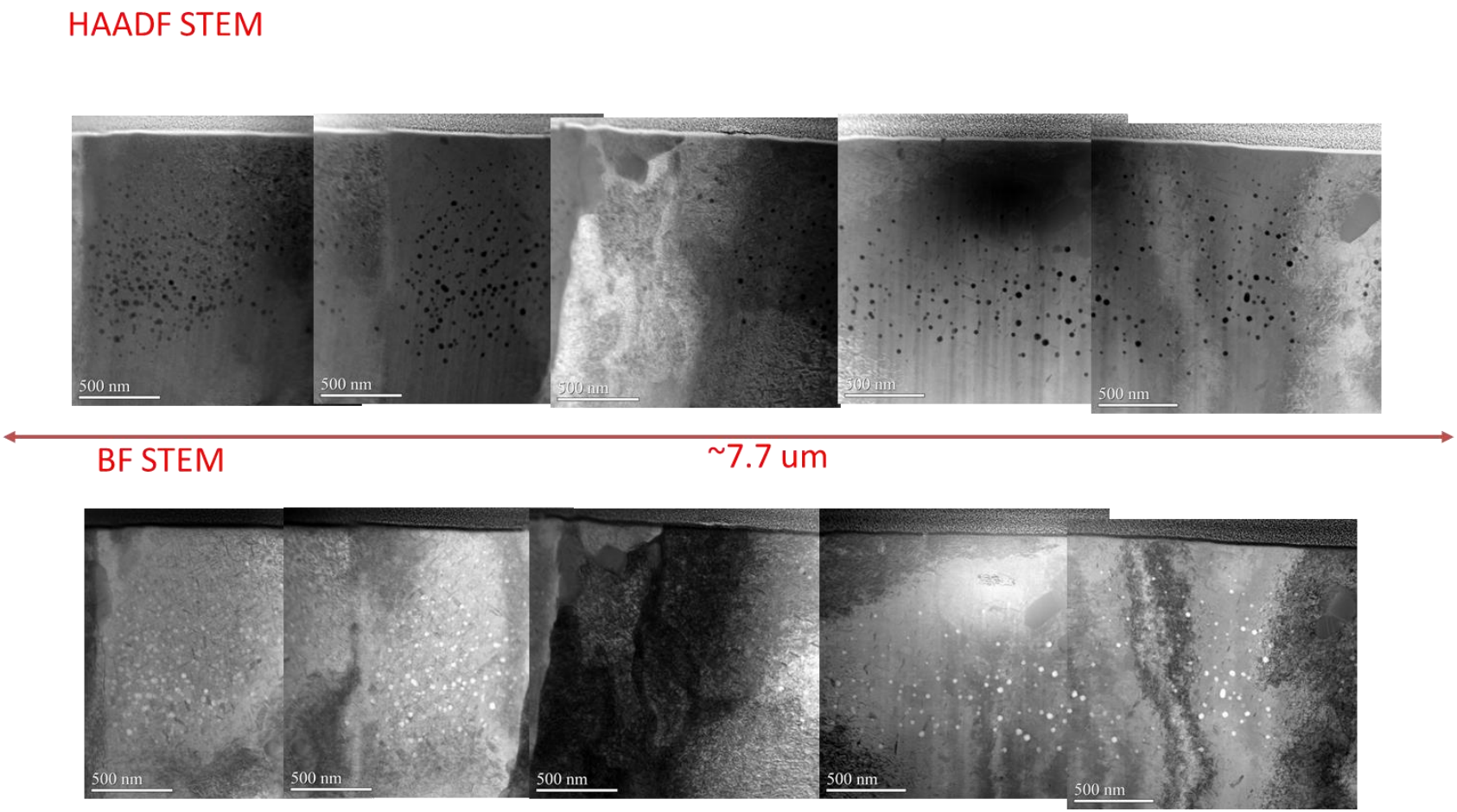

Figure B24. HAADF and corresponding BF STEM images for a liftout from the 300 dpa, 100 apppm He, excess carbon condition.

EXCESS CARBON CAMPAIGN:300 DPA:460ºC:1000 APPM HE

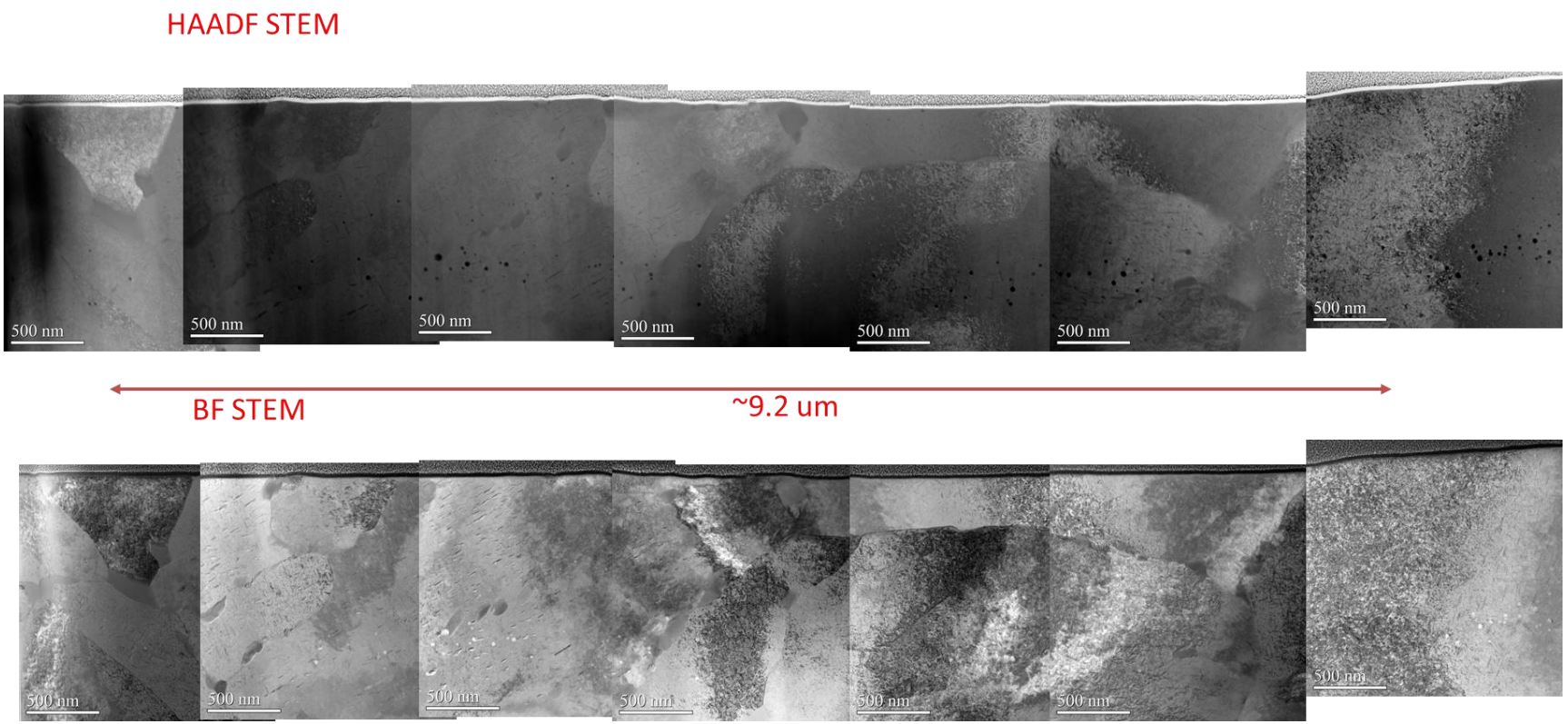

Figure B25. HAADF and corresponding BF STEM images for a liftout from the 300 dpa, 1000 apppm He, excess carbon condition.

EXCESS CARBON CAMPAIGN:450 DPA:460ºC:0 APPM HE

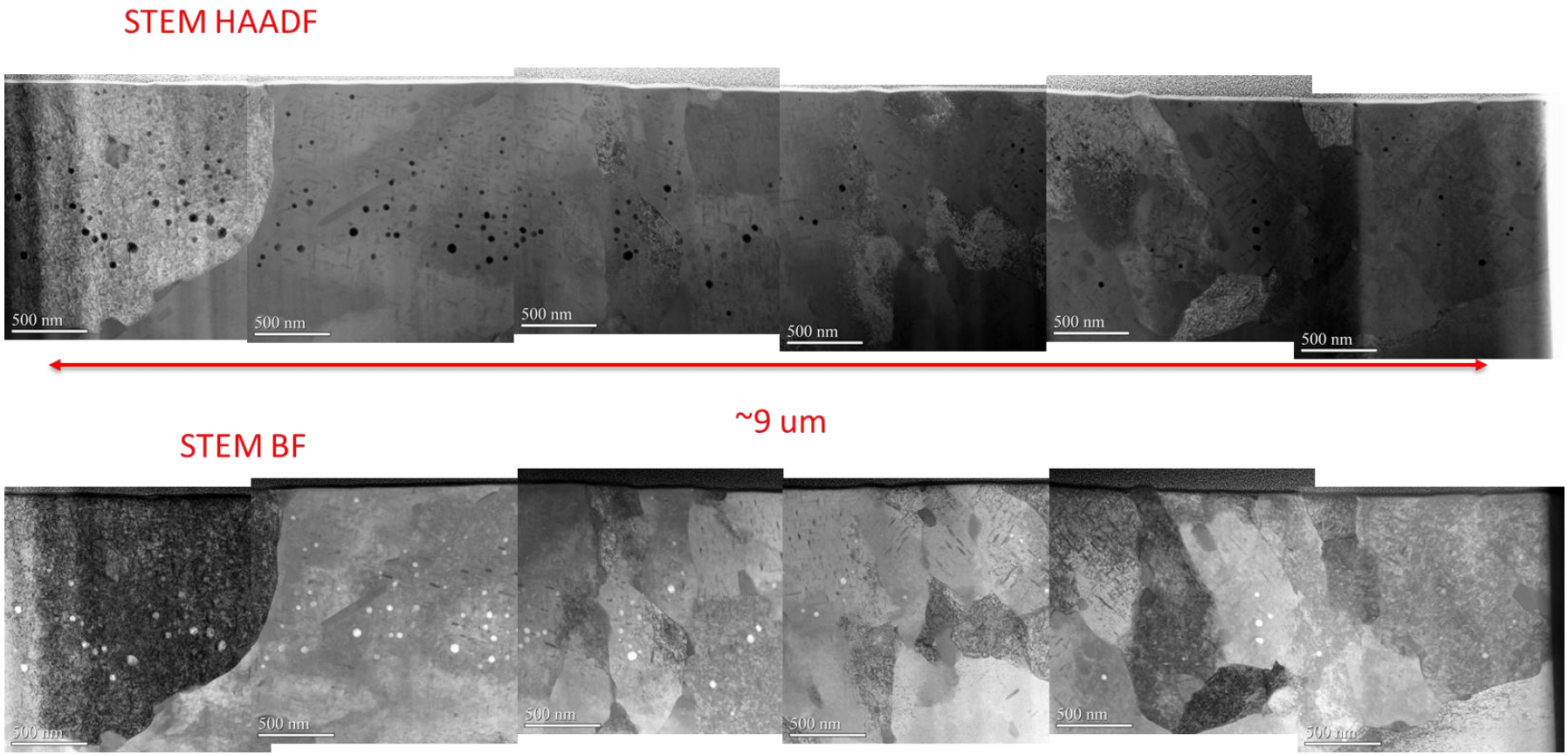

Figure B26. HAADF and corresponding BF STEM images for a liftout from the 450 dpa, 0 apppm He, excess carbon condition.

EXCESS CARBON CAMPAIGN:450 DPA:460ºC:1 APPM HE

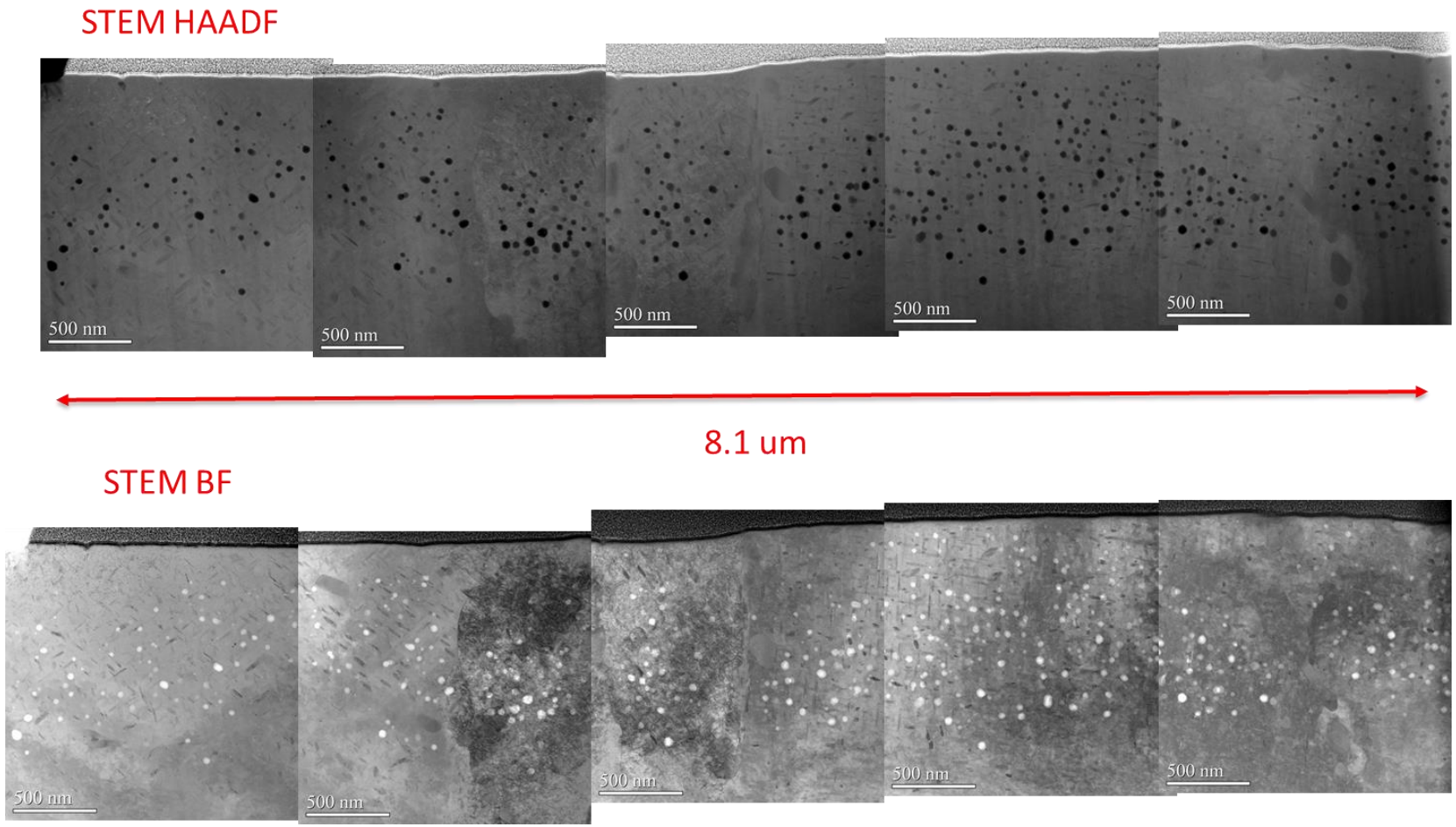

Figure B27. HAADF and corresponding BF STEM images for a liftout from the 450 dpa, 1 apppm He, excess carbon condition.

EXCESS CARBON CAMPAIGN:450 DPA:460ºC:10 APPM HE

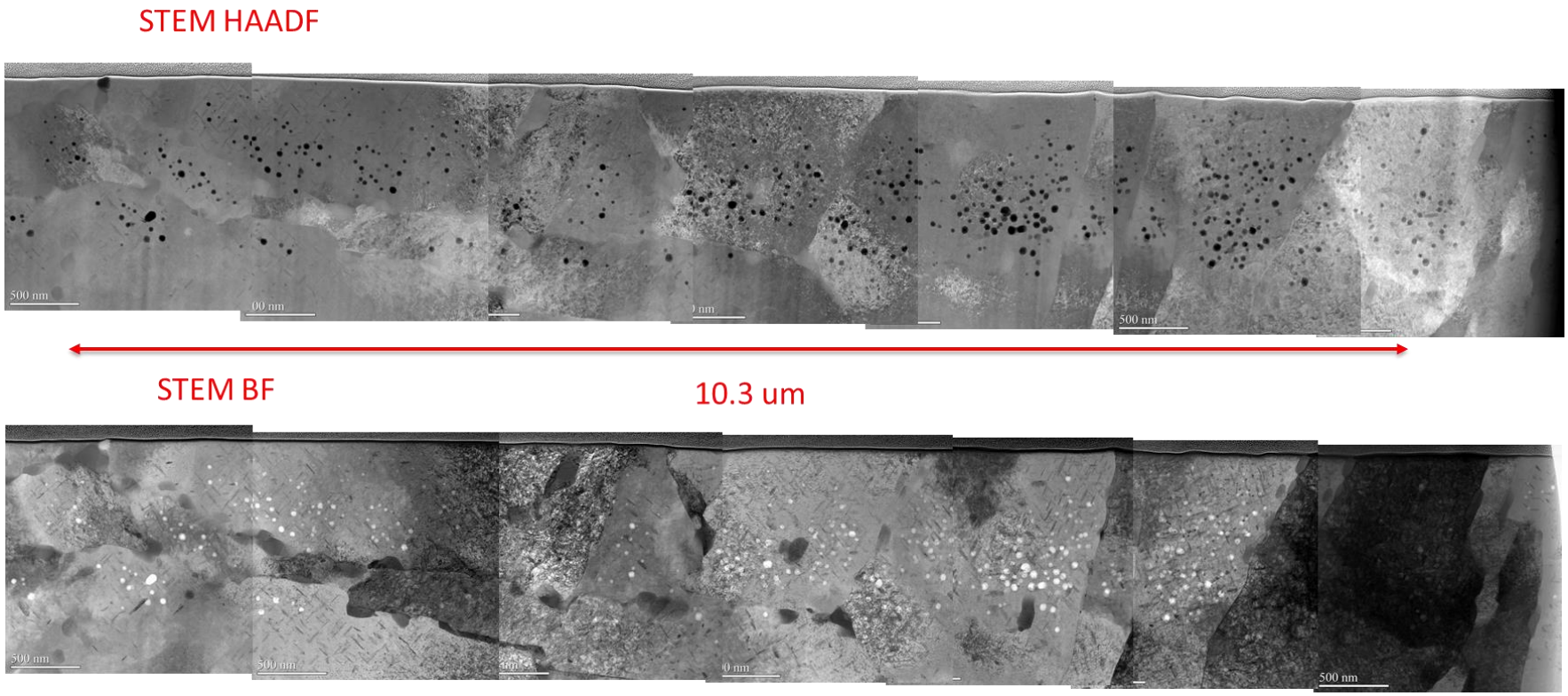

Figure B28. HAADF and corresponding BF STEM images for a liftout from the 450 dpa, 10 apppm He, excess carbon condition.

EXCESS CARBON CAMPAIGN:450 DPA:460ºC:100 APPM HE

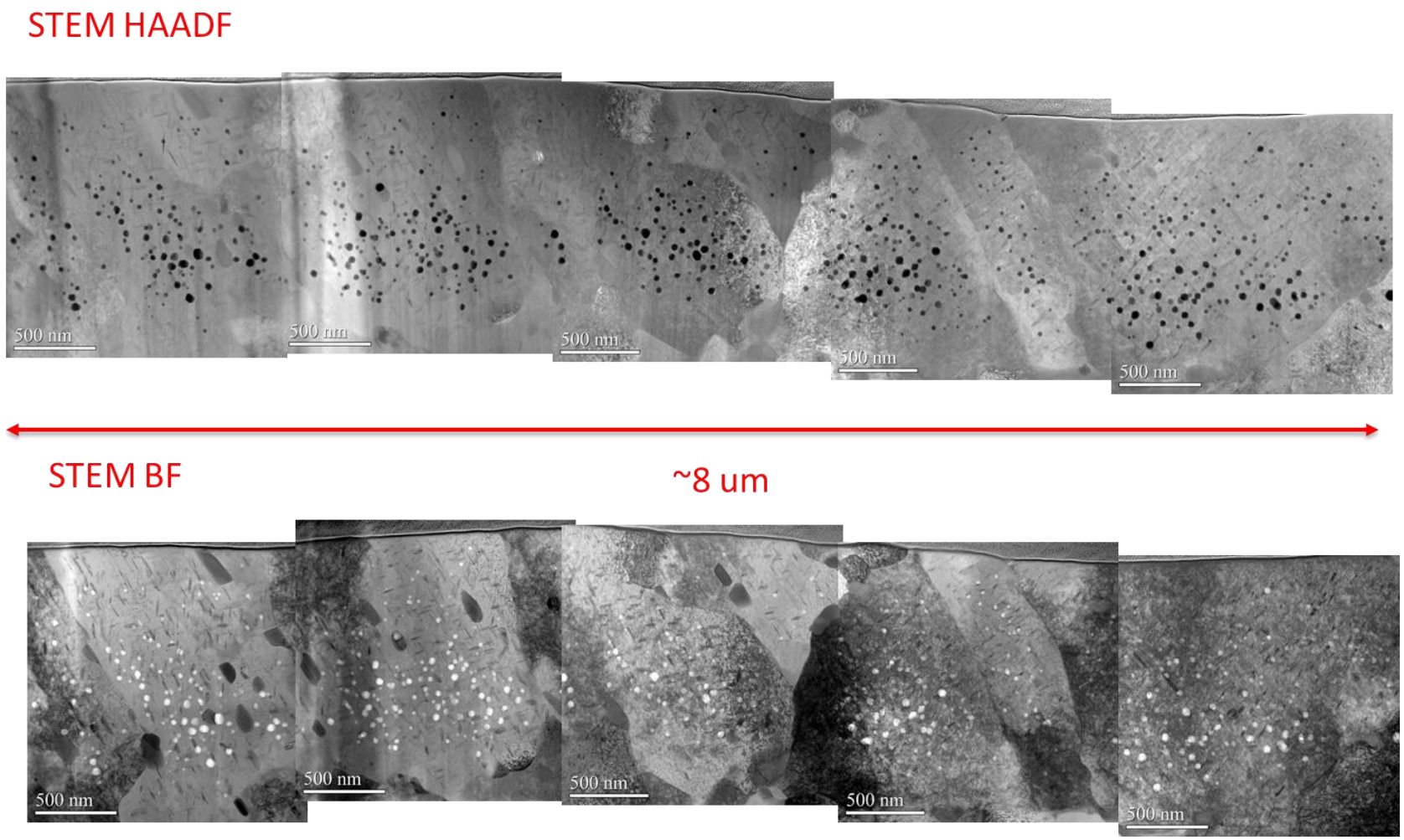

Figure B29. HAADF and corresponding BF STEM images for a liftout from the 450 dpa, 100 apppm He, excess carbon condition.

EXCESS CARBON CAMPAIGN:450 DPA:460ºC:1000 APPM HE

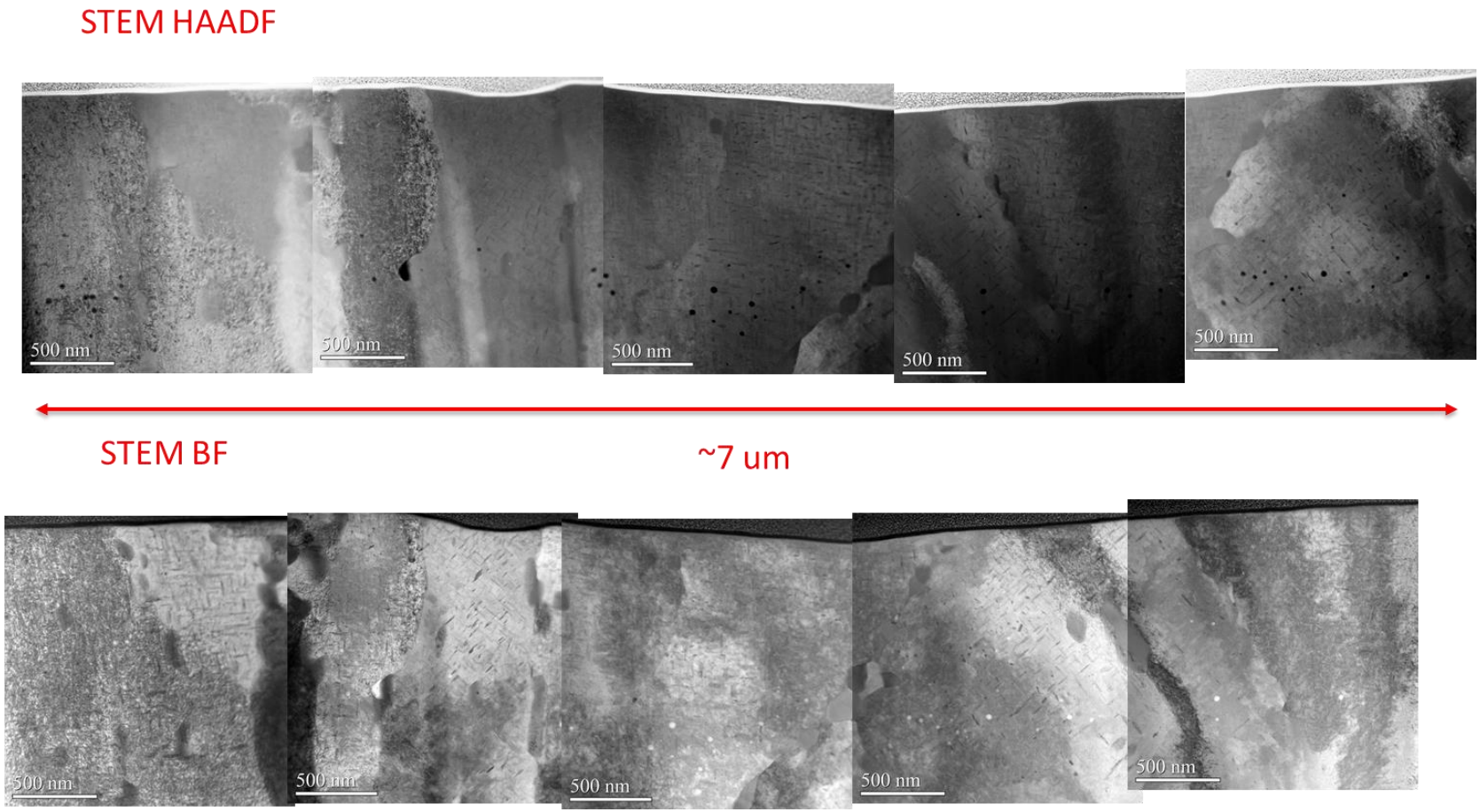

Figure B30. HAADF and corresponding BF STEM images for a liftout from the 450 dpa, 1000 apppm He, excess carbon condition.

APPENDIX C: CAVITY DEPTH PROFILES AND DISTRIBUTIONS

Cavity diameter, density, swelling, are shown as a function of depth within the sample for every condition studied in this thesis. Cavity distributions from the profiling are shown for the 500-700 nm depth range. Bubble populations are not considered in the depth profiling and distributions.

NOMINAL CARBON CAMPAIGN:50 DPA:460ºC:0 APPM HE

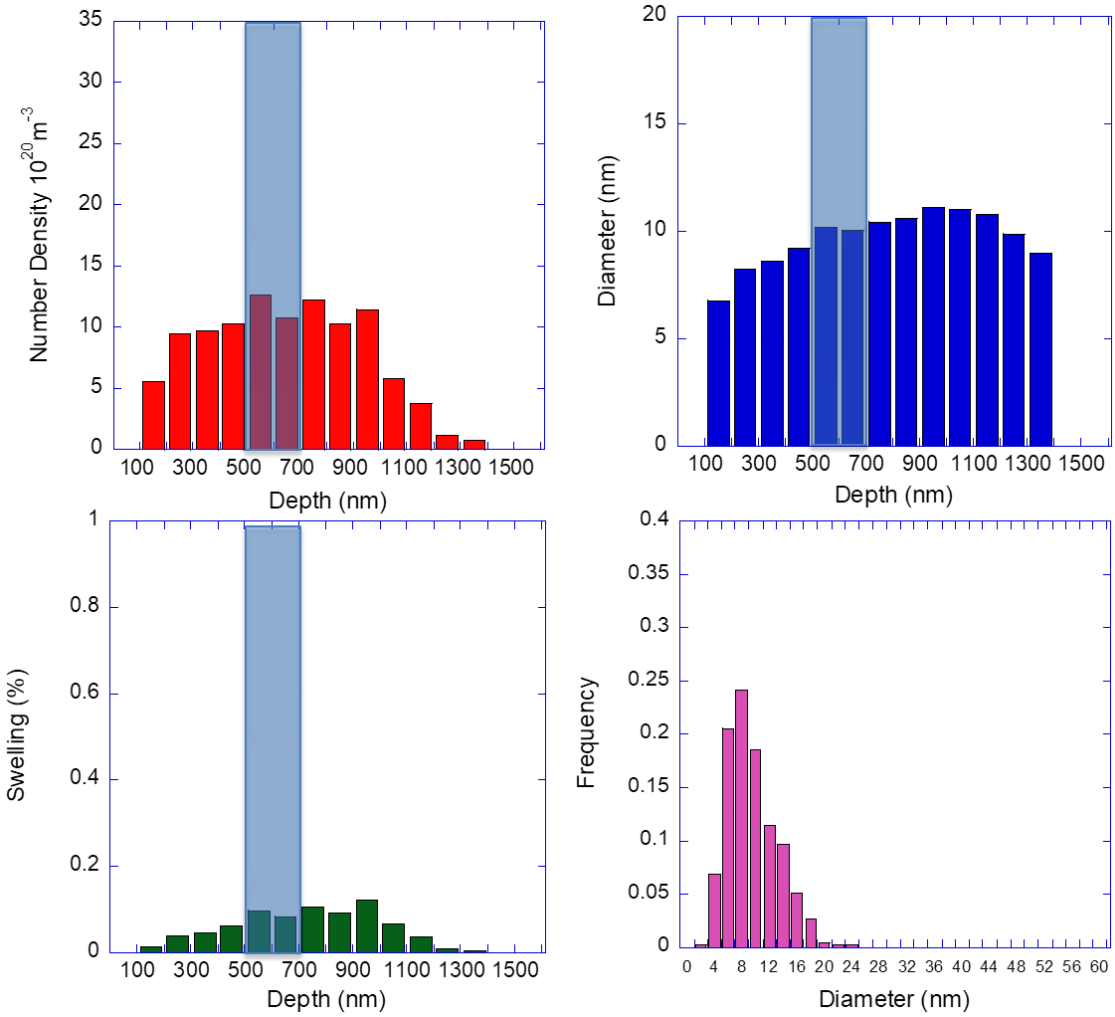

Figure C1. Cavity diameter, density and swelling are plotted as a function of depth for the 50 dpa, 0 appm He, nominal carbon condition. The cavity distribution at 500-700 nm is also shown.

NOMINAL CARBON CAMPAIGN:50 DPA:460ºC:1 APPM HE

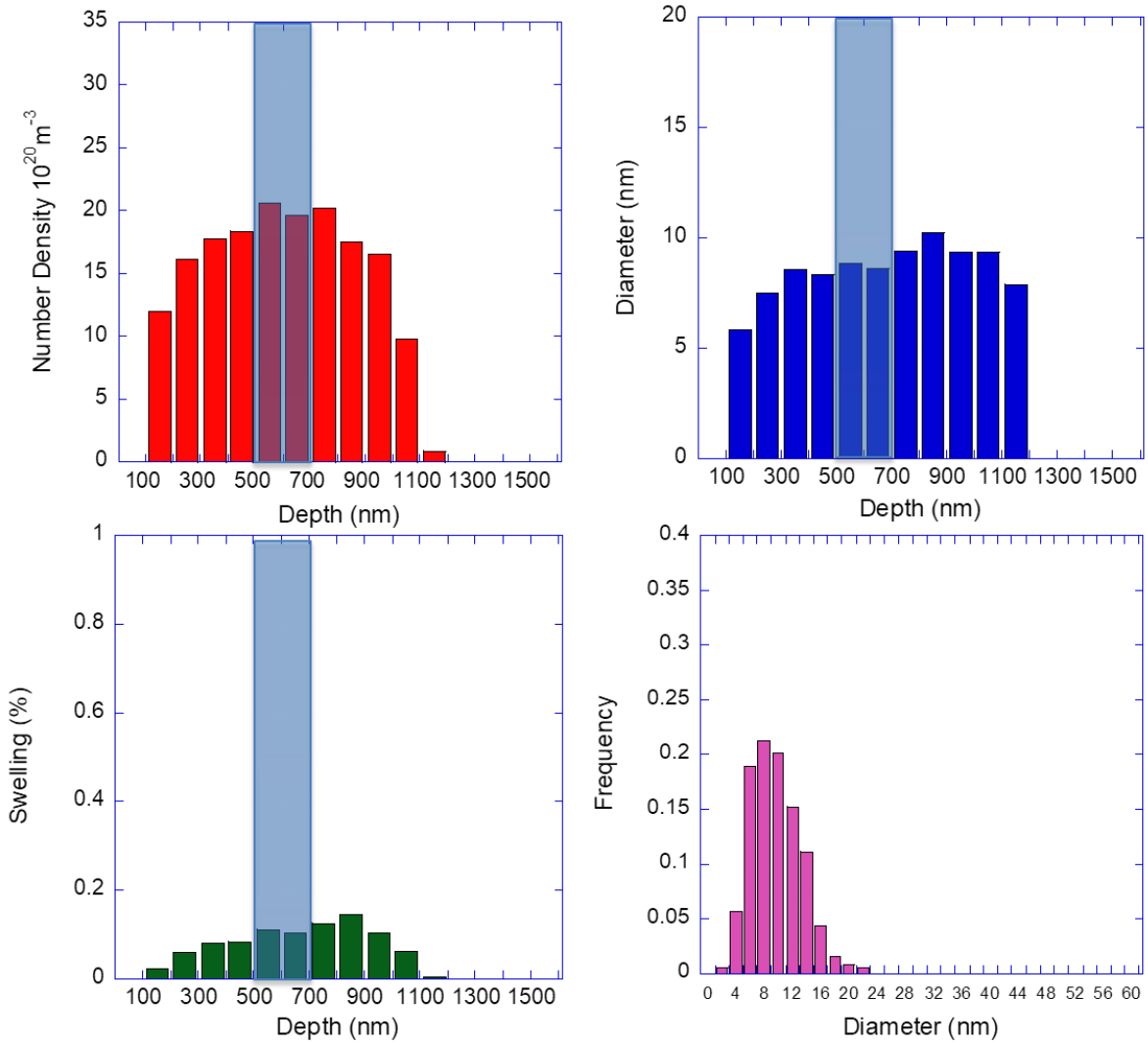

Figure C2. Cavity diameter, density and swelling are plotted as a function of depth for the 50 dpa, 1 appm He, nominal carbon condition. The cavity distribution at 500-700 nm is also shown.

NOMINAL CARBON CAMPAIGN:50 DPA:460ºC:10 APPM HE

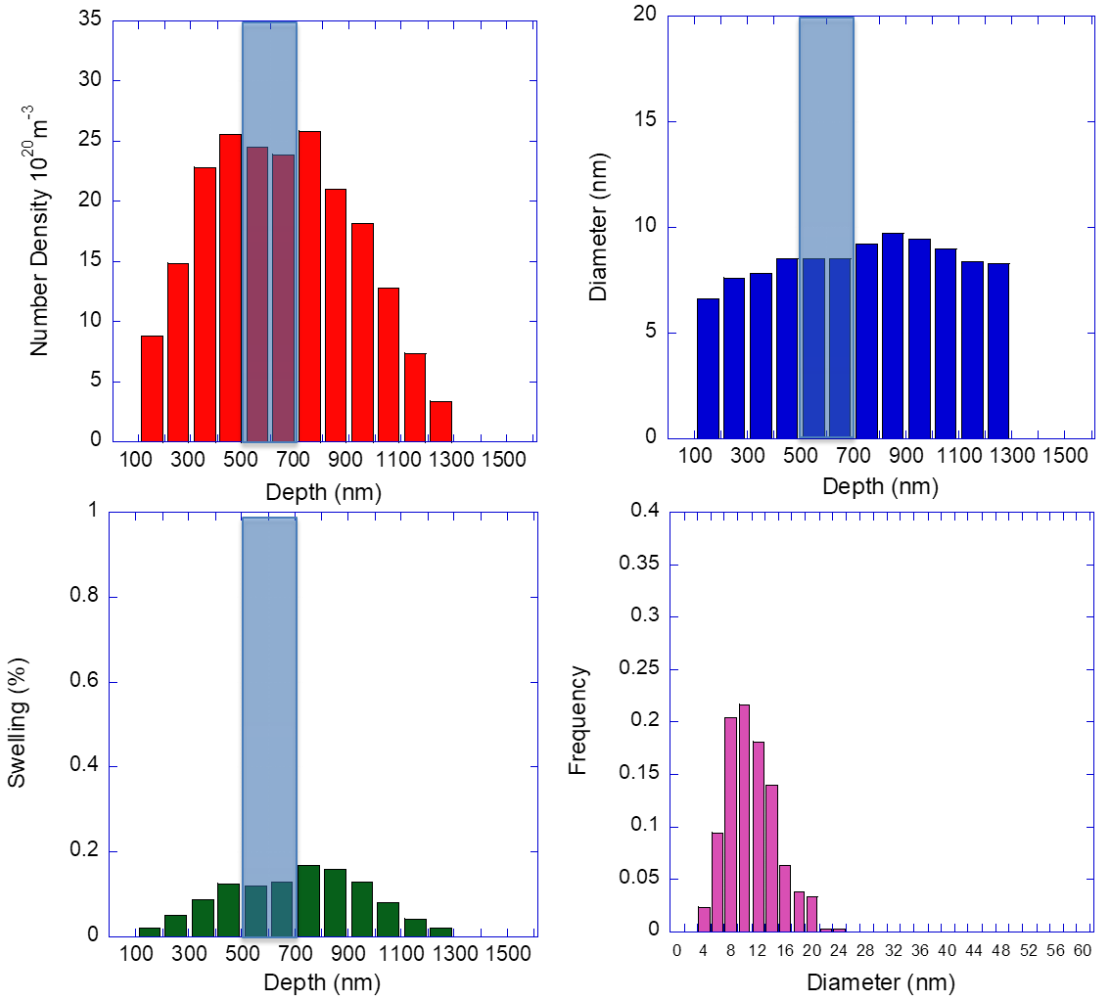

Figure C3. Cavity diameter, density and swelling are plotted as a function of depth for the 50 dpa, 10 appm He, nominal carbon condition. The cavity distribution at 500-700 nm is also shown.

NOMINAL CARBON CAMPAIGN:50 DPA:460ºC:100 APPM HE

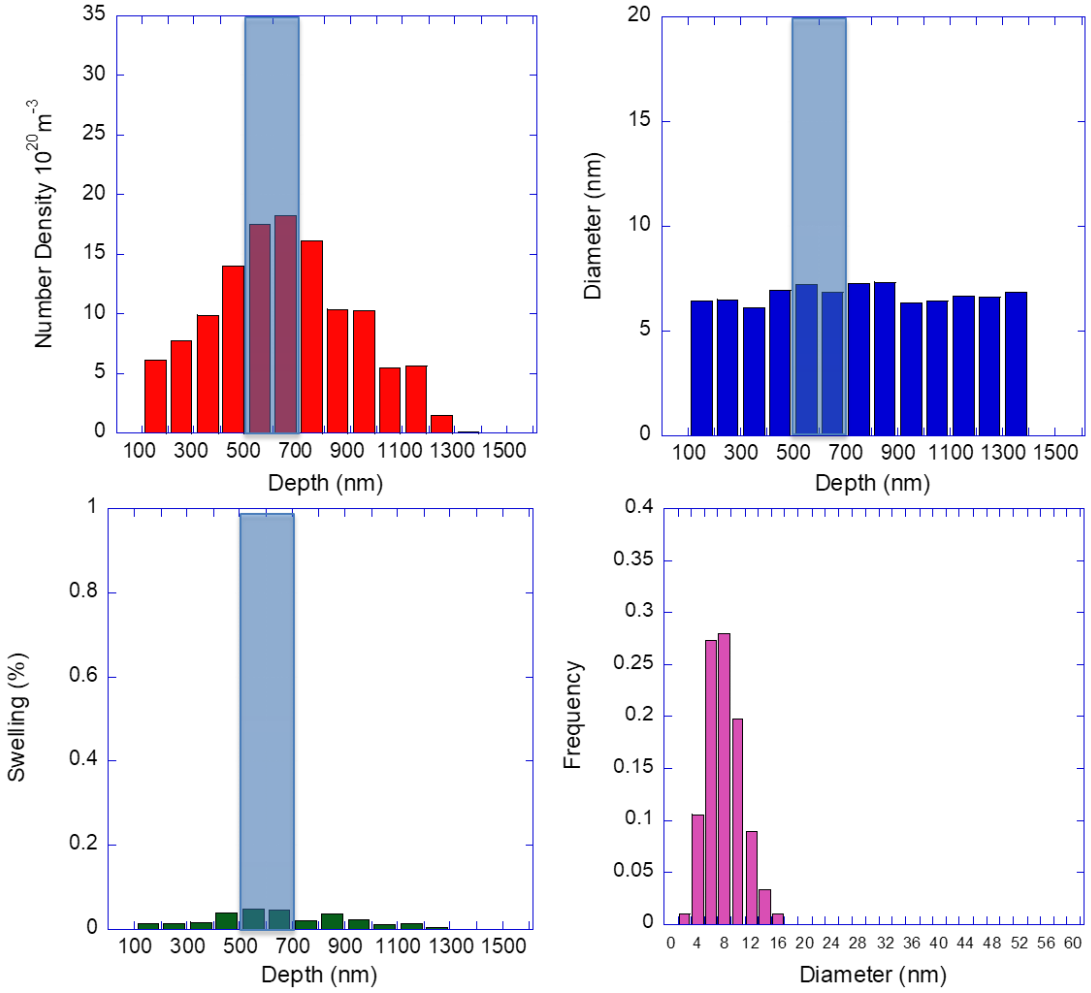

Figure C4. Cavity diameter, density and swelling are plotted as a function of depth for the 50 dpa, 100 appm He, nominal carbon condition. The cavity distribution at 500-700 nm is also shown.

NOMINAL CARBON CAMPAIGN:50 DPA:460ºC:1000 APPM HE

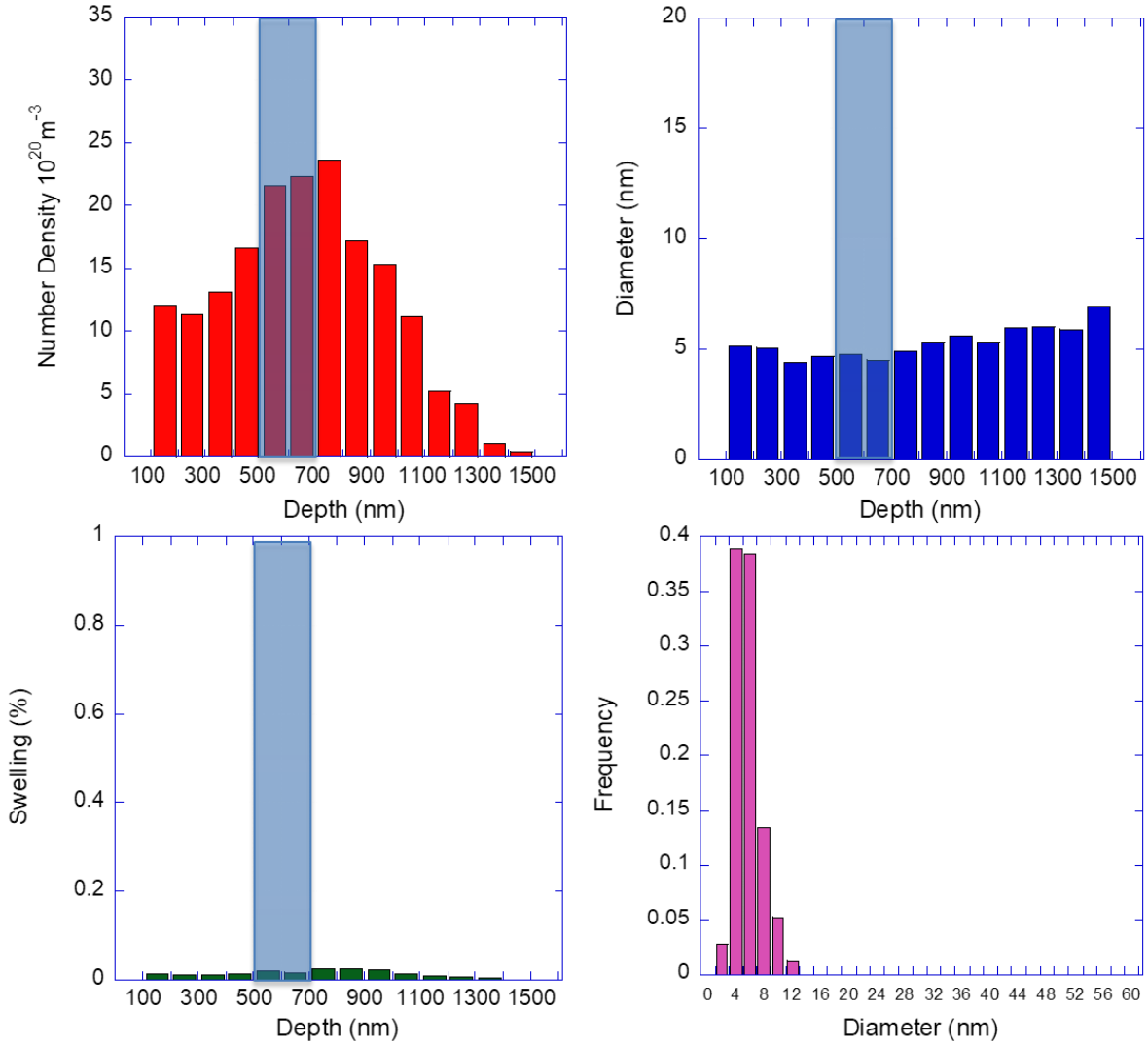

Figure C5. Cavity diameter, density and swelling are plotted as a function of depth for the 50 dpa, 1000 appm He, nominal carbon condition. The cavity distribution at 500-700 nm is also shown.

NOMINAL CARBON CAMPAIGN:150 DPA:460ºC:0 APPM HE

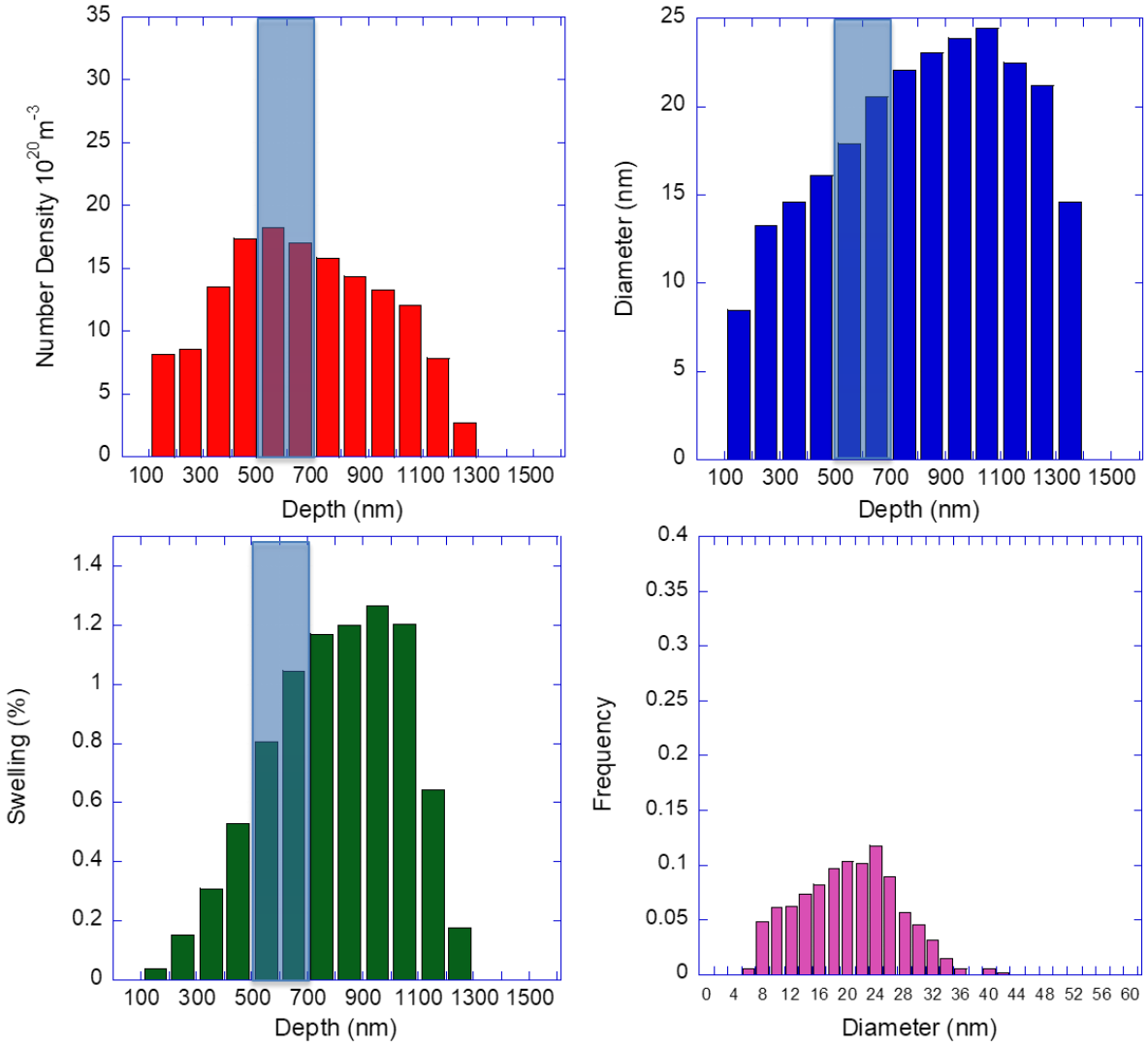

Figure C6. Cavity diameter, density and swelling are plotted as a function of depth for the 150 dpa, 0 appm He, nominal carbon condition. The cavity distribution at 500-700 nm is also shown.

NOMINAL CARBON CAMPAIGN:150 DPA:460ºC:1 APPM HE

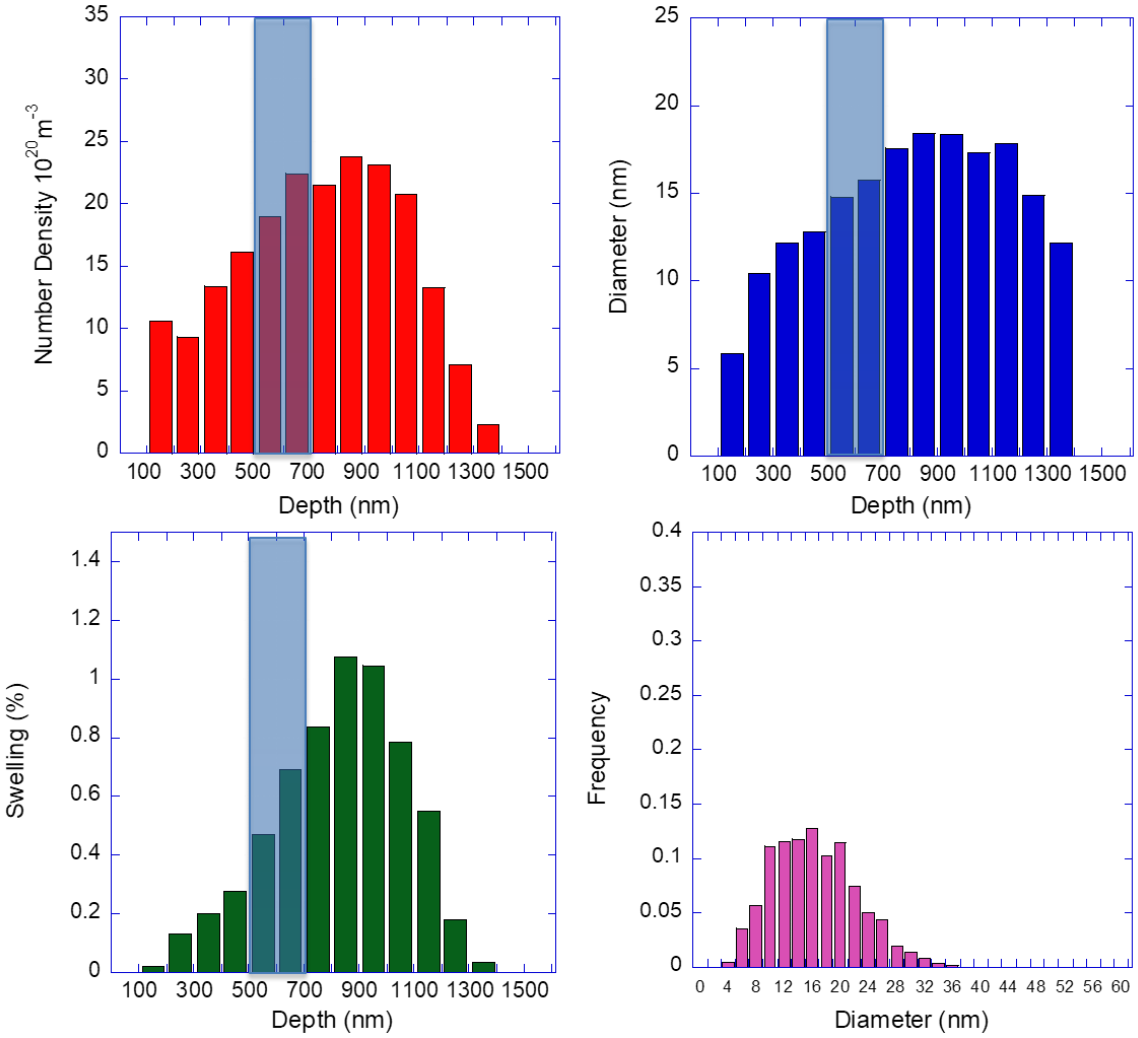

Figure C7. Cavity diameter, density and swelling are plotted as a function of depth for the 150 dpa, 1 appm He, nominal carbon condition. The cavity distribution at 500-700 nm is also shown.

NOMINAL CARBON CAMPAIGN:150 DPA:460ºC:10 APPM HE

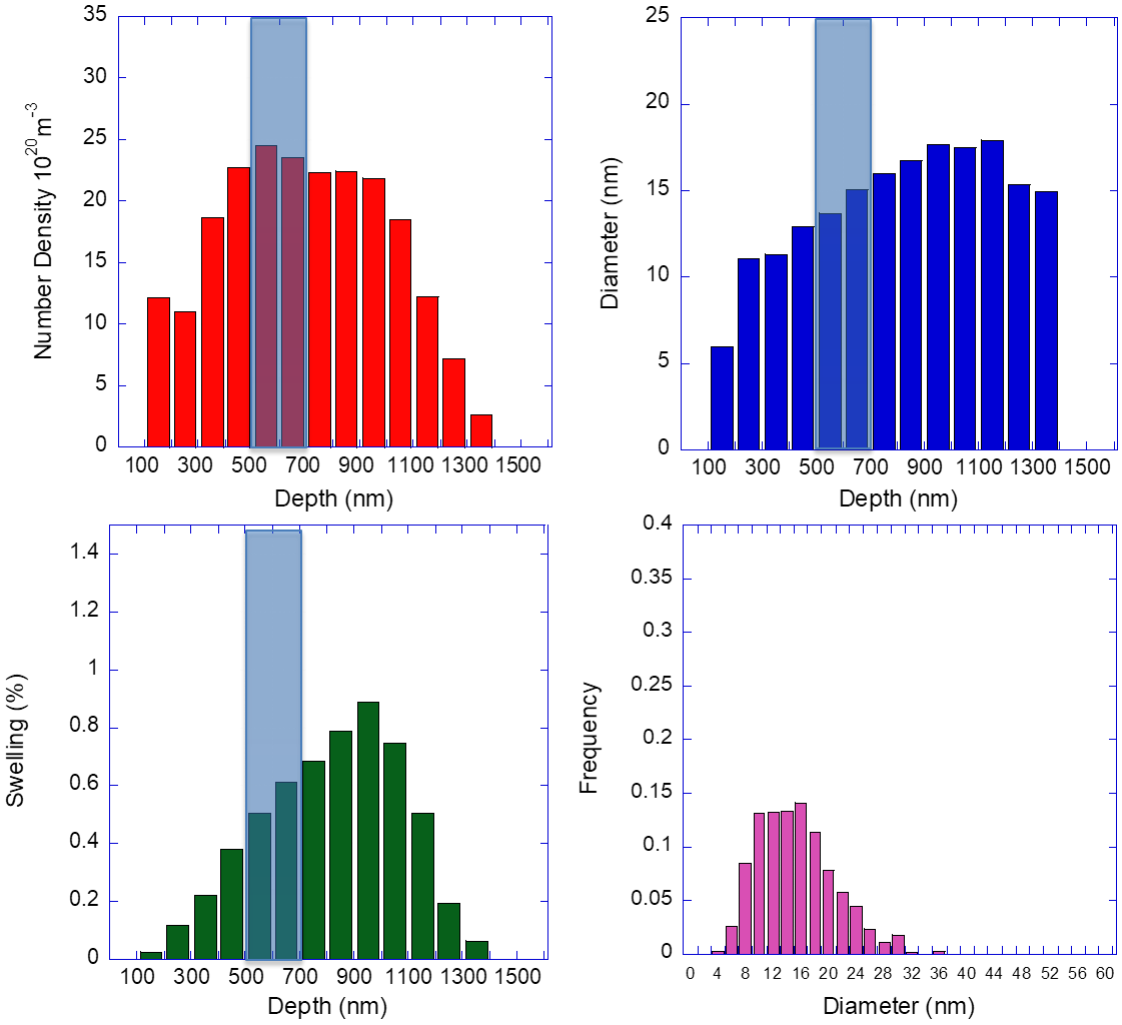

Figure C8. Cavity diameter, density and swelling are plotted as a function of depth for the 150 dpa, 10 appm He, nominal carbon condition. The cavity distribution at 500-700 nm is also shown.

NOMINAL CARBON CAMPAIGN:150 DPA:460ºC:100 APPM HE

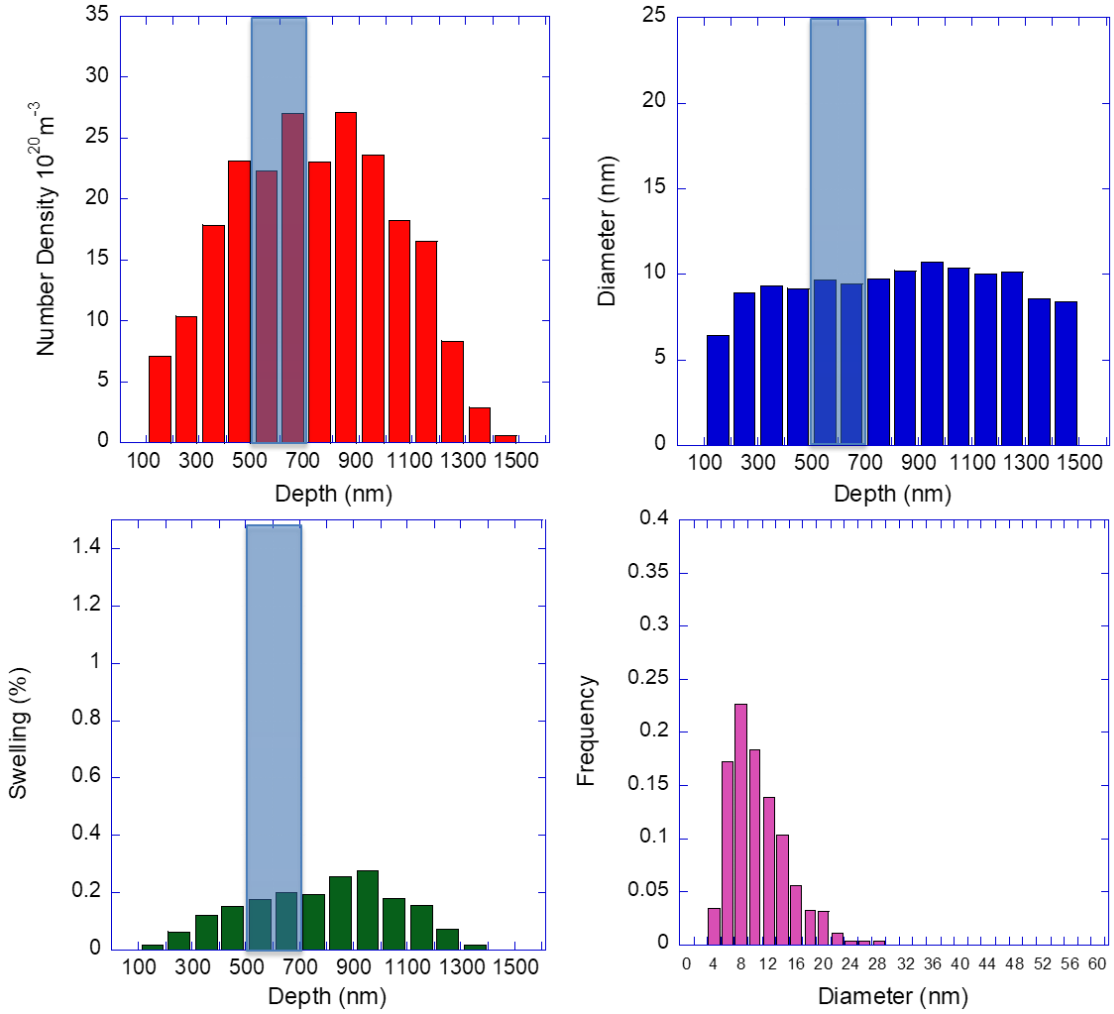

Figure C9. Cavity diameter, density and swelling are plotted as a function of depth for the 150 dpa, 100 appm He, nominal carbon condition. The cavity distribution at 500-700 nm is also shown.

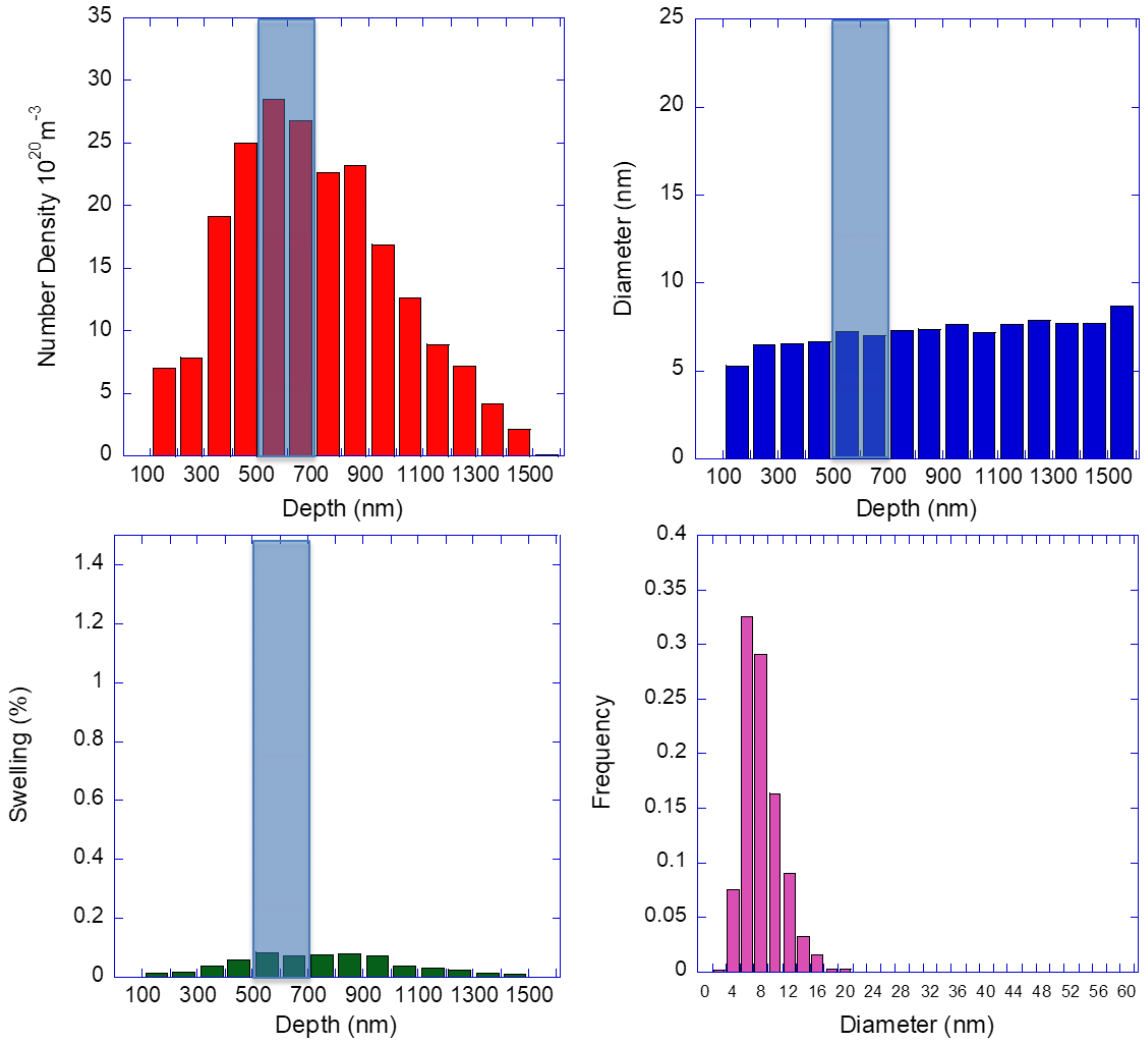

Figure C10. Cavity diameter, density and swelling are plotted as a function of depth for the 150 dpa, 1000 appm He, nominal carbon condition. The cavity distribution at 500-700 nm is also shown.

NOMINAL CARBON CAMPAIGN:300 DPA:460ºC:0 APPM HE

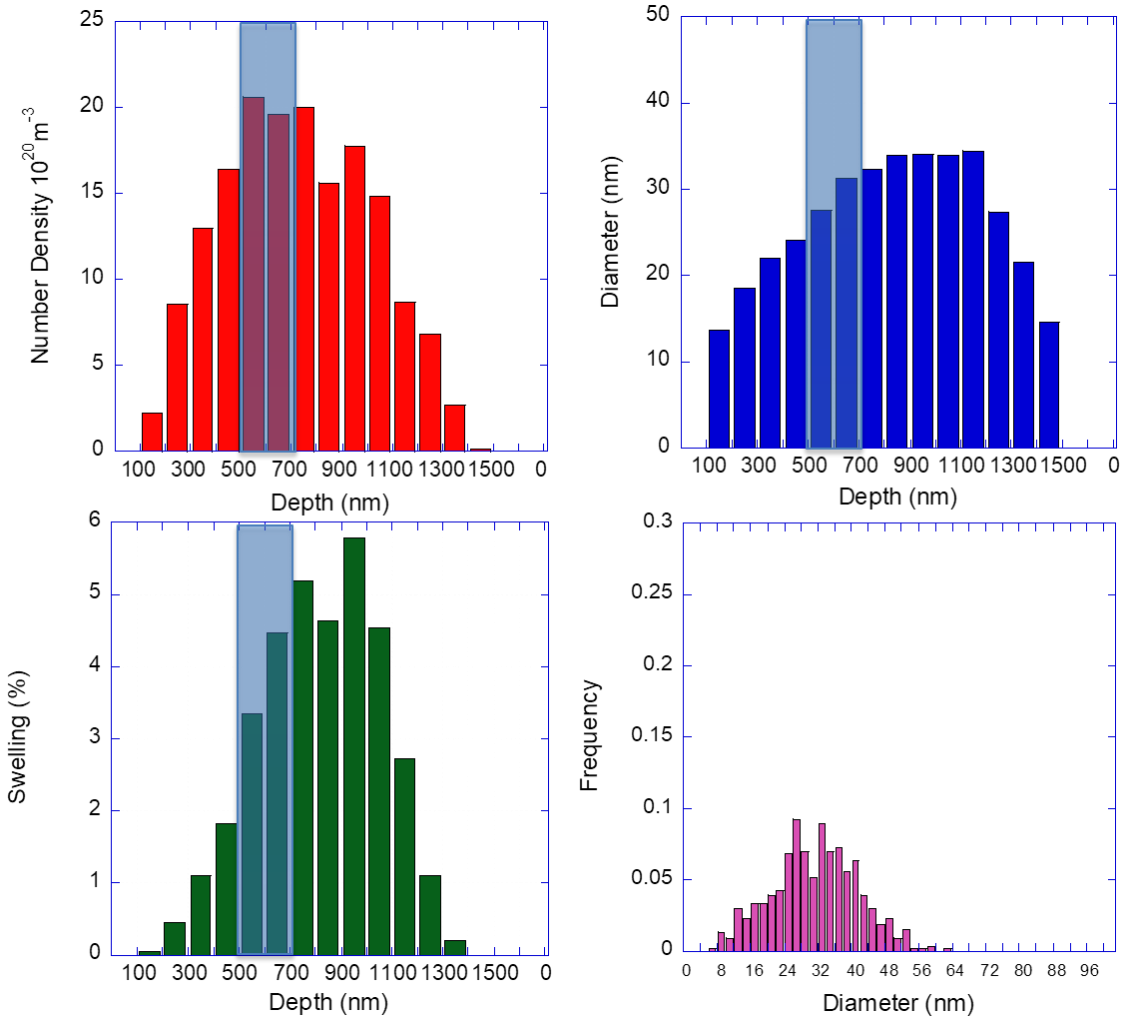

Figure C11. Cavity diameter, density and swelling are plotted as a function of depth for the 300 dpa, 0 appm He, nominal carbon condition. The cavity distribution at 500-700 nm is also shown

NOMINAL CARBON CAMPAIGN:300 DPA:460ºC:1 APPM HE

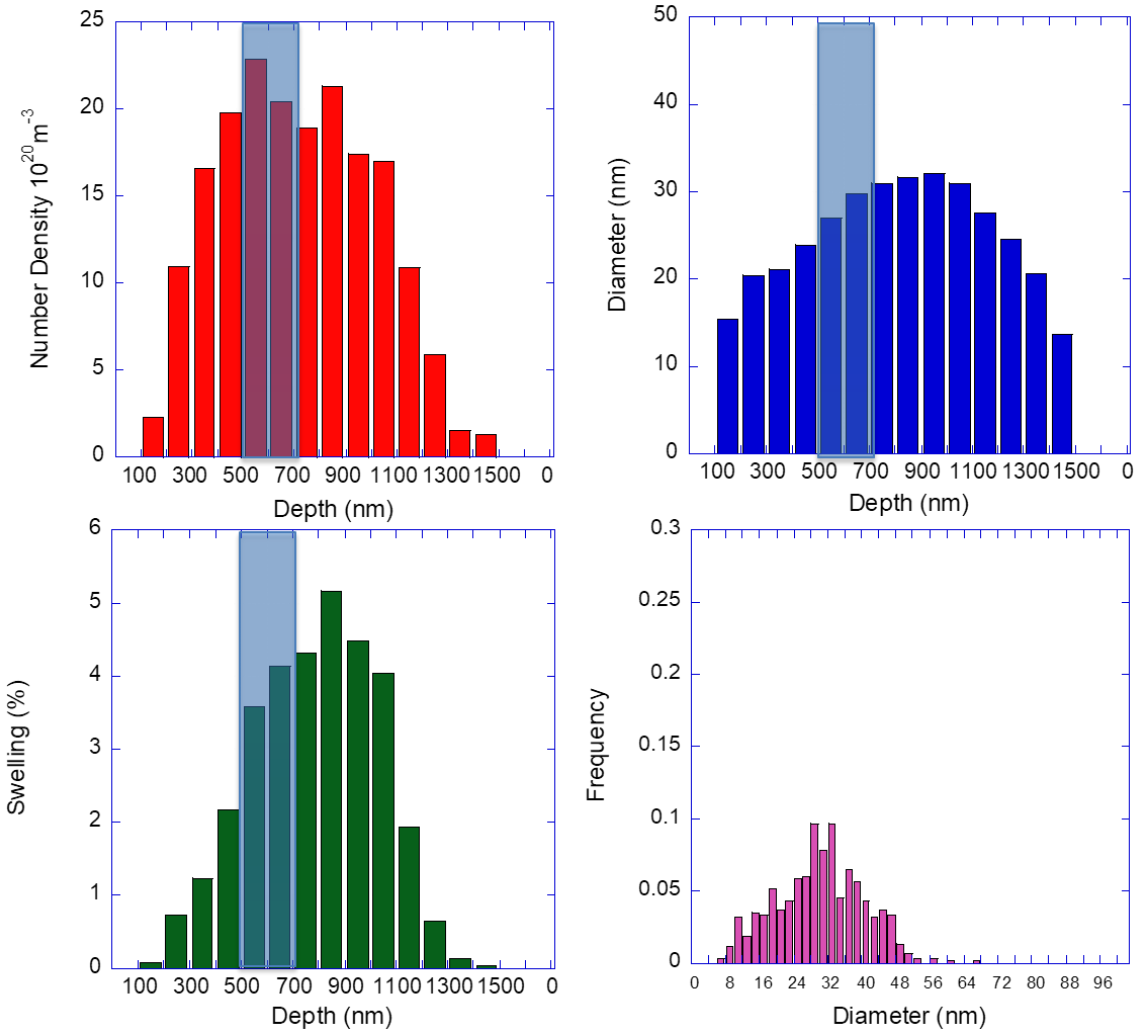

Figure C12. Cavity diameter, density and swelling are plotted as a function of depth for the 300 dpa, 1 appm He, nominal carbon condition. The cavity distribution at 500-700 nm is also shown.

NOMINAL CARBON CAMPAIGN:300 DPA:460ºC:10 APPM HE

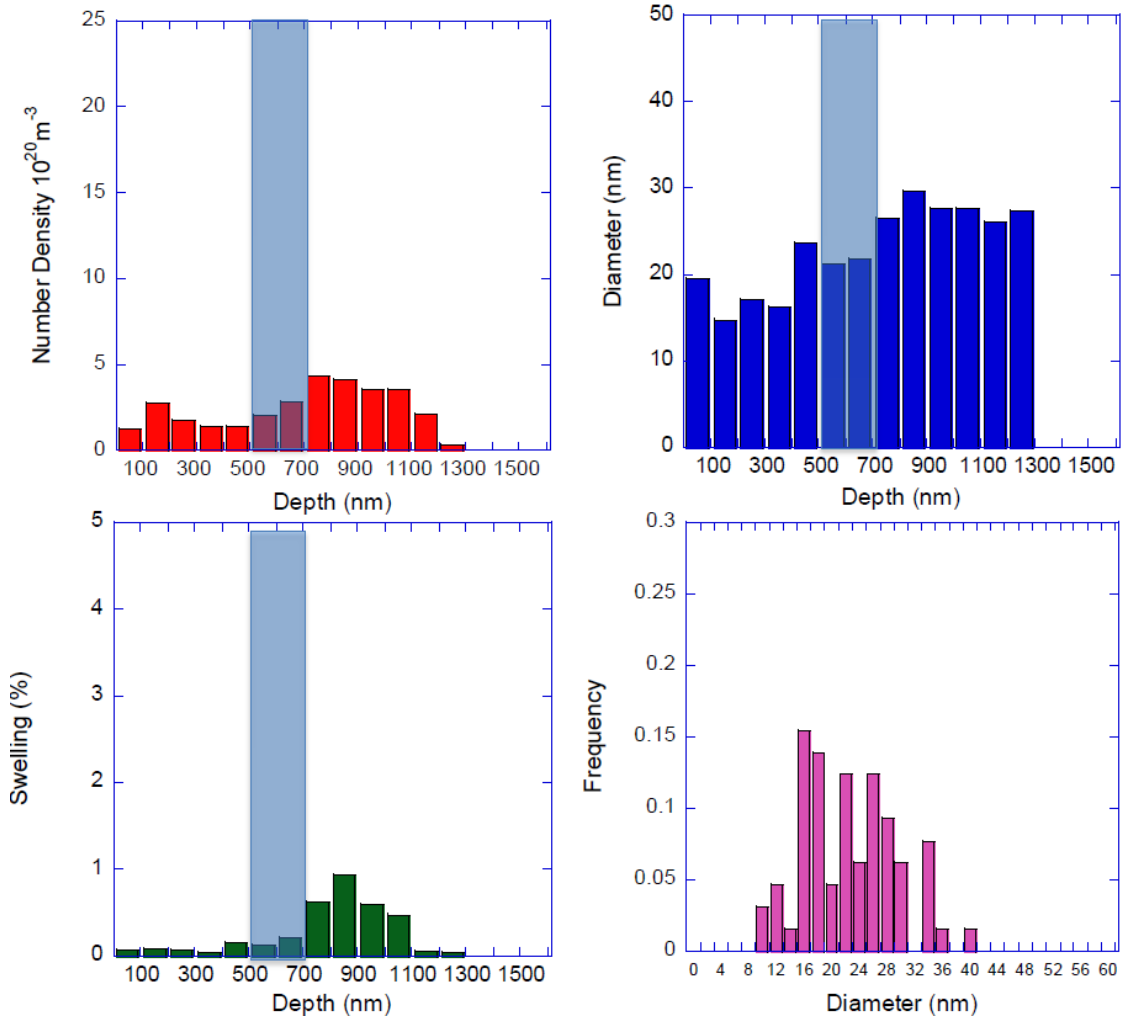

Figure C13. Cavity diameter, density and swelling are plotted as a function of depth for the 300 dpa, 10 appm He, nominal carbon condition. The cavity distribution at 500-700 nm is also shown.

NOMINAL CARBON CAMPAIGN:300 DPA:460ºC:100 APPM HE

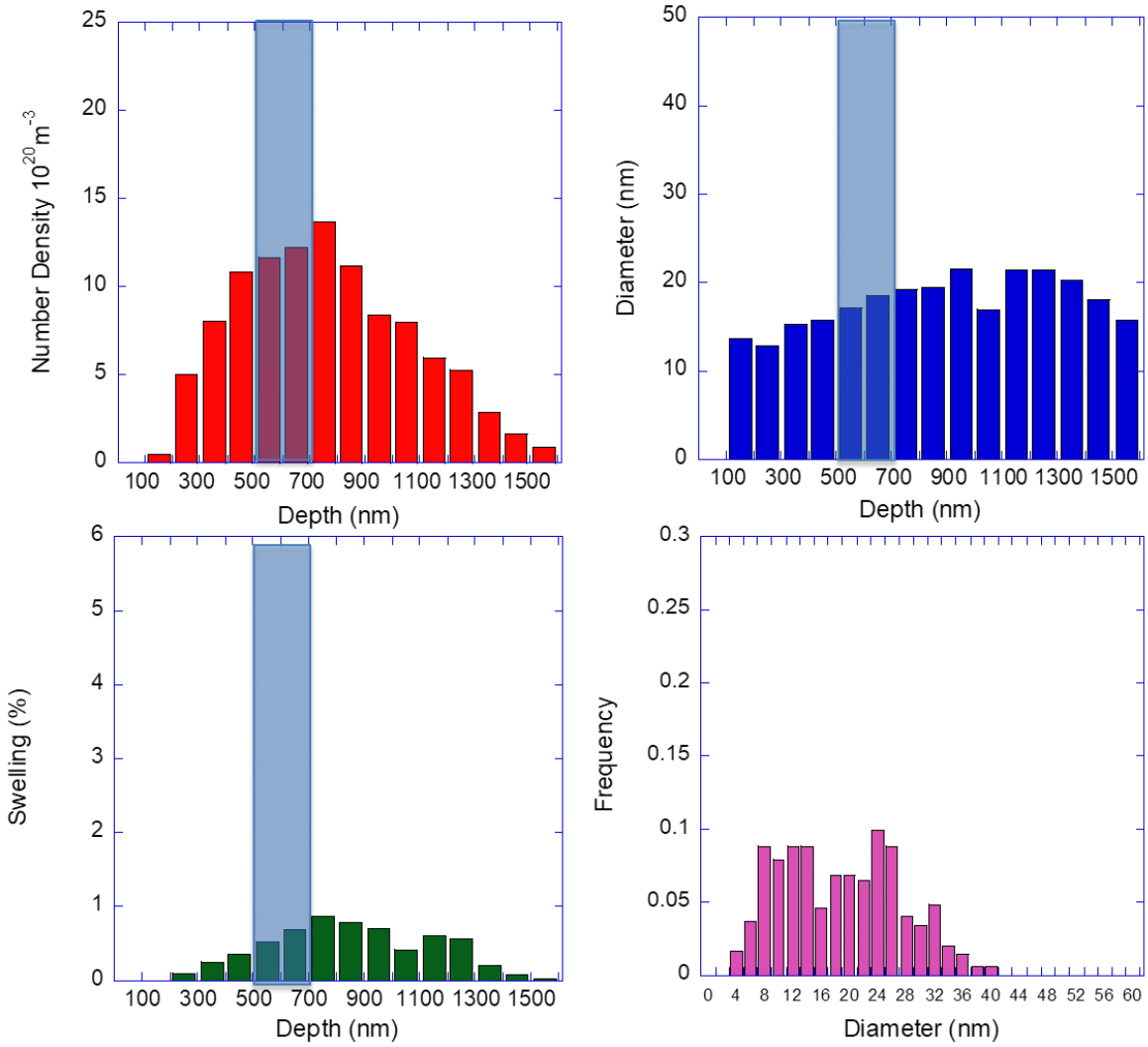

Figure C14. Cavity diameter, density and swelling are plotted as a function of depth for the 300 dpa, 100 appm He, nominal carbon condition. The cavity distribution at 500-700 nm is also shown.

NOMINAL CARBON CAMPAIGN:300 DPA:460ºC:1000 APPM HE

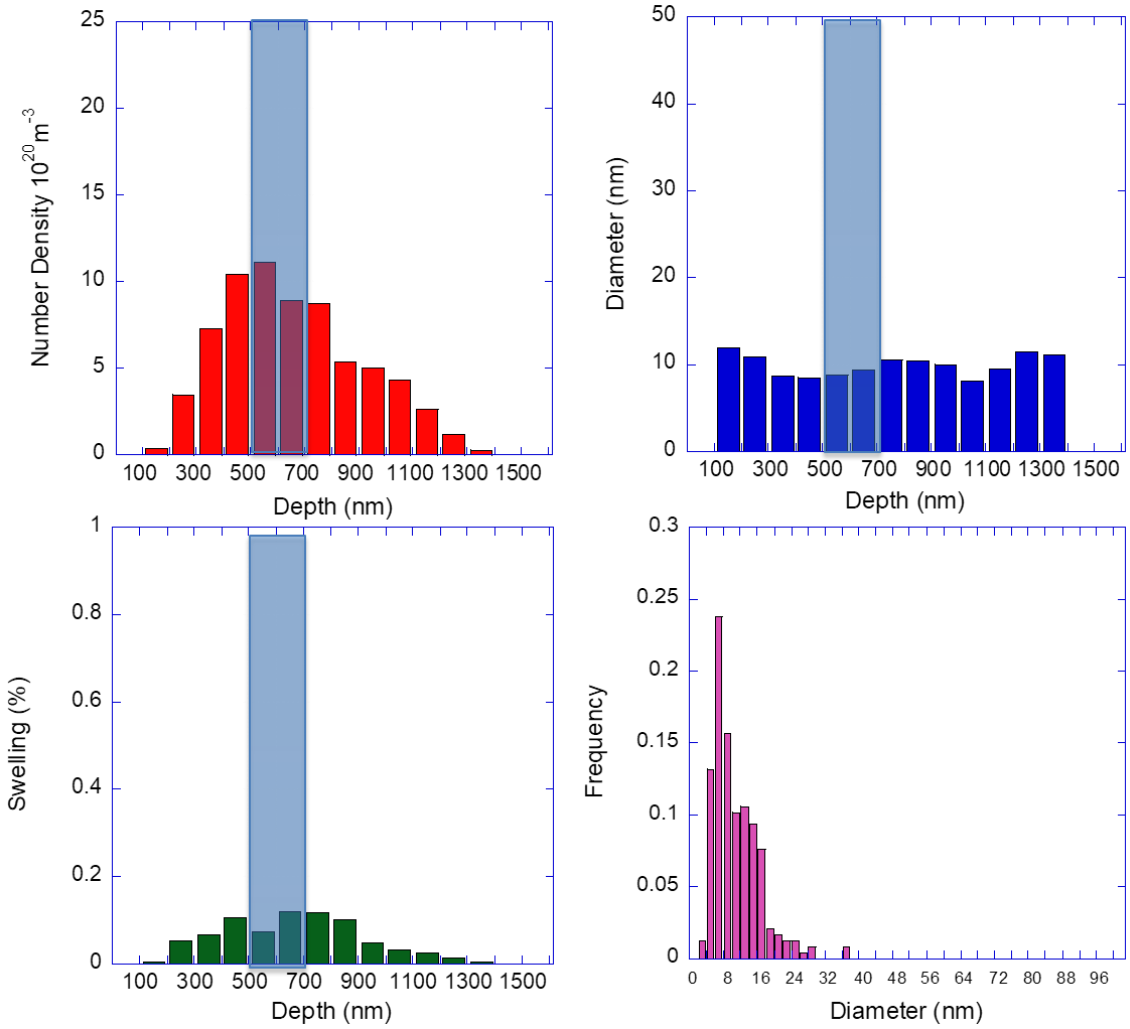

Figure C15. Cavity diameter, density and swelling are plotted as a function of depth for the 300 dpa, 1000 appm He, nominal carbon condition. The cavity distribution at 500-700 nm is also shown.

EXCESS CARBON CAMPAIGN:150 DPA:460ºC:0 APPM HE

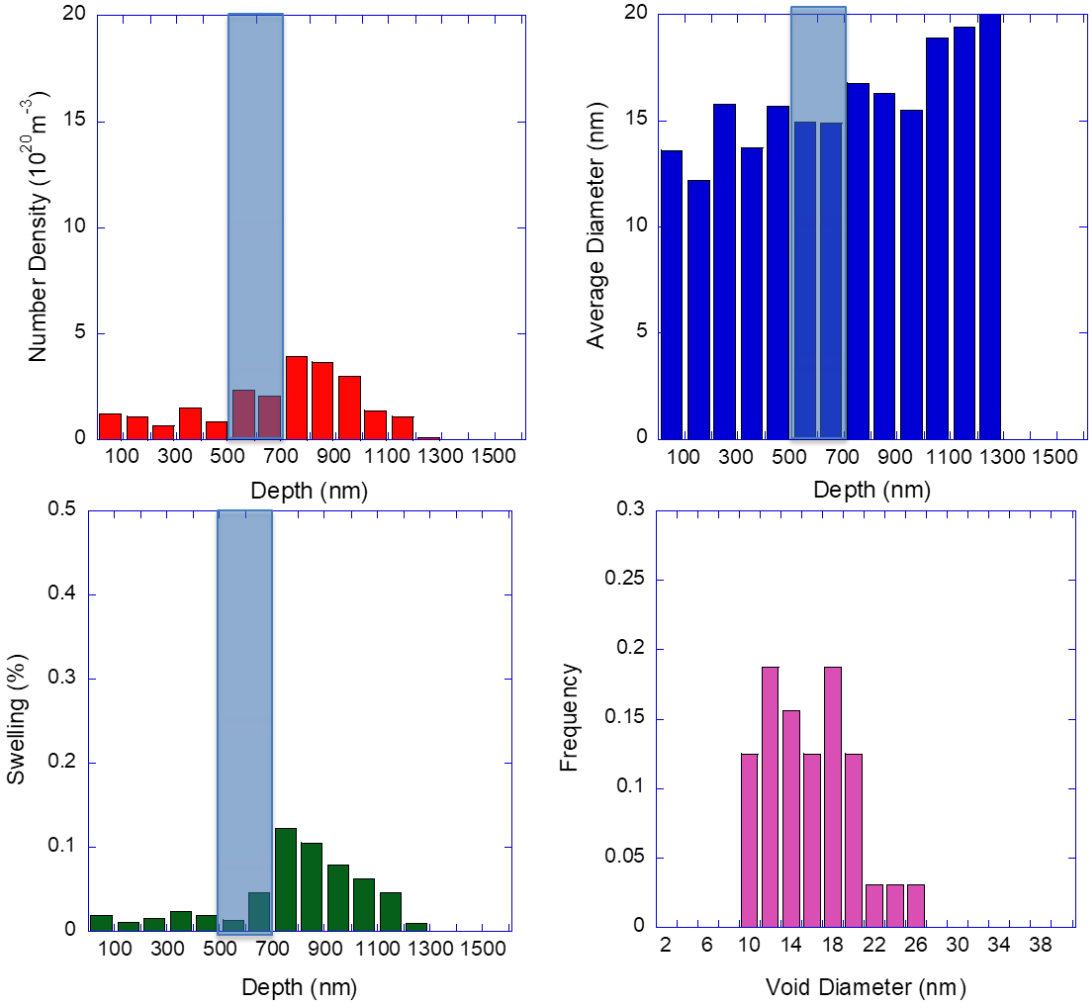

Figure C16. Cavity diameter, density and swelling are plotted as a function of depth for the 150 dpa, 0 appm He, excess carbon condition. The cavity distribution at 500-700 nm is also shown.

EXCESS CARBON CAMPAIGN:150 DPA:460ºC:1 APPM HE

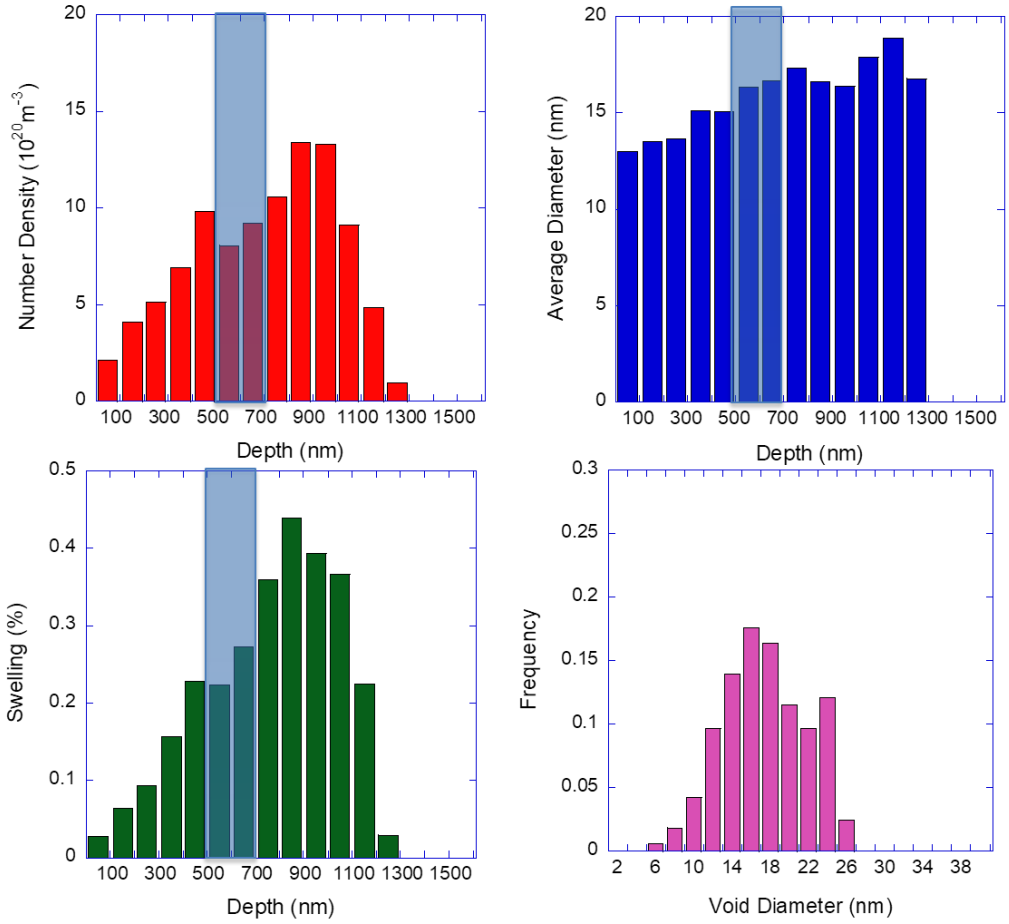

Figure C17. Cavity diameter, density and swelling are plotted as a function of depth for the 150 dpa, 1 appm He, excess carbon condition. The cavity distribution at 500-700 nm is also shown.

EXCESS CARBON CAMPAIGN:150 DPA:460ºC:10 APPM HE

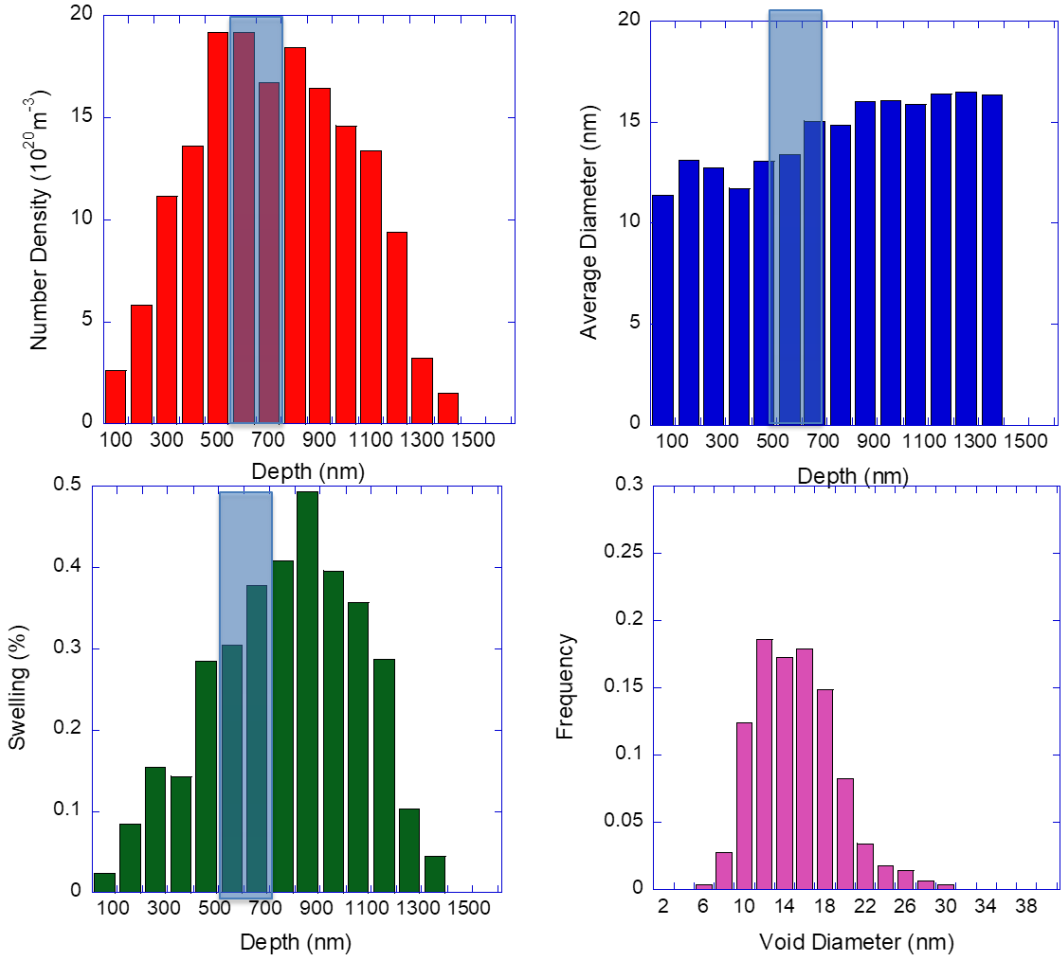

Figure C18. Cavity diameter, density and swelling are plotted as a function of depth for the 150 dpa, 10 appm He, excess carbon condition. The cavity distribution at 500-700 nm is also shown.

EXCESS CARBON CAMPAIGN:150 DPA:460ºC:100 APPM HE

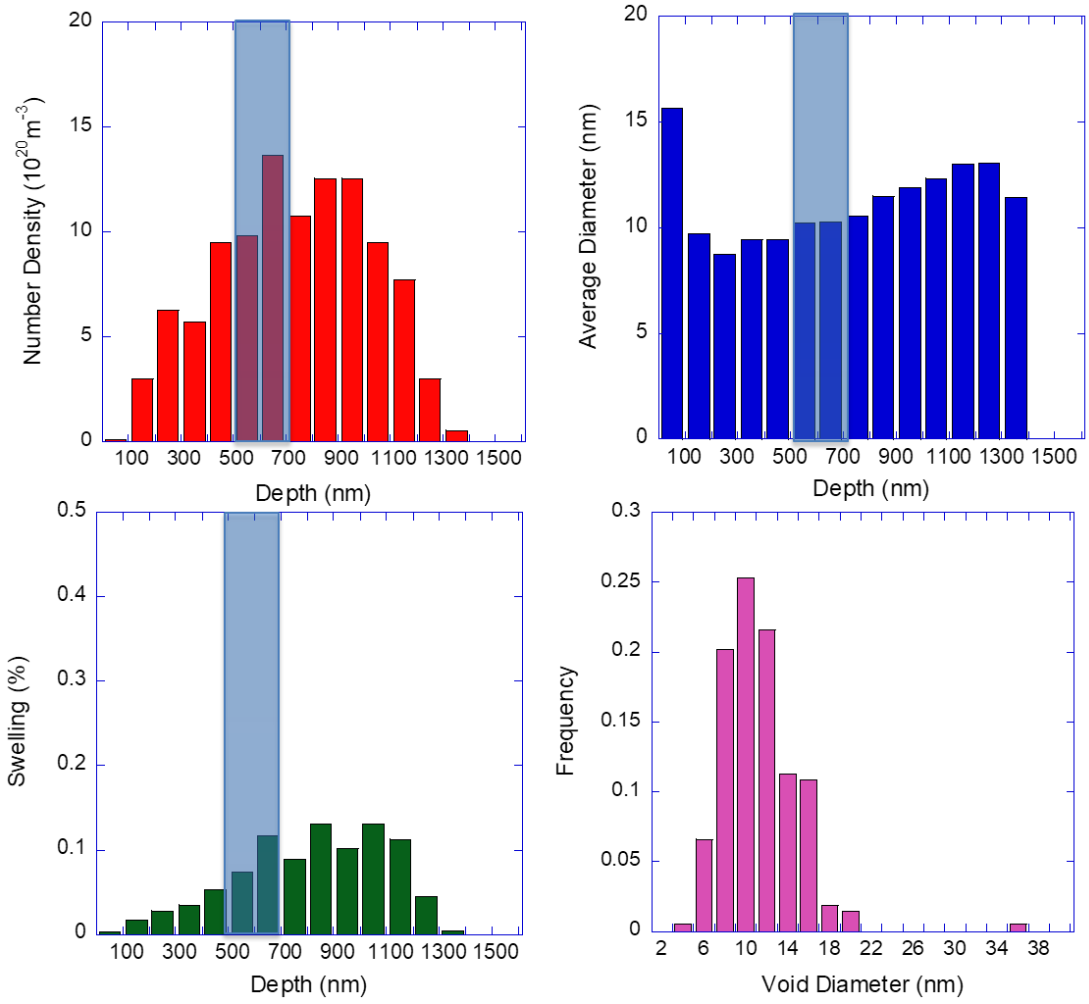

Figure C19. Cavity diameter, density and swelling are plotted as a function of depth for the 150 dpa, 100 appm He, excess carbon condition. The cavity distribution at 500-700 nm is also shown.

EXCESS CARBON CAMPAIGN:150 DPA:460ºC:1000 APPM HE

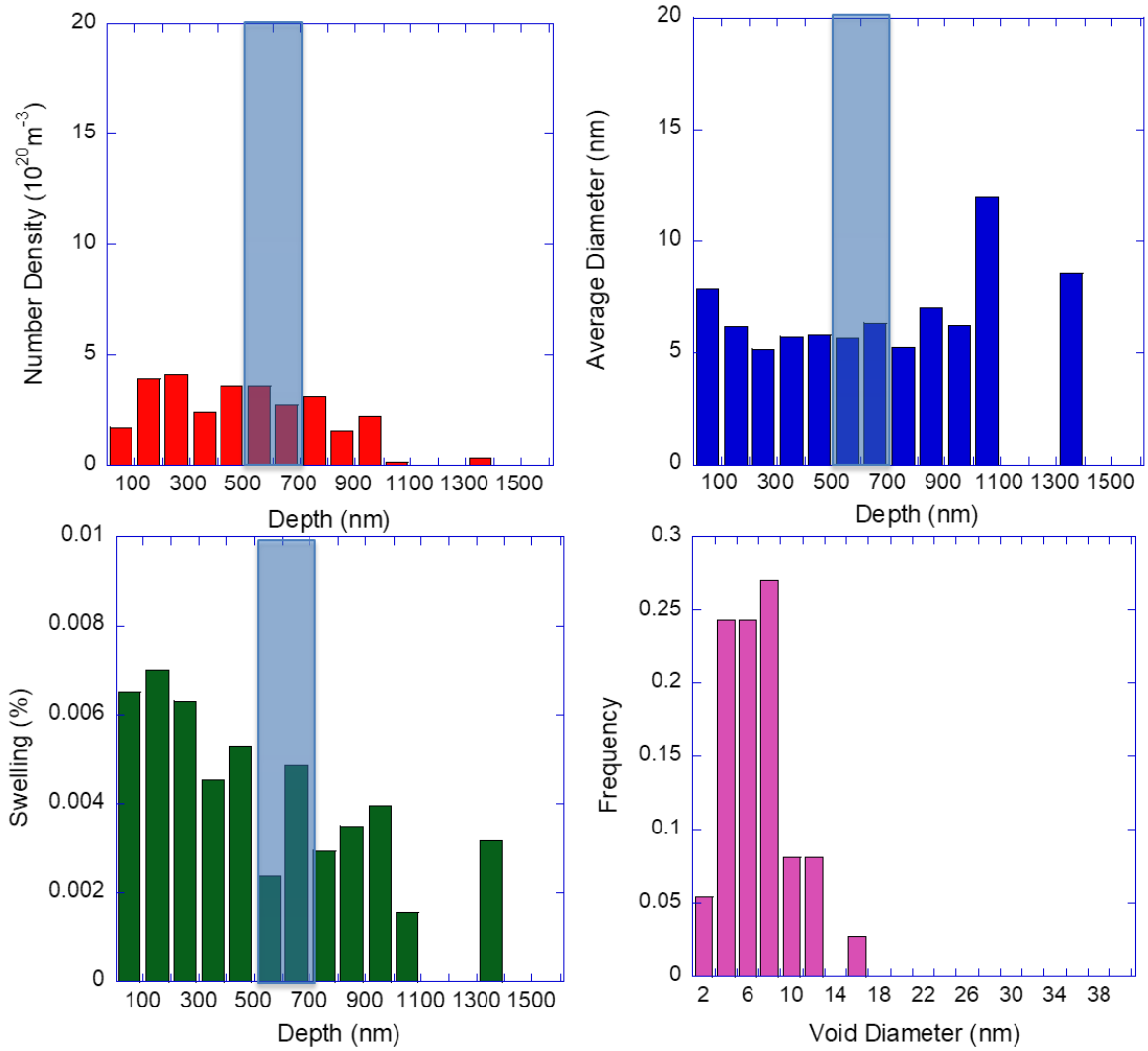

Figure C20. Cavity diameter, density and swelling are plotted as a function of depth for the 150 dpa, 1000 appm He, excess carbon condition. The cavity distribution at 500-700 nm is also shown.

EXCESS CARBON CAMPAIGN:300 DPA:460ºC:0 APPM HE

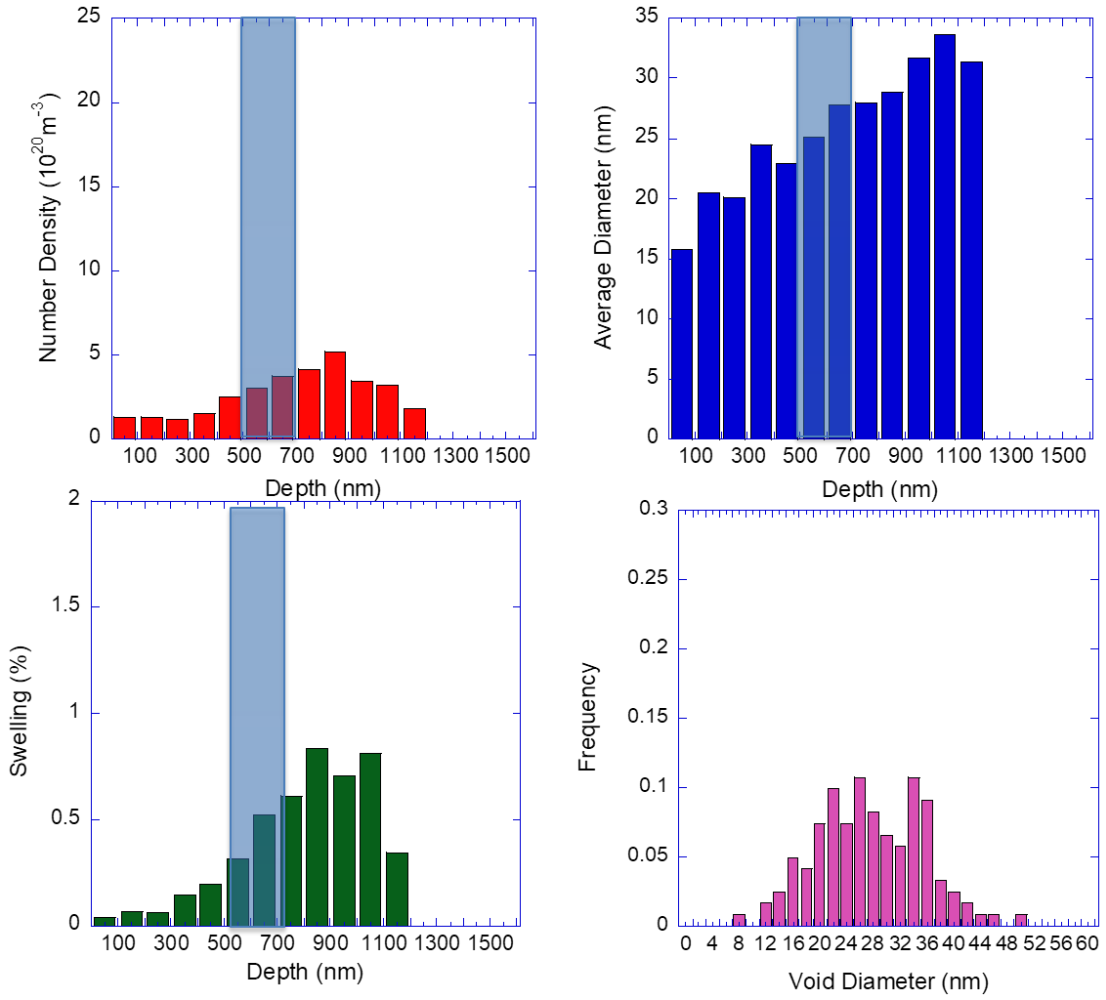

Figure C21. Cavity diameter, density and swelling are plotted as a function of depth for the 300 dpa, 0 appm He, excess carbon condition. The cavity distribution at 500-700 nm is also shown.

EXCESS CARBON CAMPAIGN:300 DPA:460ºC:1 APPM HE

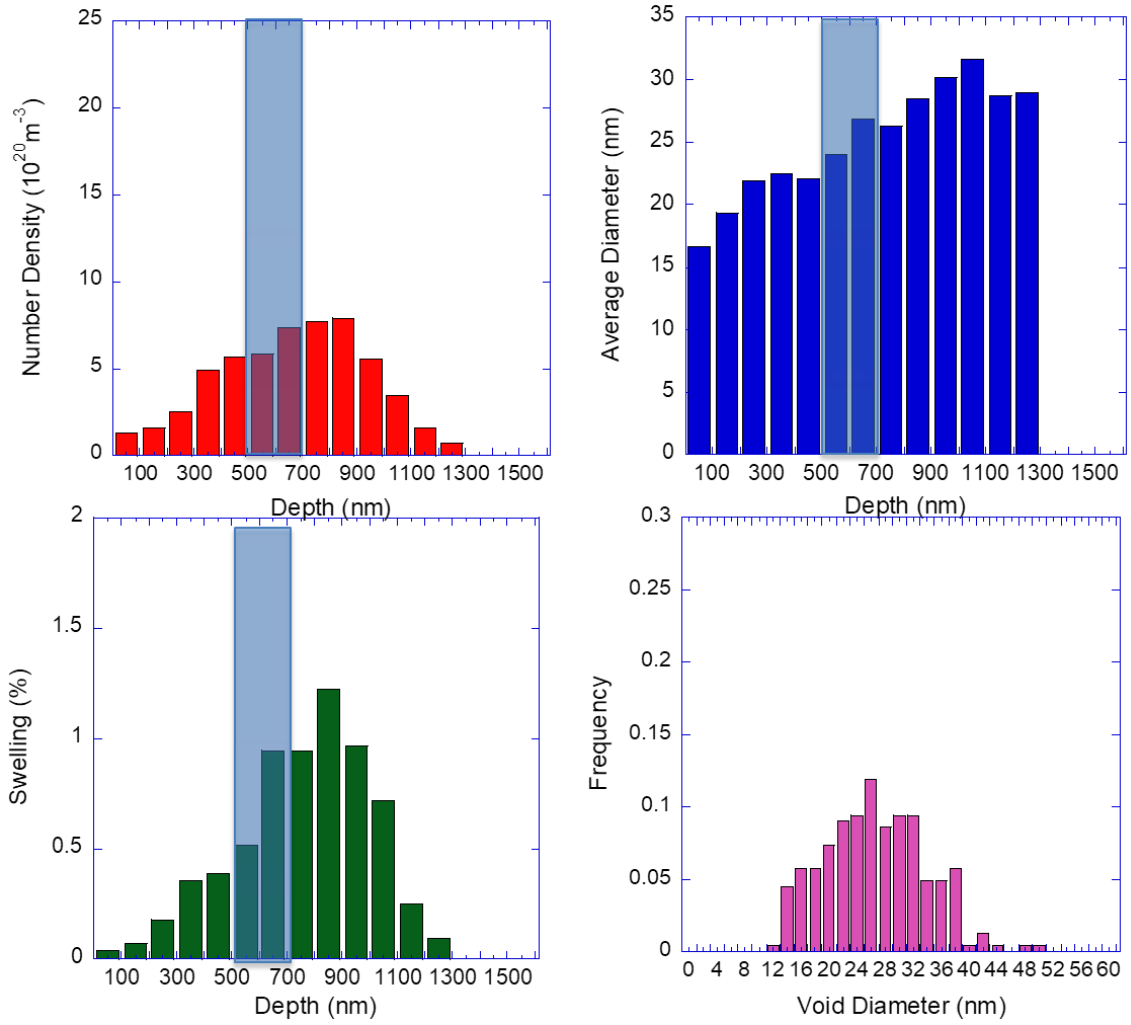

Figure C22. Cavity diameter, density and swelling are plotted as a function of depth for the 300 dpa, 1 appm He, excess carbon condition. The cavity distribution at 500-700 nm is also shown.

EXCESS CARBON CAMPAIGN:300 DPA:460ºC:10 APPM HE

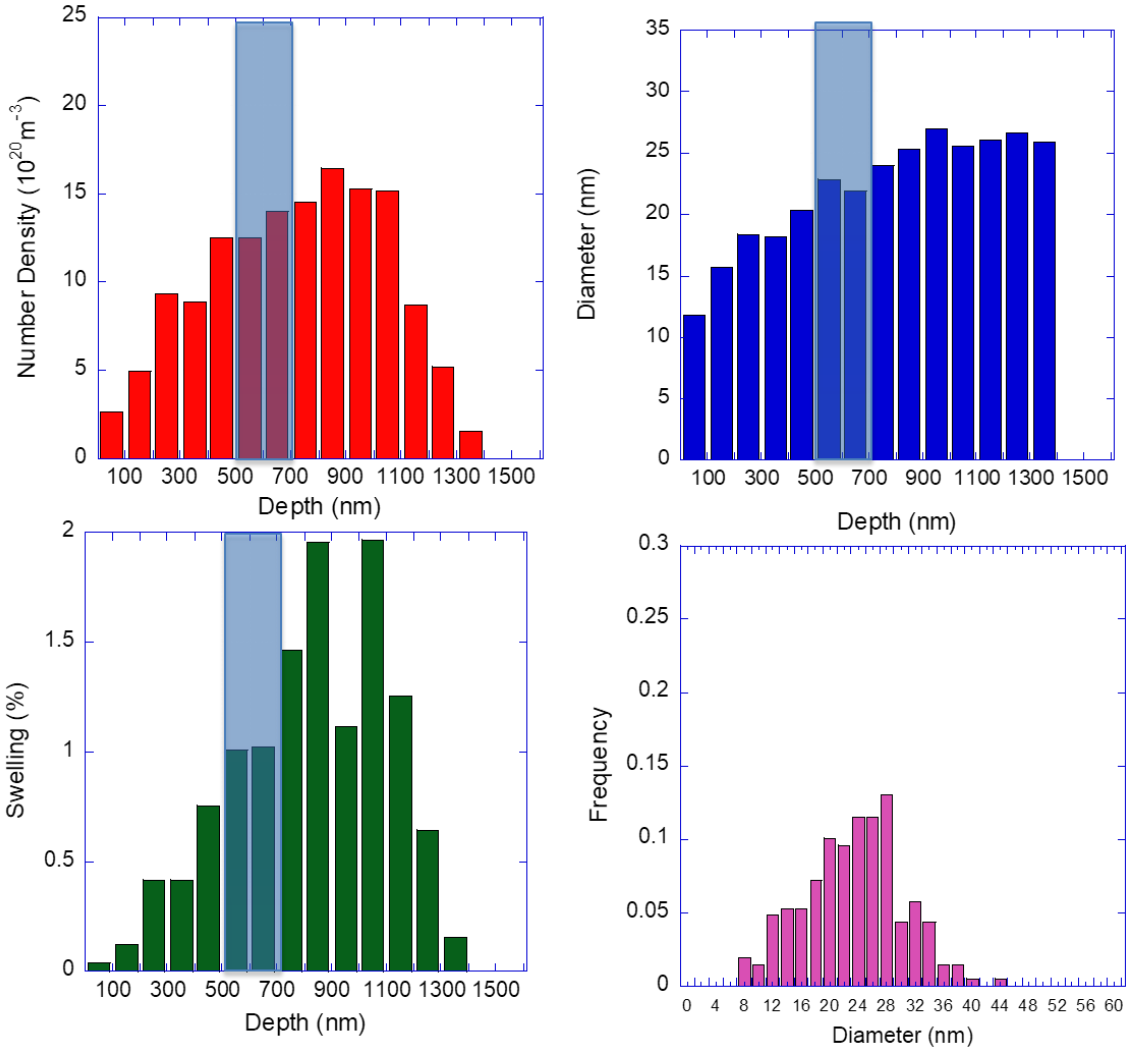

Figure C23. Cavity diameter, density and swelling are plotted as a function of depth for the 300 dpa, 10 appm He, excess carbon condition. The cavity distribution at 500-700 nm is also shown.

EXCESS CARBON CAMPAIGN:300 DPA:460C:100 APPM HE

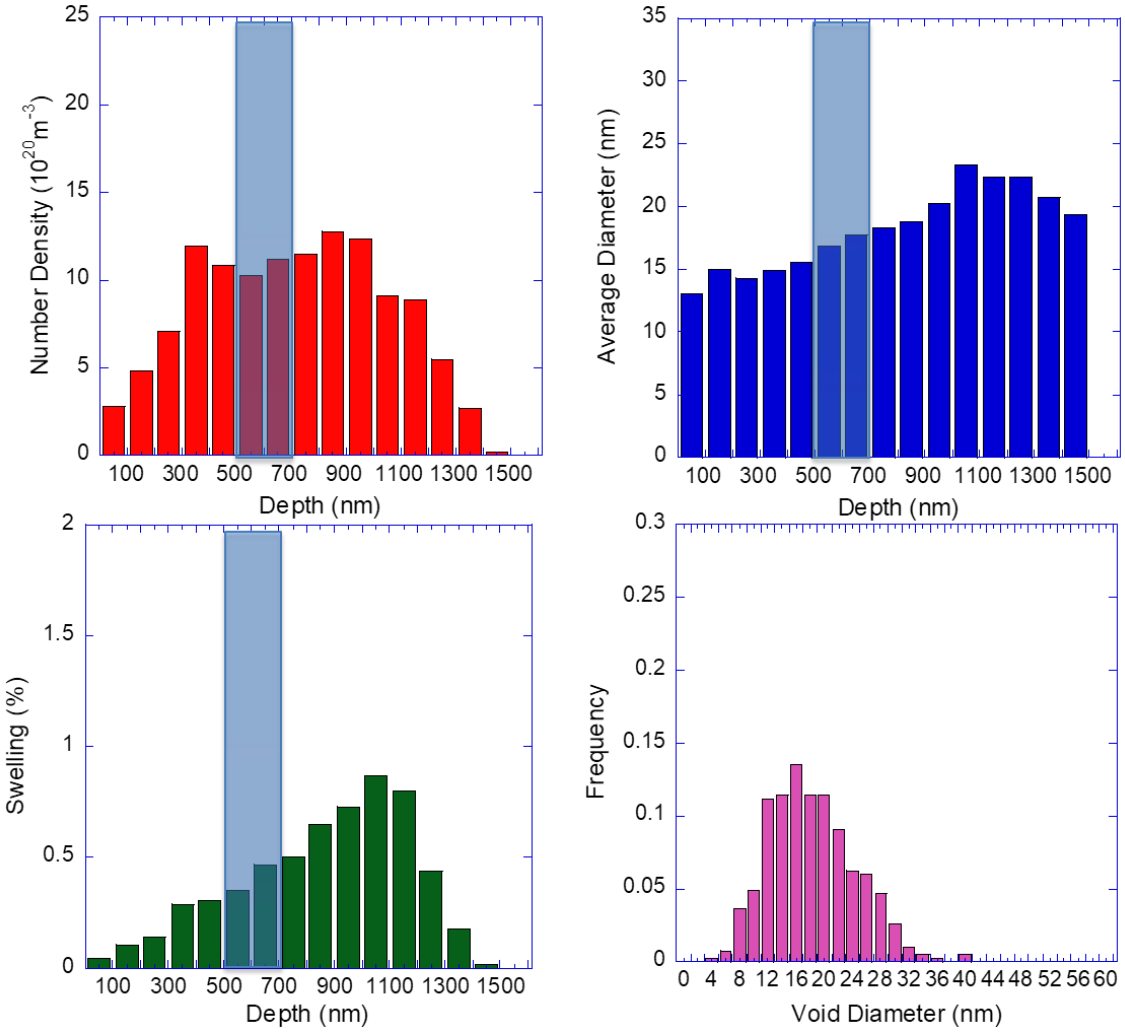

Figure C24. Cavity diameter, density and swelling are plotted as a function of depth for the 300 dpa, 100 appm He, excess carbon condition. The cavity distribution at 500-700 nm is also shown.

EXCESS CARBON CAMPAIGN:300 DPA:460ºC:1000 APPM HE

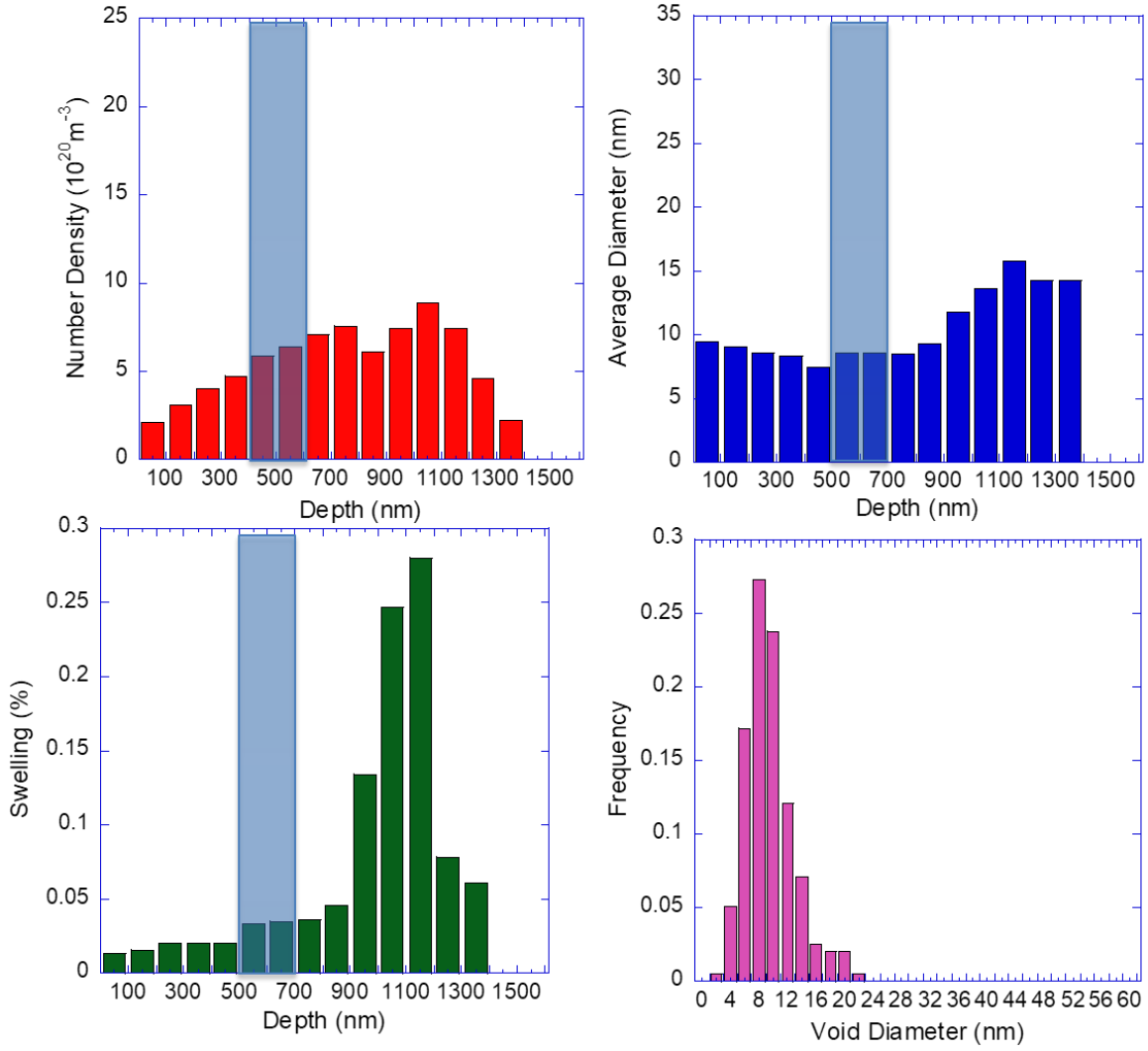

Figure C25. Cavity diameter, density and swelling are plotted as a function of depth for the 300 dpa, 1000 appm He, excess carbon condition. The cavity distribution at 500-700 nm is also shown.

EXCESS CARBON CAMPAIGN:450 DPA:460ºC:0 APPM HE

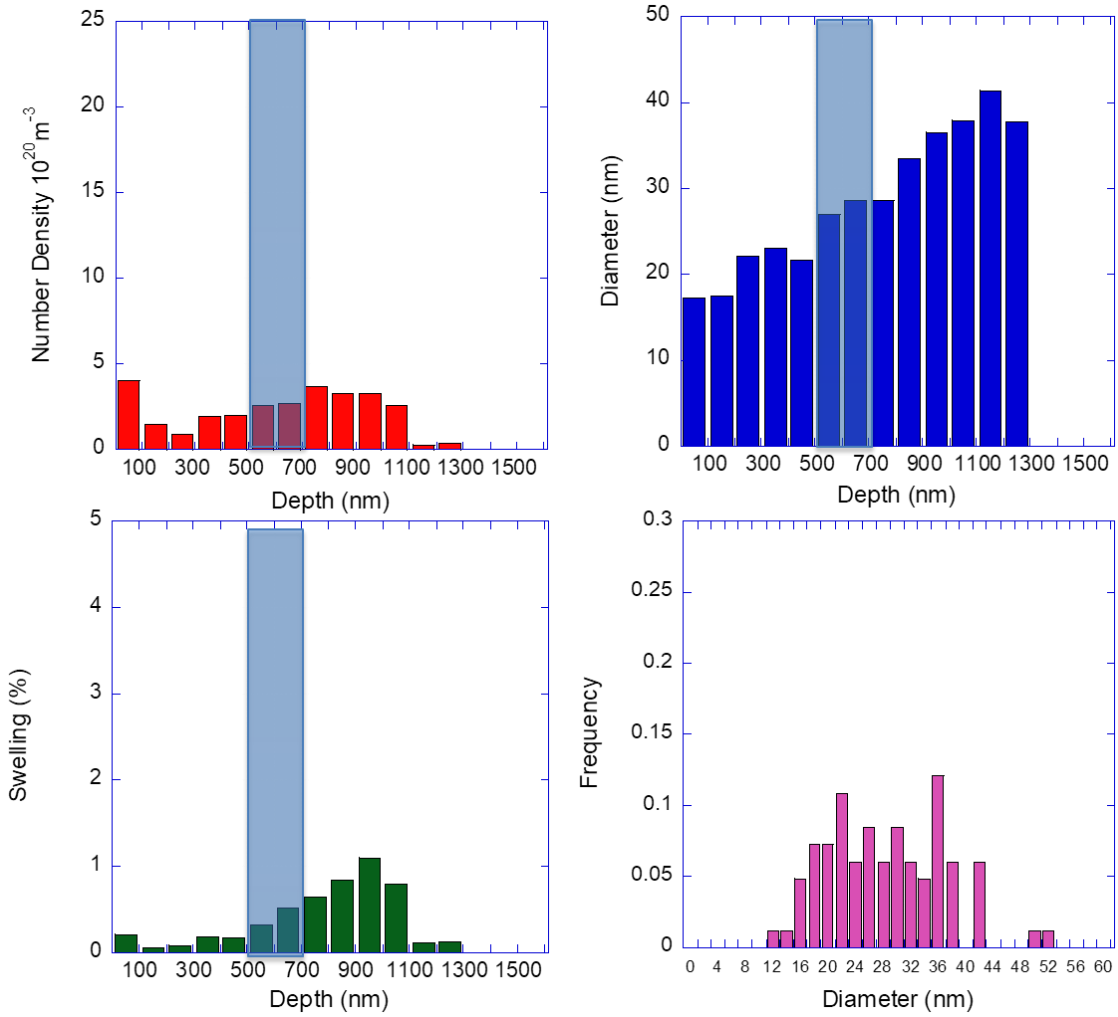

Figure C26. Cavity diameter, density and swelling are plotted as a function of depth for the 450 dpa, 0 appm He, excess carbon condition. The cavity distribution at 500-700 nm is also shown.

EXCESS CARBON CAMPAIGN:450 DPA:460ºC:1 APPM HE

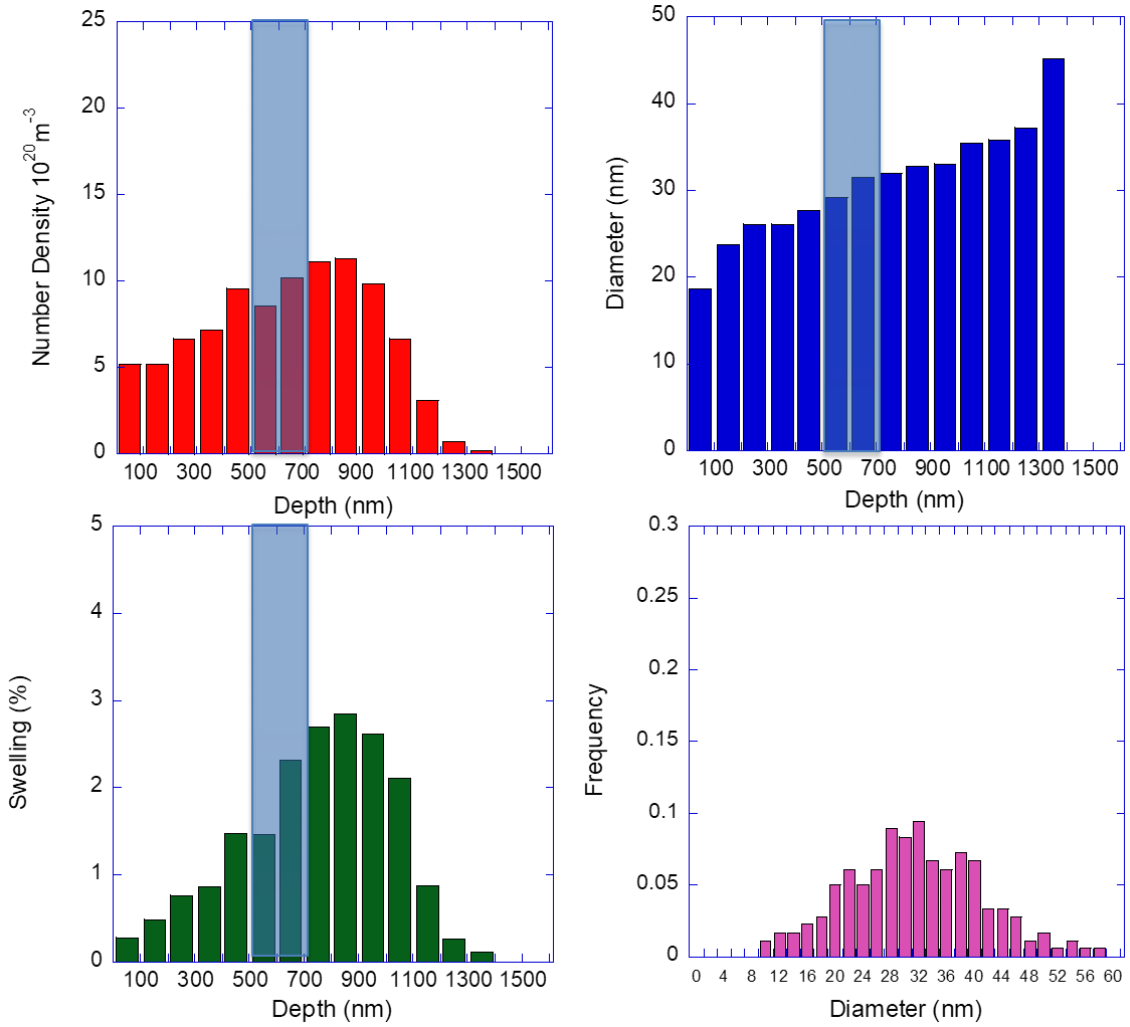

Figure C27. Cavity diameter, density and swelling are plotted as a function of depth for the 450 dpa, 1 appm He, excess carbon condition. The cavity distribution at 500-700 nm is also shown.

EXCESS CARBON CAMPAIGN:450 DPA:460ºC:10 APPM HE

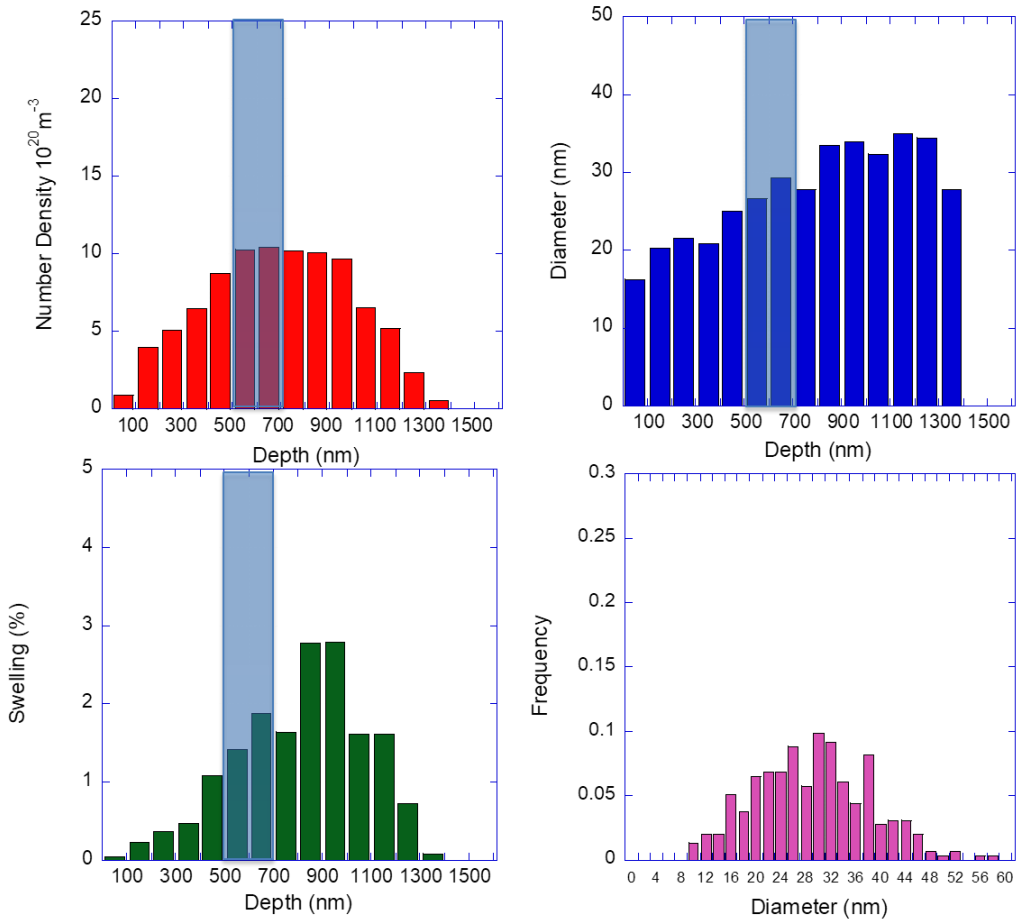

Figure C28. Cavity diameter, density and swelling are plotted as a function of depth for the 450 dpa, 10 appm He, excess carbon condition. The cavity distribution at 500-700 nm is also shown.

EXCESS CARBON CAMPAIGN:450 DPA:460ºC:100 APPM HE

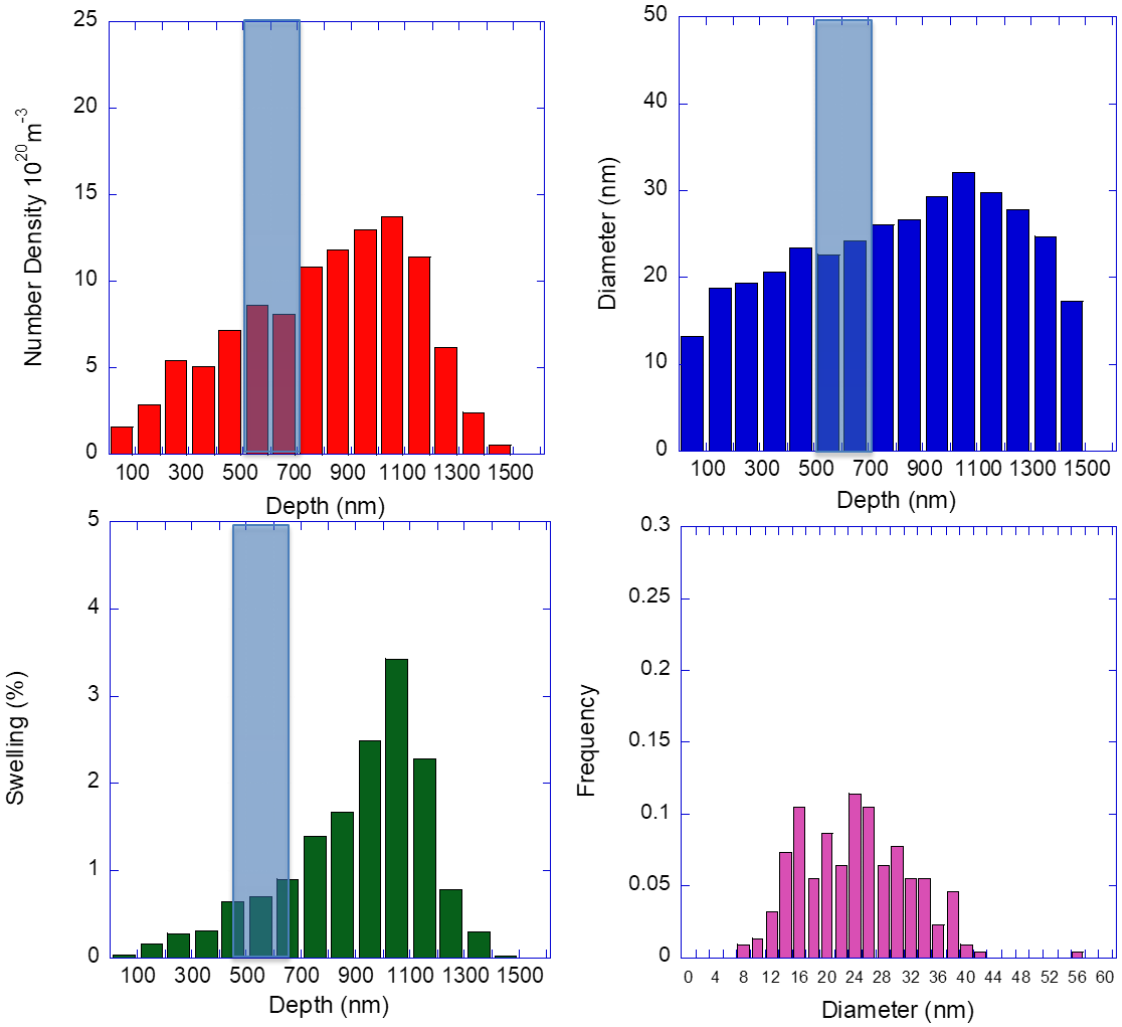

Figure C29. Cavity diameter, density and swelling are plotted as a function of depth for the 450 dpa, 100 appm He, excess carbon condition. The cavity distribution at 500-700 nm is also shown.

EXCESS CARBON CAMPAIGN:450 DPA:460ºC:1000 APPM HE

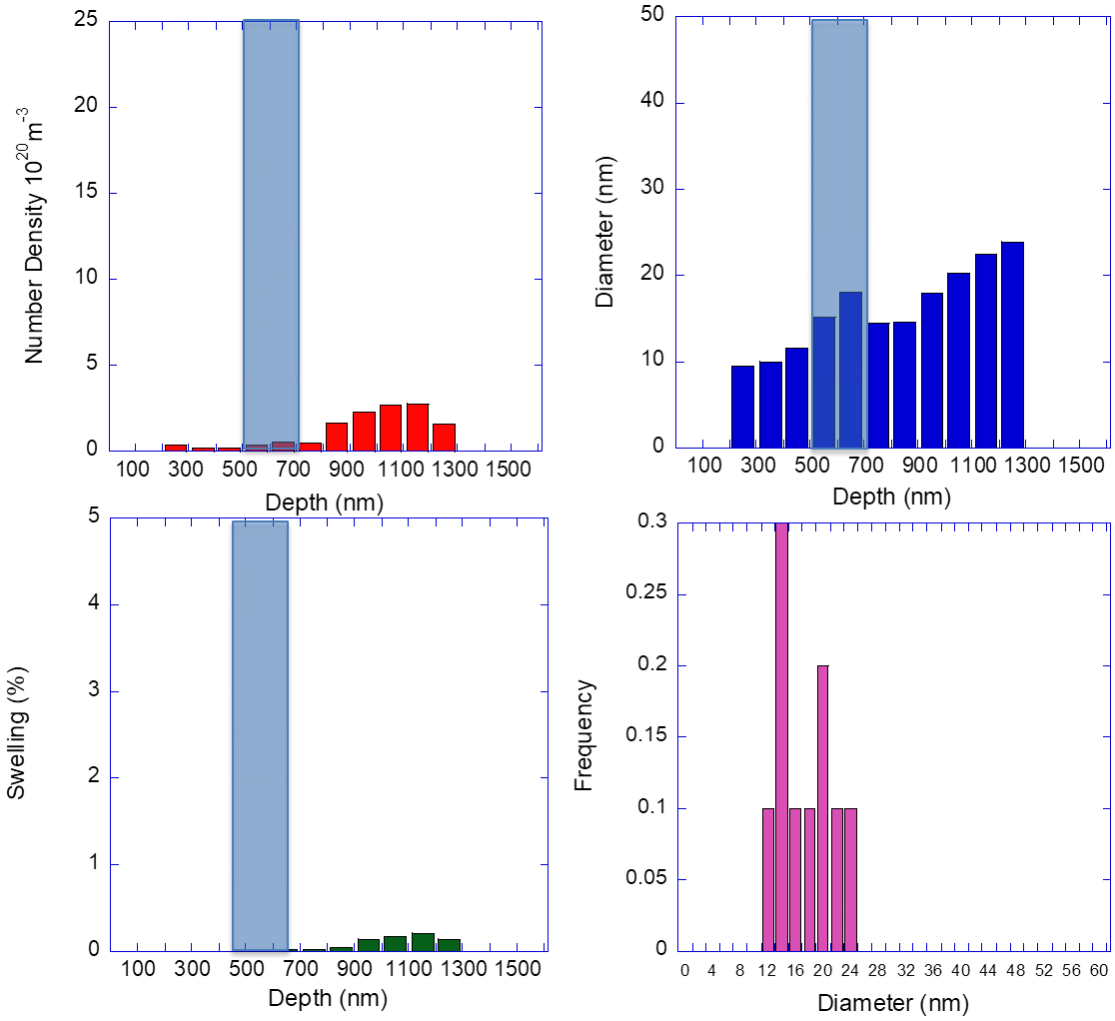

Figure C30. Cavity diameter, density and swelling are plotted as a function of depth for the 450 dpa, 1000 appm He, excess carbon condition. The cavity distribution at 500-700 nm is also shown.

APPENDIX D: CALCULATION OF VACANCY SUPERSATURATION FOR CRITICAL CAVITY RADIUS

The vacancy supersaturation is defined as C_v / C_v^o, where C_v is the steady-state concentration of vacancies in the solid, and C_v^o is the concentration of thermal vacancies. C_v was calculated assuming a low temperature, high sink density regime as per [15]. The equation for C_v is given as:

$$C_v = -\frac{K_{is}}{2K_{iv}} + \left[\frac{K_0 K_{is}}{K_{iv} K_{vs}} + \frac{K_{is}^2 C_s^2}{4K_{iv}^2} \right]^{1/2} \tag{D.1}$$

where K_{is}, K_{iv} and K_{vs} are recombination constants, K_0 is the damage rate (in displacements/volume/sec) and C_s is the concentration of sinks. The recombination constants were calculated using the following equations:

$$K_{is} = 4\pi r_i D_i \tag{D.2}$$

$$K_{iv} = 4\pi r_i D_i \tag{D.3}$$

$$K_{vs} = 4\pi r_i D_v \tag{D.4}$$

where r_i is the interaction radius, estimated as 10 times the lattice parameter, and D_i and D_v are the diffusion coefficients for interstitials and vacancies. D_i and D_v were calculated using the following equations:

$$D_i = \nu a^2 \exp\left(\frac{-E_m^i}{kT} \right) \tag{D.5}$$

$$D_v = \nu a^2 \exp\left(\frac{-E_m^v}{kT} \right) \tag{D.6}$$

where ν is the frequency factor, a is the lattice parameter, k is the Boltzmann constant, T is the irradiation temperature, and E_m^i and E_m^v are the migration energies for vacancies and interstitials, respectively.

The equation for the thermal vacancy concentration, C_v^o, is given as:

$$C_v^o = \frac{1}{\Omega}\exp\left(\frac{S_f}{k}\right)\exp\left(\frac{-E_f}{kT}\right) \tag{D.7}$$

where Ω is the atomic volume (a^3), S_f is the vacancy entropy of formation, and E_f is the vacancy formation energy. The necessary parameters for these equations are summarized in **Table D.1.**

Table D.1 Parameters used for calculation of vacancy super-saturation

Symbol	Definition	Value	Ref.
T	Irradiation Temperature	460°C	-
Ω	Atomic Volume	2.38×10^{-29} m^{-3}	-
K_o	Damage Rate	1×10^{-3} dpa/s	-
E_v^m	Vacancy Migration Energy	0.63 eV	[14]
E_f	Vacancy Formation Energy	1.6 eV	[14]
E_i^m	Interstitial Migration Energy	0.22 eV	[14]
a	Lattice Parameter	0.288 nm	-
ν	Diffusion Frequency Factor	10^{13} s^{-1}	-
S_f	Vacancy formation entropy	$2.17k$	-
C_s	Sink density	10^{-10} nm^{-3}	-

REFERENCES

[1] G.S. Was, J.T. Busby, T. Allen, E.A. Kenik, A. Jenssen, S.M. Bruemmer, J. Gan, A.D. Edwards, P.M. Scott, P.L. Andresen, Emulation of neutron irradiation effects with protons : validation of principle, J. Nucl. Mater. 300 (2002) 198–216.

[2] G.S. Was, Z. Jiao, E. Getto, K. Sun, A.M. Monterrosa, S.A. Maloy, O. Anderoglu, B.H. Sencer, M. Hackett, Emulation of reactor irradiation damage using ion beams, Scr. Mater. 88 (2014) 33–36. doi:10.1016/j.scriptamat.2014.06.003.

[3] S.J. Zinkle, L.L. Snead, Opportunities and limitations for ion beams in radiation effects studies : Bridging critical gaps between charged particle and neutron irradiations, Scr. Mater. (2017). doi:10.1016/j.scriptamat.2017.06.041.

[4] I.L. Singer, Absorption of carbon from residual gases during Ti implantation of alloys, Appl. Phys. Lett. 43 (1983) 457. doi:10.1063/1.94387.

[5] J.G. Gigax, H. Kim, E. Aydogan, F.A. Garner, S. Maloy, J.G. Gigax, H. Kim, E. Aydogan, F.A. Garner, S. Maloy, Beam-contamination-induced compositional alteration and its neutron-atypical consequences in ion simulation of neutron-induced void swelling, Mater. Res. Lett. 0 (2017) 1–8. doi:10.1080/21663831.2017.1323808.

[6] K. Farrell, M.B. Lewis, N.H. Packan, Simultaneous Bombardment with Helium, Hydrogen, and Heavy Ions to Simulate Microstructural Damage from Fission or Fusion Neutrons, Scr. Metall. 12 (1978) 1121–1124.

[7] F.. Garner, M.. Toloczko, B.. Sencer, Comparison of swelling and irradiation creep behavior of fcc-austenitic and bcc-ferritic/martensitic alloys at high neutron exposure, J. Nucl. Mater. 276 (2000) 123–142. doi:10.1016/S0022-3115(99)00225-1.

[8] E. Getto, Z. Jiao, A.M. Monterrosa, K. Sun, G.S. Was, Effect of pre-implanted helium on void swelling evolution in self-ion irradiated HT9, J. Nucl. Mater. 462 (2015) 458–469. doi:10.1016/j.jnucmat.2015.01.045.

[9] X. Wang, A.M. Monterrosa, F. Zhang, H. Huang, Q. Yan, Z. Jiao, G.S. Was, L. Wang, Void swelling in high dose ion-irradiated reduced activation ferritic–martensitic steels, J. Nucl. Mater. 462 (2015) 119–125. doi:10.1016/j.jnucmat.2015.03.050.

[10] I.L. Singer, Carburization of steel surfaces during implantation of Ti ions at high fluences Carburization of steel surfaces during implantation of Ti ions at high fluences, 419 (1983). doi:10.1116/1.571934.

[11] I.L. Singer, Surface analysis, ion implantation and tribological processes affecting steels, Appl. Surf. Sci. 18 (1984) 28–62. http://www.sciencedirect.com/science/article/pii/0378596384900370.

[12] G.S. Was, S. Taller, Z. Jiao, A.M. Monterrosa, D. Woodley, D. Jennings, T. Kubley, F. Naab, O. Toader, E. Uberseder, Resolution of the Carbon Contamination Problem in Ion Irradiation Experiments, Nucl. Instruments Methods Phys. Res. Sect. B Beam Interact. with Mater. Atoms. Accepted (2017).

[13] D.R. Harries, R.L. Klueh, High-Chromium Ferritic and Martensitic Steels for Nuclear Applications, 2001.

[14] J.J. Penisten, The Mechanism of Radiation- Induced Segregation in Ferritic-Martensitic Steels, Ph.D. Thesis. (2012).

[15] G.S. Was, Fundamentals of Radiation Materials Science: Metals and Alloys, Springer, 2007.

[16] B.H. Sencer, J.R. Kennedy, J.I. Cole, S. a. Maloy, F. a. Garner, Microstructural analysis of an HT9 fuel assembly duct irradiated in FFTF to 155dpa at 443°C, J. Nucl. Mater. 393 (2009) 235–241. doi:10.1016/j.jnucmat.2009.06.010.

[17] B.H. Sencer, J.R. Kennedy, J.I. Cole, S. a. Maloy, F. a. Garner, Microstructural stability of an HT-9 fuel assembly duct irradiated in FFTF, J. Nucl. Mater. 414 (2011) 237–242. doi:10.1016/j.jnucmat.2011.03.050.

[18] D.S. Gelles, Microstructural examination of commercial ferritic alloys at 200 dpa, J. Nucl. Mater. 237 (1996) 293–298.

[19] D. Gelles, Microstructural examination of commercial ferritic alloys at 200 dpa, J. Nucl. Mater. 237 (1996) 293–298. http://www.sciencedirect.com/science/article/pii/S002231159600222X (accessed February 4, 2014).

[20] M.B. Toloczko, F.A. Garner, Irradiation creep and void swelling of two LMR heats of HT9 at 400C and 160 dpa, J. Nucl. Mater. 237 (1996) 289–292.

[21] M.. Toloczko, F.A. Garner, Variability of Irradiation Creep and Swelling of HT9 Irradiated to High Neutron Fluence at 400-600C, Eff. Radiat. Mater. 18th Symp. (1999) 765–779.

[22] M.B. Toloczko, F.A. Garner, C.R. Eiholzer, Irradiation creep and swelling of the US fusion heats of HT9 and 9CrklMo to 208 dpa at - 4OV ’ C *, 215 (1994) 604–607.

[23] J.J. Kai, R.L. Klueh, Microstructural analysis of neutron-irradiated martensitic steels, J. Nucl. Mater. 230 (1996) 116–123.

[24] J.M. Vitek, R.L. Klueh, Microstructure of 9Cr-1MoVNb Steel Irradiated to 36 dpa at Elevated Temperatures in HFIR, J. Nucl. Mater. 123 (1984) 254–259.

[25] E.A. Little, Microstructural evolution in irradiated ferritic-martensitic steels: transitions to high dose behaviour, 206 (1993) 324–334.

[26] G.R. Odette, On mechanisms controlling swelling in ferritic and martensitic alloys, J. Nucl. Mater. 157 (1988) 921–927.

[27] A.. Dvoriashin, S.. Porollo, Y.. Konobeev, F.A. Garner, Influence of high dose neutron irradiation on microstructure of EP-450 ferritic–martensitic steel irradiated in three Russian fast reactors, J. Nucl. Mater. 329–333 (2004) 319–323. doi:10.1016/j.jnucmat.2004.04.309.

[28] A. Ward, S. Fisher, A Comparison of Heavy Ion-Irradiated Ferritic and Austenitic Steels in the Early Stages of Damage, Eff. Radiat. Mater. 15th Int. Symp. ASTM STP 1125. (1992) 1167–1179.

[29] G. Ayrault, Cavity Formation During Single and Dual-Ion Irradiation in a 9Cr-1Mo Ferritic Alloy, J. Nucl. Mater. 114 (1983) 34–40.

[30] R. Hide, K. Kusanagi, M. Taguchi, Microstructural Change in Ferritic Steels Under Heavy Ion Irradiation, Eff. Radiat. Mater. 14th Int. Symp. ASTM STP 1046. (1989) 61–72.

[31] K. Asano, Y. Kohno, A. Kohyama, T. Suzuki, H. Kusanagi, Microstructural Evolution of an Oxide Dispersion Strengthened Steel Under Charged Particle Irradiation, J. Nucl. Mater. 155–157 (1988) 928–934.

[32] R. Sindelar, J.J. Kai, D. Plumton, R. Dodd, G. Kulcinski, Microstructural Modification of 21/4 Cr-1Mo Steel by Irradiation with 14 MeV Nickel Ions, Nucl. Instruments Methods Phys. Res. 16 (1986) 260–269.

[33] A.M. Dvoriashin, V.D. Dmitriev, V.S. Khabarov, The Effect of Neutron Irradiation on the Microstructure and Tensile Properties of 1Cr13Mo2NbVB Steel, Eff. Radiat. Mater. 15th Int. Symp. (1992) 1180–1189.

[34] J.J. Kai, G.L. Kulcinski, 14 MeV nickel-ion irradiated HT-9 ferritic steel with and without helium pre-implantation, J. Nucl. Mater. 175 (1990) 237–243. doi:10.1016/0022-3115(90)90212-6.

[35] F.A. Smidt, P.R. Malmberg, J.A. Sprague, J.E. Westmoreland, Swelling Behavior of Commercial Ferritic Alloys, EM-12 and HT-9, as Assessed by Heavy Ion Bombardment, Irradiat. Eff. Microstruct. Prop. Met. (1976) 227–241.

[36] E. Wakai, T. Sawai, K. Furuya, a. Naito, T. Aruga, K. Kikuchi, S. Yamashita, S. Ohnuki, S. Yamamoto, H. Naramoto, S. Jistukawa, Effect of triple ion beams in ferritic/martensitic steel on swelling behavior, J. Nucl. Mater. 307–311 (2002) 278–282. doi:10.1016/S0022-3115(02)01076-0.

[37] M.B. Toloczko, F.A. Garner, V.N. Voyevodin, V. V. Bryk, O. V. Borodin, V. V. Mel'Nychenko, A.S. Kalchenko, Ion-induced swelling of ODS ferritic alloy MA957 tubing to 500 dpa, J. Nucl. Mater. 453 (2014) 323–333. doi:10.1016/j.jnucmat.2014.06.011.

[38] L.K. Mansur, Theory of transitions in dose dependence of radiation effects in structural alloys, J. Nucl. Mater. 206 (1993) 306–323. doi:10.1016/0022-3115(93)90130-Q.

[39] T.A. Kenfield, W.K. Appleby, H.J. Busboom, W.L. Bell, SWELLING OF TYPE-316

STAINLESS STEEL AT HIGH FLUENCES IN EBR-II, i (1978) 85–97.

[40] I.-S. Kim, J.. Hunn, N. Hashimoto, D.. Larson, P.. Maziasz, K. Miyahara, E.. Lee, Defect and void evolution in oxide dispersion strengthened ferritic steels under 3.2 MeV Fe+ ion irradiation with simultaneous helium injection, J. Nucl. Mater. 280 (2000) 264–274. doi:10.1016/S0022-3115(00)00066-0.

[41] E.H. Lee, L.K. Mansur, Unified theoretical analysis of experimental swelling data for irradiated austenitic and ferritic/martensitic alloys, Metall. Trans. A. 21 (1990) 1021–1035. doi:10.1007/BF02656524.

[42] P. Dubuisson, D. Gilbon, J. Seran, Microstructural evolution of ferritic-martensitic irradiated in the fast breeder reactor Phenix, J. Nucl. Mater. 205 (1993) 178–189.

[43] R.L. Sindelar, A Comparison of the Response of 316 SS and the P7 Alloy to Heavy-Ion Irradiation, Ph.D. Thesis. (1985).

[44] S.J. Zinkle, E.H. Lee, Effect of Oxygen on Vacancy Cluster Morphology in Metals, Metall. Trans. A. 21A (1990).

[45] S.J. Zinkle, L.E. Seitzman, W.G. Wolfer, Energy calculations for pure metals, Philos. Mag. A. 55 (2006). doi:10.1080/01418618708209803.

[46] R.E. Stoller, G.R. Odette, A comparison of the relative importance of helium and vacancy accumulation in void nucleation, Radiat. Induc. Chang. Microstruct. 13th Int. Symp. (1987) 358–370.

[47] R.E. Stoller, The influence of helium on microstructural evolution: Implications for DT fusion reactors, J. Nucl. Mater. 174 (1990) 289–310.

[48] K. Farrell, P.J. Maziasz, E.H. Lee, L.K. Mansur, Modification of Radiation Damage Microstructure by Helium, Radiat. Eff. 78 (1983) 277–295.

[49] K. Farrell, Experimental Effects of Helium on Cavity Formation During Irradiation - A Review, Radiat. Eff. 53 (1980) 175–194.

[50] N.H. Packan, K. Farrell, Simulation of First Wall Damage: Effects of the Method of Gas Implantation, J. Nucl. Mater. 86 (1979) 677–681.

[51] Z. Jiao, N. Ham, G.S. Was, Microstructure of helium-implanted and proton-irradiated T91 ferritic/martensitic steel, J. Nucl. Mater. 367–370 A (2007) 440–445. doi:10.1016/j.jnucmat.2007.03.118.

[52] S.J. Zinkle, K. Farrell, Void swelling and defect cluster formation in reactor-irradiated copper, J. Nucl. Mater. 168 (1989) 262–267.

[53] S.J. Zinkle, K. Farrell, Microstructure and cavity swelling in reactor-irradiated dilute copper-boron alloy, J. Nucl. Mater. 179–181 (1991) 994–997. doi:10.1016/0022-3115(91)90258-9.

[54] S.J. Zinkle, G.L. Klucinski, R.W. Knoll, Microstructure of copper following high dose 14MeV Cu ion irradiation, J. Nucl. Mater. 138 (1986) 46–56. doi:10.1016/0022-3115(86)90254-0.

[55] B.N. Singh, S.J. Zinkle, Defect accumulation in pure fcc metals in the transient regime: a review, J. Nucl. Mater. 206 (1993) 212–229.

[56] Y.N. Osetsky, A. Serra, B.N. Singh, S.I. Golubov, Structure and properties of clusters of self-interstitial atoms in fcc copper and bcc iron, Philos. Mag. A. 80 (2000) 2131–2157. doi:10.1080/01418610008212155.

[57] J.M. Leitnaker, E. Bloom, J.O. Stiegler, The Effect of Minor Constituents on Swelling in Stainless Steel, J. Nucl. Mater. 49 (1973) 57–66.

[58] M.J. Makin, G.P. Walters, A.J.E. Foreman, The Void Swelling Behaviour of Electron Irradiated Type 316 Austenitic Steel, J. Nucl. Mater. 95 (1980) 155–170.

[59] D.M. Follstaedt, J.A. Knapp, S.T. Picraux, Carbon-induced amorphous surface layers in Ti-implanted Fe, 330 (1980). doi:10.1063/1.91893.

[60] G.J. Thomas, W. Bauer, Carbide formation on Nb surfaces during high-temperature H irradiation, 490 (1975). doi:10.1116/1.568570.

[61] T.M. Williams, The Effect of Soluble Carbon on Void Swelling and Low Dose Dislocation Structures in Type 316 Austenitic Stainless Steel Irradiated with 46.5 MeV Ni6+ Ions, J. Nucl. Mater. 88 (1980) 217–225.

[62] E.A. Little, Void-Swelling in Irons and Ferritic Steels I. Mechanisms of swelling suppression, J. Nucl. Mater. 87 (1979) 11–24.

[63] D. Terentyev, K. Heinola, A. Bakaev, E.E. Zhurkin, Carbon – vacancy interaction controls lattice damage recovery in iron, Scr. Mater. 86 (2014) 9–12. doi:10.1016/j.scriptamat.2014.04.003.

[64] C. Xu, In-Situ Proton Irradiation Creep of FM Steel T91, Ph.D. Thesis. (2014).

[65] F. Naab, Personal communication, (2018).

[66] J.F. Ziegler, M.D. Ziegler, J.P. Biersack, Nuclear Instruments and Methods in Physics Research B SRIM – The stopping and range of ions in matter (2010), Nucl. Inst. Methods Phys. Res. B. 268 (2010) 1818–1823. doi:10.1016/j.nimb.2010.02.091.

[67] R.E. Stoller, M.B. Toloczko, G.S. Was, A.G. Certain, S. Dwaraknath, F.A. Garner, On the use of SRIM for computing radiation damage exposure, Nucl. Instruments Methods Phys. Res. Sect. B Beam Interact. with Mater. Atoms. 310 (2013) 75–80. doi:10.1016/j.nimb.2013.05.008.

[68] J.G. Gigax, E. Aydogan, T. Chen, D. Chen, L. Shao, Y. Wu, W.Y. Lo, Y. Yang, F.A. Garner, The influence of ion beam rastering on the swelling of self-ion irradiated pure iron at 450 C, J. Nucl. Mater. 465 (2015). doi:10.1016/j.jnucmat.2015.05.025.

[69] E. Getto, Z. Jiao, a. M. Monterrosa, K. Sun, G.S. Was, Effect of irradiation mode on the microstructure of self-ion irradiated ferritic-martensitic alloys, J. Nucl. Mater. 465 (2015) 116–126. doi:10.1016/j.jnucmat.2015.05.016.

[70] T. Malis, S.C. Cheng, R.F. Egerton, EELS Log-Ratio Technique for Specimen-Thickness Measurement in the TEM, J. Electron Microsc. Tech. (1988) 193–200.

doi:10.1002/jemt.1060080206.

[71] C.M. Parish, K.G. Field, Application of STEM characterization for investigating radiation effects in BCC Fe-based alloys, (2017). doi:10.1557/jmr.2015.32.

[72] S. Smith, L. Guttman, Measurement of Internal Boundaries in Three-Dimensional Structures By Random Sectioning, J. Met. Trans. (1953) 81–87.

[73] E. Getto, K. Sun, G.S. Was, Characterization of M2X formed during 5 MeV Fe2 + irradiation, J. Nucl. Mater. 485 (2016) 7–12. doi:10.1016/j.jnucmat.2016.12.027.

[74] X. Wang, Q. Yan, G.S. Was, L. Wang, Void swelling in ferritic-martensitic steels under high dose ion irradiation : Exploring possible contributions to swelling resistance, Scr. Mater. 112 (2016) 9–14. doi:10.1016/j.scriptamat.2015.08.032.

[75] A.D. Brailsford, L.K. Mansur, The effect of precipitate-matrix interface sinks on the growth of voids in the matrix, J. Nucl. Mater. 104 (1981) 1403–1408. doi:10.1016/0022-3115(82)90796-6.

[76] M. Mayer, SIMNRA , a Simulation Program for the Analysis of NRA , RBS and ERDA, Proc. 15th Int. Conf. Appl. Accel. Res. Ind. 475 (1999).

[77] A.F. Gurbich, Nuclear Instruments and Methods in Physics Research B SigmaCalc recent development and present status of the evaluated cross-sections for IBA, Nucl. Inst. Methods Phys. Res. B. 371 (2016) 27–32. doi:10.1016/j.nimb.2015.09.035.

[78] C.R. Gossett, V. Nuclear, R. Analysis, 2 Expenmental difficulties with the (3He , a) reaction, 191 (1981) 335–340.

[79] O. V Borodin, V.N. Voyevodin, V.F. Zelenskij, M. Ivan, P. V Platonov, R. Borodin, Radiation Damage Studies of the 10 to 13 % Chromium-Containing Steels and Alloys Irradiated with Heavy Ions, Eff. Radiat. Mater. 15th Int. Symp. ASTM STP 1125. (1992) 1157–1166.

[80] P.J. Maziasz, Formation and Stability of Radiation-Induced Phases in Neutron-Irradiated Austenitic and Ferritic Steels, J. Nucl. Mater. 169 (2008) 95–115.

[81] E. Getto, K. Sun, A.M. Monterrosa, Z. Jiao, M.J. Hackett, G.S. Was, Void swelling and microstructure evolution at very high damage level in self-ion irradiated ferritic-martensitic steels, J. Nucl. Mater. 480 (2016) 159–176. doi:10.1016/j.jnucmat.2016.08.015.

[82] A. Hishinuma, L.K. Mansur, Critical Radius for Bias-Driven Swelling - A Further Analysis and its Application to Bimodal Cavity Size Distributions, 118 (1983) 91–99.

[83] A. Hishinuma, J. Vitek, J. Horak, E. Bloom, Effect of Preinjected Helium on Swelling and Microstructure of Neutron Irradiated Pressurized Tubes of Type 316 Stainless Steel, Eff. Radiat. Mater. 11th Int. Symp. ASTM STP 782. (1982) 92–107.

[84] D. Carpentier, T. Jourdan, Y. Le Bouar, M.. Marinica, Effect of saddle point anisotropy of point defects on their absorption by dislocations and cavities, Acta Mater. 136 (2017) 323–334. doi:10.1016/j.actamat.2017.07.013.

[85] V.A. Borodin, A.I. Ryazanov, C. Abromeit, Void bias factors due to the anisotropy of the point defect diffusion, J. Nucl. Mater. 207 (1993) 242–254.

[86] M.P. Surh, W.G. Wolfer, Accurate Mean Field Void Bias Factors for Radiation Swelling Calculations, J. Comput. Mater. Des. 14 (2007) 419–424. doi:10.1007/s10820-007-9052-2.

[87] A.A. Kohnert, M. Alice, B.D. Wirth, Molecular statics calculations of the biases and point defect capture volumes of small cavities, J. Nucl. Mater. 499 (2018) 480–489. doi:10.1016/j.jnucmat.2017.12.005.

[88] Q. Li, C.M. Parish, K.A. Powers, M.K. Miller, Helium solubility and bubble formation in a nanostructured ferritic alloy q, 445 (2014) 165–174.

[89] R. Sugano, K. Morishita, H. Iwakiri, N. Yoshida, Effects of dislocation on thermal helium desorption from iron and ferritic steel, J. Nucl. Mater. 307–311 (2002) 941–945. doi:10.1016/S0022-3115(02)01098-X.

[90] P.D. Edmondson, C.M. Parish, Y. Zhang, A. Hallén, M.K. Miller, Helium bubble distributions in a nanostructured ferritic alloy q, 434 (2013) 210–216.

[91] E. Getto, G. Vancoevering, G.S. Was, The co-evolution of microstructure features in self-ion irradiated HT9 at very high damage levels, J. Nucl. Mater. 484 (2017) 193–208. doi:10.1016/j.jnucmat.2016.12.006.

[92] T.M. Williams, B.L. Eyre, Void-swelling in solution-treated FV548 steel irradiated in a high-voltage electron microscope, J. Nucl. Mater. 59 (1976) 18–28. doi:10.1016/0022-3115(76)90004-0.

[93] C.J. Ortiz, M. Caturla, C. Fu, F. Willaime, Influence of carbon on the kinetics of He migration and clustering in α-Fe from first principles, Phys. Rev. B. 80 (2009) 134109. doi:10.1103/PhysRevB.80.134109.

[94] E. Getto, The Co-Evolution of Microstructure Features in Self-Ion Irradiated HT9 at Very High Damage Levels, 2016.

[95] H. Takahasi, T. Takeyama, S. Nakahigashi, M. Terasawa, Carbon Segregation Around Voids in C+ Ion-Irradated Iron, J. Nucl. Mater. 98 (1981) 227–230.

[96] K. Ono, K. Arakawa, K. Hojou, Formation and migration of helium bubbles in Fe and Fe – 9Cr ferritic alloy, J. Nucl. Mater. 311 (2002) 1507–1512.

[97] J. Pu, L. Yang, X.T. Zu, F. Gao, A molecular dynamics study of helium bubble stability during high-energy displacement cascades in a-iron, Phys. B. 398 (2007) 65–70. doi:10.1016/j.physb.2007.04.091.

[98] N.M. Ghoniem, Nucleation and growth theory of cavity evolution under conditions of cascade damage and high helium generation, J. Nucl. Mater. 174 (1990) 168–177.

[99] H. Trinkaus, B.N. Singh, Helium accumulation in metals during irradiation – where do we stand?, J. Nucl. Mater. 323 (2003) 229–242. doi:10.1016/j.jnucmat.2003.09.001.

[100] R.S. Nelson, The Stability of Gas Bubbles in an Irradiation Environment, J. Nucl. Mater.

31 (1969) 153–161.

[101] P. Dauben, R.P. Wahi, H. Wollenberger, Bubble Nucleation and Growth in an Fe-12 at% Cr Ferritic Alloy Under He+ Implantation and Fe+ Irradiation, J. Nucl. Mater. 141–143 (1986) 723–726.

[102] K. Morishita, R. Sugano, B.D. Wirth, MD and KMC modeling of the growth and shrinkage mechanisms of helium – vacancy clusters in Fe, J. Nucl. Mater. 323 (2003) 243–250. doi:10.1016/j.jnucmat.2003.08.019.

[103] G. Lucas, R. Schäublin, Stability of helium bubbles in alpha-iron : A molecular dynamics study, J. Nucl. Mater. 386–388 (2009) 360–362. doi:10.1016/j.jnucmat.2008.12.128.

[104] M.J. Demkowicz, A. Misra, A. Caro, The role of interface structure in controlling high helium concentrations, Curr. Opin. Solid State Mater. Sci. 16 (2012) 101–108. doi:10.1016/j.cossms.2011.10.003.

[105] W. Kesternich, Helium trapping at dislocations , precipitates and grain boundaries, 7579 (2017). doi:10.1080/00337578308207376.

[106] A. Kashinath, P. Wang, J. Majewski, J.K. Baldwin, Y.Q. Wang, M.J. Demkowicz, Detection of helium bubble formation at fcc-bcc interfaces using neutron reflectometry, J. Appl. Phys. 43505 (2014).

[107] A. Kashinath, A. Misra, M.J. Demkowicz, Stable Storage of Helium in Nanoscale Platelets at Semicoherent Interfaces, 86101 (2013) 1–5. doi:10.1103/PhysRevLett.110.086101.

[108] H.L. Heinisch, F. Gao, R.J. Kurtz, E. a. Le, Interaction of helium atoms with edge dislocations in α-Fe, J. Nucl. Mater. 351 (2006) 141–148. doi:10.1016/j.jnucmat.2006.02.027.

[109] M.J. Caturla, C.J. Ortiz, Effect of self-interstitial cluster migration on helium diffusion in iron, 362 (2007) 141–145. doi:10.1016/j.jnucmat.2007.01.017.

[110] M.K. Miller, P.D. Edmondson, C.M. Parish, Y. Zhang, A. Halle, Helium entrapment in a nanostructured ferritic alloy, 65 (2011) 731–734. doi:10.1016/j.scriptamat.2011.07.024.

[111] S. Zhang, E. Yu, S. Gates, W. Cassata, J. Makel, M. Andrew, C. Bartel, A.W. Weimer, R. Faller, P. Stroeve, Helium interactions with alumina formed by atomic layer deposition show potential for mitigating problems with excess helium in spent nuclear fuel, J. Nucl. Mater. (2017). doi:10.1016/j.jnucmat.2017.11.029.

[112] S. Fréchard, M. Walls, M. Kociak, J.P. Chevalier, J. Henry, D. Gorse, Study by EELS of helium bubbles in a martensitic steel, J. Nucl. Mater. 393 (2009) 102–107. doi:10.1016/j.jnucmat.2009.05.011.